



BİNGÖL
ÜNİVERSİTESİ

e-ISSN 2149-6366

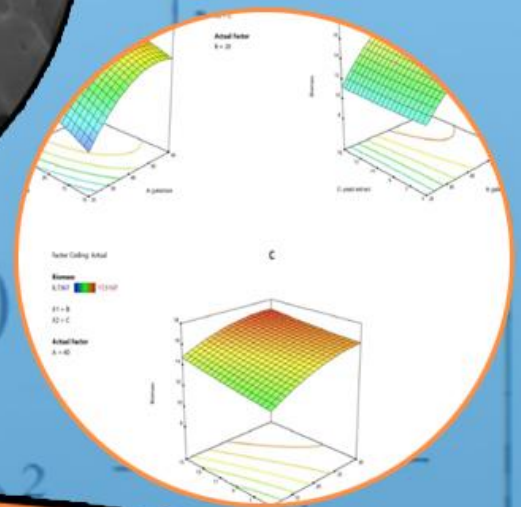
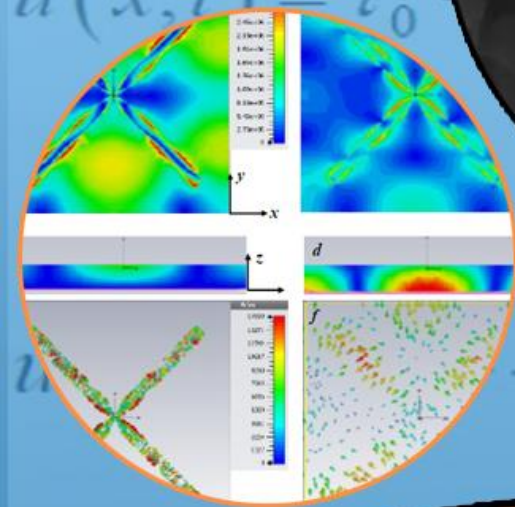
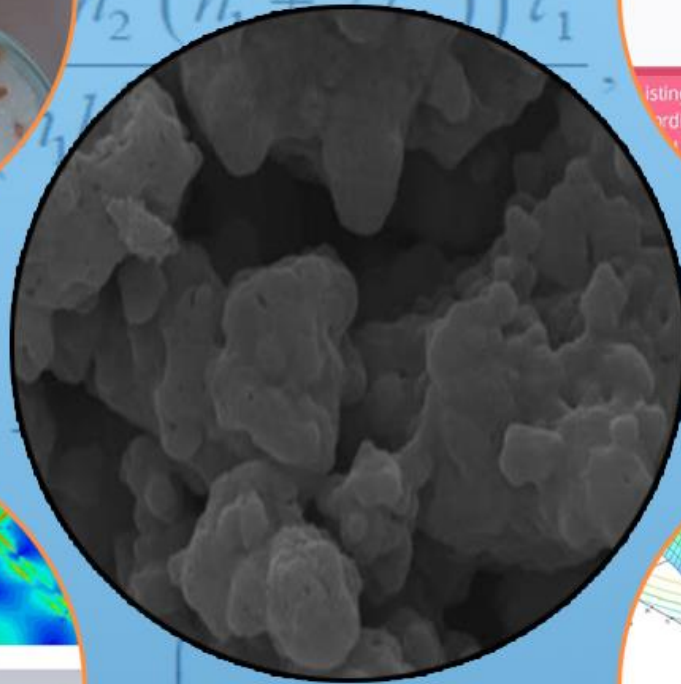
Cilt 13, Sayı 2, Haziran 2024
Volume 13, Issue 2, June 2024

TDFD

TÜRK DOĞA ve FEN DERGİSİ

TURKISH JOURNAL OF NATURE AND SCIENCE

TJNS



www.dergipark.gov.tr/tdfd

Bingöl Üniversitesi Fen Bilimleri Enstitüsü tarafından
yayımlanmaktadır.

Published by Bingöl University Institute of Science

ULAKBİM

TRDİZİN

TÜRK DOĞA VE FEN DERGİSİ

Amaç

Türk Doğa ve Fen Dergisi, Dergipark tarafından yayınlanan Bingöl Üniversitesi Fen Bilimleri Enstitüsüne ait ulusal ve hakemli bir dergidir. Türk Doğa ve Fen Dergisi, Türkiye ve dünyanın her yerinden gelen doğa ve fen bilimlerinin her alanında özgün, yayımlanmamış, yayımlanmak üzere başka yere gönderilmemiş makale, derleme ve sempozyum değerlendirmesi gibi çalışmaların bilim alemine sunulması amacıyla kurulmuştur.

Kapsam

Türk Doğa ve Fen Dergisinde Mühendislik, Ziraat, Veterinerlik, Fen ve Doğa Bilimleri alanlarından olmak üzere Türkçe ve İngilizce hazırlanmış orijinal makale, derleme ve sempozyum değerlendirmesi gibi çalışmalar yayımlanır. Türk Doğa ve Fen Dergisi sadece online sistemde yayımlanmakta olup ayrıca kağıt baskısı bulunmamaktadır.

Merhaba...

Türk Doğa ve Fen Dergisi, Dergipark tarafından yayımlanmakta olup Bingöl Üniversitesi Fen Bilimleri Enstitüsüne aittir. Bahar ve güz dönemi olmak üzere yılda iki defa çıkarılan ulusal hakemli bir dergi olarak ilk sayısını 2012 bahar döneminde yayımlamıştır. Türk Doğa ve Fen Dergisi, Türkiye ve dünyanın her yerinden gelen doğa ve fen bilimlerinin her alanında özgün, yayımlanmamış, yayımlanmak üzere başka yere gönderilmemiş makale, derleme ve sempozyum değerlendirmesi gibi çalışmaların bilim alemine sunulması amacıyla kurulmuştur. İlk sayısından bugüne kesintisiz olarak faaliyetlerini sürdürmektedir.

Türk Doğa ve Fen Dergisi sadece online sistemde yayımlanmakta olup ayrıca kağıt baskısı bulunmamaktadır. Dergimize gelen her çalışma öncelikle Turnitin intihal programında taranmaktadır. Dergimizde editörlerin, hakemlerin ve yazarların, uluslararası yayım etik kurallarına uyması ve makalelerin yazım kurallarına uyumlu olması zorunluluğu vardır.

Yazarlar yayımlanmak üzere dergimize gönderdikleri çalışmalarını ile ilgili telif haklarını zorunlu olarak Bingöl Üniversitesi Türk Doğa ve Fen Dergisi'ne devretmiş sayılırlar. Yazarlardan herhangi bir ücret talep edilmemektedir. Yazarların değerlendirmeleri, dergimizin resmi görüşü olarak kabul edilemez. Çalışmaların her türlü sorumluluğu yazarlarına aittir. Araştırma ürünleri için etik kurul raporu gerekli ise, çalışma üzerinde bu raporun alınmış olduğu belirtilmeli ve kurul raporu sisteme kaydedilmelidir. Araştırma ile ilgili intihal, atıf manipülasyonu, sahte veri uydurma vb. suistimallerin tespit edilmesi halinde yayım ve etik ilkelerine göre davranılır. Bu durumda çalışmanın yayımlanmasını önlemek, yayımdan kaldırmak ya da başka işlemler yapmak için gerekli işlemler takip edilmektedir.

Dergimizde, kaynak gösteriminde uluslararası Vancouver sistemine geçilmiştir. Ayrıca dergimiz, Creative Commons ile lisanslanmak suretiyle dergimizde yayımlanan makalelerin paylaşımı, kaynak gösterimi ve yayımlanmasında dergi ve yazar haklarını korumaya almıştır. 2018 yılı güz döneminden itibaren makaleler, uluslararası yazar kimlik numarası ORCID No'su ile yayımlanmaktadır.

Dergi ekibi, dergimizin ulusal ve uluslararası indekslerce taranan bir dergi olması yönünde çalışmalarını titizlikle sürdürmektedir. Dergimize gösterilen ilgi bu yönde bizleri teşvik etmeye devam edecektir.

Bingöl Üniversitesi Fen Bilimleri Enstitüsü tarafından yayımlanmaktadır

EDİTÖRLER (YAYIN) KURULU

BAŞEDİTÖR

Doç. Dr. Ekrem DARENDELİOĞLU

Bingöl Üniversitesi, Fen-Edebiyat Fakültesi, Moleküler Biyoloji ve Genetik
Bölümü

E-Mail: edarendelioglu@bingol.edu.tr

EDİTÖR YARDIMCILARI

Doç. Dr. Adnan AYNA

Bingöl Üniversitesi, Fen-Edebiyat Fakültesi, Kimya Bölümü

E-Mail: aayna@bingol.edu.tr

Dr. Öğr. Üyesi Mücahit ÇALIŞAN

Bingöl Üniversitesi, Mühendislik-Mimarlık Fakültesi, Bilgisayar Mühendisliği

E-Mail: mcalisan@bingol.edu.tr

EDİTÖRLER

Fen ve Doğa Bilimleri

Doç. Dr. İkram ORAK

Bingöl Üniversitesi, Sağlık Hizmetleri Meslek Yüksekokulu, Tıbbi Hizmetler ve
Teknikler

E-Mail: iorak@bingol.edu.tr

Prof. Dr. Selami SELVİ

Balıkesir Üniversitesi, Altınoluk Meslek Yüksekokulu, Bitkisel ve Hayvansal
Üretim Bölümü

E-Mail: sselvi2000@yahoo.com

Prof. Dr. Refik KESKİN

Sakarya Üniversitesi, Fen-Edebiyat Fakültesi, Matematik Bölümü

E-Mail: rkeskin@sakarya.edu.tr

Prof. Dr. Halim ÖZDEMİR

Sakarya Üniversitesi, Fen-Edebiyat Fakültesi, Matematik Bölümü

E-Mail: hozdemir@sakarya.edu.tr

Prof. Dr. Zafer ŞİAR

Bingöl Üniversitesi, Fen-Edebiyat Fakültesi, Matematik Bölümü
E-Mail: zsiar@bingol.edu.tr

Prof. Dr. Uğur ÇAKILCIOĞLU

Munzur Üniversitesi, Pertek Sakine Genç Meslek Yüksekokulu, Bitki Morfolojisi
ve Anatomisi Bölümü
E-Mail: ucakilcioglu@yahoo.com

Doç. Dr. Kamuran DİLSİZ

Bingöl Üniversitesi, Fen-Edebiyat Fakültesi, Fizik Bölümü
E-Mail: kdilsiz@bingol.edu.tr

Doç. Dr. Şükran KONCA

Bakırçay Üniversitesi, Mühendislik ve Mimarlık Fakültesi, Temel Bilimler,
Matematik Bölümü
E-Mail: sukran.konca@bakircay.edu.tr

Doç. Dr. İdris YAZGAN

Kastamonu Üniversitesi, Fen Edebiyat Fakültesi, Biyoloji
E-Mail: idrisyazgan@gmail.com

Doç. Dr. Abdulcabbar YAVUZ

Gaziantep Üniversitesi, Mühendislik Fakültesi, Metalurji ve Malzeme Mühendisliği
E-Mail: ayavuz@gantep.edu.tr

Doç. Dr. Bünyamin ALIM

Bayburt Üniversitesi, Teknik Bilimler Meslek Yüksekokulu, Elektrik ve Enerji
Bölümü
E-Mail: balim@bayburt.edu.tr

Dr. Öğr. Üyesi Mustafa Şükrü KURT

Erzurum Teknik Üniversitesi, Fen Fakültesi, Temel Bilimler
E-Mail: mustafa.kurt@erzurum.edu.tr

Dr. Öğr. Üyesi Sinan SAĞIR

Karamanoğlu Mehmetbey Üniversitesi, Fizik
E-Mail: sinansagir@kmu.edu.tr / sinan.sagir@cern.ch

Doç. Dr. Murat AYDEMİR

Erzurum Teknik Üniversitesi, Fen Fakültesi, Temel Bilimler

E-Mail: murat.aydemir@erzurum.edu.tr

Mühendislik Bilimleri

Prof. Dr. Figen KOREL

İzmir Yüksek Teknoloji Enstitüsü, Gıda Mühendisliği Bölümü

E-Mail: figenkorel@iyte.edu.tr

Prof. Dr. Kubilay ASLANTAŞ

Afyon Kocatepe Üniversitesi, Teknoloji Fakültesi, Makine Mühendisliği Bölümü

E-Mail: aslantas@aku.edu.tr

Prof. Dr. Hamit Özkan GÜLSOY

Marmara Üniversitesi, Teknoloji Fakültesi, Metalurji ve Malzeme Mühendisliği
Bölümü

E-Mail: ogulsoy@marmara.edu.tr

Prof. Dr. Ali Adnan HAYALOĞLU

İnönü Üniversitesi, Mühendislik Fakültesi, Gıda Mühendisliği Bölümü

E-Mail: adnan.hayaloglu@inonu.edu.tr

Prof. Dr. Barbara SAWICKA

University of Life Sciences in Lublin, Department of Plant Production Technology
and Commodities Sciences

E-Mail: barbara.sawicka@gmail.com

Prof. Dr. İbrahim GÜNEŞ

Giresun Üniversitesi, Mühendislik Fakültesi, İnşaat Mühendisliği Bölümü

E-Mail: ibrahim.gunes@giresun.edu.tr

Doç. Dr. Serhat ŞAP

Bingöl Üniversitesi, Teknik Bilimler Meslek Yüksekokulu, Elektrik ve Enerji
Bölümü

E-Mail: ssap@bingol.edu.tr

Doç. Dr. Sırma YEĞİN

Ege Üniversitesi, Mühendislik Fakültesi, Gıda Mühendisliği Bölümü
E-Mail: sirma.yegin@ege.edu.tr

Doç. Dr. Hasan OĞUL

Sinop Üniversitesi, Mimarlık ve Mühendislik Fakültesi, Nükleer Enerji
Mühendisliği
E-Mail: hogul@sinop.edu.tr

Doç. Dr. Murat YILMAZTEKİN

İnönü Üniversitesi, Mühendislik Fakültesi, Gıda Mühendisliği Bölümü
E-Mail: murat.yilmaztekin@inonu.edu.tr

Doç. Dr. Ferhat AYDIN

Sakarya Uygulamalı Bilimler Üniversitesi, Teknoloji Fakültesi, İnşaat
Mühendisliği Bölümü
E-Mail: ferhata@subu.edu.tr

Dr. Öğr. Üyesi Nurullah DEMİR

Bingöl Üniversitesi, Mühendislik ve Mimarlık Fakültesi, Gıda Mühendisliği
Bölümü
E-Mail: ndemir@bingol.edu.tr

Doç. Dr. Ahmet GÜNER

Bingöl Üniversitesi, Mühendislik ve Mimarlık Fakültesi, Elektrik ve Elektronik
Mühendisliği Bölümü
E-Mail: aguner@bingol.edu.tr

Dr. Öğr. Üyesi Tahir AKGÜL

Sakarya Uygulamalı Bilimler Üniversitesi, Teknoloji Fakültesi, İnşaat
Mühendisliği Bölümü
E-Mail: tahirakgul@subu.edu.tr

Dr. Erhan Sulejmani

University of Tetova, Faculty of Food Technology and Nutrition
E-Mail: erhan.sulejmani@unite.edu.mk

Dr. Hacène Medjoudj

Larbi Ben M'Hidi University of Oum El Bouaghi, Food Science Department
E-Mail: medjoudjh@yahoo.com

Dr. Avinash Lakshmikanthan

Nitte Meenakshi Institute of Technology, Department of Mechanical Engineering,
Karnataka, India
E-Mail: avinash.laks01@gmail.com

Dr. Manjunath Patel GC

PES Institute of Technology and Management, Department of Mechanical
Engineering, Karnataka, India
E-Mail: manju09mpm05@gmail.com

Sağlık Bilimleri

Doç. Dr. Aydın Şükrü BENGÜ

Bingöl Üniversitesi, Sağlık Hizmetleri Meslek Yüksekokulu, Tıbbi Hizmetler ve
Teknikler
E-Mail: abengu@bingol.edu.tr

Dr. Öğr. Üyesi Dilhun Keriman ARSERİM UÇAR

Bingöl Üniversitesi, Sağlık Bilimleri Fakültesi, Beslenme ve Diyetetik Bölümü
E-Mail: dkucar@bingol.edu.tr

Dr. Öğr. Üyesi Abdullah TUNÇ

Bingöl Üniversitesi, Sağlık Bilimleri Fakültesi, İş Sağlığı ve Güvenliği Bölümü
E-Mail: atunc@bingol.edu.tr

Dr. Öğr. Üyesi Ramazan GÜNDOĞDU

Bingöl Üniversitesi, Sağlık Hizmetleri Meslek Yüksekokulu, Eczane Hizmetleri
E-Mail: rgundogdu@bingol.edu.tr

Dr. Alexander HERGOVICH

UCL Cancer Institute, Faculty of Medical Sciences, Department of Cancer Biology,
UCL, London, UK
E-Mail: a.hergovich@uc.ac.uk

Dr. Valenti GOMEZ

UCL Cancer Institute, Faculty of Medical Sciences, Department of Oncology,
UCL, London, UK

E-Mail: valentin.gomez@ucl.ac.uk

Veterinerlik Bilimleri

Doç. Dr. Cüneyt ÇAĞLAYAN

Bilecik Şeyh Edebali Üniversitesi, Tıp Fakültesi, Temel Tıp Bilimleri Bölümü,
Tıbbi Biyokimya Anabilim Dalı

E-Mail: cuneyt.caglayan@bilecik.edu.tr

Prof. Dr. Fatih Mehmet KANDEMİR

Atatürk Üniversitesi, Veteriner Fakültesi, Veteriner Hekimliği Temel Bilimler

E-Mail: fmehmet.kandemir@atauni.edu.tr

Doç. Dr. Akın KIRBAŞ

Bozok Üniversitesi, Veteriner Fakültesi, Klinik Bilimler Bölümü

E-Mail: akindahiliye55@yahoo.com

Doç. Dr. Emrah Hicazi AKSU

Atatürk Üniversitesi, Veteriner Fakültesi, Klinik Bilimler Bölümü

E-Mail: emrahaksu@atauni.edu.tr

Ziraat Bilimleri

Doç. Dr. Zeynep DUMANOĞLU

Bingöl Üniversitesi, Ziraat Fakültesi, Biyosistem Mühendisliği Bölümü

E-Mail: zdumanoglu@bingol.edu.tr

Prof. Dr. Kağan KÖKTEN

Bingöl Üniversitesi, Ziraat Fakültesi, Tarla Bitkileri Bölümü

E-Mail: kahafe1974@yahoo.com

Prof. Dr. Mustafa SÜR MEN

Adnan Menderes Üniversitesi, Ziraat Fakültesi, Tarla Bitkileri Bölümü

E-Mail: mustafa.surmen@adu.edu.tr

Prof. Dr. Banu YÜCEL

Ege Üniversitesi, Ziraat Fakültesi, Hayvan Yetiştirme Anabilim Dalı, Zootekni
Bölümü

E-Mail: banu.yucel@ege.edu.tr

Doç. Dr. Hakan İNCİ

Bingöl Üniversitesi, Ziraat Fakültesi, Zootekni Bölümü

E-Mail: hinci@bingol.edu.tr

TEKNİK EDİTÖRLER

Dr. Nimetullah KORKUT

Bingöl Üniversitesi, BİNÜZEM, Bilgisayar Teknolojileri

E-Mail: nkorkut@bingol.edu.tr

Öğr. Gör. MEHMET VURAL

Bingöl Üniversitesi, Genç Meslek Yüksek Okulu, Bilgisayar Teknolojileri

E-Mail: mvural@bingol.edu.tr

DİL EDİTÖRÜ

Öğr. Gör. Dr. Ahmet KESMEZ

Bingöl Üniversitesi, Yabancı Diller Yüksekokulu, İngilizce Bölümü

E-Mail: akesmez@bingol.edu.tr

İÇİNDEKİLER/CONTENTS

<p>The Effect of Boriding Temperature and Time on the Structural and Mechanical Properties of a High-speed Steel</p> <p>Hasan Onur TAN^{1*}, Selçuk ATASOY¹, Sıtkı AKTAŞ¹</p> <p>¹ Giresun University, Engineering Faculty, Mechanical Engineering Department, Giresun, Türkiye Hasan Onur TAN ORCID No: 0000-0003-3796-9889 Selçuk ATASOY ORCID No: 0000-0003-0712-7904 Sıtkı AKTAŞ ORCID No: 0000-0002-9143-6752</p> <p>* <i>Corresponding author: hasan.tan@giresun.edu.tr</i></p> <p>(Received: 15.02.2024, Accepted: 25.03.2024, Online Publication: 28.06.2024)</p>	<p>1</p>
<p>Theoretical Examination of the 3-[1-(5-Amino-[1,3,4]thiadiazol-2-yl)-2-(1H-imidazol-4-yl)-ethylimino]-2,3-dihydro-indol-2-one Molecule</p> <p>Efdal ÇİMEN¹, Veysel TAHİROĞLU^{2*}</p> <p>¹ Kafkas University, Kars Vocational School, Chemistry and Chemical Processing Technologies, Kars, Türkiye ² Şırnak University, Health Sciences Faculty, Nursing Department, Şırnak, Türkiye Efdal ÇİMEN ORCID No: 0000-0003-2461-5870 Veysel TAHİROĞLU ORCID No: 0000-0003-3516-5561</p> <p>*<i>Corresponding author: veysel.tahiroglu@sirnak.edu.tr</i></p> <p>(Received: 18.12.2023, Accepted: 30.03.2024, Online Publication: 28.06.2024)</p>	<p>6</p>
<p>Investigation of The Effect of Molding Material Difference on Design in GGG70 Ductile Cast Iron Production</p> <p>Mete ŞEKERDEN¹, Muhammet Emin KESKİN^{2*}, Melek DURMUŞ³, Murat ÇOLAK⁴</p> <p>¹ Bayburt Üniversitesi, Fen Bilimleri Enstitüsü, Makine Mühendisliği Bölümü, Bayburt, Türkiye ² Bayburt Üniversitesi, Fen Bilimleri Enstitüsü, Makine Mühendisliği Bölümü, Bayburt, Türkiye ³ Necmettin Erbakan Üniversitesi, Fen Bilimleri Enstitüsü, Makine Mühendisliği Bölümü, Konya, Türkiye ⁴ Bayburt Üniversitesi, Teknik Bilimler Meslek Yüksekokulu, Elektronik ve Otomasyon Bölümü, Bayburt, Türkiye Mete ŞEKERDEN ORCID No: 0009-0002-3862-9480 Muhammet Emin KESKİN ORCID No: 0000-0003-4342-6303 Melek DURMUŞ ORCID No: 0009-00061439-3759 Murat ÇOLAK ORCID No: 0000-0002-8255-5987</p> <p>*<i>Corresponding author: emnkskn47@hotmail.com</i></p> <p>(Received: 21.08.2023, Accepted: 05.04.2024, Online Publication: 28.06.2024)</p>	<p>14</p>

<p>Karyological Variation of <i>Clethrionomys glareolus</i> (Mammalia: Rodentia) from Türkiye</p> <p>Ahmet Yesari SELÇUK^{1*}  , Perinçek Seçkinozan ŞEKER¹ </p> <p>¹ Department of Forestry, Artvin Vocational School, Artvin Çoruh University, Artvin, Türkiye Ahmet Yesari SELÇUK ORCID No: 0000-0002-2785-2823 Perinçek Seçkinozan ŞEKER ORCID No: 0000-0002-6103-4840</p> <p><i>*Corresponding author: ahmetyesari@gmail.com</i></p> <p>(Received: 16.01.2024, Accepted: 17.04.2024, Online Publication: 28.06.2024)</p>	<p>21</p>
<p>In Vitro Cytotoxic Effects of Some <i>Fumaria L.</i> (Papaveraceae) Species Methanolic Extracts on Cancer Cell Lines</p> <p>Pelin YILMAZ SANCAR^{1*}  , Irmak İÇEN TAŞKIN² </p> <p>¹ Fırat University, Faculty of Science, Department of Biology, Elazığ, Türkiye ² İnönü University, Faculty of Science, Department of Molecular Biology and Genetics, Malatya, Türkiye</p> <p>Pelin YILMAZ SANCAR ORCID No: 0000-0002-6134-622X Irmak İÇEN TAŞKIN ORCID No: 0000-0002-1612-0563</p> <p><i>*Corresponding author: peyilmaz@firat.edu.tr</i></p> <p>(Received: 24.04.2023, Accepted: 17.04.2024, Online Publication: 28.06.2024)</p>	<p>25</p>
<p>Expert Recommendation System to Promote Development-Focused Universities</p> <p>Bayraktar Mehmet Yasar^{1*}  , Kaya Mehmet² </p> <p>¹(Bingöl Üniversitesi, Mühendislik Fakültesi, Bilgisayar Mühendisliği,1200, Bingöl, Türkiye) ²(Fırat Üniversitesi, Mühendislik Fakültesi, Bilgisayar Mühendisliği,2300, Elazığ, Türkiye)</p> <p>Mehmet Yaşar Bayraktar ORCID No: 0000-0003-3182-120X Mehmet KAYA ORCID No: 0000-0003-2995-8282</p> <p><i>*Corresponding author: mehmetyasarbayraktar@hotmail.com</i></p> <p>(Received: 29.11.2023, Accepted: 19.04.2024, Online Publication: 28.06.2024)</p>	<p>30</p>
<p>Investigation of the Impact of Tool Pin Geometry and Feed Rate Speed in Friction Stir Lap Welding of 7075 and 5182 Aluminum Alloys</p> <p>Ömer EKİNCİ^{1*} </p> <p>¹ Sivas University of Science and Technology, Faculty of Aviation and Space Sciences, Department of Astronautical Engineering, Sivas, Türkiye Ömer Ekinci ORCID No: 0000-0002-0179-6456</p> <p><i>*Corresponding author: omerekinci@sivas.edu.tr</i></p> <p>(Received: 09.01.2024, Accepted: 10.05.2024, Online Publication: 28.06.2024)</p>	<p>34</p>
<p>Antibacterial Effect of Combined Use of Amoxicillin Trihydrate And <i>Cupressus sempervirens</i> Leaf Extract on Some Gram-Negative Bacteria</p> <p>Alican Bahadır SEMERCİ^{1,2*}  , Tuğba ONGUN SEVİNDİK² </p> <p>¹Necmettin Erbakan University, Ereğli Vocational School of Health Services, Konya, Türkiye ²Sakarya University, Sciences Faculty, Biology Department, Sakarya, Türkiye Alican Bahadır SEMERCİ ORCID No: 0000-0001-9502-9321 Tuğba ONGUN SEVİNDİK ORCID No: 0000-0001-7682-0142</p> <p><i>*Corresponding author: alicanbahadirsemerci@gmail.com</i></p> <p>(Received: 11.01.2024, Accepted: 14.05.2024, Online Publication: 28.06.2024)</p>	<p>43</p>

<p>Inequalities For Strongly s-Convex Functions Via Atangana-Baleanu Fractional Integral Operators</p> <p>Ebru YÜKSEL^{1*} </p> <p>¹ Ağrı İbrahim Çeçen University, Faculty of Science and Letters, Department of Mathematics, Ağrı, Türkiye Ebru YÜKSEL ORCID No: 0000-0001-7081-5924</p> <p><i>*Corresponding author: eyuksel@agri.edu.tr</i></p> <p>(Received: 24.01.2024, Accepted: 20.05.2024, Online Publication: 28.06.2024)</p>	<p>49</p>
<p>Refractive Index Sensor Based on Terahertz Metamaterial Absorber with High Sensitivity and Quality Factor for Sensing Applications</p> <p>Ahmet TEBER^{1*} </p> <p>¹ Bayburt University, Department of Electrical and Energy, Bayburt, Türkiye Ahmet TEBER ORCID No: 0000-0002-7361-2302</p> <p><i>*Corresponding author: ahmetteber@bayburt.edu.tr</i></p> <p>(Received: 30.12.2023, Accepted: 24.05.2024, Online Publication: 28.06.2024)</p>	<p>61</p>
<p>Persulfate Assisted Sonocatalytic Process for the Degradation of Reactive Yellow 145 Dye in Aqueous Solution</p> <p>Özkan GÖRMEZ^{1*} </p> <p>¹Mersin University, Science Faculty, Chemistry Department, Mersin, Türkiye Özkan GÖRMEZ ORCID No: 0000-0002-1360-9275</p> <p><i>*Corresponding author: ozkan.grmz@gmail.com</i></p> <p>(Received: 17.11.2023, Accepted: 28.05.2024, Online Publication: 28.06.2024)</p>	<p>69</p>
<p>Experimental Investigation of Photovoltaic Panel Surface Temperatures and Electricity Production in Summer</p> <p>Perihan ÇULUN^{1*} </p> <p>¹Bingöl University, Engineering and Architecture Faculty, Mechanical Engineering Department, Bingöl, Türkiye Perihan ÇULUN ORCID No: 0000-0002-1797-9695</p> <p><i>*Corresponding author: pculun@bingol.edu.tr</i></p> <p>(Received: 28.02.2024, Accepted: 08.06.2024, Online Publication: 28.06.2024)</p>	<p>77</p>
<p>Evaluation of the Effect of Different Extraction Temperatures on the Synthesis of Silver Nanoparticles from <i>Ocimum basilicum</i> (Basil) Plant</p> <p>İlkay Ünal^{1*} , Burcu Aydoğdu² </p> <p>¹ Munzur University, Faculty of Fine Arts, Design and Architecture Education, Department of Gastronomy and Culinary Arts, Tunceli, Turkey ² Munzur University Faculty of Engineering, Department of Mechanical Engineering, Tunceli, Turkey</p> <p>İlkay ÜNAL ORCID No: 0000-0002-1587-4187 Burcu AYDOĞDU ORCID No: : 0000-0002-3309-1995</p> <p><i>*Corresponding author: ilkayunal@munzur.edu.tr</i></p> <p>(Received: 18.03.2024, Accepted: 09.06.2024, Online Publication: 28.06.2024)</p>	<p>88</p>

<p>Optimization of Medium Components for Enhanced Expression of Recombinant Human Vascular Endothelial Growth Factor (VEGF₁₆₅) in <i>Kluyveromyces lactis</i> GG799</p> <p>Hülya KUDUĞ CEYLAN^{1*} , Cafer MEYDAN² , Ayşe NALBANTSOY² , Murat ELİBOL² </p> <p>¹ Tokat Gaziosmanpaşa University, Faculty of Pharmacy, Department of Basic Pharmaceutical Sciences, Tokat, Türkiye</p> <p>² Ege University, Faculty of Engineering, Department of Bioengineering, İzmir, Türkiye</p> <p>Hülya KUDUĞ CEYLAN ORCID No: 0000-0003-0365-2760 Cafer MEYDAN ORCID No: 0000-0001-6201-4860 Ayşe NALBANTSOY ORCID No: 0000-0002-9108-4451 Murat ELİBOL ORCID No: 0000-0002-6756-6290</p> <p><i>*Corresponding author: hulya.kudug@gop.edu.tr</i></p> <p>(Received: 28.04.2024, Accepted: 10.06.2024, Online Publication: 28.06.2024)</p>	95
<p>Effect of cAMP-dependent Phosphodiesterase Activity on <i>NTH1</i> Gene Expression and Reserve Carbohydrate Metabolism</p> <p>Tülay TURGUT GENÇ^{1*} </p> <p>¹ Çanakkale Onsekiz Mart University, Science Faculty, Biology Department, Çanakkale, Türkiye</p> <p>ORCID No: 0000-0001-5074-3572</p> <p><i>*Corresponding author: tturgutgenc@comu.edu.tr</i></p> <p>(Received: 22.11.2023, Accepted: 10.06.2024, Online Publication: 28.06.2024)</p>	106
<p>A Study of Effects of Organic Origin Liquid Seaweed on Germination Radicle and Plumule Growth in Winter Cereal Genus</p> <p>Ali Rahmi KAYA^{1*} , Mustafa YILDIRIM¹ , Songül ÇİFTÇİ SAKİN¹ </p> <p>¹ Kahramanmaraş Sütçü İmam University, Faculty of Agriculture, Department of Field Crops, Kahramanmaraş, Türkiye</p> <p>Ali Rahmi KAYA ORCID No: 0000-0003-0318-6034 Mustafa YILDIRIM ORCID No: 0000-0002-9523-4007 Songül ÇİFTÇİ SAKİN ORCID No: 0000-0002-5157-2709</p> <p><i>*Corresponding author: alirahmikaya@ksu.edu.tr</i></p> <p>(Received: 03.01.2023, Accepted: 12.06.2024, Online Publication: 28.06.2024)</p>	114
<p>Superconductivity in Brain</p> <p>Özden ASLAN ÇATALTEPE^{1*} </p> <p>¹ İstanbul Gedik University, Engineering Faculty, Department of Mechatronics Engineering, İstanbul, Türkiye</p> <p>Özden ASLAN ÇATALTEPE ORCID No: 0000-0003-4520-9839</p> <p><i>*Corresponding author: ozden.aslan@gedik.edu.tr</i></p> <p>(Received: 24.08.2023, Accepted: 05.04.2024, Online Publication: 28.06.2024)</p>	121

Aurora Kinases: Their Role in Cancer and Cellular Processes

Sibel SARI^{1*} , Elif Rumeysa ÖZSOY² 

¹Abdullah Gul University, Faculty of Life and Natural Sciences, Department of Molecular Biology and Genetics, Kayseri, Türkiye

²Abdullah Gul University, Graduate School of Engineering and Science, Department of Bioengineering, Kayseri, Türkiye

Sibel SARI ORCID No: 0000-0002-2505-5804

Elif Rumeysa ÖZSOY ORCID No: 0009-0008-6040-9875

**Corresponding author: sibel.sari@agu.edu.tr*

(Received: 30.04.2023, Accepted: 14.05.2024, Online Publication: 28.06.2024)

The Effect of Boriding Temperature and Time on the Structural and Mechanical Properties of a High-speed Steel

Hasan Onur TAN^{1*}, Selçuk ATASOY¹, Sıtkı AKTAŞ¹

¹Giresun University, Engineering Faculty, Mechanical Engineering Department, Giresun, Türkiye

Hasan Onur TAN ORCID No: 0000-0003-3796-9889

Selçuk ATASOY ORCID No: 0000-0003-0712-7904

Sıtkı AKTAŞ ORCID No: 0000-0002-9143-6752

* Corresponding author: hasan.tan@giresun.edu.tr

(Received: 15.02.2024, Accepted: 25.03.2024, Online Publication: 28.06.2024)

Keywords

Boriding,
Boriding
temperature,
Boriding time,
M42 steel,
Mechanical
properties

Abstract: In this study, the effect of boriding temperature and time on the structural and mechanical properties of M42 high speed steel were investigated. Samples placed in Ekabor II powder were exposed to pack boriding treatment at 900°C and 1000°C for 4 hour and at 950°C for 2, 4 and 6 hours. Scanning electron microscope (SEM) images indicate that boron diffuses into the samples and a sawtooth-like cross-sectional morphology is formed. The presence of boron has also been proven by Energy Dispersive X-ray spectrometry (EDX). In addition, it was determined that boron layer thickness increased with increasing boriding temperature. When the microhardness values were examined, it was observed that the sample borided at the highest temperature had the highest hardness value and the hardness values decrease with the decreasing of boriding temperature. Similar results were also obtained regarding the boriding time. The highest microhardness and layer thickness values were obtained after 6 hours of boriding. Additionally, it was observed that the hardness values of borided samples decreased as they moved from the surface to the inner parts.

1

Borlama Sıcaklığının ve Süresinin M42 Çeliğinin Yapısal ve Mekanik Özelliklerine Etkisi

Anahtar Kelimeler

Borlama,
Borlama
sıcaklığı,
Borlama
süresi,
M42 çeliği,
Mekanik
özellikler

Öz: Bu çalışmada borlama sıcaklığının ve süresinin M42 yüksek hız çeliğinin yapısal ve mekanik özellikleri üzerine etkisi incelenmiştir. Ekabor II tozu içerisine yerleştirilen numuneler 900°C ve 1000°C derecede 4 saat; 950°C derecede 2, 4 ve 6 saat kutu borlama işlemine maruz bırakılmıştır. Taramalı elektron mikroskop (SEM) görüntüleri incelendiğinde borun numunelerin içerisine difuz ettiği ve testere dişlisine benzer kesit morfolojisi olduğu görülmektedir. Borun varlığı enerji dağılım x-ışını spektrometresi (EDX) ile de ispatlanmıştır. Bunun yanında, borlama sıcaklığın artmasıyla bor tabaka kalınlıklarının da arttığı tespit edilmiştir. Mikrosertlik değerleri incelendiğinde en yüksek sıcaklıkta borlanan numunenin en yüksek sertlik değerine sahip olduğu ve borlama sıcaklığının düşmesiyle beraber sertlik değerlerinin azaldığı tespit edilmiştir. Benzer sonuçlar borlama süresiyle ilgili olarak da görülmüştür. En yüksek mikrosertlik ve tabaka kalınlığı değerleri 6 saatlik borlama sonucunda elde edilmiştir. Ayrıca, borlanmış numunelerin yüzeyden iç kısımlara doğru gidildikçe sertlik değerlerinin düştüğü görülmüştür.

1. INTRODUCTION

Surface hardening is a primary method for enhancing certain mechanical properties of materials. Processes, such as carburizing, nitriding, and boriding, have been widely used to improve the materials' surface properties. In general, these processes are more cost-effective than replacing machinery components with ones made from pricier materials [1]. Boriding is a thermochemical

reaction based on the diffusion of boron into the substrate material, forming a hard surface coating consisting of mixed boron compounds [2-5]. Due to its relatively small atomic radius, boron can easily diffuse into various materials such as steels, non-ferrous alloys, and some superalloys [6-8]. The boriding process of the samples is carried out by heating them in the temperature range of 973 K to 1323 K for 0.5 hours to 12 hours [9-11]. Depending on boriding parameters and the chemical

composition of the material, the diffusion of boron atoms leads to the formation of iron and metallic borides in the material [12-14]. When it is sufficiently applied to the surface, high hardness values provide valuable wear, corrosion and heat resistance [15-17]. Boriding can be performed by various methods such as solid, liquid, gas, plasma, and paste [11, 12, 14, 18-20]. Among these, pack boriding is carried out using commercial boriding material containing BC_4 , KBF_4 and SiC (Ekabor) [18]. This method is the most commonly used boriding method due to its simplicity and ease of applicability without requiring post process surface cleaning [15, 18, 20, 21]. Depending on the concentration of diffused boron atoms, the boride layer usually forms as tetragonal Fe_2B (8 wt% B) and/or orthorhombic FeB (16 wt% B) [20-22]. Generally, while the FeB phase has higher hardness, the Fe_2B phase exhibits better toughness [4, 20, 21].

High-speed steels are commonly used in milling cutters, reamers, taps, broaches, saw teeth, drill bits, strip saws, and guide production [23-25]. The selected M42 high-speed steel is known for its high toughness due to its 8% cobalt content. Additionally, due to the cobalt in its structure, it stands out as an ideal material in lathes used for processing aluminum and alloys, brasses, automatic steels, and drilling punches requiring high temperature and wear resistance [23-26]. In this study, the effect of boriding temperature and time on the structural and mechanical properties of M42 steel was investigated by boriding the steel at 900°C, 950°C, and 1000°C for 4 hours, and additionally at 950°C for 2, 4, and 6 hours.

2. MATERIAL AND METHOD

In this study, M42 steel, chemical composition of the steel is provided in Table 1, with dimensions of $\varnothing 12.5 \times 10$ mm was utilized. The surfaces of the test specimens were polished using SiC abrasive papers of 80, 150, 360, 500, 800, and 1200 grit sizes, respectively. The boriding process was carried out using commercial Ekabor II powder with the pack boriding method. The samples were placed in a cylindrical stainless-steel crucible containing Ekabor II powder. The furnace was heated to 900°C, 950°C, and 1000°C, respectively, before placing the crucible, and the samples were borided in a preheated furnace for 4 hours. Additionally, to determine the effect of boriding time, samples were borided at 950°C for 2, 4, and 6 hours. Subsequently, they were allowed to cool to room temperature. Thereafter, to determine the thickness of the boride layer, the borided samples were cut in half, polished using SiC papers followed by 3 μm and 1 μm diamond suspensions, and then etched in a 5% Nital solution after cleaning with alcohol. The etched samples were examined using a scanning electron microscope (SEM) (ZEISS EVO LS 10) to determine the thickness of the boride layer. Additionally, the elemental composition of the samples was determined using energy-dispersive X-ray spectroscopy (EDX) method. The phase structure of the borided samples was analyzed in the range of 30° to 90° using X-ray diffraction (XRD) (GNR Europe 600 XRD). XRD studies were performed with parameters of 40kV and 15mA. $CuK\alpha$ radiation with a wavelength of 1.542 Å was used to identify the phases. Microhardness

measurements were conducted using the Vickers method under a load of 100 g and at intervals of 20 μm . At least 5 measurements were taken, and the average value was calculated.

3. RESULTS AND DISCUSSION

SEM images of the cross-sections of M42 steels subjected to boriding at 900°C, 950°C, and 1000°C for 4 hours are shown in Figure 1, while SEM images of the cross-sections of M42 steels subjected to boriding at 950°C for 2, 4, and 6 hours are provided in Figure 2. The EDX results of M42 steel borided for 2, 4, and 6 hours at 950°C are given in Table 2. The thickness of the boride layers which were determined by evaluating of SEM images, are presented in Table 3. Upon examining the thickness of the boride layers based on the boriding duration was found as 28.1 μm , 47.5 μm , and 52.5 μm for 2, 4, and 6 hours, respectively. Additionally, thickness of boride layer of M42 steel which was borided at 900°C, 950°C, and 1000°C for 4 hours, was measured as 29.7 μm , 47.5 μm , and 71.4 μm , respectively. It is observed that as the boriding temperature and time increase, the thicknesses of the boride layers also increase, with the highest thickness reached at 4 hours of boriding at 1000°C. Moreover, the boriding layers exhibit a morphology resembling sawtooth, which can be attributed to the diffusion of boron atoms into the base material. In addition, the EDX results that shows boron rates (weight %) increased from 8.72 to 10.77, confirm the diffusion of boron. As indicated, with increasing temperature and time, the diffusion rate increases, leading to an increase in boride layer thicknesses [2-6].

Table 1. Chemical composition of M42 steel

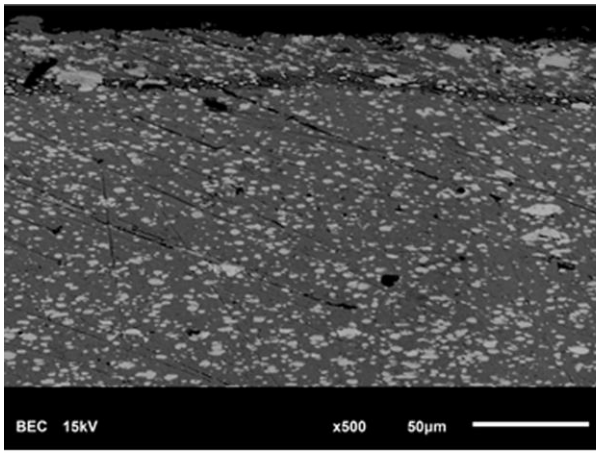
C	Mo	Co	Cr	W	V	Si	Mn
1.1	9.2	8	4	1.5	1.1	0.5	0.2

Table 2. EDX results obtained from the cross-sectional surface of M42 steel borided for 2, 4, and 6 hours at 950°C

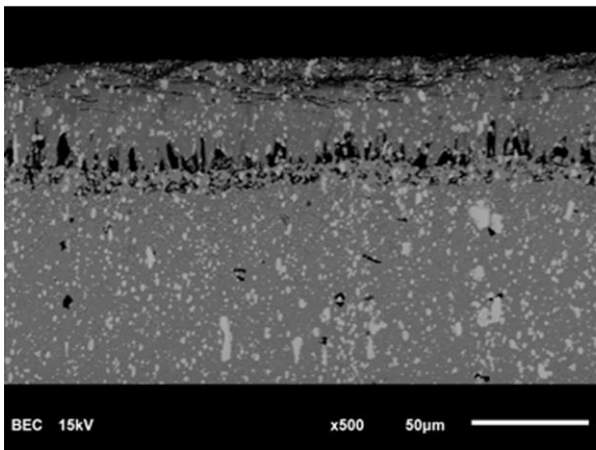
Element	Weight %			Atomic %		
	2 h	4 h	6 h	2 h	4 h	6 h
B	8.72	9.98	10.77	27.88	29.46	31.82
C	11.74	10.32	9.2	31.18	27.45	26.48
V	1.46	1.31	1.3	0.91	0.89	0.82
Cr	3.5	3.32	3.54	2.15	2.04	2.29
Fe	47.73	52.73	54.09	27.27	30.15	32.6
Co	5.74	5.8	6.1	3.11	3.15	3.49
Mo	15.5	11.6	8.63	5.16	3.86	3.11
W	4.36	4.15	3.76	0.76	0.72	0.69

Table 3. The boride layer thickness values obtained from borided M42 steel at different temperature and time

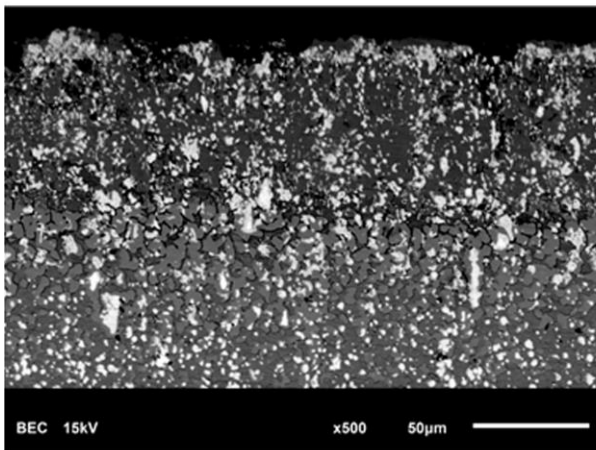
Boriding temperature (°C)	Boriding time (hour)	Boride layer thickness (μm) ($\pm 1\%$)
900	4	29.7
950	2	28.1
950	4	47.5
950	6	52.5
1000	4	71.2



(a)



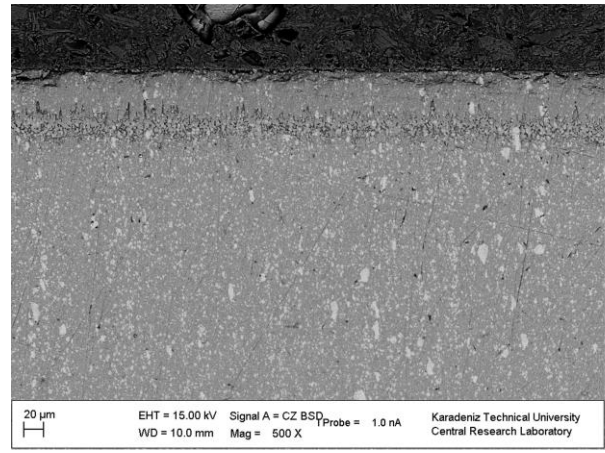
(b)



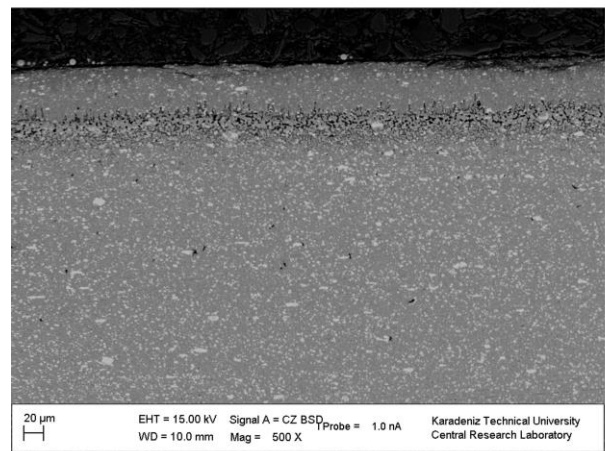
(c)

Figure 1. SEM images of M42 steel borided at (a) 900°C, (b) 950 °C and (c) 1000°C for 4 hours

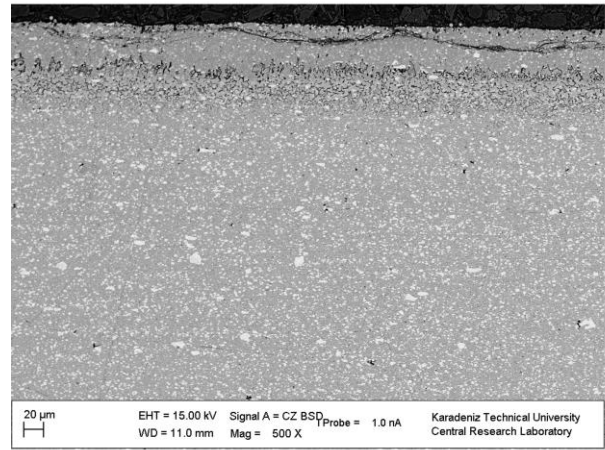
The XRD results of the untreated M42 steel and the M42 steel borided at 950°C for 4 hours are provided in Figure 3. The XRD indicates that the boride layers consist of FeB and Fe₂B phases as shown in Figure 3b. Generally, while the FeB phase is harder than the Fe₂B phase, it has lower toughness, making its presence undesirable. Since, it can deform more easily and lead to fracture and spalling under



(a)



(b)



(c)

Figure 2. SEM images of M42 steel borided at (a) 2 hours, (b) 4 hours and (c) 6 hours at 950°C.

high loads due to its brittleness [2]. Furthermore, the presence of the FeB phase on the surface also reduces corrosion resistance [3]. To prevent the formation of FeB phase, the chemical composition of the boriding powder, boriding temperature and time should be selected appropriately for the material to be borided.

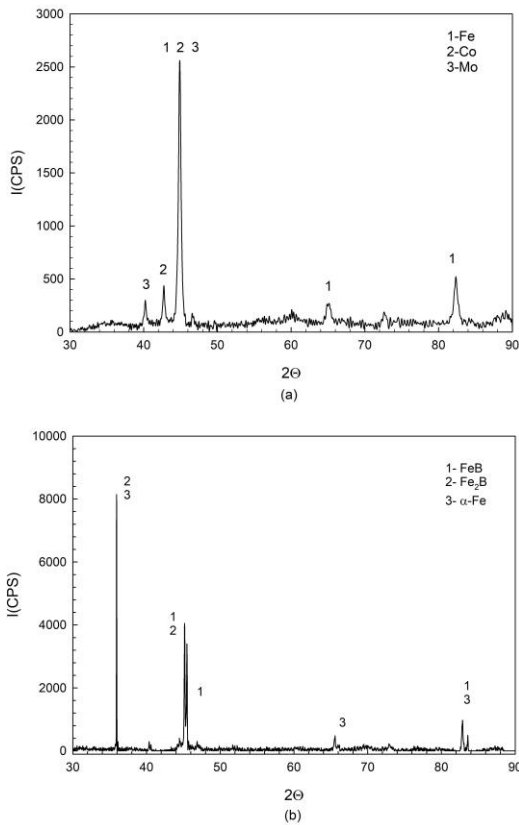


Figure 3. XRD results of M42 steel under conditions of (a) untreated and (b) borided at 950°C for 4 hours.

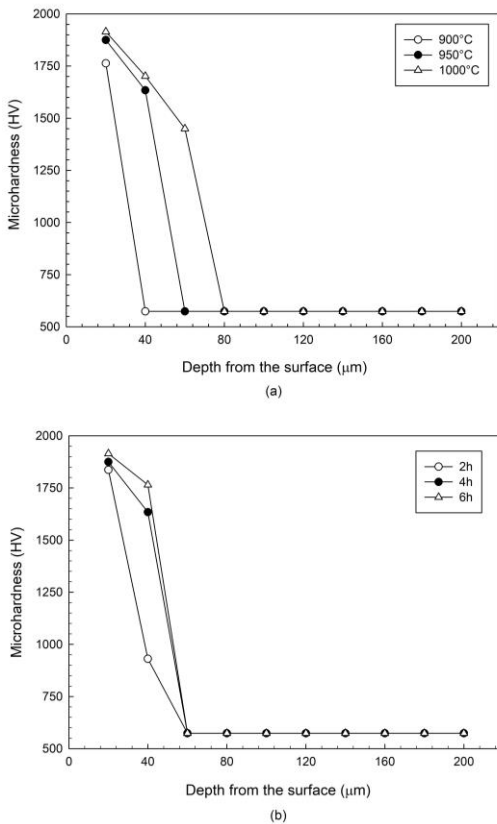


Figure 4 The cross-sectional microhardness values varying with the depth for M42 steel for (a) 4 hours at different temperatures and (b) 950° for different durations

The curves showing the variation of microhardness values, obtained from cross section of borided M42 steel, at different temperatures and time with depth are given in

Figure 4. The hardness values of the borided layer range from 930 HV to 1914 HV. As can be seen in Figure 4, the hardness values of the borided samples decreased as depth increases from the surface towards the interior. Additionally, it is noted that the hardness of the boride layer formed on the surface increased with the increase of boriding temperature and time.

4. CONCLUSION

The phase structure, thickness boride layer, and microhardness values of M42 high-speed steel subjected to boriding at different temperatures for 4 hours and at varying time at a constant temperature were investigated. It was found that as the boriding temperature increased, the thickness of the layer increased from 29.7 μm to 71.2 μm, and as the boriding time increased, it increased from 28.1 μm to 52.5 μm. Additionally, in the EDX analysis of borided M42 steel at different times, the Boron element ratio increased from 8.72% to 10.77%. The structural analysis of the same sample also indicated the formation of FeB and Fe₂B phases as a result of the boriding process. It was concluded that boron diffused into the M42 steel, and the diffusion depth increased with increasing temperature and time and as a result of this surface hardness increased.

Acknowledgement

This study was financially supported by the Scientific Research Projects Unit of Giresun University under project number FEN-BAP-A-240222-23.

REFERENCES

- [1] Ruiz-Trabolsi PA, Chino-Ulloa A, Miranda-Hernandez JG, Tadeo-Rosas R, Carrera-Espinoza R, Velazquez JC, et al. A Comparative Analysis of the Tribological Behavior of Hard Layers Obtained by Three Different Hardened-Surface Processes on the Surface of AISI 4140 Steel. *Crystals*. 2022;12(2).
- [2] Balusamy T, Narayanan TSNS, Ravichandran K, Park IS, Lee MH. Pack boronizing of AISI H11 tool steel: Role of surface mechanical attrition treatment. *Vacuum*. 2013;97:36-43.
- [3] Cimenoglu H, Atar E, Motallebzadeh A. High temperature tribological behaviour of bonded surfaces based on the phase structure of the boride layer. *Wear*. 2014;309(1-2):152-8.
- [4] Gök MS, Küçük Y, Erdoğan A, Öge M, Kanca E, Günen A. Dry sliding wear behavior of borided hot-work tool steel at elevated temperatures. *Surface and Coatings Technology*. 2017;328:54-62.
- [5] Handbook A. Heat treating. ASM international Materials Park, OH; 1991.
- [6] Bindal C, Üçisik AH. Characterization of borides formed on impurity-controlled chromium-based low alloy steels. *Surf Coat Tech*. 1999;122(2-3):208-13.
- [7] Hudáková M, Kusý M, Sedlická V, Grgáč P. Analysis of the boronized layer on K190PM tool steel. *Mater Tehnol*. 2007;41(2):81-4.
- [8] Keddám M. Simulation of the growth kinetics of FeB and Fe₂B phases on the AISI M2 borided steel:

- Effect of the paste thickness. *International Journal of Materials Research*. 2009;100(6):901-5.
- [9] Abdellah ZN, Keddam M, Elias A. Evaluation of the effective diffusion coefficient of boron in the FeB phase in the presence of chemical stresses. *International Journal of Materials Research*. 2013;104(3):260-5.
- [10] Gunes I. Kinetics of borided gear steels. *Sadhana-Acad P Eng S*. 2013;38(3):527-41.
- [11] Gunes I. Wear Behaviour of Plasma Paste Boronized of AISI 8620 Steel with Borax and BO Paste Mixtures. *J Mater Sci Technol*. 2013;29(7):662-8.
- [12] Kayali Y, Günes I, Ulu S. Diffusion kinetics of borided AISI 52100 and AISI 440C steels. *Vacuum*. 2012;86(10):1428-34.
- [13] Kulka M, Kulka M, Castro. *Current trends in boriding*; Springer; 2019.
- [14] Von Matuschka A, Boronizing H. Son Inc. Philadelphia, USA. 1980.
- [15] He XL, Xiao HP, Ozaydin MF, Balzuweit K, Liang H. Low-temperature boriding of high-carbon steel. *Surf Coat Tech*. 2015;263:21-6.
- [16] Vitry V, Kanta AF, Delaunois F. Mechanical and wear characterization of electroless nickel-boron coatings. *Surf Coat Tech*. 2011;206(7):1879-85.
- [17] Yildiz I, Çelik AG, Gunes I. Characterization and Diffusion Kinetics of borided Ni-Mg Alloys. *Prot Met Phys Chem+*. 2020;56(5):1015-22.
- [18] Bican O, Bayca SU, Ocak-Araz S, Yamaneli B, Tanis NA. Effects of the Boriding Process and of Quenching and Tempering after Boriding on the Microstructure, Hardness and Wear of Aisi 5140 Steel. *Surf Rev Lett*. 2020;27(6).
- [19] Keddam M, Chentouf SM. A diffusion model for describing the bilayer growth (FeB/FeB) during the iron powder-pack boriding. *Appl Surf Sci*. 2005;252(2):393-9.
- [20] Prince M, Raj GS, Kumar DY, Gopalakrishnan P. Boriding of Steels: Improvement of Mechanical Properties - a Review. *High Temp Mater P-U.S*. 2022;26(2):43-89.
- [21] Erdogan A. Investigation of high temperature dry sliding behavior of borided H13 hot work tool steel with nanoboron powder. *Surf Coat Tech*. 2019;357:886-95.
- [22] Campos-Silva I, Ortiz-Domínguez M, López-Perrusquia N, Meneses-Amador A, Escobar-Galindo R, Martínez-Trinidad J. Characterization of AISI 4140 borided steels. *Appl Surf Sci*. 2010;256(8):2372-9.
- [23] Hoyle G. *High speed steels*. (No Title). 1988.
- [24] Llewellyn D, Hudd R. *Steels: metallurgy and applications*; Elsevier; 1998.
- [25] Zhou XF, Zhu WL, Jiang HB, Fang F, Tu YY, Jiang JQ. A New Approach for Refining Carbide Dimensions in M42 Super Hard High-speed Steel. *J Iron Steel Res Int*. 2016;23(8):800-7.
- [26] Luo Y, Guo H, Sun X, Mao M, Guo J. Effects of Austenitizing Conditions on the Microstructure of AISI M42 High-Speed Steel. *Metals*. 2017;7(1).

Theoretical Examination of the 3-[1-(5-Amino-[1,3,4]thiadiazol-2-yl)-2-(1H-imidazol-4-yl)-ethylimino]-2,3-dihydro-indol-2-one Molecule

Efdal ÇİMEN¹ , Veysel TAHİROĞLU^{*2} 

¹ Kafkas University, Kars Vocational School, Chemistry and Chemical Processing Technologies, Kars, Türkiye

² Şırnak University, Health Sciences Faculty, Nursing Department, Şırnak, Türkiye

Efdal ÇİMEN ORCID No: 0000-0003-2461-5870

Veysel TAHİROĞLU ORCID No: 0000-0003-3516-5561

*Corresponding author: veysel.tahiroglu@sirnak.edu.tr

(Received: 18.12.2023, Accepted: 30.03.2024, Online Publication: 28.06.2024)

Keywords

Density functional theory, Molecular electrostatic potential, Natural orbital bonding

Abstract: The vibration frequencies, associated vibrational motions, and theoretically ideal molecular structure of the 3-[1-(5-Amino-[1,3,4]thiadiazol-2-yl)-2-(1H-imidazol-4-yl)-ethylimino]-2,3-dihydro-indol-2-one (1) molecule were investigated using the Gaussian09 software program. The theoretically ideal chemical structure of the molecule (1), its vibration frequencies and the accompanying vibration movements of the molecule were examined. Quantum chemical computations have been performed utilizing the SDD and 6-311G base set of DFT(RB3LYP) methods. The molecule was subjected to the highest occupied molecular orbital (HOMO), the lowest unoccupied molecular orbital (LUMO) investigations to ascertain charge transfer. The molecule's stability was investigated using Natural Orbital Bonding (NBO) analysis as a function of both hyperconjugative interaction and charge delocalization. Molecular Electrostatic Potential (MEP) was performed using a Density Functional Theory (DFT) technique. Both estimated DFT algorithms have comparable geometric parameters.

6

3-[1-(5-Amino-[1,3,4]tiadiazol-2-il)-2-(1H-imidazol-4-il)-etilimino]-2,3-dihidro-indol-2-on Molekülün Teoriksel İncelenmesi

Anahtar Kelimeler

Yoğunluk fonksiyonel teorisi, Moleküler elektrostatik potansiyel, Doğal orbital bağlanma

Öz: 3-[1-(5-Amino-[1,3,4]tiadiazol-2-il)-2-(1H-imidazol-4-il)-etilimino]-2,3-dihidro-indol-2-on (1) molekülünün titreşim frekansları, ilişkili titreşim hareketleri ve teorik olarak ideal moleküler yapısı Gaussian 09 yazılım programı kullanılarak araştırıldı. Molekül (1)'in teorik olarak ideal kimyasal yapısı, titreşim frekansları ve molekülün buna eşlik eden titreşim hareketleri incelenmiştir. Kuantum kimyasal hesaplamalarını gerçekleştirmek için DFT(RB3LYP) yaklaşımlarının SDD ve 6-311G temel seti kullanıldı. Moleküldeki yük aktarımı için en yüksek dolu moleküler yörünge (HOMO), en düşük boş moleküler yörünge (LUMO) analizleri yapılmıştır. Molekülün stabilitesi, hem hiperkonjugatif etkileşimin hem de yük delokalizasyonunun bir fonksiyonu, Doğal Orbital Bağlanma (NBO) analizi kullanılarak araştırıldı. MEP, bir Yoğunluk fonksiyonel teorisi (DFT) tekniği kullanılarak gerçekleştirildi. Tahmin edilen her iki DFT algoritması da karşılaştırılabilir geometrik parametrelere sahiptir.

1. INTRODUCTION

The azomethine group, often referred to as the imine functional group, is a component of Schiff base derivatives, which are compounds that have become more well-known due to their biological activity, including antibacterial, anticancer, antifungal, and antimicrobial qualities [1]. These substances represent the largest class of photochromic materials with potential for use in optoelectronic devices. In recent years,

potential applications have focused on the electrochemical characteristics and nonlinear optical (NLO) behavior of Schiff base ligands with various substituents that have different electron-donating and electron-withdrawing groups [2]. Furthermore, because of their selectivity, synthetic flexibility and sensitivity to transition metal ions, The ligands of Schiff bases are important in inorganic alchemy [3]. Schiff bases metal complexes produced from heterocyclic compounds with ligand atoms of nitrogen, oxygen, and sulfur are employed in therapeutic and pharmaceutical applications

[4]. Thiophene and its derivatives play an essential role in heterocyclic chemistry. They are utilized as charge-carrying molecules in technologies such as transistors, supercapacitors, Electrochromic substances, chemical solar panels, and organic light-emitting diodes, and nonlinear optical materials [5]. In recent years, potential applications have focused on the electrochemical characteristics and nonlinear optical (NLO) behavior of Schiff base ligands with various substituents that have different groups that donate electrons and groups that remove electrons [6]. Physical and chemical characteristics of chemical and biological systems may now be predicted because to advances in computational chemistry. Furthermore, theoretical considerations substantially aid actual spectroscopic research. Density Functional Theory (DFT) is widely used in computing the UVeVis, FT-IR, and NMR spectra, charge distributions, HOMO-LUMO energies, and nonlinear optical (NLO) behavior of certain thiophene derivatives. Such substances have shown reliable findings that are compatible with experimental data [7].

The quantum chemical model of matter is known as density functional theory (DFT). Physicists, chemists, and materials workers prefer this model because simulation results are comparable to experimental studies. It reduces simulation time without affecting accuracy by considering the collective effect of electrons [8]. This is different from other models accepted in scientific studies. Thomas (1927) and Fermi (1928) also helped solve the many-electron problem in the years when the Hartree and Hartree-Fock methods emerged. Thomas and Fermi proposed the original density functional theory of quantum systems. This method explains how density functional theory (DFT) works, but is not precise enough for modern electronic structure calculations [9].

2. MATERIAL AND METHOD

DFT was calculated using the (B3LYP)/SDD and 6-311G techniques using Gaussian 09 software. For conformational analysis, a quasi-experimental approach is used. The form of the final molecule was optimized as the initial stage in the computer study. The vibrational frequencies, optimal geometries, and energies of molecular structure of the molecule (1) have been calculated utilizing the DFT approach in the Gaussian 09 software. The DFT/(B3PW91/B3LYP) approaches and the 6-311G base set based software package have been used to develop the Lee's-Yang-Parr correlation function. ChemBio Ultra Drive 3D and GaussView

6.0.16 were used to capture the visualization and input file [10]. The binding affinity of the molecule was calculated using the Maestro Molecular Modeling platform and the Schrödinger, LLC model (model 6.0.16.) [11]. This experiment made use of the Gaussian 09W package software. To do theoretical computations on the examined chemical, the Density Functional Theory (DFT) technique was performed. The DFT computations utilized the B3LYP mixed functional, which consists of Becke's three-parameter exchange functional and Lee, Yang, and Parr's correlation functional and is one of the most widely used exchange-correlation functionals [12]. SDD and 6-311G base sets have been used to achieve geometry optimizations, geometric parameters, and minimal molecular energies of the molecule. Mulliken charges, molecular electrostatic potential surfaces and frontier orbitals have been calculated utilizing the B3LYP/SDD/6-311G method. However, using the same procedure, LUMO and HOMO energies of the molecule (1) were calculated and ΔE energy differences were obtained for each method using these data.

3. RESULTS AND DISCUSSION

3.1. Structure Details and Analysis

A molecule's geometry is related to the bond angle and bond length between the atoms of that molecule and is one of the most important factors that directly affects the magnitude of the molecule's the dipole moment [13]. The B3LYP method with SDD and 6-311G basis sets was utilized for geometric optimization computations to explore the the molecule (1) influence of the DFT technique on geometric features. Some angles bonding and lengths bonding of the molecule (1) obtained by the help of the Gaussian 0.9 program are given in Table 1 [14]. The largest deviation appears in the C14-S15 structural by a bond length of 1.84342 Å. Another structure with the largest deviation appears in the C12-C13 structural by a bond length of 1.57546 Å. This is because there are N and O atoms, which are strong electron-withdrawing groups, attached to the C8 atom. The largest deviation in trihedral structures was determined in the N7-C8-O10 structure with the bond angle of 125.85439°. In tetrahedral structures, The bond angle between C16-S15-C14-N18 was found to have the greatest variation, 1.15446°. The lowest change in bond length in the C2-H26 structure was determined to be -0.00568 Å. The smallest change in bond angle in trihedral structures is N7-C8-O10 -17.33484 and N11-C12-C13-C20 -0.04996, respectively.

Table 1. Theoretically determined some bond lengths (Å) and angles (°) of the molecule (1).

Bond Lengths	B3LYP/ SDD	B3LYP/ 6-311G	Bond Lengths	B3LYP/ SDD	B3LYP/ 6-311G
C1-C2	1.41136	1.39999	C12-H30	1.09577	1.08991
C3-C4	1.39675	1.38731	C13-H32	1.09525	1.08899
C5-C6	1.39944	1.38960	C22-H35	1.07906	1.07388
C5-C9	1.47519	1.46960	C4-N7	1.42102	1.41565
C8-C9	1.54551	1.53122	C9-N11	1.29193	1.28326
C12-C13	1.57546	1.56918	C16-N19	1.37067	1.35878
C12-C14	1.50288	1.49309	C22-N21	1.33629	1.32775
C13-C20	1.49968	1.49095	N17-N18	1.40712	1.40407
C20-C24	1.39034	1.37705	C8-O10	1.25112	1.24445
C2-H26	1.08736	1.08168	C14-S15	1.84342	1.84935
Bond Angles	B3LYP/ SDD	B3LYP/ 6-311G	Bond Angles	B3LYP/ SDD	B3LYP/ 6-311G
C1-C2-C3	121.43395	121.43000	C1-C6-H28	121.50067	121.57496
C3-C4-C5	121.85055	121.74364	H31-C13-H32	108.51955	108.31528
C5-C9-C8	105.39422	105.54416	N7-C8-O10	108.51955	125.85439
C12-C13-C20	112.58595	112.98100	C14-S15-C15	84.25298	83.96123
C4-N7-C8	111.97479	112.02741	N18-N17-C16	112.25886	112.68447
Planar Bond Angles	B3LYP/ SDD	B3LYP/ 6-311G	Planar Bond Angles	B3LYP/ SDD	B3LYP/ 6-311G
C3-C2-C1-C6	-0.00748	0.00085	N21-C22-N23-C24	-0.00094	-0.02212
C4-C5-C9-C8	0.90158	1.09487	C16-S15-C14-N18	1.06657	1.15446
C4-N7-C8-C9	0.88384	1.07379	N11-C12-C13-C20	-179.06379	-179.11375
N11-C9-C8-O10	-2.79432	-3.23090	O10-C8-N7-H29	0.81900	0.76218

3.2. Mulliken Atomic Charges

Atomic charge is utilized to predict electrostatic potentials across molecule boundaries, evaluate charge transfer, and evaluate electronegativity equalization [15]. Mulliken atomic charges of the molecule (1) The gas phase were determined using the B3LYP theory SDD basis set and B3LYP theory 6-311G basis set and are given in Table 2 [16]. It has been noted that the

electronegative atoms (N7, N11, N17, N18, N21, N23 and O10) in the molecule have negative charge values. The charge values of these atoms are; It was calculated as -0.447, -0.004, -0.104, -0.058, -0.116, -0.321 and -0.263 (a.u.). Utilizing the RB3LYP procedure with the 6-311G base set, a) bond lengths, b) mulliken charge, c) structure optimization d) atomic mass are given in Figure 1 [16].

Table 2. Mulliken atomic charges of the molecule (1).

	B3LYP/ SDD	B3LYP/ 6-311G		B3LYP/ SDD	B3LYP/ 6-311G
C1	-0.233	-0.183	N7	-0.447	-0.834
C2	-0.173	-0.130	N11	-0.004	-0.251
C3	-0.343	-0.067	N17	-0.104	-0.261
C4	0.279	0.332	N18	-0.058	-0.180
C5	0.193	-0.181	N21	-0.116	-0.367
C6	-0.340	0.003	N23	-0.321	-0.321
C8	0.115	0.559	S15	0.237	0.279
C9	-0.145	0.000	H26	0.224	0.155
C12	-0.150	-0.268	H27	0.234	0.170
C13	-0.467	-0.372	H28	0.265	0.187
C14	-0.133	0.065	H30	0.289	0.250
C16	-0.135	-0.228	H31	0.221	0.200
C20	0.238	-0.006	H34	0.335	0.344
C22	-0.235	0.224	H35	0.257	0.196
C24	-0.342	0.182	H36	0.210	0.336
O10	-0.263	-0.382	H37	0.287	0.210

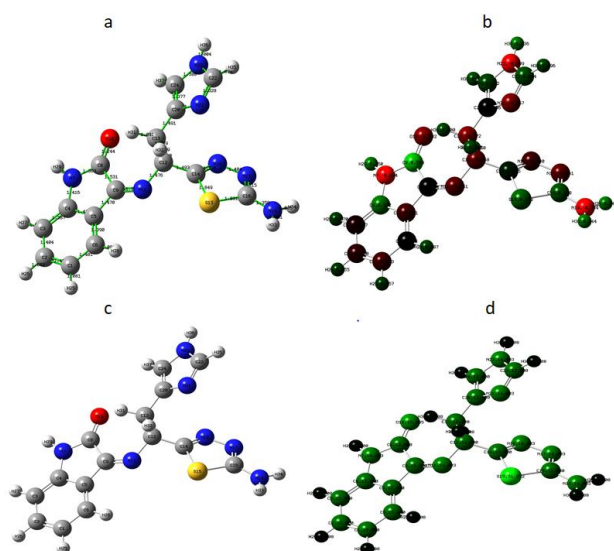


Figure 1. Molecule with DFT/B3LYP/6-311G basis set (1) a) bond lengths, b) relative charge, c) structure optimization d) atomic mass.

3.3. HOMO and LUMO Analysis

The lowest unoccupied molecular orbital (LUMO) and the highest occupied molecular orbital (HOMO) are very significant two orbitals in molecules [17]. The eigenvalues and gap energies of LUMO and HOMO represent the bioactivity of a chemical [18]. A chemical with a short gap between its border orbitals is more polarizable and has lower kinetic stability and increased chemical reactivity [19]. Because the HOMO, being the outside orbital holding electrons, tries to transfer electrons as electron donors, the HOMO's energy directly impacts the ionization potential. Although, LUMO might receive electrons, and its energy is proportional to its electron affinities [20]. The eigenvalues and energy deficits of HOMO and LUMO chemicals indicate the molecule's biological activity. Two key chemical orbitals have been studied for the HOMO and LUMO energies, as illustrated in Figures 2 and 3 [21]. In Table 3 [22] is shown the computed quantum chemical factor (in eV) for low energy suitability of molecule (1) using DFT/B3LYP/SDD and DFT/B3LYP/6-311G techniques.

The orbital energies of LUMO and HOMO might be used to calculate electron affinity and ionization energy as follows: $A = -E_{\text{LUMO}}$, $I = -E_{\text{HOMO}}$, $(\mu = -(I+A)/2)$ and $\eta = (I-A)/2$. An electrophilic system is one that resists transferring electrons with its surroundings and can store more electrons than a non-electrophilic system [23]. It is a more accurate indicator of total chemical reactivity since it includes data on durability (hardness) as well as electron transfer (Potential chemical). The affinity of electrons and potential for ionization are the chemical species, and the formulas $\eta = (I-A)/2$ and $\mu = -(I+A)/2$ are used

to calculate the chemical potential and hardness, respectively (A) [24]. The components from which the title compound is created do not spontaneously dissolve because of the complex's stable and negative chemical potential, which results from its negativity. The stiffness of an electron nebule in a chemical structure is its resistance to distortion caused by minor perturbations during chemical processing. Hardness is a notion used in physics and chemistry, although it cannot be seen physically. Though soft systems can be substantially and highly polarized, hard systems are less polarized and often tiny [25].

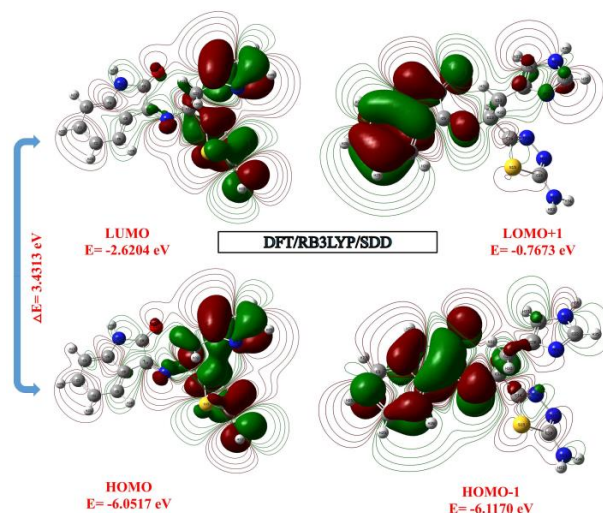


Figure 2. Boundary molecular orbitals of the molecule (1) as per the DFT/B3LYP/SDD phase.

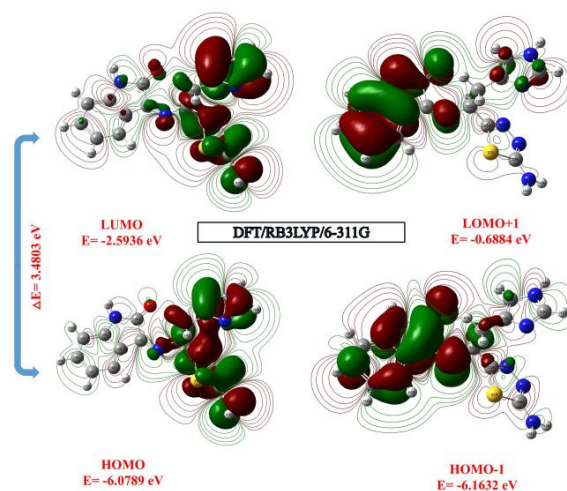


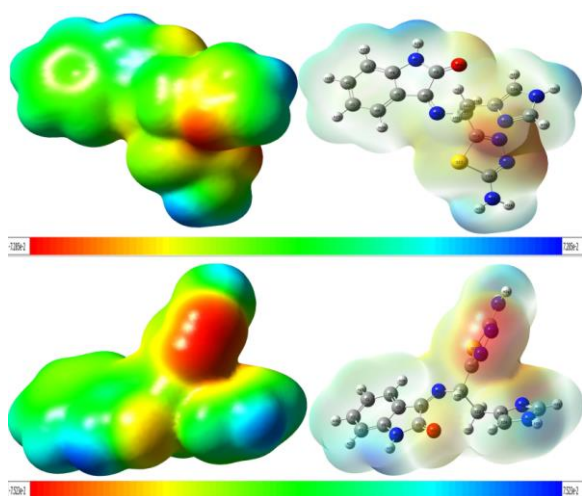
Figure 3. Boundary molecular orbitals of the molecule (1) as per the DFT/B3LYP/6-311G level.

Table 3. Calculated quantum chemical parameters*(in eV) to low energy compatibilities by DFT/RB3LYP/SDD-DFT/RB3LYP/6-311G methods of the molekül (1).

Molecules Energy		DFT/ B3LYP SDD	DFT/B3LYP 6-311G
E_{LUMO}		-2.6204	-2.5986
E_{HOMO}		-6.0517	-6.0789
E_{LUMO+1}		-0.7673	-0.6884
E_{HOMO-1}		-6.1170	-6.1632
Energy Gap	$(\Delta E)E_{HOMO} - E_{LUMO}/$	3.4313	3.4803
Ionization Potential	$(I = -E_{HOMO})$	6.0517	6.0789
Electron Affinity	$(A = -E_{LUMO})$	2.6204	2.5986
Chemical hardness	$(\eta = (I - A)/2)$	1.7156	1.7401
Chemical softness	$(s = 1/2 \eta)$	0.8578	0.8700
Chemical Potential	$(\mu = -(I + A)/2)$	-4.3360	-4.3387
Electronegativity	$(\chi = (I + A)/2)$	1.8102	1.7993
Electrophilicity index	$(\omega = \mu^2/2 \eta)$	5.4793	5.4089

3.4. Molecular Electrostatic Potential (MEP)

MEP may be used to describe hydrogen bond interactions in addition to electrophilic and nucleophilic activities. It has been correlated with electron density (ED) [26]. The electrostatic potential $V(r)$ is highly appropriated to research procedures requiring molecular identification, like interactions between receptors and drugs and enzymes and substrates. Because these two species initially perceive one other through the lens of their potential [27]. The electrophilic and nucleophilic portions of the examined compound have been predicted utilising the B3LYP/SDD and B3LYP/6-311G basis sets utilizing MEP in optimal geometry. As demonstrated in Figure 4 [28], MEP's negative (yellow or red) regions show electrophilic reacting, whereas favorable (blue) areas represent nucleophilic reactivity.

**Figure 4.** Molecular electrostatic potential field of molecule (1) utilising DFT/B3LYP and DFT/B3LYP methods with SDD and 6-311G basis set.

3.5. Non-Linear Optical Properties (NLO)

Nonlinear optical characteristics (NLO) are computationally predicted using polarizability (α) and hyperpolarizability (β) values [29]. Polarizability defines optical characteristics in organic-based materials. The hyperpolarizability of a material impacts the performance of its nonlinear optical characteristics. To show NLO qualities, a molecule's polarizability, hyperpolarizability, and dipole moment must be high, and the HOMO-LUMO energy difference must be modest [30]. Using the B3LYP/SDD(d,p) and B3LYP/6-311G method and basis sets, the hyperpolarization (β), polarization (α), and electric dipole moment (μ) of the molekül (1), NLO activity were measured. In the Table 4 [31] has been showed the calculated NLO values. The mean values of the polarizability (α), static dipole moment (μ), and total first static hyperpolarizability (β) of the x, y, and z components have been obtained from equations Equality 1-4." The total values molecule (1) determined using the DFT/B3LYP/SDD and DFT/B3LYP/6-311G methods are 3.48×10^{-30} esu and 3.55×10^{-30} esu, respectively.

$$\mu = (\mu_x^2 + \mu_y^2)^{1/2} \quad (1)$$

$$\alpha = 2^{-1/2} [(\alpha_{xx} - \alpha_{yy})^2 + (\alpha_{yy} - \alpha_{zz})^2 + (\alpha_{zz} - \alpha_{xx})^2 + 6\alpha_{xx}^2]^{1/2} \quad (2)$$

$$\beta_{Total} = (\beta^2_x + \beta^2_y + \beta^2_z)^{1/2} \quad (3)$$

$$= [(\beta_{xxx} + \beta_{xyy} + \beta_{xzz})^2 + (\beta_{yyy} + \beta_{yxx} + \beta_{yzz})^2 + (\beta_{zzz} + \beta_{zxx} + \beta_{zyy})^2]^{1/2} \quad (4)$$

Table 4. The dipole moments (Debye), polarizability (au), components, and total value of molecule (1) are computed using the SDD and 6-311G basis sets using the DFT/B3LYP technique.

Parameters	B3LYP/ SDD	B3LYP/ 6-311G	Parameters	B3LYP/ SDD	B3LYP/ 6-311G
μ_x	-3.1262	-2.6959	β_{xxx}	-41.5112	-19.4581
μ_y	-0.3183	-0.4954	β_{yyy}	42.6236	37.5772
μ_z	-0.9230	-0.7217	β_{zzz}	1.8263	3.7207
$\mu(D)$	3.2751	2.8344	β_{xyy}	124.3641	126.6830
α_{xx}	-101.7798	-102.7201	β_{xxy}	-39.9238	-37.7491
α_{yy}	-113.3843	-114.9895	β_{xxz}	9.7610	14.4029
α_{zz}	-157.9199	-157.9704	β_{xzz}	-22.5224	-21.2227
α_{xy}	2.9098	3.0128	β_{yzz}	-0.7940	-0.7190
α_{xz}	-3.0550	-2.7397	β_{yyz}	0.7671	2.6970
α_{yz}	-10.5986	-9.3997	β_{xyz}	-1.8619	0.8662
α (au)	-185.172	-184.8441	β (esu)	3.48×10^{-30}	3.55×10^{-30}

3.6. NBO Analysis

To better understand the intermolecular interactions of our compound, NBO analysis was performed on the optimized structures [32]. The NBO analysis software from the Gaussian 09W program package was utilized. The DFT (B3LYP) approach is used in the comparisons in the Table 5 [33] to demonstrate the percentages of individual bond electrons for and bonds in distinct bonds, as well as variations in the percentages of electrons in s,

p, and d orbitals on each atom. A quadratic is used for molecule (1). Fock matrix was used to forecast the relationship between the receiver (j) and the donor (i). The stabilizing value associated with delocalization is projected to be as follows Equality 5 to every donor (i) and recipient

$$E(2) = \Delta E_{ij} = q_i \frac{(F_{i,j})^2}{(\epsilon_i - \epsilon_j)} \quad (5)$$

The NBO element of the Fock matrix is $F(i,j)$, the diagonal elements are i and j , and the donor orbital occupancy is q_i . The higher the stabilization energy, the more electrons are likely to be transferred to acceptor orbitals [2]. The electron density, $E(2)$, $E(j)-E(i)$, and $f(i,j)$ values, as well as NBO computations, are shown in Table 5 [33] for a few chosen donors and acceptors. The interplay between the stabilization energy $E(2)$, full and unfilled NBO type Lewis orbitals, and electron delocalization from bonding (BD) to antibonding (BD*) orbitals is characterized by NBO analysis. Bond (σ/π) and anti-bond (σ^*/π^*) interactions also contribute considerably to structural stability, with the $\pi(C5-C6)/\pi^*(C3-C4)$ interaction having the highest E value of 30.17 kcal/mol. (2), followed by the $\pi(C1-C2)/\pi^*(C5-C6)$ interaction with 7.54 kcal/mol.

Table 5. Selected NBO results of molecule (1) are computed set using the DFT/B3LYP technique and the SDD basis set.

NBO(i)	Type	Occupancies	NBO(j)	Type	Occupancies	$E(2)^a$ (Kcal/mol)	$E(j)-E(i)^b$ (a.u.)	$F(i,j)^c$ (a.u)
C1-C2	σ	1.98122	C1-C6	σ^*	0.01327	1.42	1.22	0.037
C1-C6	σ	1.97809	C1-H25	σ^*	0.01442	0.71	1.20	0.026
C1-C2	π	1.66611	C5-C6	π^*	0.35889	22.55	0.29	0.072
C2-C3	σ	1.97584	C4-N7	σ^*	0.02889	7.11	1.05	0.077
C3-C4	π	1.66701	C1-C2	π^*	0.33082	22.19	0.29	0.072
C4-C5	σ	1.96039	C9-N11	σ^*	0.01657	4.61	1.26	0.068
C5-C6	π	1.64491	C3-C4	π^*	0.37349	24.68	0.27	0.074
C6-H28	σ	1.97628	C1-C2	σ^*	0.01546	4.67	1.05	0.063
C8-C9	σ	1.97087	C5-C6	σ^*	0.02306	5.61	1.19	0.073
C8-O10	π	1.97119	C9-N11	π^*	0.14278	0.63	0.39	0.043
C9-N11	π	1.88665	C8-O10	π^*	0.29819	12.18	0.30	0.057
C5-C6	π	1.64491	C9-N11	π^*	0.14278	18.13	0.26	0.065
C13-H32	σ	1.97613	C20-C24	σ^*	0.03128	5.94	1.04	0.070
C14-S15	σ	1.97035	C16-N19	σ^*	0.02406	5.55	1.04	0.068
C14-N18	π	1.93607	C16-N17	π^*	0.39043	7.77	0.31	0.048
C16-N17	π	1.90315	C14-N18	π^*	0.26756	12.27	0.32	0.059
N17-N18	σ	1.97117	C12-C14	σ^*	0.03547	5.47	1.17	0.072
N19-H34	σ	1.98397	S15-C16	σ^*	0.09479	5.68	0.78	0.061
C20-C24	π	1.82681	N21-C22	π^*	0.37577	16.39	0.26	0.061
N21-C22	π	1.87079	C20-C24	π^*	0.31090	21.22	0.33	0.078
C22-H35	σ	1.98014	C20-N21	σ^*	0.02637	4.77	0.98	0.061
N23-C24	σ	1.98435	C13-C20	σ^*	0.02161	5.78	1.21	0.075
C20-C24	σ	1.97960	C13-H31	σ^*	0.01500	0.96	0.44	0.046
C22-N23	σ	1.99080	C24-H37	σ^*	0.01152	2.84	1.32	0.055
N23-C24	σ	1.98435	C13-C20	σ^*	0.02161	5.78	1.21	0.075
N23-C24	σ	1.98435	C22-H35	σ^*	0.01802	2.88	1.29	0.054
N23-H36	σ	1.99062	C20-C24	σ^*	0.03128	1.92	1.26	0.044
C24-H37	σ	1.98165	C22-N23	σ^*	0.03752	3.76	0.95	0.054

4. CONCLUSION

Important geometric data like as bond angles and bond lengths of the structure's atoms were gathered as a consequence of molecular optimization. The B3LYP/6-31G and B3LYP//SDD techniques were used to calculate the different (E) between the compound's HOMO and LUMO energy levels depending on the solvent. The energy difference between LUMO and HOMO did not vary importantly as the solvent polarity rose, implying that the solvent polarity had no influence on the contact of the chemical and the creation of the action. The Mulliken charge distribution method was used to collect information on the charge distribution on the atoms as well as the various features of the molecular structures. Furthermore, the MEP map discovered by employing the compound's DFT/RB3LYP/6-31G and DFT/B3LYP/SDD base sets. The area has been discovered to be surrounding the methyl and hydrogen atoms, and these properties supplied us with knowledge about the regions of the chemical where non-covalent interactions may occur.

REFERENCES

- [1] Taslimi P, et al. Metal contained Phthalocyanines with 3,4-Dimethoxyphenethoxy substituents: their anticancer, antibacterial activities and their inhibitory effects on some metabolic enzymes with molecular docking studies. *Journal of Biomolecular Structure and Dynamics*, 2022; 40(7): p. 2991-3002.
- [2] Ulaş Y. 2-((1H-indol-1-il)(naftalen-1-il)metil)fenol Bileşiğinin Sentezi ve NLO Özelliklerinin Quantum Kimyasal Hesaplamalarla İncelenmesi. *Caucasian Journal of Science*. 2022; 9(2): p. 184-195.
- [3] Liu X. and J.-R Hamon. Recent developments in penta-hexa- and heptadentate Schiff base ligands and their metal complexes. *Coordination Chemistry Reviews*. 2019; 389: p. 94-118.
- [4] Abu-Dief A.M. and Mohamed I.M.A. A review on versatile applications of transition metal complexes incorporating Schiff bases. *Beni-Suef University Journal of Basic and Applied Sciences*, 2015; 4(2): p. 119-133.
- [5] Betiha M.A, et al. Oxidative desulfurization using graphene and its composites for fuel containing thiophene and its derivatives. *Egyptian Journal of Petroleum*. 2018; 27(4): p. 715-730.
- [6] Cowan R.D. Theoretical Calculation of Atomic Spectra Using Digital Computers. *Journal of the Optical Society of America*. 1968; 58(6): p. 808-818.
- [7] Karakurt T. 3-[(E)-2-(4-fenil-1,3-tiyazol-2-yl)hidrazin-1-yiliden]-indolin-2-on Bileşiğinin Tautomer Yapısı Üzerinde Gaz ve Katı Fazında Teorik Hesaplamalar. *Afyon Kocatepe Üniversitesi Fen Ve Mühendislik Bilimleri Dergisi*. 2020; 20(1): p. 96-102.
- [8] Michael J. Frisch B.S. Gustavo Scuseria, Mike Robb, Richard Cheeseman Jr, Giovanni Scalmani, Barone villagrande, Benedetta Mennucci, Gaussian 09, in gaussian. Inc., Wallingford. 2009.
- [9] Callaway J. and N.H March. *Density Functional Methods: Theory and Applications*, in Solid State Physics. H. Ehrenreich, D. Turnbull, and F. Seitz, Editors. 1984; Academic Press. p. 135-221.
- [10] Tanriverdi A.A, et al. Structural and Spectral Properties of 4-(5-methyl-[1,2,4] triazolo [1,5-a] pyrimidine-7-yloxy) phthalonitrile: Analysis by TD-DFT Method, ADME Analysis, and Molecular Docking Simulations. *Journal of the Institute of Science and Technology*. 2022; 12(4): p. 2340-2351.
- [11] Kökbudak Z, Türkmenoğlu B, and Akkoç S. A New Schiff Base Molecule Prepared from Pyrimidine-2-thione: Synthesis, Spectral Characterization, Cytotoxic Activity, DFT, and Molecular Docking Studies. *Adiyaman University Journal of Science*. 2022; 12(1): p. 9-25.
- [12] Abu-Awwad F, and Politzer P. Variation of parameters in Becke-3 hybrid exchange-correlation functional. *Journal of Computational Chemistry*. 2000; 21(3): p. 227-238.
- [13] Gören K, Bağlan M, and Çakmak İ. Theoretical Investigation of ¹H and ¹³C NMR Spectra of Diethanol Amine Dithiocarbamate RAFT Agent. *Journal of the Institute of Science and Technology*. 2022; 12(3): p.1677-1689.
- [14] Yüksek H, et al. B3LYP ve HF Temel Setleri Kullanılarak Bazı 3-Alkil-4-(2-asetoksi-3-metoksibenzilidenamino)-4,5-dihidro-1H-1,2,4-triazol-5-on Bileşiklerinin Deneysel ve Teorik Özelliklerinin İncelenmesi. *Celal Bayar University Journal of Science*. 2017; 13(1): p.193-204.
- [15] Bağlan M, Gören K, and Yildiko Ü. DFT Computations and Molecular Docking Studies of 3-(6-(3-aminophenyl)thiazolo[1,2,4]triazol-2-yl)-2H-chromen-2-one(ATTTC) Molecule. *Hittite Journal of Science and Engineering*. 2023; 10(1): p. 11-19.
- [16] Beytur M, and Yüksek H. 3-Fenil-4-(3-Sinnamoiloksibenzilidenamino)-4,5-Dihidro-1H-1,2,4-Triazol-5-On Molekülünün Spektroskopik Özellikleri. *Caucasian Journal of Science*. 2018; 5(2): p. 65-80.
- [17] Bağlan M., Gören K, and Yildiko Ü. HOMO–LUMO, NBO, NLO, MEP analysis and molecular docking using DFT calculations in DFPA molecule. *International Journal of Chemistry and Technology*. 2023; 7(1): p. 38-47.
- [18] Mumit M.A, et al. DFT studies on vibrational and electronic spectra, HOMO–LUMO, MEP, HOMA, NBO and molecular docking analysis of benzyl-3-N-(2,4,5-trimethoxyphenylmethylene)hydrazinecarbodithioat e. *Journal of Molecular Structure*. 2020; 1220: p.128715.
- [19] Bağlan M, Yildiko Ü, and Gören K. DFT Calculations And Molecular Docking Study In 6-(2-Pyrrolidinone-5-Yl) Epicatechin Molecule From Flavonoids. *Eskişehir Teknik Üniversitesi Bilim ve Teknoloji Dergisi B - Teorik Bilimler*. 2023; 11(1): p. 43-55.

- [20] Brownell L.V, et al. Highly Systematic and Efficient HOMO–LUMO Energy Gap Control of Thiophene-Pyrazine-Acenes. *The Journal of Physical Chemistry C*. 2013; 117(48): p. 25236-25247.
- [21] Jiang D, and Dai S. Circumacenes versus periacenes: HOMO–LUMO gap and transition from nonmagnetic to magnetic ground state with size. *Chemical Physics Letters*. 2008; 466(1): p. 72-75.
- [22] Zhang T, et al. Clarifying the Adsorption of Triphenylamine on Au(111): Filling the HOMO–LUMO Gap. *The Journal of Physical Chemistry C*. 2022; 126(3): p. 1635-1643.
- [23] Choudhary V, et al. DFT calculations on molecular structures, HOMO–LUMO study, reactivity descriptors and spectral analyses of newly synthesized diorganotin(IV) 2-chloridophenylacetohydroxamate complexes. *Journal of Computational Chemistry*. 2019; 40(27): p. 2354-2363.
- [24] Zhuo L, Liao G.W, and Yu Z. A Frontier Molecular Orbital Theory Approach to Understanding the Mayr Equation and to Quantifying Nucleophilicity and Electrophilicity by Using HOMO and LUMO Energies. *Asian Journal of Organic Chemistry*. 2012; 1(4): p. 336-345.
- [25] Pereira F, et al. Machine Learning Methods to Predict Density Functional Theory B3LYP Energies of HOMO and LUMO Orbitals. *Journal of Chemical Information and Modeling*. 2017; 57(1): p. 11-21.
- [26] Bağlan M., Yıldiko Ü, and Gören K. Computational Investigation of 5,5-trihydroxy-3,7-dimethoxy-4-O-biflavone from Flavonoids Using DFT Calculations and Molecular Docking. *Adıyaman University Journal of Science*. 2022; 12(2): p. 283-298.
- [27] Uysal Ü.D, Berber H, and Aydoğdu Erdönmez A. 2-Etoksi-6-[(E)-(2-Hidroksifenil)imino]metil]fenol Türevi Schiff Bazlarının Sentezi ve Teorik Çalışmalar. *Süleyman Demirel Üniversitesi Fen Bilimleri Enstitüsü Dergisi*. 2020; 24(2): p. 419-431.
- [28] Luque F.J, et al. SCRF calculation of the effect of water on the topology of the molecular electrostatic potential. *The Journal of Physical Chemistry*. 1993; 97(37): p. 9380-9384.
- [29] Öztürk N, et al. Structural, Spectroscopic (FT-IR, Raman and NMR), Non-linear Optical (NLO), HOMOLUMO and Theoretical (DFT/CAM-B3LYP) Analyses of N-Benzyloxycarbonyloxy-5-Norbornene-2,3-Dicarboximide Molecule. *Süleyman Demirel Üniversitesi Fen Bilimleri Enstitüsü Dergisi*. 2018; 22(1): p. 107-120.
- [30] Eranlı C.C, and Koşar B. Investigation of Physical and Chemical Properties of 2-[(2-hydroxy-4-nitrophenyl)aminomethylene]-Cyclohexa-3,5-Dien-1(2h)-One By DFT Method. *Journal of Science and Technology of Dumlupınar University*. 2016(2015 Özel Sayısı); p. 109-126.
- [31] Bhuiyan M.D.H, et al. Synthesis, linear & non linear optical (NLO) properties of some indoline based chromophores. *Dyes and Pigments*. 2011; 89(2): p. 177-187.
- [32] Kuş N, and Ilican S. 4-Florobenzil Alkolün Konformasyon ve Orbital Etkileşimlerinin DFT Metodu ile Teorik Çalışması. *Süleyman Demirel Üniversitesi Fen Bilimleri Enstitüsü Dergisi*. 2019; 23(3): p. 797-804.
- [33] Sebastian S. and Sundarag N. The spectroscopic (FT-IR, FT-IR gas phase, FT-Raman and UV) and NBO analysis of 4-Hydroxypiperidine by density functional method. *Spectrochimica Acta Part A: Molecular and Biomolecular Spectroscopy*. 2010; 75(3): p. 941-952.

Investigation of The Effect of Molding Material Difference on Design in GGG70 Ductile Cast Iron Production

Mete ŞEKERDEN¹ , Muhammet Emin KESKİN^{2*} , Melek DURMUŞ³ , Murat ÇOLAK⁴ 

¹Bayburt Üniversitesi, Fen Bilimleri Enstitüsü, Makine Mühendisliği Bölümü, Bayburt, Türkiye

²Bayburt Üniversitesi, Fen Bilimleri Enstitüsü, Makine Mühendisliği Bölümü, Bayburt, Türkiye

³Necmettin Erbakan Üniversitesi, Fen Bilimleri Enstitüsü, Makine Mühendisliği Bölümü, Konya, Türkiye

⁴Bayburt Üniversitesi, Teknik Bilimler Meslek Yüksekokulu, Elektronik ve Otomasyon Bölümü, Bayburt, Türkiye

Mete ŞEKERDEN ORCID No: 0009-0002-3862-9480

Muhammet Emin KESKİN ORCID No: 0000-0003-4342-6303

Melek DURMUŞ ORCID No: 0009-00061439-3759

Murat ÇOLAK ORCID No: 0000-0002-8255-5987

*Corresponding author: emnkskn47@hotmail.com

(Received: 21.08.2023, Accepted: 05.04.2024, Online Publication: 28.06.2024)

Keywords

GGG70,
Moulding
design,
Mould
rigidity,
Hot spot,
SolidCast

Abstract: The casting process involves filling a prepared mould cavity with molten metal, which takes the shape of the container. While the liquid metal takes the shape of the container it is in, the method is attractive, while the volumetric changes during the liquid-solid transformation reveal the importance of moulding design for the manufacture of solid parts. Especially in cast irons, moulds with the same design may produce different results depending on the changing casting and foundry conditions because the volumetric change that occurs during the solidification of ductile cast irons is affected by many parameters and develops differently than in steel and aluminium castings. This study used model wet and resin molding materials to create single and double-riser moulding and castings with different section thicknesses. The importance of the type of mold material used in castings and the number of feeders for the robust production of the cast part was evaluated using experimental and modeling techniques. When the results were examined, it was seen that the shrinkage risk was lower with resin mould than with green sand moulding. In addition, depending on the riser connection point, the importance of the riser neck has emerged.

Kalıp Malzemesi Farkının GGG70 Küresel Grafitli Dökme Demir Üretiminde Kalıplama Tasarımı Üzerine Etkisinin İncelenmesi

Anahtar Kelimeler

GGG70,
Kalıplama
tasarımı,
Kalıp
rijitliği,
Sıcak nokta,
SolidCast.

Öz: Döküm yöntemi ergitilmiş sıvı metalin hazırlanmış kalıp boşluğuna doldurulması ile parça imalatını kapsamaktadır. Sıvı metalin bulunduğu kabın şeklini alması, yöntemi cazip hale getirirken, sıvı katı dönüşümü esnasındaki hacimsel değişiklikler sağlam parça imalatı için kalıplama tasarımının önemini ortaya çıkarmaktadır. Özellikle dökme demirlerde aynı tasarıma sahip kalıplarda değişen döküm ve dökümhane şartlarına bağlı olarak farklı sonuçlar ortaya çıkarabilmektedir. Çünkü küresel grafitli dökme demirlerin katılaşması sırasında oluşan hacimsel değişim birçok parametreden etkilenerek, çelik ve alüminyum dökümlerindekinden farklı şekilde gelişmektedir. Bu çalışmada, farklı kesit kalınlıkları içerecek şekilde tasarlanan model yaş ve reçineli kalıp malzemeleri ile tek ve çift besleyicili olarak kalıplama ve dökümler yapılmıştır. Dökümlerde kalıp malzemesinin değişimine bağlı olarak besleyici sayısının döküm parçaların sağlam imalatındaki önemi deneysel ve modelleme teknikleri ile değerlendirilmiştir. Sonuçlar incelendiğinde aynı kalıplama tasarımında reçineli kalıp ile yapılan ölçümlerde yaş kalıp kumuna nazaran çekinti riskinin daha az ortaya çıktığı görülmüştür. Ayrıca besleyici bağlantı noktasına bağlı olarak besleyici boğazının önemi ortaya çıkmıştır.

1. INTRODUCTION

Cast irons have a wide variety of properties such as strength, hardness, toughness, high corrosion resistance, easy machinability and vibration damping. In cast irons, the shape, and shape of the carbon in the internal structure after solidification determines the type of cast iron. Classification in cast iron determines variables such as the chemical composition of the material, cooling rate, production method, and heat treatment methods after production [1]. Ductile iron is one of the types of cast iron where carbon is formed as graphite spheres due to the addition of small amounts of spheroidizers like magnesium and cerium to the molten iron before casting [1,2]. Ductile iron is a type of material with perfect castability, easy machinability, wear resistance, high strength to low weight ratio, fatigue strength, high corrosion resistance and toughness. Due to these properties, it is a widely used material in the machinery and automobile industries for structural components such as machine tool bearings, bearings, rolling mills, pistons, cylinders and pump housings [3].

In shaping methods using the casting method, the solidification stage is important for the mechanical properties of the material, depending on the product's internal structures. Inoculation is crucial to achieve desired mechanical properties in the spheroidization of ductile cast iron materials [4]. The microstructures of cast irons show different properties depending on their chemical composition, added inoculation element, casting parameters, and cooling conditions [5]. The mechanical properties of ductile cast iron castings largely depend on the volume, size, distribution, sphericity, and quantity of graphite in cast iron [6]. Changes in the matrix structure and sphericity of graphite can affect mechanical properties, influenced by alloying elements and ambient conditions during solidification. [7]. Ductile cast irons, which are widely used in the automotive and energy industries, can be further strengthened by changing the process parameters or applying an additional heat treatment [8]. When the literature is examined, it is seen that the material properties are improved by changing the casting conditions, heat treatment, and added alloying elements. In a study, the effect of the austempering process on the microstructure and wear properties of cast irons was investigated. And as a result, it was determined that as the amount of Al increased, the ferrite ratio and the amount of graphite in the matrix increased, while the sphericity of the graphites was impaired [9]. In a different study, the effect of normalized heat treatment on the microstructural change and mechanical properties of unalloyed ductile cast iron after annealing at intermediate critical austenitizing temperatures was investigated. At the end of the examination, they concluded that the processes performed differed considerably in the microstructure and the mechanical properties were improved. [10].

To obtain the material with the desired properties, the solidification process of the material, the mold material and the molding design are very important, apart from

the addition of the alloy element. [11]. We can define it as a molding design, which is finally integrated with the runners and risers of the part. The ability to make a part sound depends on molding design considerations such as modulus, volume, feed path, and hot spot criteria [12]. In the design, it is necessary to determine the location, number, and size of the riser depending on the geometry of the part. The hot spot, defined as the isolated region during solidification, is the most important criterion in the design of the riser, both in determining the number of risers and in determining the riser locations. The hot spot can be multiple and of different sizes depending on the part geometry and casting conditions. [11-17]. In addition, in the molding design of cast irons, there are also difficulties because the volumetric change occurs in the form of shrinkage and expansion due to the increase in density during solidification. The resulting shrinkage and expansion are affected by many parameters such as mold material, chemical composition, alloy overtemperature, inoculation quality, solidification time of casting (modulus), and casting speed. High carbon equivalent, high mold rigidity, high solidification time (high modulus), high inoculation quality (high nodularity), low casting temperature (low excess heat) and low casting to reach high dilation press and consequently lowly shrinkage [18-20].

The difficulties encountered in molding design and the need for intensive experience have been developed with the developments in computer technologies and modelling studies. Macro and micro-size errors in the cast part can be predicted to a large extent thanks to modelling programs. In this way, the runner-riser design can be designed on these simulation applications by determining which number and size of the risers are needed and in which position they will be placed on the 3D solid model. Modelling of the designed product can be done on the computer and many necessary results after casting can be obtained without any cost or loss of labour. [21-24].

With casting simulation programs, the riser design stages of cast irons are outlined;

- Determining the hot spots of the cast part and the modules of these regions,
- Calculation of percentage values of shrinkage time, net expansion or contraction depending on factors such as the chemical composition of the alloy to be cast, casting temperature, mould rigidity and casting modulus
- Determining the location, volume and quantity of the required riser (if necessary) according to the calculated values,
- We can sort it out as the design is completed and the results are evaluated [16,17].

In this study, a model with different section thicknesses was designed experimentally. Moulding and castings were made by applying changing casting parameters. As parameters, castings were made in green sand mould and resin moulding sand in accordance with two different designs, with a single top riser and a double top riser. The designs were supported by the computer-aided 3D

drawing program SolidWorks, and the modelling studies were supported by SolidCast casting simulation programs. After casting, the samples were cut from the locations determined in the modelling program and penetrant tests were applied, and microstructure samples were taken from the parts of the castings with different cross-sectional thicknesses and the sphericity was determined with image analysis software. Modelling and actual casting results were compared. Thus, in this study, the importance of moulding sand and the number of risers connected to the hot spot in the robust manufacture of cast parts were evaluated by experimental and modelling techniques.

2. MATERIAL AND METHOD

In this study, the design of the model with different cross-sections was done to examine the effect of the feeder path under changing casting conditions. The model given in Figure 1 is aimed to require a single or double riser depending on whether the feeding path remains open or close.

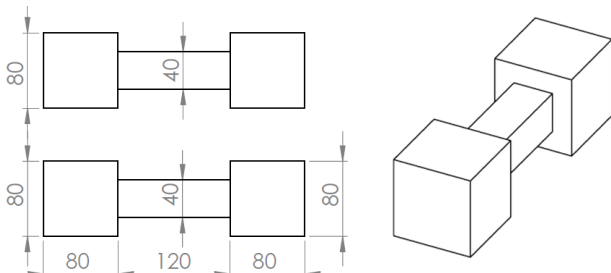


Figure 1. Dimensional drawing of casting model.

Model design studies were carried out from the SolidWorks program and solidification models were made with SolidCast software. As the first step of the moulding design, the model was solidified in the SolidCast program without runner and riser. Thus, the hot spots and modulus of the part were determined. When the module of the relevant part is determined as 1.42 cm, 2 hot spots appear. However, in the evaluations made with the modelling program, it has been determined that the feeding path will remain open at module values above 1.2 cm. The volumetric change curve and required riser dimensions were determined by SolidCast casting simulation software, depending on the relevant part weight, casting material mould rigidity, and chemical composition values. Example images of calculations taken from SolidCast software are given in Figure 2.

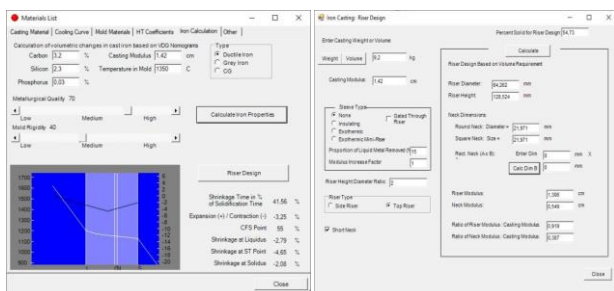
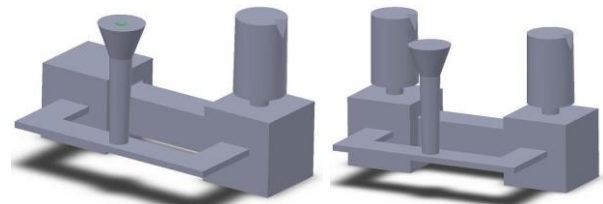


Figure 2. a) Volumetric change curve calculation from SolidCast software, b) Specifying riser sizes in the Riser Design Wizard.

As seen in Figure 2. a, the carbon, silicon and phosphorus values of the alloy, and the temperature of the casting part in the mould were entered and volumetric change curve calculations were made depending on the module value calculated by the program. In the volumetric change curve calculation, there are also the metallurgical quality and mould rigidity values that vary depending on the foundry and are the focus of the study. Relevant values are values ranging from 0 to 100, differing according to mould material and foundry spheroidization and inoculation procedure. After the volumetric change curve calculation, the riser design was started. In the riser design tab specific to cast irons in Figure 2. b, optional required features (sleeve type, riser height: diameter ratio, riser type etc.) are entered and riser calculations are started. In this study, riser type was preferred as the top riser and riser height, diameter and throat linkup measure were determined hence. Within the scope of the study, single and double-riser moulding designs were made according to the use of green sand moulding and resinous moulding sand in the calculations of the volumetric change curve, and considering the differences in spheroidization and inoculation efficiency, and keeping the feeding path open. Moulding design drawings in accordance with the dimensions determined by the SolidCast program were made with the SolidWorks program as seen in Figure 3.



a) Single riser design b) Double riser design

Figure 3. Moulding design images.

In order to compare all the results obtained from the experiments in accordance with the design, the cast sample model, risers and runners were produced as free models. Moulding and casting processes were carried out in 2 commercially operating foundries. Moulds were prepared with green sand moulding in one of the foundries where the experiments were carried out, and moulding was made with alpha-set resin sand in the other foundry. Melting operations were carried out in induction furnaces located in the companies. After melting, castings after spheroidization and inoculation processes were carried out by both companies depending on their own application procedures. After the casting parts were removed from the moulds, the runners and risers were cut and examined.

The samples taken from the thermal centre of the thin and thick sections of the part for microstructure investigations were evaluated with the image analysis system after grinding and polishing. Microstructure examinations were performed using Clemex Vision Lite image analysis software on images taken from the Nikon Eclipse L150 optical microscope. With the modeling simulation program, the globalization of the samples, the

average diameter of the spheres and the dispersion rate of the globalization were determined as a percentage.

After the casting samples were cut vertically from the centre of the thick section and medium thin section regions on the right and left, their surfaces were processed by milling and subjected to penetrant tests. Liquid penetrant testing is a non-destructive testing method and is used to detect invisible superficial defects such as cracks. Commercially used BETA BT68 penetrant paint was applied to the surfaces to be examined with cleaning liquid after machining. Here, it is aimed to see the pores formed on the surface, which cannot be detected with the naked eye. After a certain period of time, the paint fills into the pores on the applied surface. After waiting for enough, the paint special spray surface is applied and the surface is cleaned with a cloth. After removing the penetrant paint from the surface, BETA BT70 developer was applied to the section surface by spraying, so that the penetrant paint filled into the pores became visible as macro, and the pore status of the relevant surface was determined.

Modeling studies were carried out with the help of solidcast casting program.. After the designs in STL format were transferred to the program, the alloy and thermo physical properties were defined. The thermophysical values of the casting alloy are shown in Figure 4 for the CU DI Ferr alloy corresponding to the ferritic ductile iron alloy in the database of the simulation program.

Property	Value	Unit
Thermal Conductivity	41.51	W/m-K
Specific Heat	460.24	J/Kg-K
Density	7176.064	kg/m ³
Initial Temperature	1371.111	C
Solidification Temperature	1128.378	C
Freezing Range	41.667	C
Latent Heat of Fusion	230115.6	J/Kg

Figure 4. CI DI Ferr alloy values.

3. RESULTS

The values related to the analysis results of the samples taken for the control of the chemical composition of the alloys used in the casting experiments are given in Table 1.

Table 1. Chemical composition of the casting alloy used in the experiments

Element (%)	C	Si	Mn	Cr	Ni	Cu	Mg	P	S	Fe
	3.22	2.34	0.3	0.04	0.04	0.14	0.021	0.06	0.04	Bal.

When the result is examined, it is understood that the chemical analyzes were determined as expected depending on the alloy additions added to the furnace and it is in accordance with the GGG70 alloy standard.

3.1. Microstructure and Image Analysis Results

The microstructure pictures taken at 50X magnification obtained from the thin and thick sections of the cast samples are given in Figure 5. The average image analysis results for the processing of the images are given. In Table 2, the % sphericity, mean sphere diameter and per cent area measurements of the samples were taken from the pictures taken at 100X magnification in order to cover a wider area.

Table 2. Image analysis measurement results

Riser Status	Section Location	% Sphericity	Sphere Diameter (µm)	% Spherical Graphite Amount	Number Spheres (Piece)
Green Sand Top Single	Thin	83.8	20.8	9.6	224
	Thick	83.3	24.5	9.2	198
Green Sand Top Double	Thin	84.1	22.4	9.7	215
	Thick	83.9	26.3	9.9	193
Resin Top Single	Thin	87.5	20.2	10.1	235
	Thick	87.2	23.9	9.6	198
Resin Top Double	Thin	86.8	25.6	9.7	206
	Thick	88.6	28.9	9.8	191

First of all, the suitability of the spheroidization and inoculation process of the materials produced in both foundries was evaluated from the microstructure drawings and image analysis results. Depending on the evaluations, as seen in Figure 5, most of the graphite appeared in spherical form. When the results given in Table 2 are examined, while the globocity is measured at more or less 83% in wet moulding sand, the globocity value in moulds prepared with resinous sand. It has been found to be around 87%. This shows that the inoculation and spherization processes of the foundries are sufficient and appropriate. A striking point in all castings is the change in sphere diameter depending on the change in section thickness. As the section thickness increased, an increment was observed in the mean diameters of the graphites, which were formed due to the prolongation of the solidification time. Depending on the solidification time in the microstructures occurring in the section thicknesses, larger graphite formation in the thick section area draws attention. Similarly, in cases made with double risers, when the whole of the cast is considered, it has been determined that the graphites that appear due to the prolongation of the solidification time tend to grow. In studies on the subject, it has been reported that the diameter of the sphere increases with the increase of the modulus and the number of spheres per unit area decreases [25-30]. When the effect of the moulding sand difference on the microstructure is examined, it is noteworthy that the graphite form, though not in size, appears in a more regular formation in the resinous mould. It is thought that this situation is caused by the prevention of the expansion of the mould during the expansion of the alloy, depending on the die rigidity, so that the sphericity ratio of the graphite increases.

3.2. Penetrant Test Results and Comparison with Modeling Results

Porosity investigations due to insufficient feeding on the cross-sectional surface of the cast samples were carried out by penetrant tests. The test results of the vertically cut surfaces from the centre of the thin and thick section regions of the model are given in Figure 7. In Figure 7, the modelling results are also given and thus the results obtained are compared. Modelling results are result images of shrinkage risk with 99.8% precision.

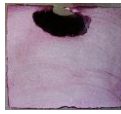

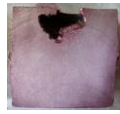
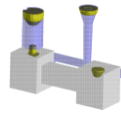
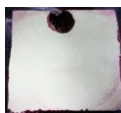
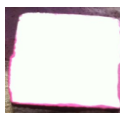

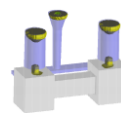

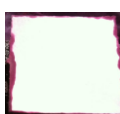

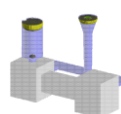
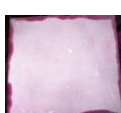


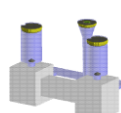
		Left Thick Section	Medium Thin Section	Right Thick Section	Modelling Result
Wet Molding Sand	Top Single				
	Top Couple				
Resin Molding Sand	Top Single				
	Top Couple				

Figure 7. Casting experiments penetrant test and modeling result images.

The simulation and actual castings results seen compatible with acceptable error margin. When the results are examined in general, it is observed that the design is suitable and there is no error in the resin mould, while errors occur in castings made with green sand. This may be related to the hardness of the resin mould being much stronger than the green sand mould. It is thought that there is no error in the expansion that occurs during the induration of the cast iron, as the casting part can't sprawl in the gum mould due to the high rigidity of the mould. While the difference between green sand moulding sand and resinous moulding sand properties is entered in the modelling program, different values and casting iron properties and sand differences are specified in the "Mold Rigidity" section of the mould rigidity section. As a result of modelling matches, models were made by entering 40 for wet moulding sand and 90 for resinous moulding sand. When the results of the casting samples made with wet moulding sand with a single riser from the top are examined, it is seen that there is a clear shrinkage in both of the thick sections. As a result of the evaluations made regarding this situation, it is thought that the narrow riser throat connection and the expansion of the mold dimensions during the expansion of the green mould sand caused the current situation. As can be seen from the penetrant test results and modelling results, there is no shrinkage risk on the cast part when the relevant design is poured into moulds

prepared with resinous sand. It is thought that the errors that occur when the same design is produced with wet moulding sand are caused by the opening of the riser's throat due to expansion and not feeding the mould sufficiently. When the shrinkage rates in the feeder are examined depending on the moulding sand change; Although there was more shrinkage in the feeder in green moulding sand, it was observed that the casting sample sizes increased due to the expansion of the mould dimensions. However, although there is less shrinkage in the riser in the resin mould, it has been observed that there is no shrinkage in the cast part due to the expansion effect due to the solidification of the feeder's throat after feeding the mould. When castings made with resin moulding sand with a double riser from the top are examined, it is understood that there is no shrinkage risk on the part like single feeder castings made into resin moulds. In the literature, there are many studies in which consistent results are obtained as a result of modelling of castings and the importance of expansion pressure and casting errors due to hot spots are emphasized. And it is understood that they are compatible with the results within the scope of the study [31-38].

4. DISCUSSION AND CONCLUSION

The results obtained from the study, in which the casting of GGG70 material in single and double riser green and resinous sand moulds was examined comparatively with modelling techniques, are given below;

- In cast iron castings, foundry conditions have a significant impact on riser design.
- When parts with the same design are cast under different casting conditions, significant differences are observed in the results.
- When the sample microstructures are examined, the solidification period is efficient on the sphere diameter and dimension. Sphere diameters formed in thin-section regions with smaller modulus are relatively smaller in diameter by showing a more homogeneous distribution compared to regions with large cross-sections.
- It has been observed that the mould rigidity is not very good, and when moulding with green sand moulding, the casting part expands during solidification and expands the mould, and the dimensions of the output casting part are larger. In this case, the part is also scrapped due to an error in the part due to insufficient feeding.
- The required feeder design varies according to GGG70 chemical composition, casting temperature, casting modulus, mould rigidity (moulding sand material used), and inoculation quality (metallurgical conditions). When these conditions change for the same model, the riser requirement can be single or double.
- While designing the riser in cast irons, the volumetric expansion features show the shrinkage expansion together. For this reason, especially the throat connection should be chosen carefully while designing, and the situations called vomiting should be prevented by calculating to complete the solidification of the throat at the point where the expansion starts in the part after shrinkage.
- Cast simulation programs are efficient device for riser blueprint and give results consistent with real casting



results when pouring conditions are transferred to the program exactly.

REFERENCES

- [1] Stefanescu, D. M. (2005). Solidification and modeling of cast iron—A short history of the defining moments. *Materials Science and Engineering: A*, 413, 322-333.
- [2] Fredriksson, H., Stjernedahl, J., & Tinoco, J. (2005). On the solidification of nodular cast iron and its relation to the expansion and contraction. *Materials Science and Engineering: A*, 413, 363-372.
- [3] Park, Y. K., Ha, K., Bae, K. C., Shin, K. Y., Lee, K. Y., Shim, D. S., & Lee, W. (2022). Mechanical properties and wear resistance of direct energy deposited Fe–12Mn–5Cr–1Ni-0.4 C steel deposited on spheroidal graphite cast iron. *Journal of Materials Research and Technology*, 19, 3484-3497.
- [4] Karadeniz, E., Çolak, M., & Barutçu, F. (2017). GGG-60 Küresel Grafitli Dökme Demir Üretiminde Aşılmalı Türü Ve Miktarının İyileştirme Ve Mekanik Özelliklere Etkisinin İncelenmesi. *Niğde Ömer Halisdemir Üniversitesi Mühendislik Bilimleri Dergisi*, 6(1), 275-282.
- [5] Kasvayee, K. A., Ghassemali, E., Svensson, I. L., Olofsson, J., & Jarfors, A. E. (2017). Characterization and modeling of the mechanical behavior of high silicon ductile iron. *Materials Science and Engineering: A*, 708, 159-170.
- [6] Labrecque, C., & Gagne, M. (1998). Ductile iron: Fifty years of continuous development. *Canadian metallurgical quarterly*, 37(5), 343-378.
- [7] Sołniski, M. S., Kordas, P., Skurka, K., & Jakubus, A. (2016). Investigations of ferritic nodular cast iron containing about 5-6% aluminium. *Archives of Foundry Engineering*, 16.
- [8] Adebayo, A. O., Ajibola, O. O., Owa, A. F., Borisade, S. G., Alaneme, K. K., & Oyetunji, A. (2021). Characterisation and dry sliding wear behaviour of 2.29 wt% aluminium-alloyed ductile iron. *Materials Today: Proceedings*, 38, 1152-1158.
- [9] Rıdvan, G. E. C. Ü. (2022). Küresel grafitli dökme demirlerin aşınma davranışına alüminyum ilavesinin ve östemplleme ısıl işleminin etkilerinin incelenmesi. *Niğde Ömer Halisdemir Üniversitesi Mühendislik Bilimleri Dergisi*, 11(2), 1-1.
- [10] Kayaalp, K., Şahin, Ö., & Kiliçli, V. (2022). Normalize Isıl İşleminde Arakritik Östenitleme Sıcaklığının Küresel Grafitli Dökme Demirin Mikroyapı Ve Mekanik Özellikleri Üzerine Etkisi. *Konya Journal of Engineering Sciences*, 10(3), 692-703.
- [11] Kayıkçı, R., & Neşet, A. K. A. R. (2007). Farklı kesit kalınlıklarına sahip büyük hacimli bir çelik dökümün simülasyon teknikleri ile tasarlanması. *Politeknik Dergisi*, 10(4), 395-401.
- [12] Çolak, M. (2020). OPTICast yazılımı ile döküm endüstrisinde kalıplama tasarımı optimizasyonu uygulaması. *Gümüşhane Üniversitesi Fen Bilimleri Dergisi*, 10(3), 545-551.
- [13] Çolak, M., & Kayıkçı, R. (2005). Döküm simülasyon programları üzerine bir değerlendirme. *Metal Dünyası*, 189, 2-4.
- [14] Çolak, M., & Şirin, S. (2010). SolidCast Döküm Simülasyon Programıyla Kalıplama Tasarımının İşlem Basamakları. *Metal Dünyası Dergisi*, 202, 2-5.
- [15] Franssman, H. (2007). Hızlı ve Doğru Yolluk ve Besleyici Dizaynı için Döküm Simülasyon Programlarının Pratik Kullanımı. *Metal Dünyası*, 164, 30-31.
- [16] Schmidt, D. C. (2007). The Basics of Solidification, Gating and Riser Design of Cast Irons, AFS Wisconsin Regional Conference, Finite Solutions Inc Slinger WI, February 8.
- [17] Meredith, J. F. (2008). Solving porosity problems in graphitic iron castings. *Casting Solutions Pty Ltd Moorebank, NSW, Australia*.
- [18] Çolak, M., & Şekerden, M. (2022). Modelling And Validation Of Effect Of Binder Type On Feeding Behaviour Of Spheroidal Graphite Cast Iron. *International Journal of Cast Metals Research*, 35(1-3), 9-16.
- [19] Çolak, M., & Kaya, S. (2021). Investigation of the effect of inoculant and casting temperature on fluidity properties in the production of spheroidal graphite cast iron. *Transactions of the Indian Institute of Metals*, 74, 205-214.
- [20] İ. Arda, S. Şirin, M. Çolak, R. Kayıkçı. Küresel Grafitli Dökme Demir Dökümlerinde Hacimsel Değişime Etki Eden Faktörlerin İncelenmesi. 6 th International Advanced Technologies Symposium (IATS'11), 16-18 May 2011, Elazığ, Türkiye
- [21] Çolak, M., Arslan, İ., & Gavgalı, E. (2018). Gri Dökme Demirlerin Katılma Modellemesi ve Gerçek Dökümler ile Karşılaştırması. *Engineering Sciences*, 13(4), 280-290.
- [22] Asan, Y. E., & Çolak, M. (2022). Modeling the Effect of Pour Height, Casting Temperature and Die Preheating Temperature on the Fluidity of Different Section Thicknesses in Permanent Mold Casting of Al12Si Alloys. *Erzincan University Journal of Science and Technology*, 15(Special Issue I), 14-27.
- [23] Çolak, M., & Dispınar, D. (2021). The influence of metallostatic pressure, grain refiner, and modification on the critical solid fraction (CSF) of cast A380 alloy. *Journal of Engg. Research Vol*, 9(4B), 269-280.
- [24] Teke, Ç., Çolak, M., Taş, M., & İpek, M. (2019). Modeling of the impact of initial mold temperature, Al5Ti1B and Al10Sr additions on the critical fraction of solid in die casting of aluminum alloys using fuzzy expert system. *Polish Acad Sciences Inst Physics*.
- [25] Dogan, O. N., Schrems, K. K., & Hawk, J. A. (2003). Microstructure of thin-wall ductile iron castings (No. DOE/ARC-2004-041). *Albany Research Center (ARC), Albany, OR (United States)*.
- [26] Pedersen, K. M., Hattel, J. H., & Tiedje, N. (2006). Numerical modelling of thin-walled hypereutectic

- ductile cast iron parts. *Acta materialia*, 54(19), 5103-5114.
- [27] Bockus, S., & Zaldarys, G. (2009). Influence of the section size and holding time on the graphite parameters of ductile iron production. *Metalurgija*, 48(1), 19-22.
- [28] Guzel, E., Yuksel, C., Bayrak, Y., Sen, O., & Ekerim, A. (2014). Effect of section thickness on the microstructure and hardness of ductile cast iron. *Materials Testing*, 56(4), 285-288.
- [29] Alabbasian, F., Boutorabi, S. M. A., & Kheirandish, S. (2016). Effect of inoculation and casting modulus on the microstructure and mechanical properties of ductile Ni-resist cast iron. *Materials Science and Engineering: A*, 651, 467-473.
- [30] Megahed, H., El-Kashif, E., Shash, A. Y., & Essam, M. A. (2019). Effect of holding time, thickness and heat treatment on microstructure and mechanical properties of compacted graphite cast iron. *Journal of Materials Research and Technology*, 8(1), 1188-1196.
- [31] Çolak, M., Şirin, S., Kayıkcı, R., & Bilgin, Ö. (2010). Küresel Grafitli Dökme Demir Dökümlerinde Simülasyon Tekniği ile Besleyici Tasarımı ve Uygulamaları, 3. Uluslararası Döküm ve Çevre Sempozyumu (IFES 2009), İstanbul, Türkiye.
- [32] Kayıkcı, R., & Nergiz, M. (2010). Besleyicisiz Döküm Yöntemi ile Dökülen Bir Küresel Grafitli Dökme Demir Dökümün İncelenmesi in: 3. Uluslararası Döküm ve Çevre Sempozyumu (IFES2009), Ocak.
- [33] Ravi, B., & Joshi, D. (2007). Feedability analysis and optimisation driven by casting simulation. *Indian Foundry Journal*, 53(6), 71-78.
- [34] Mozammil, S., Karloopia, J., & Jha, P. K. (2018). Investigation of porosity in Al casting. *Materials Today: Proceedings*, 5(9), 17270-17276.
- [35] Guo, Z., Saunders, N., Miodownik, A. P., & Schillé, J. P. (2005). Modelling of materials properties and behaviour critical to casting simulation. *Materials Science and Engineering: A*, 413, 465-469.
- [36] Nimbalkar, S. L., & Dalu, R. S. (2016). Design optimization of gating and feeding system through simulation technique for sand casting of wear plate. *Perspectives in Science*, 8, 39-42.
- [37] Choudhari, C. M., Narkhede, B. E., & Mahajan, S. K. (2014). Casting design and simulation of cover plate using AutoCAST-X software for defect minimization with experimental validation. *Procedia Materials Science*, 6, 786-797.
- [38] Sutaria, M., Gada, V. H., Sharma, A., & Ravi, B. (2012). Computation of feed-paths for casting solidification using level-set-method. *Journal of Materials Processing Technology*, 212(6), 1236-1249.

Karyological Variation of *Clethrionomys glareolus* (Mammalia: Rodentia) from Türkiye

Ahmet Yesari SELÇUK^{1*} , Perinçek Seçkinozan ŞEKER¹ 

¹ Department of Forestry, Artvin Vocational School, Artvin Çoruh University, Artvin, Türkiye
Ahmet Yesari SELÇUK ORCID No: 0000-0002-2785-2823
Perinçek Seçkinozan ŞEKER ORCID No: 0000-0002-6103-4840

*Corresponding author: ahmetyesari@gmail.com

(Received: 16.01.2024, Accepted: 17.04.2024, Online Publication: 28.06.2024)

Keywords
Chromosome,
C-banding,
AgNOR
staining

Abstract: Conventionally stained, C-banded and AgNOR-stained karyotypes of *Clethrionomys glareolus* were studied in Samsun, Türkiye. The autosomal and sexual chromosome pairs were determined by using the conventional, constitutive heterochromatin and nucleolus organizer region (C-, and AgNOR) staining techniques. The diploid chromosome number of a female *C. glareolus* specimen was found as $2n = 56$, $NFa = 56$, and $NF = 58$. The karyotype consisted of a pair of small metacentric and 26 pairs of acrocentric chromosomes of different sizes. The X chromosomes were large acrocentrics. Similar to the result of past karyotype studies on *C. glareolus*, the C-positive and C-negative heterochromatin blocks were observed in the karyotype. As a difference from the results of a previous study, NORs were localized on the six acrocentric chromosome pairs instead of seven pairs. Thus, a chromosomal variation among *C. glareolus* populations was determined due to variability in the number of NOR-bearing autosomes. In this way, it contributed to the determination of intraspecific variations of this species and to Türkiye's biodiversity at the level of genetic diversity.

21

Türkiye'den *Clethrionomys glareolus*'un (Mammalia: Rodentia) Karyolojik Varyasyonu

**Anahtar
Kelimeler**
Kromozom,
C-bantlama,
AgNOR
boyama

Öz: Bu çalışmada, Türkiye'den elde edilen *Clethrionomys glareolus* türünün standart, C-bantlı ve AgNOR-bantlı karyotipleri incelendi. Otozomal kromozomları ve eşey kromozomları, standart, C-bantlama ve AgNOR boyama (C- ve AgNOR) teknikleri kullanılarak belirlendi. *C. glareolus* örneğinin diploid kromozom sayısı $2n = 56$, $NFa = 56$ ve $NF = 58$ şeklindedir. Karyotipte, bir çift küçük metasentrik ve 26 çift farklı boyutlarda akrosentrik kromozomlar bulunmaktadır. X kromozomları büyük akrosentrik şeklindedir. *C. glareolus* üzerinde geçmişte yapılan karyotip çalışmalarının sonucuna benzer şekilde, karyotipte C-pozitif ve C-negatif heterokromatin bölgeler olduğu belirlendi. Bu çalışmanın sonuçlarında, Ag-NOR bölgelerinin altı akrosentrik kromozom çifti üzerinde lokalize olduğu tespit edildi. Böylece, Ag-NOR taşıyan kromozomların sayısındaki değişkenliğe bağlı olarak *C. glareolus* popülasyonları arasında kromozomal bir varyasyon olduğu belirlendi. Bu çalışma ile *C. glareolus* türünün tür içi varyasyonlarının belirlenmesine ve Türkiye biyoçeşitliliğine genetik çeşitlilik düzeyinde katkı sağlanmış oldu.

1. INTRODUCTION

The bank vole (or red-back vole), *Clethrionomys glareolus* is a rodent species that lives in mixed and deciduous forests consisting of coniferous and broad-leaved trees. This species is widely distributed in the Palearctic region. Its distribution range extends from Europe to Central Asia [1-3]. In Türkiye, this species is widely distributed in the Black Sea Mountains and the Marmara Region across the forests found in the northern line of Türkiye. Also, an isolated population of the

species lives in Uludağ, Bursa [15]. The karyotype of *C. glareolus* is characterized by the value of a diploid number of chromosomes $2n = 56$, the number of autosomal chromosome arms $NFa = 56$, and the fundamental number of chromosomal arms $NF = 60$. The morphology of sex chromosomes is variable [5-8]. The X chromosome is acrocentric, while the Y chromosome is metacentric in Turkish populations or acrocentric in European populations. [4, 5, 9-14]. So far, few studies have been conducted in Türkiye revealing the karyological characteristics of *C. glareolus*. In these studies, both traditional and banded karyotypes (C-

banded and AgNOR stained) of the populations of this species were examined. Accordingly, the standard karyotype of this species included a small metacentric pair and 26 acrocentric pairs in decreasing size. The X chromosome was a large acrocentric; the Y chromosome was a small metacentric [4, 13, 14]. The samples used in these studies were mainly obtained from the localities in the northwestern Anatolia (from Bolu, Kocaeli, Uludağ, and Karabük) and did not represent all populations of the species distributed along the northern line. Therefore, there may be a lack of information about the potential variations in the karyotype of other populations of the species within its distribution range. A few karyotype studies previously performed on the samples from the northwestern Black Sea have not revealed any variation among the species' populations, but according to mitochondrial DNA sequence variations, *C. glareolus* populations are divided into two different geographical lineages in Türkiye, the eastern and the western Black Sea lineages, by the Kızılırmak Valley [15].

Chromosomes are known as the phenotype of the genotype, and although it is not as powerful a molecular marker as DNA sequences, karyotype studies aimed at determining chromosomal variations are still frequently used in rodent systematics to determine intraspecific variations [14]. By detecting variability in the number, morphology, and constitutive heterochromatin, condensed or nucleolus organizer regions (C-, G-, and AgNOR banding) patterns of chromosomes between populations, it may be possible to obtain significant phylogenetic, taxonomic, and even findings that may result in the identification of new taxa [16-18]. Also, the detection of variable karyotypes within populations of any species can help to understand and document the biodiversity at the genetic diversity level. Therefore, this study aimed to compare the conventional karyotypes of *C. glareolus* and their constitutive heterochromatin and nucleolus organizer regions (C- and AgNOR banding) patterns with previously conducted studies and to contribute to the next karyological studies. Thus, potential intraspecific variations will be revealed and a contribution to the biological diversity of our country.

2. MATERIAL AND METHOD

Karyotype analysis was performed on a female specimen of *C. glareolus* collected from Samsun (altitude: 450 m, North Anatolia, 41° 25' 10.03''N 36° 03' 58.54''E, 12, Apr. 2021). Karyotype preparations were prepared from the captured animals during the field work performed in accordance with the legal permission (no: E-21264211-288.04 -1071462) given by the Ministry of Agriculture and Forestry, General Management of Nature Conservation and National Parks of the Republic of Turkey. The karyotype preparations, including metaphase chromosome plates, were provided from the fresh femoral bone marrow cells of colchicine-treated animals [19]. The autosomal and sexual chromosome pairs were determined by using the conventional, constitutive heterochromatin and nucleolus organizer region (C-, and AgNOR) staining techniques. According to the chromosome staining techniques by Sumner [20]

and Howell and Black [21], constitutive heterochromatin (positive C-banded regions) and nucleolus organizer regions (NORs) were detected in the karyotype. In total, 10 slides were prepared and approximately 20 well-spread metaphase plates were investigated. The diploid number of chromosomes (2n), the fundamental number of chromosomal arms (NF), and the fundamental numbers of autosomal arms (NFa), together with the X and the Y chromosomes were organized from largest to smallest. All chromosomes were classified as the metacentric or acrocentric according to their centromere positions, consistent with Levan et al., [22]. The karyotype preparations of the specimen examined were deposited at the Artvin Çoruh University, Artvin, Türkiye.

3. RESULTS

The conventional, C-, and AgNOR-banded karyotype of *C. glareolus* from Samsun (Türkiye) was studied. The karyotype of a female *C. glareolus* specimen was in the form of $2n = 56$, $NFa = 56$, and $NF = 58$. In the conventional karyotype, the autosomal set comprised a pair of small metacentric (no: 1) and 26 pairs of different sizes of acrocentric chromosomes (nos:2-27).

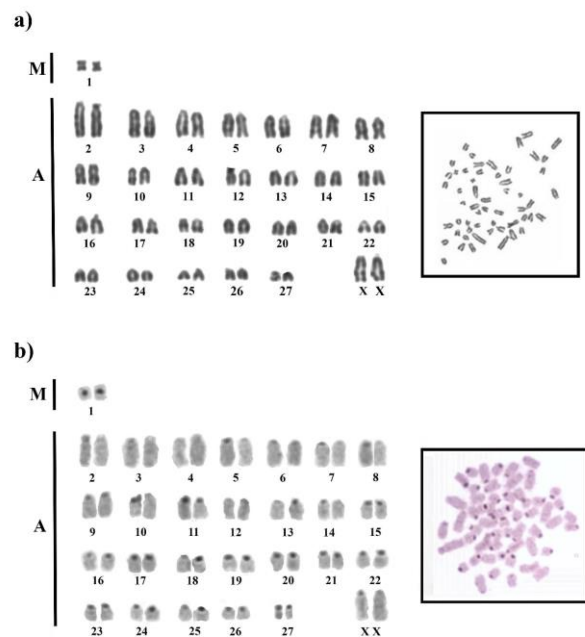


Figure 1. Conventional karyotype (a), C-banded karyotype (b) of a female *C. glareolus* specimen from Samsun, Türkiye, M: metacentric pair, A: acrocentric pairs.

The X chromosomes were large acrocentric. In the C-banded karyotype, acrocentric autosomal chromosomes contained both C-positive (no: 3 and nos: 5-27) and C-negative (no: 2 and 4) bands. The centromere region was clearly visible in the small metacentric chromosome pair (no: 1). X chromosomes showed C-positive bands (Figure 1).

In the AgNOR-stained karyotype of *C. glareolus*, nucleolus organizer regions were localized on the six pairs of acrocentric autosomal chromosomes (nos: 2, 5, 12, 14, 15, and 20). While three chromosome pairs (nos:

2, 5 and 15) had heteromorphic NORs, other NOR-bearing chromosomes were homomorphic (Figure 2).

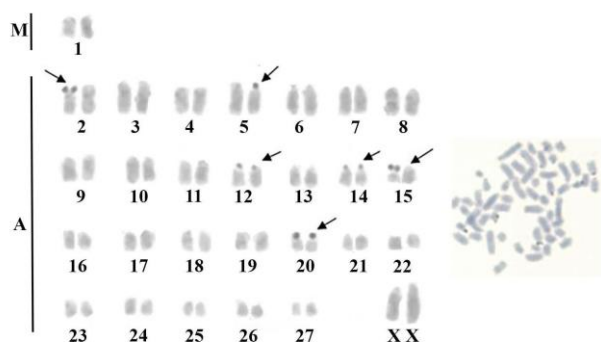


Figure 2. AgNOR-stained karyotype of a female *C. glareolus* specimen from Samsun, Türkiye. Arrows show NOR bearing chromosomes, M: metacentric pair, A: acrocentric pairs.

4. DISCUSSION AND CONCLUSION

This study presents the conventional, C- and AgNOR-stained karyotype of *C. glareolus* from Samsun, Türkiye. The standard karyotype of *C. glareolus* with the values of $2n = 56$, $NFa = 58$, and $NF = 58$ is compatible with the previously determined karyotypes in the studies carried out within the distribution area of the species [4-6, 8-13, 16]. According to the C-banded patterns revealed by this study, the heterochromatin distribution in the karyotype was observed in most of the chromosome pairs, except for the second and fourth pairs. Supporting this result, Arslan et al. [13], observed a similar situation in their karyotype study including no C-positive band for the fifth pair. A similar case was seen in the karyotypes of specimens from Australia and Greece [10, 12, 23].

AgNOR staining has frequently been used in rodent systematics to determine intraspecific variations, since NORs in the karyotypes may be located on the different chromosome and may be present in different numbers [24-29]. Variation in the distribution and the number of NORs has been previously reported in *C. glareolus* populations from different regions. In the karyological study conducted on the Bulgarian population, the NORs in the karyotype of *C. glareolus* were reported to be present on three autosomal chromosome pairs [30]. According to the results of the study including specimen from the north-western Black Sea region conducted by Arslan et al. [13], NORs present in seven acrocentric autosomal pairs, consisting of two homologous and five heteromorphic pairs. As a difference from that study, it was determined that NORs were present in six acrocentric chromosome pairs (three homologous and three heteromorphic) in the karyotype of the specimen from Samsun in the current study. Considering this result, it can be stated that there are intraspecific chromosomal variations in *C. glareolus* populations, which are known to have an uninterrupted distribution in the northern part of Türkiye. Analyses based on mitochondrial DNA sequence variations showed that *C. glareolus* populations in Türkiye have two distinct geographical lineages with genetic differences east and west of the Kızılırmak River [16]. Previous karyotype

studies on this species include populations distributed west of the Kızılırmak River [4, 13]. The sample examined in this study was obtained from the east of the river and differs from western populations in terms of the number of NORs in its karyotype. It is thought that this is a significant finding that supports intra-specific genetic variations as proposed by mitochondrial DNA variations. In conclusion, karyotype analysis, which is frequently used in systematic studies due to its easy applicability, has enabled the determination of intraspecific variations of *C. glareolus* and contributed to the biodiversity of Türkiye at the level of genetic diversity.

Acknowledgement

We would like to thank Dr. Haluk Kefelioğlu for his contributions to laboratory, field studies, review and editing.

REFERENCES

- [1] Shenbrot GI, Krasnov BR. Atlas of the Geographic Distribution of the Arvicoline Rodents of the World (Rodentia, Muridae: Arvicolinae). Sofia: Pensoft; 2005.
- [2] Kryštufek B, Vohralík V. Mammals of Turkey and Cyprus. Rodentia I: Sciuridae, Dipodidae, Gliridae, Arvicolinae. Založba Annales: Koper; 2005.
- [3] Wilson DE, Reeder DM. Mammal Species of the World: A Taxonomic and Geographic Reference. 3rd ed. The Johns Hopkins University Press: Baltimore; 2005.
- [4] Çolak E, Yiğit N, Özkurt Ş, Sözen M. Karyotype of *Clethrionomys glareolus* (Schreber, 1780) (Mammalia: Rodentia) in Turkey. Turk J Zool. 1997;21(2):123-125.
- [5] Král B. Chromosome characteristics of Muridae and Microtidae from Czechoslovakia. Acta Sc Nat Brno. 1972;6(12):1-78.
- [6] Živković S, Petrov B, Soldatović B, Savić I. Two morphologically different Y chromosomes in the bank vole (*Clethrionomys glareolus* Schreb.) from Serbia (Yugoslavia). Acta Vet. 1975;25: 241-246.
- [7] Vorontsov NN, Lyapunova EA, Ivanitskaya EY, Nadler CF, Kral B, Kozlovsky AI, et al. Variability of sex-chromosomes in mammals. 1. Geographical variability of morphology of y-chromosome in voles of genera *Clethrionomys* (Rodentia, Microtinae). Genetika 1978;14(8): 1432-1446.
- [8] Vujošević M, Blagojević J. Y chromosome polymorphism in the bank vole *Clethrionomys glareolus* (Rodentia, Mammalia). Zeitschrift Fur Säugetierkunde-International Journal of Mammalian Biology. 1997;62:53-57.
- [9] Král B, Zima J, Herzig-Straschil B, Štěrba O. Karyotypes of certain small mammals from Austria. Folia Zool. 1979;28(1): 5-11.
- [10] Gamperl R. Chromosomal evolution in the genus *Clethrionomys*. Genetica. 1982;57:193-197.
- [11] Zima J, Král B. Karyotypes of European Mammals I. Inst Lands Ecol. 1984;18 (7): 1-51.

- [12] Mitsainas GP, Rovatsos MT, Karamariti I, Giagia-Athanasopoulou E. Chromosomal studies on Greek populations of four small rodent species. *Folia Zool.* 2008;57:337–346.
- [13] Arslan A, Zima J, Yorulmaz T, Gözütok S, Toyran K. Chromosome banding pattern in fat dormouse and bank vole (Mammalia: Rodentia) from Turkey. *Folia Biol.* 2013;61(1-2):47-51.
- [14] Arslan A, Zima, J. Karyotypes of the mammals of Turkey and neighbouring regions: a review, *Folia Zool.* 2014;63(1):1–62, 2014.
- [15] Çolak R, Karacan, GO, Kandemir I, Çolak E, Kankılıç T, Yiğit N, et al. Genetic variations of Turkish bank vole, *Myodes glareolus* (Mammalia: Rodentia) inferred from mtDNA, Mitochondrial DNA Part A. 2016;27(6):4372-4379.
- [16] Zima J. Chromosomal evolution in small mammals (Insectivora, Chiroptera, Rodentia). *Hystrix.* 2000;11(2):5-15.
- [17] Dobigny G, Ducroz JF, Robinson TJ, Volobouev V. Cytogenetics and cladistics. *Syst Biol.* 2004;53(3): 473-48.
- [18] Gündüz İ, Jaarola M, Tez C, Yenyurt C, Polly PD, Searle JB. Multigenic and morphometric differentiation of ground squirrels (Spermophilus, Scuriidae, Rodentia) in Turkey, with a description of a new species. *Mol Phylogenet Evol.* 2007;43:916-935.
- [19] Ford CE, Hamerton JL. A colchicine, hypotonic citrate, squash sequence for mammalian chromosomes. *Stain Tech.* 1956;31:247-251.
- [20] Summer AT. A simple technique for demonstrating centromeric heterochromatin. *Expl Cell Res.* 1972;75:304-306.
- [21] Howell WM, Black DA. Controlled silver staining of nucleolus organizer regions with a protective colloidal developer: a 1-step method. *Experientia.* 1980;36:1014-1015.
- [22] Levan A, Fredga K, Sandberg AA. Nomenclature for centromeric position on chromosomes. *Hereditas.* 1964;52:201–220.
- [23] Gamperl R, Ehmann C, Bachmann K. Genome size and heterochromatin variation in rodents. *Genetica* 1982;58(3):199-212.
- [24] Sánchez A, Burgos M, Jiménez R, de La Guardia RD. Quantitative analysis of silver staining of the nucleolar organizing region in *Eliomys quercinus*. *Genome* 1989;32(6):978-982.
- [25] Suzuki H, Kurihara Y, Kanehisa T, Moriwaki K. Variation in the distribution of silver-staining nucleolar organizer regions on the chromosomes of the wild mouse, *Mus musculus*. *Mol Biol Evol.* 1990;7(3):271-282.
- [26] Zurita F, Sánchez A, Burgos M, Jiménez R, de la Guardia RD. Interchromosomal, intercellular and interindividual variability of NORs studied with silver staining and in situ hybridization. *Heredity.* 1997;78(3): 229-234.
- [27] Obara Y, Ohta M, Sasaki A. Patterns of distribution of Ag-NORs in the genus *Apodemus* and their evolutionary implications. *Chromosome Sci.* 2007;10(1):7-14.
- [28] Davidian-Britton J, Cazaux B, Catalan J. Chromosomal dynamics of nucleolar organizer regions (NORs) in the house mouse: micro-evolutionary insights. *Heredity.* 2012;108:68-74.
- [29] Suzuki T, Obara Y, Tsuchiya K, Oshida T, Iwasa MA. Ag-NORs analysis in three species of red-backed voles, with a consideration of generic allocation of Anderson's red-backed vole. *Mammal Study* 2014;39(2):91-97.
- [30] Belcheva RG, Topashka-Ancheva MN, Peshev DC, Gerassimov S. Karyological studies of some species of rodents in Bulgaria. *Savremenni postizheniya na balgarskata zoologiya, Sofia,* 1987;376-379.

In Vitro Cytotoxic Effects of Some *Fumaria* L. (Papaveraceae) Species Methanolic Extracts on Cancer Cell Lines

Pelin YILMAZ SANCAR^{1*} , Irmak İÇEN TAŞKIN² 

¹ Fırat University, Faculty of Science, Department of Biology, Elazığ, Türkiye

² İnönü University, Faculty of Science, Department of Molecular Biology and Genetics, Malatya, Türkiye

Pelin YILMAZ SANCAR ORCID No: 0000-0002-6134-622X

Irmak İÇEN TAŞKIN ORCID No: 0000-0002-1612-0563

*Corresponding author: peyilmaz@firat.edu.tr

(Received: 24.04.2023, Accepted: 17.04.2024, Online Publication: 28.06.2024)

Keywords

Fumaria,
Cytotoxic,
BEAS-2B,
SH-SY5Y,
HCT116,
A549

Abstract: The *Fumaria* L. species (Papaveraceae), is known popularly as “Şahtere”. This species, which has been proven to contain significantly rich components, is used by people to treat a number of different diseases. This study investigated the cytotoxic effects of the methanolic extracts of above-ground portions of *Fumaria asepalae* Boiss. and *Fumaria schleicheri* Soy.-Will. subsp. *microcarpa* Boiss. ex Hausskn. taxa against BEAS-2B, SH-SY5Y, HCT116 and A549 cell lines. The changes in cancer cell vitality were identified using the 3-(4,5-dimethylthiazol-2-il)-2,5-diphenyltetrazolium bromide (MTT). While the results showed that *F. asepalae* and *F. schleicheri* subsp. *microcarpa*'s methanolic extracts presented a meaningful decrease in the vitality of colon (HCT 116) cancer cells, no cytotoxic effect was achieved on lung (A549) cancer and brain (SH-SY5Y) cancer cells. Also, the herbal extracts did not create any toxic effect on healthy lung cells (BEAS-2B).

Bazı *Fumaria* L. (Papaveraceae) Türlerinin Metanolik Ekstraktlarının Kansere Hücre Hatları Üzerindeki İn Vitro Sitotoksik Etkileri

Anahtar

Kelimeler
Fumaria,
Sitotoksik,
BEAS-2B,
SH-SY5Y,
HCT116,
A549

Öz: *Fumaria* L. cinsi (Papaveraceae) halk arasında “Şahtere” olarak bilinir. Son derece zengin bileşiklere sahip olduğu kanıtlanmış olan cins, halk arasında birçok rahatsızlığın tedavisinde kullanılmaktadır. Bu çalışmada, *Fumaria asepalae* Boiss. ve *Fumaria schleicheri* Soy.-Will. subsp. *microcarpa* Boiss. ex Hausskn. taksonlarının toprak üstü kısımlarının metanolik ekstraktının BEAS-2B, SH-SY5Y, HCT116 ve A549 hücre hatlarına karşı sitotoksik özellikleri araştırıldı. Kansere hücrelerinin canlılığındaki değişiklikler 3-(4,5-dimetiltiazol-2-il)-2,5-difeniltetrazolyum bromür (MTT) yöntemi kullanılarak tespit edildi. Sonuçlar, *Fumaria asepalae* ve *F. schleicheri* subsp. *microcarpa*'nın metanolik ekstraktının özellikle kolon (HCT 116) kanseri hücrelerinin hücre canlılığında istatistiksel olarak anlamlı bir azalma olduğunu gösterirken, akciğer (A549) kanseri ve beyin (SH-SY5Y) kanseri hücreleri üzerinde sitotoksik etkinlik sağlamamıştır. Ayrıca bitkisel ekstraktlar, sağlıklı akciğer hücreleri (BEAS-2B) üzerinde ise herhangi bir toksik etki yaratmamıştır.

1. INTRODUCTION

Even though herbal drugs have been used to combat diseases since ancient times, information about their effective compounds and action mechanisms have only been known since the middle of the 19th century [1]. Some of the disadvantages of chemotherapy, one of the most preferred methods in cancer treatment, decrease the success rate of the treatment. Therefore, researching the

anti-cancer efficacy of herbal products has recently become one of the fields of interest [2].

Also, the search to support treatment with natural products due to synthetic drugs having many side-effects has brought traditional and complementary medicine practices to the forefront. This presents the consideration that using herbal products rich in biologically active components may be an important alternative to reducing high drug costs [3, 4].

The World Health Organization (WHO) has reported that the number of medicinal and aromatic herbs being used worldwide is approximately 20.000, that about 4.000 of these are widely used for therapeutic purposes, and about 2000 medical/aromatic herbs are traded worldwide while around 500 are traded in Western Europe [5, 6]. In Türkiye, the number of plants traded in the domestic market, together with the species and varieties collected from nature, is about 350 [7].

The *Fumaria* species (Papaveraceae), which is represented by 16 taxa in in Türkiye, consists of about 60 taxa worldwide [8] and has a cosmopolitan distribution in the entire European continent, especially in the Mediterranean region and Eastern and Western Europe [9]. Since *Fumaria* taxa are frequently used by communities in the treatment of many diseases, researchers have conducted research on the chemical contents of these taxa, which have shown that they are extremely rich sources of alkaloid content [10]. The presence of different types of flavonoids, steroid compounds and organic acids has also been identified in addition to alkaloid content [11]. As a result of studies conducted on different species of the genus, the literature shows that analgesic, antioxidant, hepatoprotective, antiproliferative, antiplasmodial, antibacterial, antifungal, and anti-inflammatory activities of *Fumaria* species have been proven [12, 13-18]. These activities are especially due to the isoquinoline alkaloids found in the plant, and protopine is the most common among them [19].

In this research, we aimed to contribute to the studies on the supply of raw materials as a new therapeutics from plants that grow naturally in in Türkiye. The cytotoxic activity of two taxa belonging to the genus *Fumaria* were investigated through using methanolic extracts and testing on the BEAS-2B (Healthy Human Bronchial Epithelial), SH-SY5Y (Human Neuroblastoma), HCT116 (Human Colorectal Carcinoma) and A549 (Human Lung Cancer) cell lines. To our knowledge, this the first study conducted to reveal the cytotoxic effect of *Fumaria asepala* Boiss. and *Fumaria schleicheri* Soy.-Will. subsp. *microcarpa* Boiss. ex Hausskn.

2. MATERIAL AND METHOD

2.1. Plant Material Collection and Identification

Plant materials were collected in May 2021 from Elazığ: Baskil-Sancaklı village inner road, 1410 m. in Türkiye (Lat: 38°35'13.061" Long: 38°55'23.055"). The taxonomic identification of plant materials was performed by Prof. Dr. Semsettin Civelek, who is a systematic-botanic specialist from Firat University. The collected plants were ventilated and dried in the shade for suitability for the study. Some of the specimens have been made into herbarium material and are kept under the herbarium number FUH8408 (*F. asepala*) and FUH8409 (*F. schleicheri* subsp. *microcarpa*). General appearances of plants are shown in Figure 1.

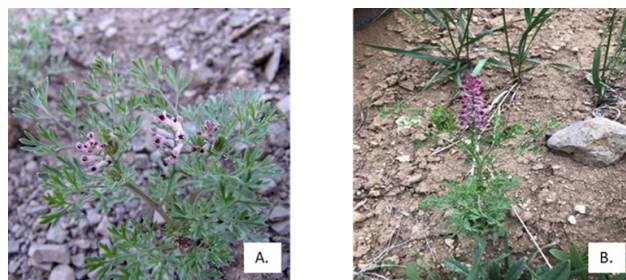


Figure 1. General appearance of *Fumaria* species: (A. *F. asepala*, B. *F. schleicheri* subsp. *microcarpa*)

2.2. Extraction Technique

All the root, leaf and flower parts of the plants were ground into powder, and 1 g of the plant sample was weighed on a precision scale and set to wait in a shaking incubator inside 100 ml 80% methanol at 35 °C for 72 hours. The mixture obtained from this was filtered using Whatman No 1 filter paper, and this process was repeated 3 times. Then, the obtained extracts were poured into sterile petri dishes and dried in a sterile cabinet until the solvent had evaporated. The dried extracts were dissolved with 99% DMSO (Dimetilsülfoksit-molecular grade), the concentrations were adjusted with DMEM (Dulbecco's Modified Eagle's Medium), and the stocks were kept at +4°C [20].

2.3. Cytotoxic Activity Assessment

The cytotoxic analysis of *F. asepala* and *F. schleicheri* subsp. *microcarpa*'s methanolic extract was done using healthy lung cells (BEAS-2B) and brain cancer (SH-SY5Y), colon cancer (HCT116) and lung cancer (A549) cell lines.

2.4. Cell Culture

Cells were grown in 25cm² flasks inside DMEM (25 mM L-Glutamine, 1% Penicillin-Streptomycin and 10% FBS (Fetal Bovine Serum)) at 37°C in 5% CO₂ atmospheric setting. When the flask base was covered with at least 95% cells, the cells were included in the experiments. A 0.25% trypsin-EDTA (Etilendiamin tetraasetik asit) solution was used for the removal of cells from the surface.

2.5. MTT Reduction Assay

The potential cytotoxicity of the tested extracts was evaluated as indicated by the MTT (3-(4,5-dimethylthiazol-2-yl)-2,5-diphenyltetrazolium bromide) Assay. In order to do this, cells were placed into the plates with 96 wells so that there were 10⁴ cells in each well. Then they were left to incubate in an incubator with 5% CO₂ at 37°C for 24 hours. After incubation, the medium in the wells was removed and added to the cells in 3 replicates at 5 different concentrations. (800, 400, 200, 100 and 50 µg/ml) from the methanolic extract of *Fumaria* species prepared in the medium. Healthy lung cell line (BEAS-2B) was used as positive control, and cell lines that no application was done on were used as negative control. The cells were left to incubate in an

incubator with 5% CO₂ at 37°C for 24 hours. After the incubation period, MTT solution (5mg/ml) was added to the wells the cells were in and incubated in a dark environment containing 5% CO₂ at 37°C for 3 hours.

After incubation, the medium was removed, and formazan crystals were dissolved with 100µl DMSO. Absorbance measurements were then made at a wavelength of 570 nm with the color change ELISA micro-plate reader (KHB ST-360) device, and cell vitality levels were calculated [21]. All MTT analyses were repeated 3 times.

2.6. Statistical Analysis

The results of the study were analyzed using SPSS statistical programming (version 22.0). The data were presented as mean ± SD. As a result of the SPSS analyses, the mean ± SD of the numerical data was provided. One-Way ANOVA test was used in the study to analyze the distributed data in the comparisons between multiple groups. A P-value of less than 0.001 was considered to be statistically significant. Tukey's tests were used for post hoc comparisons between the groups.

3. RESULTS

The cytotoxic activity of the methanolic extract of *F. asepal* and *F. schleicheri* subsp. *microcarpa* against SH-SY5Y, HCT116, A549, BEAS-2B cell lines is presented in the diagram. The cytotoxic activity of methanolic extract of *F. asepal* and *F. schleicheri* subsp. *microcarpa* is quite significant on colon cancer-HCT116 among the cell lines that were studied. This effect is stronger in *F. asepal* and relatively less in *F. schleicheri* subsp. *microcarpa*. At a concentration of 800 µg/ml, cell viability reduced to 57.08 ± 5.12% ($p < 0.001$) in *F. asepal* and 63.10 ± 14.18% ($p < 0.001$) in *F. schleicheri* subsp. *microcarpa* and it is the strongest concentration in terms of cell death rate. It was also observed that both *F. asepal* and *F. schleicheri* subsp. *microcarpa* have cytotoxic effect at 400 µg/ml, 200 µg/ml concentrations to reduce 57.42 ± 2.28 % ($p < 0.001$), 88.39 ± 6.61% ($p < 0.001$) and 80.40 ± 8.60% ($p < 0.001$), 85.35 ± 6.01% ($p < 0.001$) cell viability, respectively. While an increase was observed in the survival rate of cells due to the decrease in concentration, it was observed that the cytotoxic activity of the extracts continued down to the lowest concentration (50 µg/ml) for HCT116.

There were not significant cytotoxic activity on the other cell lines studied within both plant groups. For example, almost all concentrations of the herbal extract had a proliferative effect on both healthy lung cells and brain and lung cancer cell lines via increasing the number of living cells by almost 20%-30%. The herbal extract served as a nutrient for the cell groups that were studied, and while it was predicted to suppress cell proliferation and even kill cells, it was observed to be encouraging them to multiply. However, no toxic effects of the extracts on healthy cells were observed; on the contrary,

the extracts were observed to be promoting cell growth in both healthy and cancerous cell lines. The proliferative effect of plant extracts on cell groups is expected for healthy cells, but the fact that these extracts encourage cancerous cells to divide is evidence concluding that such extracts should not be used indiscriminately. The achieved results are presented in the live cell percentage diagram in Figure 2a-2b.

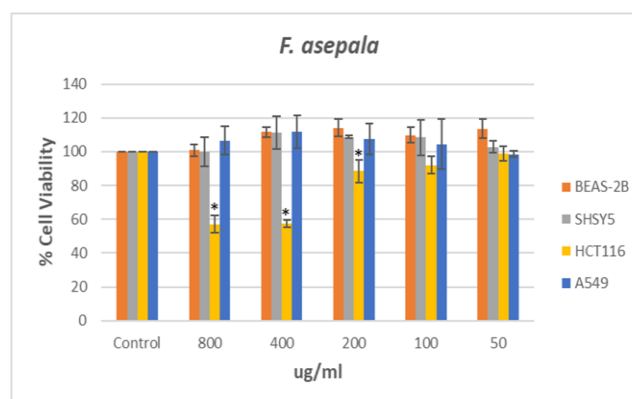


Figure 2a. Viable cell percentage diagram of *F. asepal* (* $p < 0.001$).

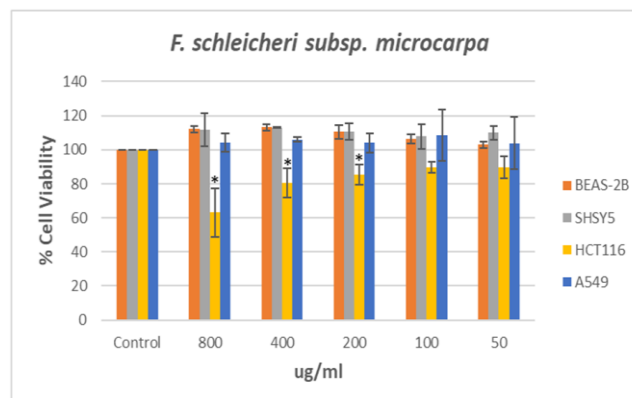


Figure 2b. Viable cell percentage diagram of *F. schleicheri* subsp. *microcarpa* (* $p < 0.001$).

4. DISCUSSION AND CONCLUSION

Many plant species belonging to the genus *Fumaria* are reported to have anticancer components that make them medically significant. Many *Fumaria* species have been utilized for biological properties such as essential oil, cytotoxicity, antimicrobial and antioxidant capacity, and very good results have been achieved. In studies conducted in this regard, it has been shown that the effects of herbal extracts on cell proliferation vary according to the type of extract used in the study and the type of cancerous cell [22].

Although there is no cytotoxic study conducted with *F. asepal* and *F. schleicheri* subsp. *microcarpa* taxa in the literature, there are studies that have been conducted with different *Fumaria* members.

Tabrizi et al. [23] have researched the antiproliferative activity of the hexane, chloroform, ethyl acetate and methanol extracts of *F. vaillantii* species on SKMEL-3, MCF-7 and K562 cell lines and suggested that the chloroform extract of the plant showed necrotic activity

against the [24-27]. Adham et al. [28] studied the effects of chloroform and ethyl acetate fractions of *F. officinalis* on CCRF-CEM, CEM/ADR 5000, NCI-H929, OPM-2 cell lines. According to their results, they discovered that the chloroform fraction of the plant was more effective against CCRF-CEM, CEM/ADR 5000 and NCI-H929 cell lines, and the ethyl acetate fraction was more effective against the OPM-2 cell line. Celik et al. [22] conducted research on Hep3B and HepG2 cell lines using methanolic extracts of *F. parviflora* and *F. capreolata* species; as a result, while no serious cytotoxic activity was determined on the cell lines studied, when compared in terms of DPPH scavenging activity and total antioxidant capacity, *F. parviflora* methanol extract was observed to have high activity in DPPH free radical scavenging and total antioxidant capacity. Similarly, Yılmaz Sancar [33] revealed the rich chemical content of *F. asepsala* and *F. schleicheri* subsp. *microcarpa* taxa and found that methanol extracts had antioxidant effect at a concentration of 1 mg/ml.

Paltinean et al. [18] determined the antioxidant, anticholinesterase, and cytotoxic potential of the *F. schleicheri* species by evaluating its alkaloid content. According to the results of their study on BJ and DLD-1 cell lines, they discovered that it did not have any cytotoxic activity against the studied cell line. Sattari et al. [29] conducted research on human breast cancer by combining AgNP (silver nanoparticles) and *F. parviflora* extract and showed that the resulting new compound had strong cytotoxic activity and could be used as strong potential nanodrugs against cancer. In the study done by Aljanaby [30], the antiparasitic, antimicrobial and cytotoxic potential of *F. officinalis* alcoholic extract and alkaloids extracted from the plant were studied. According to his results, alkaloids isolated from *F. officinalis* were more effective than alcoholic extract and showed strong effects as antiparasitic, anticancer and antibacterial agents.

Sadaoui et al. [31] researched the cytotoxic activity of protopine isolated from the *F. agraria* plant on two different breast cancer (MCF-7 and MDA-MB-231) cell lines and both of the cell lines examined displayed cytotoxicity on the examined cell lines. They also reported at the same time that MCF10A did not show any positive or negative effects on healthy breast cells. The same researcher later [32] evaluated the same extract on two different lung cancer (NCI-H23 and NCI-H460) cell lines and showed that it had strong cytotoxicity on both of the cell lines examined for protopine.

In conclusion, the cytotoxic activity of *F. asepsala* and *F. schleicheri* subsp. *microcarpa* taxa was reported for the first time in this study. The genus *Fumaria* is a single-year herbaceous genus and has a cosmopolitan distribution. These plants that grow in areas such as fields, roadsides and slopes up to 700 m above sea level are not plants with special demands. Despite this, they contain a large amount of valuable compounds such as alkaloids, salt, and tannins, and are also a source of fumaric acid. All these compounds they possess and how

easily they grow make them medically valuable. According to the study we conducted as well as the studies that already exist in literature, we can claim that the compounds in the *Fumaria* species are very valuable and can be used as potential therapeutics and as a source of raw materials in antiproliferative studies.

Acknowledgement

The authors, thanks to Prof. Dr. Semsettin CİVELEK for plant identification.

REFERENCES

- [1] Aksoy C, Yücecan S, Çiftçi N, Tayfur M, Akgün B, Taşcı N. Local plants used for treatment in cancer disease. J. of Nutr. and Dietetics. 1988;17(1): 111-120.
- [2] Yılmaz B. Investigation of Antitumoral Activity of Plant Extracts Collected from Various Regions [Master Thesis]. Tekirdağ: Namık Kemal University, Institute of Health Science; 2018.
- [3] Çoban T, Çitoğlu G, Sever B, İşcan M. Antioxidant activities of plants used in traditional medicine in Türkiye. Pharmaceutical Biology. 2003;41(8):608-613.
- [4] Goncalves S, Romano A. The medicinal potential of plants from genus *Plantago* (Plantaginaceae). Industrial Crops and Products. 2016;83(1):213-226.
- [5] Baydar H. Tıbbi, Aromatik ve Keyf Bitkileri Bilimi ve Teknolojisi. 1st ed. Türkiye: Suleyman Demirel University Publications; 2005;111-115.
- [6] Craker LE, Gardner Z, Etter SC. Herbs in American Fields: A Horticultural Perspective of Herband Medical Plant Production in the United States. Horticultural Science. 2003;38:977-983.
- [7] url-1: <http://www.turktarim.gov.tr/Haber/64/turkiye-tibbi-ve-aromatik-bitki-yetistiriciliginde-oncu-ulkelerden>.
- [8] Pérez-Gutiérrez MA, Romero-García AT, Salinas MJ, Blanca G, Fernández C, Suárez-Santiago VN. Phylogeny of the tribe Fumarieae (Papaveraceae) based on chloroplast and nuclear DNA sequences: Evolutionary and biogeographic implications. American J. of Bot. 2012;99:517-528.
- [9] Tutin TG, Burges NA, Chater AO, Edmonson JR, Heywood VH, Moore DM, et al. Psilotaceae to Platanaceae. In Flora Europaea, 2nd ed.; Cambridge, UK: Cambridge University Press; 2010;(1):306-311.
- [10] Orhan IE, Sener B, Musharraf SG. Antioxidant and hepatoprotective activity appraisal of four selected *Fumaria* species and their total phenol and flavonoid quantities. Exp. Toxicol. Pathol. 2012;64:205-209.
- [11] Sousek J, Guedon D. Alkaloids and organic acids content of Eight *Fumaria* species. Phytochem Anal. 1999;10:6-11.
- [12] Paltinean R, Mocan A, Vlase L, Gheldiu AM, Crişan G, Ielciu I, et al. Evaluation of Polyphenolic Content, Antioxidant and Diuretic

- Activities of Six *Fumaria* Species. *Molecules*. 2017;22:639-650.
- [13] Dutta R, Sharma MK, Jha MA. Review on Ethnobotanical, Phytochemistry, Bioactivities and Medicinal Mysteries of *Fumaria officinalis* (Common Fumitory). *EAS J. Pharm. Pharmacol.* 2019;1:99–105.
- [14] Al-Snafi AE. Constituents and Pharmacology of *Fumaria officinalis*-A Review. *IOSR J. Pharm.* 2020;10:17–25.
- [15] Ivanov IG, Vrancheva RZ, Marchev AS, Petkova NT, Aneva IY, Panteley DP, Georgiev VG, Pavlov AI. Antioxidant Activities and Phenolic Compounds in Bulgarian *Fumaria* Species. *Int. J. Curr. Microbiol. Appl. Sci.* 2014;3:296–306.
- [16] Zhang R, Guo Q, Kennelly EJ, Long C, Chai X. Diverse Alkaloids and Biological Activities of *Fumaria* (Papaveraceae): An Ethnomedicinal Group. *Fitoterapia*. 2020;146: 104697.
- [17] Paltinean R, Toiu A, Wauters JN, Frédéric M, Tits M, Angenot L, et al. Identification and Determination of Alkaloids in *Fumaria* Species from Romania. *Dig. J. Nanomater. Biostruct.* 2013;8:817–824.
- [18] Pältinean R, Ielciu I, Hanganu D, Niculae M, Pall E, Angenot L, et al. Biological Activities of Some Isoquinoline Alkaloids from *Fumaria schleicheri* Soy. *Will. Plants*. 2022;11(9):1202.
- [19] Vrancheva R, Ivanov I, Marchev A, Pavlov A. Qualitative and quantitative determination of protopine in *Fumaria* spp. by TLC-densitometry method. *J. Biosci. Biotechnol.* 2012;1:255–259.
- [20] Çelik AK, Yılmaz Sancar P, Icen Taskın I, Kürşat M. Investigation of the cytotoxic effect of *Lallemantia* Fisch. & C.A. Mey. species growing in Türkiye on various cancer cell lines. *Artvin Coruh University Journal of Forestry Faculty*. 2024;25(1): 104-110.
- [21] Yener I, Olmez OT, Ertaş A, Yılmaz Ma, Fırat M, Kandemir SI, Öztürk M. A detailed study on chemical and biological profile of nine *Euphorbia* species from Türkiye with chemometric approach: Remarkable cytotoxicity of *E. fistulosa* and promising tannic acid content of *E. eriophora*. *Indust. Crops and Prod.* 2018;123:442-453.
- [22] Çelik TA, Aslantürk ÖS, Yılmaz EŞ, Güzel Y. Antioxidant and Cytotoxic Activities of *Fumaria parviflora* Lam. and *Fumaria capreolata* L. *KSU J. Agric Nat.* 2022;25(4):819-827.
- [23] Tabrizi FH, Irian S, Amanzadeh A, Heidarnejad F, Gudarzi H, Salimi M. Anti-proliferative activity of *Fumaria vaillantii* extracts on different cancer cell lines. *Res Pharm Sci.* 2016;11(2):152-9.
- [24] Seyed RM, Nassiri-Asl M, Farahani-Nick Z, Savad S, Seyed KF. Protective effects of *Fumaria vaillantii* extract on carbon tetrachloride induced hepatotoxicity in rats. *Pharmacologyonline*. 2007;3:385-393.
- [25] Rathi A, Srivastava A, Shirwaikar A, Rawat A. Hepatoprotective potential of *Fumaria indica* Pugsley whole plant extracts, fractions and an isolated alkaloid protopine. *Phytomedicine*. 2008;15:470-477.
- [26] Hussain T, Hefazat HS, Sheeba F, Sweetey K, Vijayakumar M, Rao CV. Chemopreventive effect of *Fumaria indica* that modulates the oxidant antioxidant imbalance during N-nitrosodiethylamine and CCl₄-induced hepatocarcinogenesis in Wistar rats. *Asian Pacific J. of Tropical Biomed.* 2012;2:995-1001.
- [27] Ezzat M, Kian A, Bagher M, Seyedeh ZOS. Protective activity of *Fumaria vaillantii* Loisel and mono methyl fumrate on acetoaminophen induced hepatotoxicity in mice. *Int J Pharmacology*. 2012;8:177-184.
- [28] Aveen N, Adham AM, Naqishbandi TE. Cytotoxicity and apoptosis induction by *Fumaria officinalis* extracts in leukemia and multiple myeloma cell lines. *J. of Ethnopharmacology*. 2021;266:113458.
- [29] Sattari R, Khayati GR, Hoshyar R. Biosynthesis and characterization of silver nanoparticles capped by biomolecules by *fumaria parviflora* extract as green approach and evaluation of their cytotoxicity against human breast cancer MDA-MB-468 cell lines. *Materials Chem. and Physics*. 2020;241:122438.
- [30] Aljanaby A. Cytotoxicity of *Fumaria officinalis* on *Leishmania tropica*, L20B cell lines and bacteria in vitro. *J. of Global Pharma Technology*. 2019;11:171-175.
- [31] Sadaoui BK, Gontier E, Telliez MS, Lequart-Pillon M, Ouadid-Ahidouch H, Maiza F. Characterization of isoquinolin alkaloids from *Fumaria agraria* and evaluation of their antiproliferative activity against human breast cancer cell lines. *Phytothérapie*. 2015;14: 10.1007/s10298-015-0981-8.
- [32] Sadaoui BK, Maiza-Benabdesselam F, Ouadid-Ahidouch H. Antiproliferative Activity of Protopine Extract from *Fumaria agraria* Against Human Lung Cancer Cell Lines. *Phytothérapie*. 2021;0293.
- [33] Yılmaz Sancar P. Analysis of the Essential Oil Composition, Antimicrobial Activity and Antioxidant Capacity of *Fumaria asepala* Boiss. and *Fumaria schleicheri* Soy. Will. subsp. *microcarpa* Hausskn. from Turkey. *International Journal of Pure and Applied Sciences*, 2023;9(1): 29-37.

Expert Recommendation System to Promote Development-Focused Universities

Bayraktar Mehmet Yasar^{1*} , Kaya Mehmet² 

¹(Bingöl Üniversitesi, Mühendislik Fakültesi, Bilgisayar Mühendisliği, 1200, Bingöl, Türkiye)

²(Fırat Üniversitesi, Mühendislik Fakültesi, Bilgisayar Mühendisliği, 2300, Elazığ, Türkiye)

Mehmet Yaşar Bayraktar ORCID No: 0000-0003-3182-120X

Mehmet KAYA ORCID No: 0000-0003-2995-8282

*Corresponding author: mehmetyasarbayraktar@hotmail.com

(Received: 29.11.2023, Accepted: 19.04.2024, Online Publication: 28.06.2024)

Keywords
Finding
Experts,
Automatic
Candidate
Selection,
Expert
Suggestion,

Abstract: With the support given to university education in recent years, newly opened or developing universities are trying to specialize in various fields within the framework of the regional development mission. In order to achieve success, there is always a need for experts -who do successful studies and have a wide perspective- in the field sought. Reaching candidates who are experts in their field is a difficult process since it cannot be expressed with a linear/linear mathematical formula. In particular, the increasing number of recent studies, articles and reports has made the selection of experts on the subject difficult and systems that automatically find experts are needed. Reaching candidates who are experts in their field is a difficult process since it is relative. In particular, the increasing number of recent studies, articles and reports has made the selection of experts on the subject difficult and systems that automatically find experts are needed. With this study, the scientific studies published by the academicians and the co-authors in the studies will be evaluated and expert candidates "suitable for the criteria sought" will be listed. Results will be given on the basis of scoring scientific studies for the appropriate researcher criteria. To evaluate a researcher's score, an object function of the expert will be made by looking at the filtered keywords over the articles and studies written by that person. In this application, using the 'Dergi Park' database, suitable expert candidates were scored for the filtered words.

Kalkınma Odaklı Üniversiteleri Destekleyecek Uzman Öneri Sistemi

Anahtar
Kelimeler

Uzman Bulma,
Otomatik Aday
Seçimi,
Uzman Öneri

Öz: Son yıllarda üniversite eğitime sağlanan desteklerle, yeni açılmış ya da gelişmekte olan üniversiteler, bölgesel kalkınma misyonu çerçevesinde çeşitli alanlarda uzmanlaşmaya çalışmaktadırlar. Bu çerçevede başarıya ulaşmak amacıyla, alanında yetişmiş başarılı ve geniş görüş açısına sahip olan akademisyen/uzmanlara her zaman ihtiyaç duyulmaktadır. Konusunda uzman adaylara ulaşmak ise doğrusal/lineer bir matematiksel formül ile ifade edilemediğinden dolayı zorlu bir süreçtir. Özellikle, son zamanlarda yapılan çalışma, makale ve raporların gün geçtikçe artması konuyla ilgili uzman seçimini zorlaştırmış ve otomatik uzman bulma sistemlere ihtiyaç duyulmuştur. Yapılacak bu çalışmayla akademisyenlerin yayımlandığı bilimsel çalışmalar ve çalışmalardaki ortak yazarlar değerlendirilerek "aranan kriterlere uygun" uzman adayları listelenecektir. Uygun araştırmacı kriteri için bilimsel çalışmaların puanlanması esasına göre sonuç verilecektir. Bir araştırmacının puanı değerlendirilirken, o kişinin yazdığı makaleler ve çalışmalar üzerinden, filtre edilen anahtar kelimelere bakılarak, uzmana ait objektif bir sıralama yapılacaktır. Bu uygulamada "Dergi Park" sisteminin veri tabanı kullanılarak, filtrelenen kelimelere uygun uzman adayların puanlandırılması sağlanmıştır.

1. INTRODUCTION

The increase in the speed and use of the internet and computers day by day has led to the need to store almost every existing piece of information in offline or online databases. The explosion in knowledge in the database

brings to mind the idea of how these resources can be turned into a profit. While the previously used database techniques were based on querying and filtering, data mining techniques aim to discover the hidden and useful information stored in the data [1].

Data mining is the discovery of invisible or unnoticed knowledge from large-scale data. Since the aim of this study is to select experts on the subject, determining the knowledge, skills, and areas of expertise; it is crucial to choose the sources correctly to obtain meaningful information.

In addition, with the augmentation in the use of computers and technological tools, almost every organization and company has started to store their employees' areas of expertise, talents and contact information in databases. Especially in academic communities, information about the person, the schools and universities he or she attended, personal background information, specific fields of study and certificate information are kept in related tables. So, meta-databases could be used as first step to determine expert area of a person.

As a second step, documents, personal blogs, news and websites will provide much more detailed information about the expert. This process can be called as secondary source selection and document collection about the expert.

Experts often cannot express themselves well or they may use very general or specific expressions when describing their areas of expertise. In particular, updating information is dependent on people, updating the process is time-consuming and undesirable, and the information accessed in the database does not reflect the person relatively.

In addition, while data are being collected, they contain some errors called noise caused by people, environment and equipment [2]. In addition, obtaining data from different sources leads to inconsistent or incomplete information. These noisy and incomplete data obtained from these sources can be somewhat removed by using some data preprocessing techniques.

The demand for specialists must be obtain from external sources because of ever-increasing need for information in organizations and companies, and the limited number of experts in these area. For this purpose, the evaluation of expert candidates outside the organization, which is called external resources, is of great importance.

In general, expert represents people who have knowledge about a particular subject, are self-educated, have successful studies and have a broad perspective. Sometimes, they are called people who have special talents, mastery and dexterity in addition to their knowledge. The need for specialists is increasing, especially in rapidly and continuously developing fields such as health, informatics and technology. For this purpose, it is desired to create automatic expert finder systems by making use of many kinds of data sources and expert knowledge.

Previous research suggests expert-finding systems using many techniques such as information extraction, data mining, and probabilistic modeling. P@NOPTIC Expert

[3], Expertise Browser(ExB) [4], and Expert Finder [5] are some of the models that is developed as software in this regard.

The process of finding experts includes three important steps such as 'Selecting Experts' Source', 'Creating Expert Model' and 'Matching Searched Criteria with Expertise Topics' [6].

2. LITERATURE WORK

Meta databases serve to keep the skills and expertise of employees or members. Thus, general profile information of experts can be created. Moreover; projects the candidates were worked on, previous experience and background information of the candidates are recorded in the databases and certain information about the candidate is extracted. In a study conducted at NASA, a system called SAGA [7], which helps to find experts, is developed by using various educational data and profile information.

Although the process of finding talent and expertise by using the main databases seems relatively easy, the fact that experts do not like to update their knowledge or there is incomplete or erroneous information causes the solution to become complicated and expensive. In addition, the fact that the expertise information in the system is very general and irregular are the factors that make it difficult to score experts.

2.1. Document Collection of an Expert

Having knowledge of related documents belonging to the candidate is also an important factor in defining the candidate's area of expertise. The information in the related publications, reports, mails, forums and web pages can provide a detailed inference about the expert. Dumais and Nielsen reached 117 conferences and tried to find their areas of expertise by looking at the abstracts of the articles published by the researchers [8]. Moreover, Balog developed a model that finds experts by using various documents such as speech, mail, web page, and report by making use of the local document warehouse [9]. Campbell et al., on the other hand, tried to determine the fields of expertise of the users by making use of the sender and receiver information, as well as the e-mail contents and headers by using inter-mail connections [10]. However, a problem that should not be forgotten is that when determining the subject related to the mail, subject drifts (topic-drift) may be encountered. In addition, in the document collection process, name similarities are another issue that needs to be studied.

3. MATERIAL AND METHOD

In order to find the areas of specialization of a candidate, it is necessary to collect knowledge about the candidate. This type of information can be obtained from major databases (personal information, talent, expertise), online/offline documents (such as publications, forums, emails, reports, and web pages) belonging to the

candidate, or candidate's relational networks (such as social, academic and business networks). When we are searching for an expert, we generally ask these types of questions 'Who is an expert on this area' or 'Who can make this job/work better?' [6]. With in these types of queries, client is looking for an expert in a specific field. Algorithm structures such as 'Creative Probabilistic Model', 'Lay-Based Model', 'Network-Based Model', and 'Hybrid Model' are widely used in expert finding problems. The expert inference algorithm usually answers questions such as 'Finding the Candidate's Areas of Expertise', 'Exploring Evidence of Expertise', and 'Inferring the Relationship between the Questioned Subject and the Expert Candidate' [11].

There are three inputs/criteria that are important to expert search:

- Expert Candidate (EC)
- Document(D)
- Subject(S), Term in the Query (t,t ∈S)

While the expert candidate represents the people who can be experts in the subject to be sought, the documents characterize the online/offline resources that may belong to that expert. The subject represents the expert search query/criteria. While this criterion is sometimes a few keywords, sometimes it can be in a summary text to represent the expertise to be sought.

Figure 1 shows web interface for finding expert candidates who have worked on 'bee venom'. Additionally, by selecting the search source, it is possible to specify which sources data can be retrieved from.

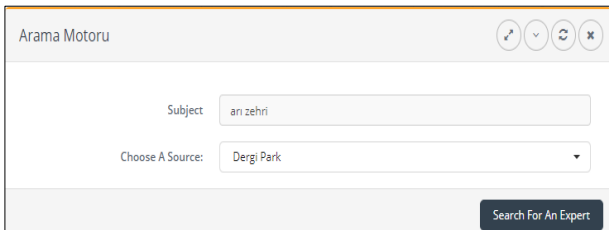


Figure 1: Determination of Expert Keywords

Figure 2 demonstrates the flowchart of the expert candidate extraction algorithm suitable for the filter. After keywords are entered into the application, article information containing these words is pulled from the specified data source. Considering each article and author information, it is placed in the fitness function.

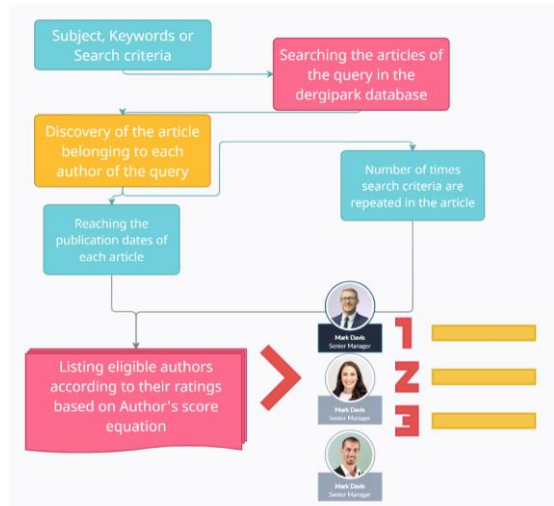


Figure 2: Workflow of sorting expert candidates suitable for the filter

In Equation 1, how the scores of each candidate author will be calculated is expressed mathematically. Thus, the content of the article written by an author is evaluated and scored according to the publication date and the number of co-authors. Here, the 'alpha(α)' coefficient can be made on a user basis by changing the publication date according to its importance. For example, in some fields (agriculture, agriculture, etc.), the time of publication of the article may not be very important, while in the field of technology and computers, the 'alpha(α)' coefficient can be changed to increase the value of time.

$$\begin{aligned}
 AuthorScore_i = & \sum_{i=0}^{i=AuthorPaperCount} (20 \\
 & - (2023 - PublishDate) * \\
 & \alpha \\
 & * \left(\left(1 + \frac{1}{SharedAuthorCount} \right) \right. \\
 & \left. * KeywordsRepetitionCount \right) \quad (1)
 \end{aligned}$$

In Figure 3, the candidates who wrote an article in the "Journal Park" database in the "Bee venom" field are listed. Universities and organizations that need experts in this field can contact these authors and sign successful projects with academicians who are experts in their fields.

ID	Name	Score	TimeBasedScore	RepetitionCount	WeightedScore
0	Ahmet DODOLOĞLU	30	270	80	127,222222222222
0	Erkan TOPAL	7	128	33	114,416666666667
0	Nurullah ÖZDEMİR	10	170	30	113,333333333333
0	Sevgi KOLAYLI	11	137	36	102,666666666667
0	Vural BAŞARAN	10	150	30	100
0	Yusuf ÇELİK	10	140	30	93,333333333333
0	Ralitsa BALKANSKA	10	110	40	91,666666666667
0	Borislav KASHAMOV	10	110	40	91,666666666667
0	Engin KILIÇ	10	190	20	84,444444444444
0	Meltem UÇAR	4	72	23	84

Figure 3: Listing successful authors in the field of 'bee venom'

4. DISCUSSION

When companies and universities search for expert candidates in their field, they generally use keywords and examine articles and studies written on the subject. Examining these studies and finding connections between authors not only took a long time, but also left the process of finding an expert to personal preference. In this study, using the 'Dergi Park' database, connections were revealed between the articles written by expert candidates and the searched keywords. In addition, the up-to-dateness of the expert candidate's work was taken into consideration, taking into account the date of acceptance of the articles and the order of the authors in the article. Thus, a system that evaluates expert knowledge based on time, author and keyword was obtained.

3. RESULTS

Finding experts, which is a difficult and time-consuming process, is automated using the contents of academic articles. Thus, it was transformed into an application that companies, organizations and universities can benefit from.

An expert evaluation system is developed by including the effect of academic articles. In particular, a more dynamic system is proposed to replace the web-sites where experts are registered, such as 'kariyer.net' and 'Linked-in', which allow searching for experts by paying fees and which need constant updating.

In addition, the fact that expert candidates remain general or specific when describing themselves and their expertise, and the need for continuous updating of their CV information makes the process of finding experts difficult. However, with the use of academic network structure and personal reports, documents and articles, it is possible for the expert to evaluate the candidate's work area and abilities in a more up-to-date and objective way.

As a result, a new expert recommendation system is presented by ensuring that the academicians who are experts in their fields that universities and organizations may need are listed in an objective way, preventing the institutions from spending too much time and effort.

REFERENCES

- [1] N. T. ., M. Y. Serkan SAVAŞ, «Veri Madenciliği Ve Türkiye'deki Uygulama,» İstanbul Ticaret Üniversitesi Fen Bilimleri Dergisi, 2011.
- [2] A. OĞUZLAR, «Veri Ön İşleme,» Erciyes Üniversitesi İktisadi ve İdari Bilimler Fakültesi Dergisi, pp. 67-76, 2003.
- [3] N. C. P. d. V. S. Peter Bailey, «Overview of the TREC 2007 Enterprise Track,» TREC, 2007.
- [4] A. & H. J. Mockus, «Expertise browser: a quantitative approach to identifying expertise,» %1 içinde Proceedings of the 24th international conference on software engineering, 2002.
- [5] M. Maybury, «Collaborative Virtual Environments for Analysis and Decision Support,» Communications of the ACM, 2001.
- [6] W. H. D. W. L. Shuyi Lin, «A survey on expert finding techniques,» Springer Science+Business Media New York, p. 260, 23 11 2017.
- [7] Becerra-Fernandez, «Locating expertise at nasa: developing a tool to leverage human capital,» Knowledge Management Review, pp. 34-37, 2001.
- [8] J. N. Susan T. Dumais, «Automating the assignment of submitted manuscripts to reviewers,» Proceedings of the 15th annual international ACM SIGIR conference on Research and development in information retrieval, pp. 233-244, 1992.
- [9] L. A. d. R. Krisztian Balog, «Formal Models for Expert Finding in Enterprise Corpora,» Proceedings of the 29th annual international ACM SIGIR conference on Research and development in information retrieval, 2006.
- [10] P. P. M. C. D. Christopher S. Campbell, «Expertise identification using email communication,» Proceedings of the twelfth international conference on Information and knowledge management , 2003.
- [11] Y. F. d. R. S. S. Krisztian Balog, Foundations and Trends in Information Retrieval, Hanover, MA 02339,USA: now Publishers Inc., 2012.

Investigation of the Impact of Tool Pin Geometry and Feed Rate Speed in Friction Stir Lap Welding of 7075 and 5182 Aluminum Alloys

Ömer EKİNCİ* 

¹ Sivas University of Science and Technology, Faculty of Aviation and Space Sciences, Department of Astronautical Engineering, Sivas, Türkiye
Ömer Ekinci ORCID No: 0000-0002-0179-6456

*Corresponding author: omerekinici@sivas.edu.tr

(Received: 09.01.2024, Accepted: 10.05.2024, Online Publication: 28.06.2024)

Keywords

Friction stir lap welding, Aluminum alloys, Tool pin geometry, Macro and microstructure, Tensile load capacity, Fracture

Abstract: 7075 and 5182 aluminum alloys are critical for aerospace and automotive applications receptively. Joining these alloys can enable more economical and efficient structures. Therefore, the weldability of these materials by friction stir lap welding (FSLW) is of great importance. In this study, the effect of tool tip geometry (conical and cylindrical screw) and welding speed (22, 37 and 51 mm min⁻¹) on the weld microstructure and mechanical properties were studied in joining 7075 and 5182 aluminum alloys with FSLW. Strong welds were acquired with both tools. However, stronger ones were made employing the conical pin tool thanks to having deeper weld penetration and denser microstructure (microstructure with smaller grains). While the resistance of the weld to the tensile load was increased with increasing feed rate for the conical pin tool because the weld area width and vertical downward penetration increased, the opposite occurred for the cylindrical screw pin tool. By the conical pin, the greatest tensile load of 13033 N in the weld made at 51mm min⁻¹, whereas by the cylindrical screw pin, the biggest 12162.5 N was achieved in the weld made at 22 mm min⁻¹. It was an indication of a stronger weld formation for both tools when the lines formed through tool shoulder on top surface of upper sheet were broken into small particles and disappeared. Proper tool feed rate value can show considerable variability depending on tool pin geometry.

7075 ve 5182 Alüminyum Alaşımlarının Sürtünme Karıştırma Bindirme Kaynağında Takım Pimi Geometrisi ve İlerleme Hızının Etkisinin Araştırılması

Anahtar Kelimeler

Sürtünme karıştırma bindirme kaynağı, Alüminyum alaşımları, Takım pimi geometrisi, Makro ve mikroyapı, Çekme yükü kapasitesi, Kırılma

Öz: 7075 ve 5182 alüminyum alaşımları sırasıyla havacılık ve otomotiv uygulamaları için çok önemlidir. Bu alaşımların birleştirilmesi daha ekonomik ve verimli yapılara olanak sağlayabilir. Bu nedenle, bu malzemelerin sürtünme karıştırma bindirme kaynağı (SKBK) ile kaynak edilebilirliği büyük önem arz etmektedir. Bu çalışmada, 7075 ve 5182 alüminyum alaşımların SKBK ile birleştirilmesinde takım uç geometrisinin (konik ve silindirik vidalı) ve kaynak hızının (22, 37 ve 51 mm dak⁻¹) kaynak mikroyapısı ve mekanik özellikleri üzerindeki etkisinin araştırılması temelinde çalışılmıştır. Her iki takım ile da güçlü kaynaklar elde edildi. Ancak konik uçlu takım kullanılarak yapılan kaynaklar daha derin nüfuziyete ve daha yoğun bir mikro (daha küçük tanelere sahip mikro yapı) yapıya sahip olması nedeniyle daha güçlü çıkmıştır. Konik uçlu takım ile ilerleme hızının artmasıyla, kaynak alanı genişliği ve dikey aşağıya doğru nüfuziyet arttığı için kaynak mukavemeti artarken, silindirik vidalı uç ile bunun tersi meydana geldi. Konik pim ile 51mm dak⁻¹'de yapılan kaynakta en büyük çekme yükü 13033 N, silindirik vida pimi ile ise 22 mm dak⁻¹'de yapılan kaynakta en büyük 12162,5 N çekme yükü elde edilmiştir. Üst levhanın üst yüzeyinde takım omuzundan dolayı oluşan çizgilerin küçük parçacıklara ayrılarak kaybolması her iki takım için de daha güçlü bir kaynak oluşumunun göstergesi olmuştur. Uygun takım ilerleme hızı değeri, takım uç geometrisine bağlı olarak önemli ölçüde değişkenlik gösterebilir.

1. INTRODUCTION

Aluminum (Al) alloys play a crucial role in aircraft and automotive applications thanks to their superior strength-to-weight ratio and good machinability. There are series of Al alloys having different chemical compositions have been developed for using in different applications. 7075 Al alloy is characterized by its high strength and generally used as structural material in aircraft fuselage panels [1]. 5182 Al alloy is characterized by its high Mg content and has outstanding formability and deep stretch forming and commonly utilized as structural material in automobile bodied [2]. Reliably joining dissimilar Al alloys can provide more flexible designs. But, traditional fusion welding techniques are not suitable for combining different Al alloys because porosity, hot cracks, brittle secondary phases, and residual stress often emerge [3] that degrade the mechanical properties of the joint. Additionally, welding Al alloys are hard by fusion welding methods since they have a strong oxide layer on their surface and high thermal conductivity [4]. Solid-state welding techniques have been shown for combining dissimilar metals. AISI 1010 low carbon steel and copper alloy were joined without intermetallic phases at the weld region by friction welding, a solid-state welding technique [5]. Friction stir welding (FSW), one of these methods, has demonstrated to be appropriate and effective in the welding different Al alloys [6]. As the maximum temperature in FSW process is below the melting point of the metals being joined and thus melting connected issues such as gas porosity, solidification cracking do not occur [7,8]. Moreover, FSW does not necessitate the use of mechanical joining elements like rivets, fasteners, which results in fabricating lighter bodies and faster manufacturing periods [8]. Furthermore, FSW is seen as one of the greatest alternative welding methods because it costs low, consumes low energy, provides strong joints, reduces weight of structures, is environmentally friendly, and requires less human ability [9]. Tool profile, rotation speed and feed rate speed are the main parameters of the FSW process [7,8,10]. Tool geometry can be regarded as having the greatest impact on heat generation and material mixing. Combination of tool shoulder diameter and profile, and pin diameter, length, and profile are all crucial factors in determining other welding variables such as tool rotational and feed rate and also the resulting weld quality [11]. Çevik et al. [12] investigated the FSW of 7075-T651 Al alloys using different tool rotation speeds (900, 1250 and 1600 rpm) and stated that the weld with the best mechanical properties was produced at the rotation speed of 900 rpm. 6061 T6 Al alloy sheet couples were welded with the FSW method using tools with different pin profiles, and it was stated that the pin shape significantly affects the weld microstructure and mechanical properties [13]. Cakan et al. [14] investigated the effects of tool rotation speed (660 and 920 rpm) and feed rate speed (18, 32 and 54 mm min⁻¹) parameters on the weld quality in the FSLW of different pure copper and AA7075-T6 Al alloy materials. It was found that the rotation speed of 660 rpm and feed rate of 32 mm min⁻¹ was the best. Lap joints are often employed, for example, in joining

stringer and skin in aircraft fuselages, and for assembling components in railway tankers, goods wagons and ship decks [15,10]. Buffa et al. [10] studied on FSLW of 2198-T4 Al alloy by using three different welding tools with cylindrical, conical and cylindrical-conical pin and they determined that welds with better mechanical properties were produced by cylindrical-conical pin tool. They also stated that increasing the welding speed (50-1000 mm min⁻¹) or decreasing the rotation speed (500-2000 rpm) improved the weld strength. Lee et al. [16] researched FSLW of 5052 Al and 6061 Al alloys using tool rotation speeds of 1250, 2500 and 3600 rpm at a constant speed of 267 mm min⁻¹ and using welding speeds of 127, 267 and 507 mm min⁻¹ at a fixed 1600 rpm. They claimed that increasing rotation speed decreased weld strength while increasing welding speed improved weld strength. Reducing weight and fuel consumption and increasing efficiency, and performance for land and aircraft vehicles can be achieved by combining dissimilar Al alloys in the production. According to the literature research I have done, there is a need for more studies on the understanding effect of tool pin profile along with the tool feed rate on weld quality in the FSLW of different types of aluminum alloys. Therefore, the weldability of 7075-T651 Al alloy to 5182 Al alloy was experimentally investigated by the FSLW method using two tools having different pin shapes and various welding speeds.

2. MATERIAL AND METHOD

On a Falco FMH-4 brand universal milling machine, a 2 mm thick 7075-T651 Al alloy sheet was put on a 5 mm thick 5182 Al alloy plate and then tightly fastened. Then, they were welded by friction stir lap welding (FSLW). FSLW experiments were carried out by conical pin tool and cylindrical screw pin tool at tool feed rates of 22, 37 and 51 mm min⁻¹ and at a constant tool tilt angle of 2 degrees clockwise and tool rotational speed of 980 revolutions per minute (rpm). Chemical composition and mechanical features of the alloys are given in Table 1 and 2, respectively. FSLW experiment variables and configuration with dimensions are given in Table 3 and Figure 1, respectively. FSLW experiment and welding tools are shown in Figure 2. Tools were manufactured from a bar made of H13 hot work tool steel material. Conical pin tool has a conical pin with a length of 3 mm, tip diameter of 3 mm and root diameter of 5 mm and a shoulder with a diameter of 16 mm while cylindrical screw pin tool has a cylindrical screw pin right hand thread pitch 0.8 mm with a length of 3 mm and a diameter of 5 mm and a shoulder with a diameter of 16 mm. The produced FSLWed samples were presented in Figure 3. After the welds were produced, they were cut on KMYDG 280 brand semi-automatic rotary belly band saw machine to acquire tensile test and macro and microstructure samples. Tensile test samples with 25 mm width based on AWS D17.3M:200X standard [17] were given in Figure 4. Cross-sectional areas of welds were ground by sandpaper up to 1500 grit and then etched by Keller's reagent (1 ml HF, 1.5 ml HCl, 2.5 ml HNO₃, and 95 ml H₂O) for 10 s to examine macro and microstructures in the welds. The etched cross-sections

of the welds were presented in Figure 6. Macro and microstructures of the welds were examined on an AOB brand inverse metal optical microscope. The hardness of the welds was attained from their cross-sections by an AOB model micro Vickers hardness tester and utilizing a 200 g load and 10 seconds dwell time. Tensile strength of the welds were obtained on SHIMADZU model 250 kN universal tensile tester by utilizing 2 mm min-1 constant cross-head speed at room temperature. Fracture surfaces of the joints were observed on JEOL JSM6510 model scanning electron microscope (SEM). X-ray Diffraction (XRD) analysis was conducted on the Rigaku MiniFlex machine using X-Ray generator (40 kV, 15 mA) and Scan speed/Duration time (4.00 °/min).

Table 1. Chemical composition of Al alloys (wt. %)

Material	Si	Fe	Cu	Mn	Mg	Cr	Zn	Ti	Al
7075-T651	0.4	0.5	1.2-2	0.3	2.1-2.9	0.18-0.28	5.1-6.1	0.2	Balance
5182	0.2	0.35	0.15	0.2-0.5	4-5	0.1	0.25	0.1	Balance

Table 2. Mechanical properties of Al alloys

Material	Yield strength (MPa)	Tensile strength (MPa)	Elongation (%)
7075-T651	470	550	10
5182	140	300	25

Table 3. FSLW experiments with variables

Sample	Welding tool with	Tool tilt angle clockwise (degree)	Tool rotation speed (rpm)	Tool plunge depth (mm)	Tool feed rate (mm min ⁻¹)
S1	Conical pin	2	980	3.6	22
S2		2	980	3.6	37
S3		2	980	3.6	51
S4	Cylindrical screw pin	2	980	3.6	22
S5		2	980	3.6	37
S6		2	980	3.6	51

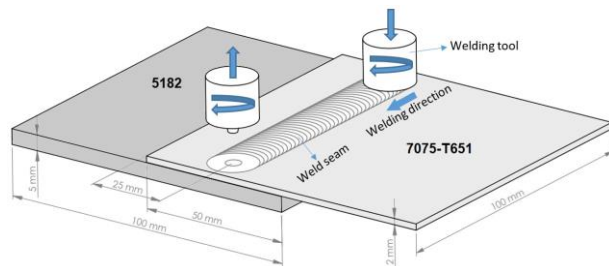


Figure 1. FSLW configuration with dimensions



Figure 2. FSLW of alloys and the used welding tools

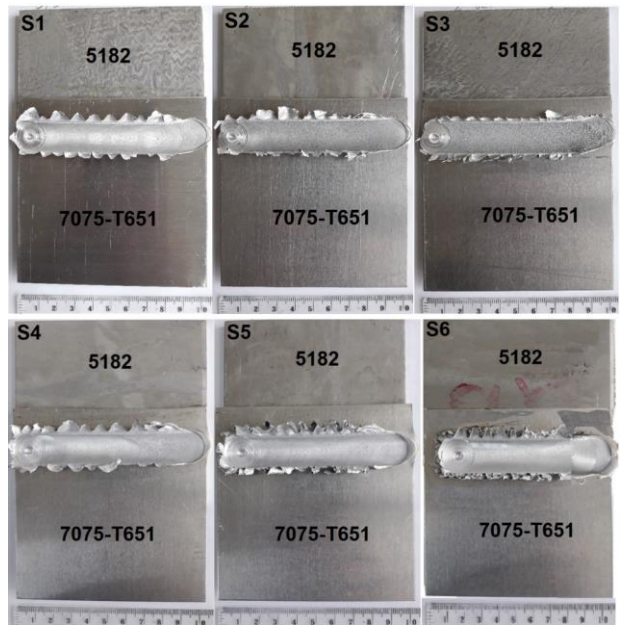


Figure 3. The FSLWed samples

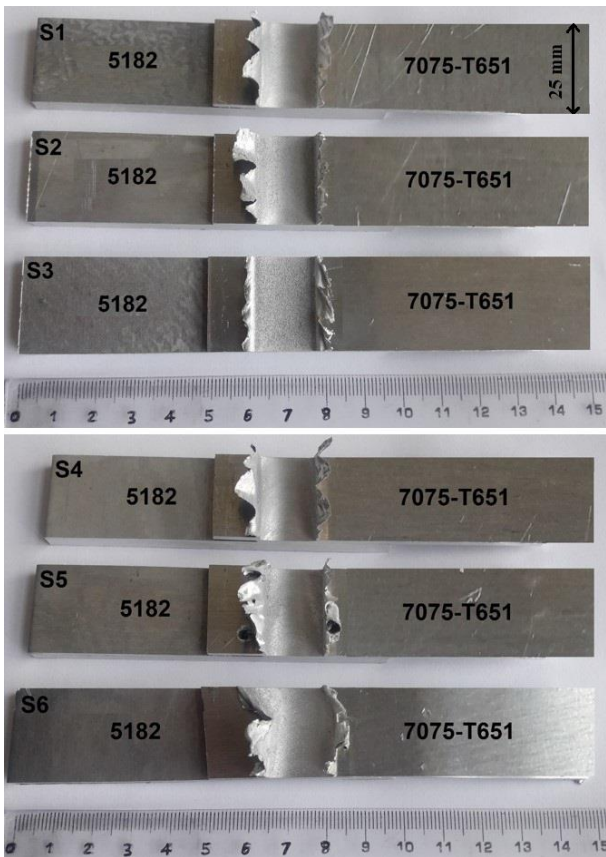


Figure 4. The tensile test samples cut from the FSLWed samples

3. RESULTS AND DISCUSSION

3.1. Macrostructural Analysis

Figure 5 illustrates the top surface appearance (weld beads) of FSLWed samples. The lines formed by the tool shoulder on the top surface of the upper sheet were broken into small particles and disappeared with the increasing tool feed rate (from weld S1 to S3) for the conical pin tool. On the other hand, the lines started to form more with increasing the welding speed (from S4 to S6) for the cylindrical screw pin tool. There are no lines formed by the tool shoulder on the top surface of weld S3, whereas slightly more than half of the top surface of weld S4 had lines formed by the tool shoulder. Figure 6 displays the macro views of the cross-sections of the FSLW joints. Figure 7 represents optical microscope images of the cross-sections. It can be seen in Figure 7 that the effective welded area width and vertical downward penetration gradually enhanced by enhancing the tool welding speed from weld S1 to S3 made through the conical pin tool. However, for the cylindrical screw pin tool, the effective welded area width and vertical downward penetration decreased when the tool feed rate was boosted from weld S4 to S6, and also voids appeared. While increasing the tool feed speed gave good results for the conical pin tool, it had negative results for the cylindrical screw pin tool. There are formations of voids observed under the weld S6 made at the highest tool feed rate for the cylindrical screw pin tool. At this highest feed rate, heat input may have been insufficient to adequately soften, plasticize and stir the material because a higher feed rate provides

less heat input. The heat on the lower side of the screw pin is less than on the upper side due to the tool shoulder contacting the upper sheet generating heat. Thus, the screw cut the material rather than mixing and allowing it to flow, leaving voids behind at the bottom. According to [18], in the FSW, a cavity takes place behind the welding tool and then filled with plasticized material that moves from the pin's front to its back.

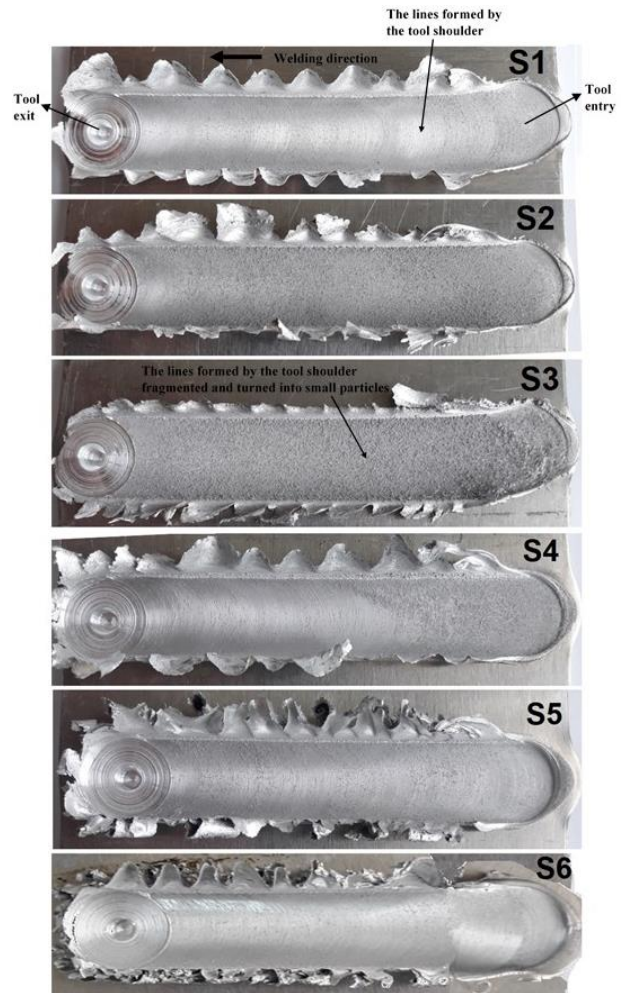


Figure 5. The top view of the FSLWed samples

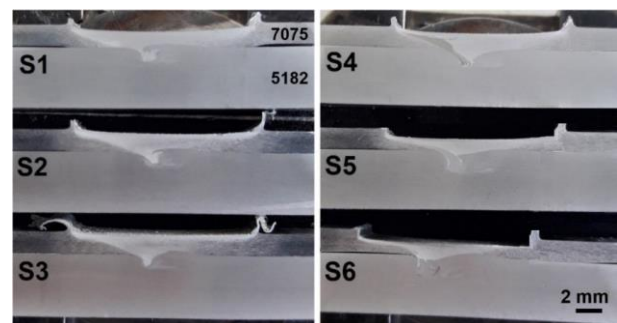


Figure 6. Cross-sections of the FSLWed samples

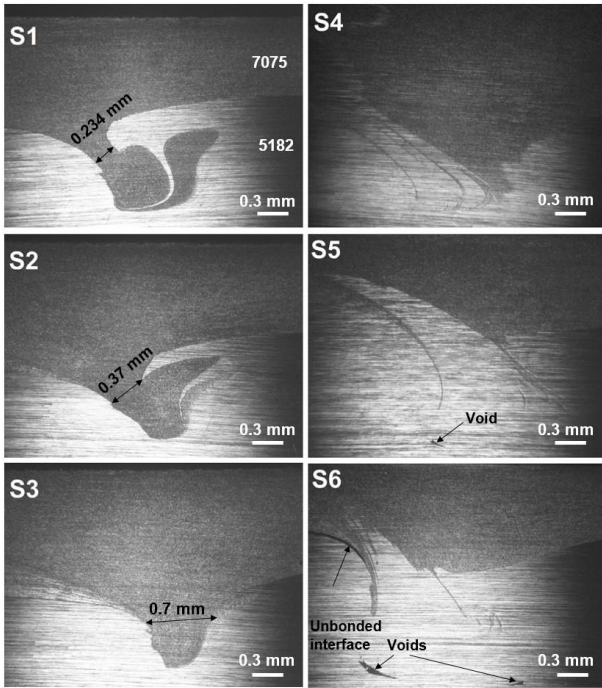


Figure 7. Optical microscope images of the cross-sections of the FSLWed samples

3.2. Microstructural Analysis

Microstructures of welds S3 and S4 are presented in Figure 8 as these are the strongest ones made employing the conical pin tool and cylindrical screw pin tool, respectively. Figure 8a, b and c show the microstructures of a, b and c regions on cross-section of the weld S3, respectively. a, b and c regions represent the welded area right at the interface of the sheets, the welded area just below the interface and thermo-mechanically affected zone (TMAZ) just next to the weld zone (stir zone), respectively. As can be seen that the microstructure of the region b contains the smallest grains and slightly smaller than the grains of the region a, however, region c has a microstructure with elongated and the largest grains. The width of region c (TMAZ) began to narrow from weld S1 to S3 with increasing welding speed for the conical pin tool since heat input decreased. On the other hand, Figure 8d and e indicate the microstructures of d and e regions on cross-section of weld S4, respectively. Region e consists of grains slightly smaller than that of region d. In general, the microstructures of the weld S3 had finer grains (denser) than that of weld S4. Hence, it can be said that the conical pin tool mixed the alloys better than the cylindrical screw pin tool. The fine-grained microstructure was formed because of intense plastic deformation and recrystallization. Similar observations were obtained in terms of grain size and orientation formed in the microstructures of the SZ and TMAZ during the FSLW of 7075 and 2024 Al alloys [19].

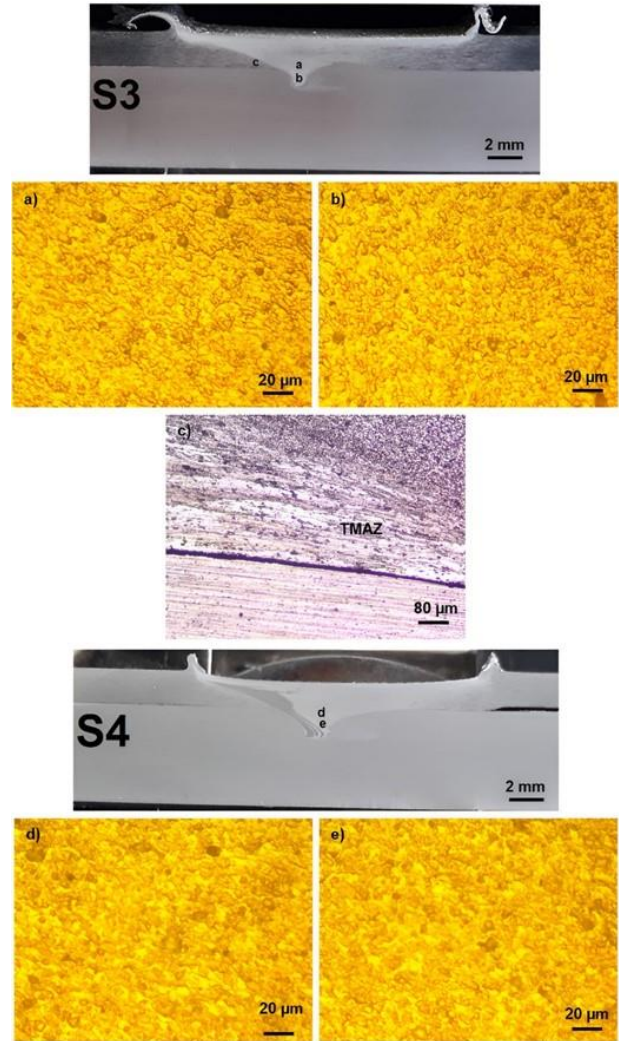


Figure 8. Microstructures of weld S3 and S4

XRD analysis of the welds S1 and S3 were presented in Figure 9. $\text{Al}_2\text{Cu}_2\text{Fe}$ phases were determined in both welds. However, the $\text{Al}_2\text{Cu}_2\text{Fe}$ phase formation was higher in the S1 weld probably because of more heat input since S1 was produced at a lower tool feed rate. According to Bayazid et al. [20], $\text{Al}_7\text{Cu}_2\text{Fe}$ is a brittle material and can seriously impair mechanical characteristics, particularly ductility. Cu increases hardness [21].

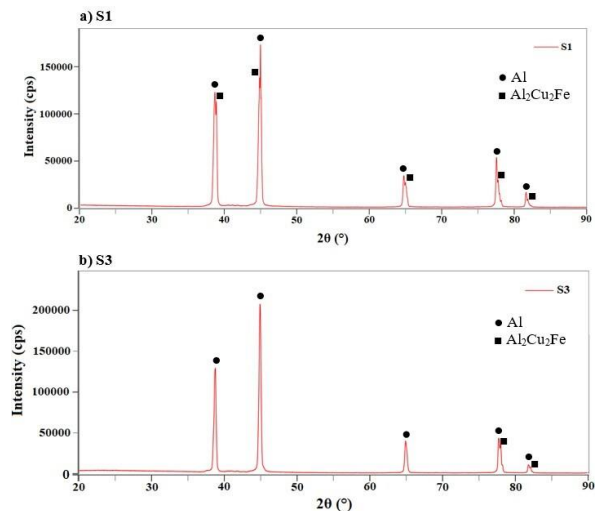


Figure 9. XRD analysis for the welds S1 and S3

3.3. Microhardness

The hardness values of the welds attained from the top 7075 sheets (just above the interface of sheets) and bottom 5182 sheets (just below the interface of the sheets) are presented in Figures 10a and b, respectively. The hardness of 7075 and 5182 metals ranged between 167 to 170, and 78 to 82 HV, respectively. It was found that there is a first decrease in the hardness and then an increase and reached a maximum in the weld center when moving on the upper sheet from 7075 base metal to the weld center, but lower than the hardness of the 7075 metal (Figure 10a). Moreover, the hardness of the weld S4 was lower than the weld S3. This is because S4 was produced at an approximately 2.3 times lower tool feed rate, which generates more heat input, resulting in the formation of bigger grains in the weld microstructure, as shown in Figure 8. On the other hand, when going from the 5182 base metal to the weld center, the hardness on the lower 5182 sheet first decreased slightly and then significantly increased and became the highest in the weld center above the hardness of the 5182 base metal (Figure 10b). The reason for the much higher hardness of the weld center than the 5182 base metal is because the 5182 material mixed with the harder 7075 material in the weld center. In general, the weld center just above the interface of the sheets had higher hardness than the weld center just below the interface of the sheets. This is because the 7075 material mixed more with the softer 5182 lower sheet material in the weld center at the bottom. In addition, while the lowest hardness values were acquired in the HAZ regions, the hardness of the TMAZ regions was slightly higher than the HAZ regions. The hardness in the weld, HAZ, and TMAZ areas appeared to be slightly lower when the weld was produced at a smaller tool feed rate. This is probably because heat input increased with a smaller tool feed rate resulting in grains growing. The weld region had higher hardness when compared to the HAZ and TMAZ regions due to most likely the smaller grains in its microstructure, as shown in Figure 8. The hardness in the weld areas where 7075 and 5182 metals were mixed became lower than that of the 7075 base metal and higher than that of the 5182 base metal. Similar results were observed in friction stir butt welding (FSBW) of 7075 and 5182 alloys, where the hardness first decreased and then increased from the base material to the weld zone [22]. Çetkin et al. [23] studied friction stir welding of 5182 alloys and they found that the hardness from the 5182 base metal to the TMAZ decreased, and later increased in the weld zone. Furthermore, it was observed that the welds made by the cylindrical screw pin tool possessed a slightly lower hardness value. This could be because this tool generated more heat input.

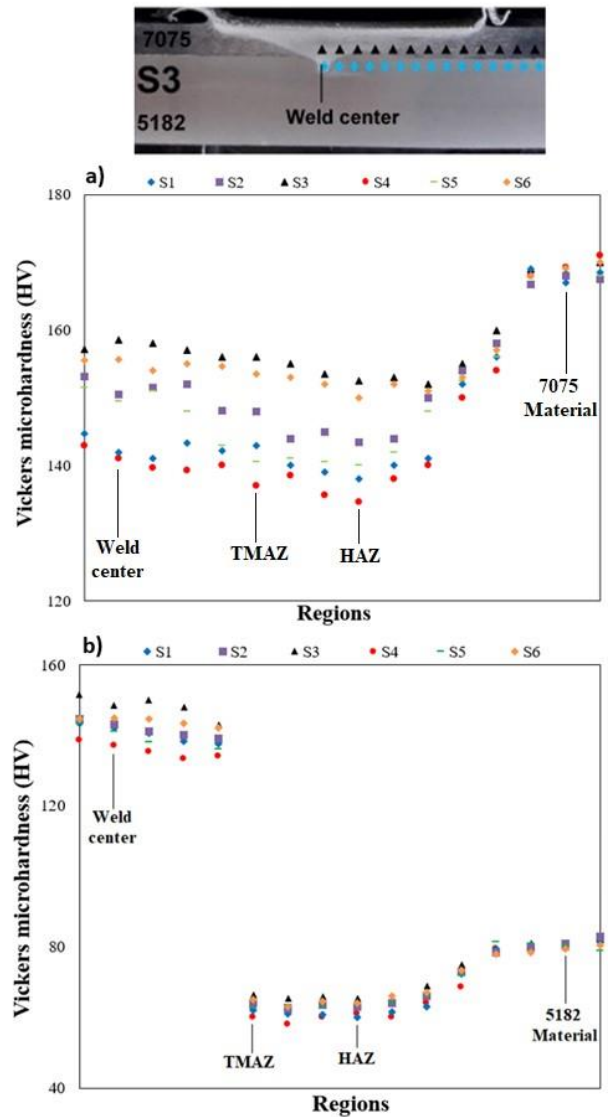


Figure 10. Hardness of the weld S3 and S4

3.4. Tensile Load Determination

Figure 11 demonstrates the tensile test results of the FSLW joints generated by the conical pin and cylindrical screw pin tools at 22, 37, and 51 mm min⁻¹ feed rates. The tensile load of the joint fabricated through the conical pin tool gradually increased with increasing of the tool feed rate, whereas the opposite of this was seen for the cylindrical screw pin tool. Welding area width and vertical downward penetration increased with an increase in the conical pin tool feed rate as seen in Figure 7, and accordingly the weld strength increased. However, when increasing the cylindrical screw pin tool feed rate speed led to a decrease in the welded area width and penetration as well as voids formed as can be seen in Figure 7, and as a result of these, the weld strength reduced. The strongest weld S3 with a tensile load of 13033 N was fabricated via the conical pin tool at 51 mm min⁻¹ while via the cylindrical screw pin, the strongest weld S4 with a tensile load of 12162.5 N was produced tool at 22 mm min⁻¹. These welds performed better strength as they had larger welded areas and higher penetration. In general, stronger joints were created by the conical pin tool. Because higher vertical

downward penetration with finer grain microstructure took place in the welds of the conical pin tool. Additionally, the concave shoulder of the conical pin tool might have assisted in more powerful weld production. Buffa et al. [10] investigated FSLW of 2198-T4 Al alloy utilizing three different welding tools with cylindrical, conical and cylindrical-conical pin. They reported that the cylindrical-conical pin tool produced stronger welds and also stated that increasing the welding speed improved the weld strength. Song et al. [19] studied the FSLW of 2024 and 7075 Al alloys and they found that the weld strength enhanced with an increase in the welding speed. Lee et al. [16] investigated the FSLW of different 5052 Al and 6061 Al alloys. They reported that higher welding speed improved the weld strength.

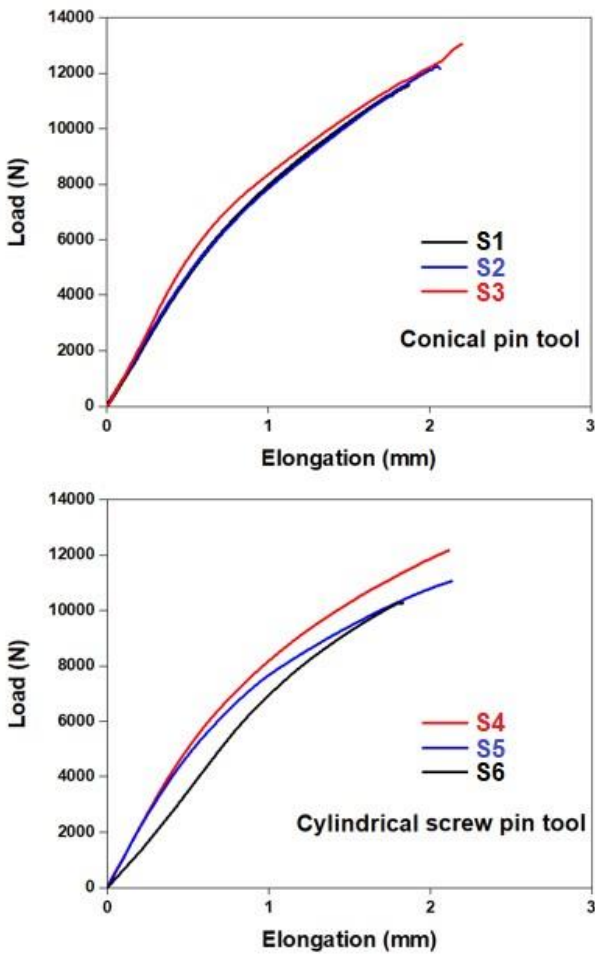


Figure 11. Tensile load-elongation curve of the FSLW welds

Cakan et al. [14] studied the FSLW of different pure copper and AA7075-T6 Al alloy materials using different tool feed rates (18, 32 and 54 mm min⁻¹) and the best joint was created at 32 mm min⁻¹. Xie et al. [24] studied the FSLW of dissimilar 304 austenitic stainless steel and Ti6Al4V alloy and they achieved a maximum tensile shear strength of 7507 N for the joint produced at the welding tool rotation speed of 600 rpm and with the feed rate of 30 mm min⁻¹. Top surface appearance of the welds in Figure 5 is giving a clue about the weld strength. When the lines formed by the tool shoulder on the top surface of the upper sheet were broken into small pieces, higher weld strength occurred. When the conical

pin tool feed rate increased from 22 to 51 mm min⁻¹, the lines formed by the tool shoulder on the top surface of upper sheet started to break into small pieces. For example, there are no tool shoulder lines formed on the top surface of the upper sheet of weld S3, the lines were totally broken into small pieces and disappeared and thus weld S3 had the highest tensile strength. Additionally, the microstructures of the conical pin welds had finer grains as can be seen in Figure 8. On the other hand, when the cylindrical screw pin tool feed rate was increased, clearer and more tool shoulder lines began to form resulting in a decrease in the weld strength. The tensile strength of the welds was found by proportioning the tensile load to the cross-sectional area. The cross-sectional area is obtained by multiplying the effective weld thickness or sheet thickness by the weld width. The effective weld thickness of the welds failed from the weld region was found by measuring the distance from the interface of the sheets to the bottom of the weld as shown in Figure 12a. For the welds broken from the upper 7075-T651 sheet, the effective sheet thickness was measured from the broken area as shown in Figure 12b. Approximately tensile strengths and efficiency of the welds are shown in Table 4. As the upper 7075-T651 sheet is thinner and failure took place from this during the tensile test, the weld efficiency was calculated based on the upper sheet with a tensile strength of 550 MPa. When looking at the tensile strength and efficiency of the welds, it generally improved with increasing tool feed rate, and maximum efficiency of 81.08 and 87.09 % were achieved at 51 mm min⁻¹ for the conical and cylindrical screw pin tools, respectively. 5182 alloy sheet has a higher tensile strength than the 5182 alloy. Generally, better welds were acquired via the tool having a conical pin. Cetkin et al. [25] investigated friction stir welding of 7075 aluminum alloys by tools with conical and triangular pins. They reported that stronger welds were made by the tool with the conical pin.

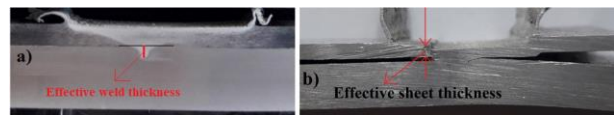


Figure 12. Representation of measuring effective weld and sheet thickness

Table 4. Tensile strength and efficiency

Weld sample	Effective weld or sheet thickness (mm)	Width of weld sample (mm)	Failure load (N)	Tensile strength (MPa)	weld efficiency (%)
S1	1.077	25	11564.45	429.506	78.09
S2	1.108	25	12242.19	441.956	80.35
S3	1.169	25	13033	445.953	81.08
S4	1.395	25	12162.50	348.745	63.40
S5	1.011	25	11057.42	437.484	79.54
S6	0.857	25	10262.50	478.996	87.09

3.5. Fracture Area Examination

Photographs of the fractured welds during tensile testing are given in Figure 13. S1, S2, S3 and S6 welds failed

from the weld area and exhibited tensile shear fracture while S3 and S4 failed from the heat-affected zone (HAZ) away from the weld area and showed tensile-type fracture. It can be seen when looking at the top of the 5182 bottom sheets of the welds made by the conical pin tool in Figure 13 that the S3 weld had a larger fractured weld area than the S1 and S2 welds. A bigger fractured weld area was observed with an increase in tool feed rate, also seen in Figure 7. Figure 14 shows the weld fracture surfaces of the strongest S3 and S4 welds produced by the conical and cylindrical screw pin tools, respectively. As can be seen, weld S3 has smaller and denser dimples than weld S4, which indicates a higher-quality weld. Weld S4 contains larger dimples. Song et al. [19] reported ductile fractures in tensile tests of FSLW welds of 2024 and 7075 Al alloys.

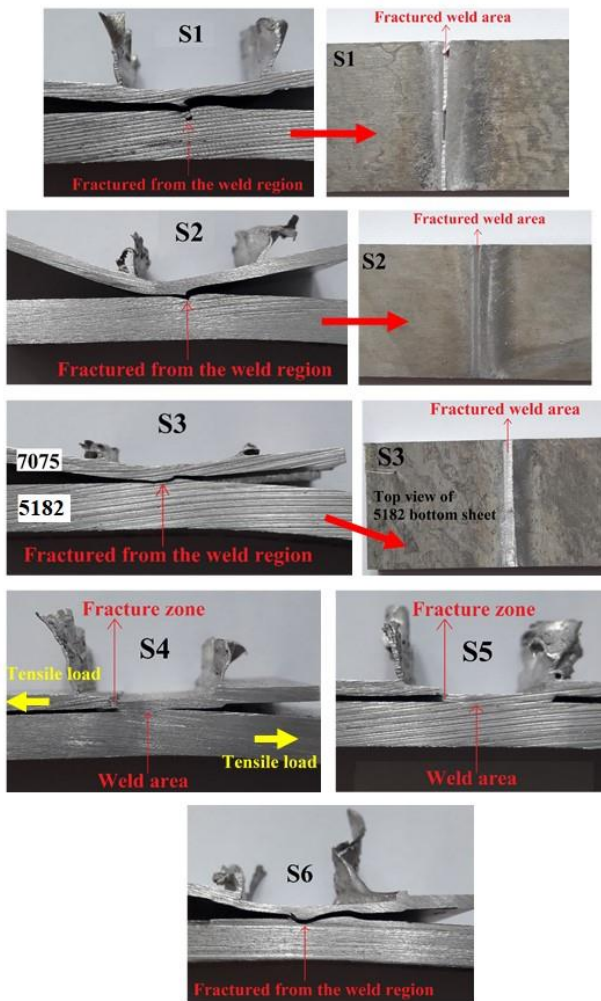


Figure 13. Photographs of the fractured welds during tensile testing

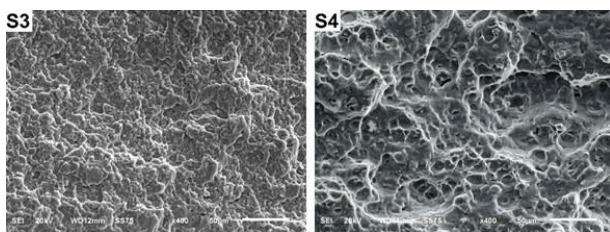


Figure 14. Fracture surface SEM images for weld S3 and S4 after tensile test

4. CONCLUSIONS

Strong FSLW welds between 7075-T651 and 5182 aluminum alloys were achieved. The results obtained are provided below.

1. The strongest weld with a tensile load of 13033 N was obtained at the welding speed of 51 mm min⁻¹ with the conical pin tool. By cylindrical screw pin tool, the weld having highest tensile load of 12162.5 N was obtained at 22 mm min⁻¹ welding speed.
2. In FSLW welding with tapered pin tools, when the feed rate was increased from 22 to 51 mm min⁻¹, the weld strength increased due to the increase in joint area and vertical downward penetration. However, exactly the opposite of this was observed for the cylindrical screw pin tool. While the strongest weld was obtained at the highest welding speed with the conical pin tool, the strongest weld was acquired at the lowest welding speed with the cylindrical screw pin tool.
3. Better welds were produced through the conical pin tool. Because the materials were stirred better via the conical pin tool and thus the joints with higher penetration, denser and harder microstructures were created. Additionally, smaller and denser dimples were seen in the weld fracture surface of the conical pin tool.
4. The more disappearance of the lines formed by the tool shoulder on the top surface of the upper sheet by breaking up into small particles meant the formation of a stronger weld.
5. All welded samples were ductile fractured, but the fracture areas of conical pin tool welds exhibited smaller and denser dimples. Both tool pin profile and feed rate showed to have a great impact on the weld quality.

REFERENCES

- [1] Christner B, Mc Coury J, Higgins S. Development and testing of friction stir welding as a joining method for primary aircraft structure. In: 4th International symposium on friction stir welding, Park City, Utah, USA, May 14-16, TWI Ltd. 2003.
- [2] Das A, Butterworth I, Masters I, Williams D. Microstructure and mechanical properties of gap-bridged remote laser welded (RLW) automotive grade AA 5182 joints. *Materials Characterization*. 2018;145:697-712.
- [3] Gibson BT, Lammlein DH, Prater TJ, Longhurst WR, Cox CD, Ballun MC, Dharmaraj KJ, Cook GE, Strauss AM. Friction stir welding: Process, automation, and control. *Journal of Manufacturing Processes*. 2014;16(1):56-73.
- [4] Xie S, Xia Z, Ding R, Li H, Bowen P. Microstructure and mechanical properties of two Al alloys welded by linear friction weld. *Materials Science and Engineering A*. 2021; 816:141261.
- [5] Caligulu U, Acik M, Balalan Z, and Kati N. The Effects of Process Parameters for Joining of AISI

- 1010-Cu Alloys by Friction Welded. *International Journal of Steel Structures*. 2021;15(4):923-931.
- [6] Kumar N, Yuan W, Mishra RS. *Friction Stir Welding of Dissimilar Alloys and Materials*. Elsevier, Oxford, 2015.
- [7] Abdollah-Zadeh A, Saeid T, Sazgari B. Microstructural and mechanical properties of friction stir welded aluminum/copper lap joints. *Journal of Alloys and Compounds*. 2008;460(1-2): 535-538.
- [8] Leal RM, Loureiro A. Effect of overlapping friction stir welding passes in the quality of welds of aluminium alloys. *Materials & Design*. 2008; 29(5):982-991. Hasund IK. The discourse markers like in English and liksom in Norwegian teenage language : A corpus-based, cross-linguistic study [dissertation]. Bergen: University of Bergen; 2003.
- [9] Balasubramanian V. Relationship between base metal properties and friction stir welding process parameters. *Materials Science and Engineering A*. 2008;480(1-2):397-403.
- [10] Buffa G, Campanile G, Fratini L, Prisco A. Friction stir welding of lap joints: influence of process parameters on the metallurgical and mechanical properties. *Materials Science and Engineering A*. 2009;519(1-2):19-26.
- [11] Bahemmat P, Rahbari A, Haghpanahi M, Besharati MK. Experimental study on the effect of rotational speed and tool pin profile on AA2024 aluminum friction stir welded butt joints. In: *Proceedings of ECTC ASME early career technical conference*. Miami, Florida, USA. 2008. p. 11-17.
- [12] Çevik B, Özçatalbaş Y, Gülenç B. Effect of tool material on microstructure and mechanical properties in friction stir welding. *Materials Testing*. 2016;58:36-42.
- [13] İş EG, Koçak K, Basar ZS, Yavuz Y, Topuz P. Effects of different profiled pins used in friction stir welding of Al 6061 T6. *Materials Testing*. 2023;65:1474-1481.
- [14] Cakan A, Ugurlu M, Kaygusuz E. Effect of weld parameters on the microstructure and mechanical properties of dissimilar friction stir joints between pure copper and the aluminum alloy AA7075-T6. *Materials Testing*. 2019;61:142-148.
- [15] Thomas WM, Norris IM, Stains DG, Watts ER. *Friction stir welding-process developments and variant techniques*. Oconomowoc, Milwaukee: The SME summit; 2005. p. 1-21.
- [16] Lee CY, Lee WB, Kim JW, Choi DH, Yeon YM, Jung SB. Lap joint properties of FSWed dissimilar formed 5052 Al and 6061 Al alloys with different thickness. *Journal of Materials Science*. 2008;43:3296-304.
- [17] AWS D17.3/D17.3M:2010. *Specification for Friction Stir Welding of Aluminum Alloys for Aerospace Applications*. American Welding Society (AWS). Miami, Florida (USA); 2009.
- [18] Threadgill PL, Leonard AJ, Shercliff HR, Withers PJ. Friction stir welding of aluminium alloys. *International Materials Reviews*. 2009;54(2):49-93.
- [19] Song Y, Yang X, Cui L, Hou X, Shen Z, Xu Y. Defect features and mechanical properties of friction stir lap welded dissimilar AA2024-AA7075 aluminum alloy sheets. *Materials and Design*. 2014;55:9-18.
- [20] Bayazid SM, Farhangi H, Asgharzadeh H, Radan L, Ghahramani A, Mirhaji A. Effect of cyclic solution treatment on microstructure and mechanical properties of friction stir welded 7075 Al alloy. *Materials Science and Engineering A*. 2016;649:293-300.
- [21] Kaplan M, İleriturk M & Balalan Z. Relationship Between Microstructure, Hardness, XRD, TGDTA Analysis, and Wear Performance of a Cast ZA Alloy. *Materials and Manufacturing Processes*. 2008;23:400-406.
- [22] Cetkina E, Çelika YH, Temiz S. Microstructure and mechanical properties of AA7075/AA5182 jointed by FSW. *Journal of Materials Processing Technology*. 2019;268:107-116.
- [23] Çetkin E., Kılıçkap E., Çelik YH. Investigation of the Effects of Welding Force, Vibration and Temperature on Mechanical Properties and Microstructure in FSW Welding. *Journal of Polytechnic*. 2023;26:(1)445-455.
- [24] Xie H, Chen X, Lu Y, Zhang M, Zhang Q. Forming mechanism and mechanical properties of dissimilar friction stir lap welds of 304 austenitic stainless steel to a Ti6Al4V alloy. *Materials Testing*. 2021; 63:889-894.
- [25] Cetkin E., Çelik YH & Kilickap E. Effect of Temperature, Force, and Vibration on Fatigue Strength of Friction Stir-Welded AA7075 Aluminum Alloy Joints. *Journal of Materials Engineering and Performance*. 2021;30:202-211.

Antibacterial Effect of Combined Use of Amoxicillin Trihydrate And *Cupressus sempervirens* Leaf Extract on Some Gram-Negative Bacteria

Alican Bahadır SEMERCİ^{1,2*} , Tuğba ONGUN SEVİNDİK² 

¹Necmettin Erbakan University, Ereğli Vocational School of Health Services, Konya, Türkiye

²Sakarya University, Sciences Faculty, Biology Department, Sakarya, Türkiye

Alican Bahadır SEMERCİ ORCID No: 0000-0001-9502-9321

Tuğba ONGUN SEVİNDİK ORCID No: 0000-0001-7682-0142

*Corresponding author: alicanbahadirsemerci@gmail.com

(Received: 11.01.2024, Accepted: 14.05.2024, Online Publication: 28.06.2024)

Keywords

Antibacterial activity, *Cupressus sempervirens*, Coliform bacteria, Synergistic effect, Wastewater

Abstract: Difficulties in the treatment of infections caused by Gram-negative bacteria have led to studies in recent years directed towards improving the effectiveness of existing antibacterial agents. In our study, the antibacterial activities of the combined use of *Cupressus sempervirens* leaf extract and amoxicillin trihydrate on *Escherichia coli* ATCC 8739, *Escherichia coli* ATCC 25922 *Salmonella typhimurium* ATCC 14028, *Salmonella abony* NCTC 6017 bacteria and 4 coliform bacteria isolated from Karaman wastewater facility were investigated using the disc diffusion method. It was determined that the mixture of amoxicillin trihydrate and *C. sempervirens* leaf extract caused a synergistic effect on *S. typhimurium* and *E. coli* ATCC 8739. In general, it was observed that *C. sempervirens* leaf extracts contributed to the existing antibacterial activity of the antibiotic amoxicillin trihydrate. In addition, three of the bacteria isolated from wastewater were found to be sensitive to the antibiotic amoxicillin trihydrate, while one was found to be resistant

Amoksisilin Trihidrat ve *Cupressus sempervirens* Yaprak Ekstraktının Birlikte Kullanımının Bazı Gram-Negatif Bakteriler Üzerindeki Antibakteriyel Etkisi

Anahtar

Kelimeler
Antibakteriyel aktivite, *Cupressus sempervirens*, Koliform bakteri, Sinerjik etki, Atıksu

Öz: Gram-negatif bakterilerin neden olduğu enfeksiyonların tedavisindeki zorluklar son yıllardaki çalışmaları mevcut antibakteriyel ajanların etkisini geliştirilmeye yönelmiştir. Çalışmamızda *Cupressus sempervirens* yaprak ekstraktı ve amoksisilin trihidrat birlikte kullanımlarının *Escherichia coli* ATCC 8739, *Escherichia coli* ATCC 25922 *Salmonella typhimurium* ATCC 14028, *Salmonella abony* NCTC 6017 bakterileri ile Karaman atık su tesisinden izole edilen 4 koliform bakteri üzerindeki antibakteriyel aktiviteleri disk difüzyon metodu kullanılarak araştırılmıştır. Amoksisilin trihidrat ve *C. sempervirens* yaprak ekstraktı karışımının *S. typhimurium* ve *E. coli* ATCC 8739 üzerinde sinerjik etkiye neden olduğu tespit edilmiştir. Genel olarak *C. sempervirens* yaprak ekstraktlarının amoksisilin trihidrat antibiyotiğinin mevcut antibakteriyel aktivitesine katkı sağladığı görülmüştür. Ayrıca amoksisilin trihidrat antibiyotiğine karşı atık sudan izole edilen bakterilerden üçünün duyarlı olduğu görülürken birinin dirençli olduğu belirlenmiştir.

1. INTRODUCTION

Water used by people during their daily activities and transferred to sewers is called domestic wastewater. Wastewater contains various pathogenic microorganisms such as viruses, bacteria, fungi, protozoa and helminths. Different types of polluting agents, such as detergents, personal care products, endocrine disruptors and pharmaceuticals are mixed into wastewater. Recent studies have focused on pharmaceuticals, particularly antibiotics, with their use increasing worldwide [1,2].

Once antibiotics get in ecosystems, they can affect the structure, development and genetic structure of microorganisms and, accordingly, change the ecological functioning of the aquatic ecosystem [3]. Generally, 30-90% of the dose taken as a result of the use of water-soluble antibiotics is excreted in human urine and feces. On the other hand, large amounts of antibiotics are mixed into wastewater due to the disposal of unused antibiotics [1,4]. Such antibiotic residues and other pharmaceutical active molecules are heavily discharged into the municipal sewage system and then transferred to the wastewater treatment plant. Antibiotics mixed into

wastewater in this way may develop resistance in microorganisms in the environment and spread this resistance to sensitive microorganisms. Ultimately, this situation creates more threats to the environment and society [5-6]. In addition, unconscious and excessive use of synthetic antibiotics used in the treatment of infections causes increased resistance in bacteria. Difficult and slow healing of resistance-related infections has negative effects on human health. Therefore, the search for new antimicrobials has attracted worldwide attention. However, since such research is slow and costly, studies aimed at increasing the effects of existing antibiotics stands out [6-7].

In recent years, treatments with a single substance have been replaced by treatments with drug combinations in the treatment of some diseases. Investigating the synergistic effects of antimicrobial agents, especially with herbal extracts, is very important in finding new treatment combinations that increase the effects of existing antimicrobials.

β -lactam antibiotics are the most widely used antibacterial compounds (approximately 70% of prescriptions) due to their ability to act on many different types of bacteria and their inhibition mechanism that disrupts bacterial cell wall formation. On the other hand, β -lactamase enzymes, which are frequently detected in Gram-negative bacilli, hydrolyze the β -lactam ring in the chemical structure of these antibiotics and render them ineffective. These enzyme groups, which hydrolyze broad-spectrum β -lactam antibiotics, negatively affect the clinical use of antibiotics [8,9].

Cupressus sempervirens L. is a decorative tree belonging to the Cupressaceae family and commonly used in parks and gardens, growing mostly in the Mediterranean region. It is also used as a pharmaceutical agent due to its antiseptic, antispasmodic, antipyretic and anti-inflammatory properties. In addition, it has been proven that extracts obtained from different parts of this plant have antibacterial properties [10,11]. Therefore, it can be used as a natural antimicrobial agent in food preservation and to treat humans against infectious diseases [12]. The use of natural antimicrobial agents together with antibiotics can also help reduce negative effects such as environmental pollution, toxicity to humans, and resistance to synthetic chemicals and drugs.

In our study, it was aimed to determine the antibacterial activity of *Cupressus sempervirens* extract, whose antibacterial activity has been proven in previous studies, and amoxicillin trihydrate antibiotic, which is widely used among the broad-spectrum penicillin group antibiotics, on gram-negative bacteria, both separately and together for the first time..

2. MATERIAL AND METHOD

2.1. Preparation of The Extract

Cupressus sempervirens leaves collected from Sakarya University Esentepe Campus were washed, cleaned and dried in a drying oven at 40°C for 10 days. Then, 10 grams of the sample from the leaves pulverized with the help of an electric grinder was placed in soxhlet cartridges and extracted with 200 mL 70% ethyl alcohol in the soxhlet apparatus for 8 hours. The solvents of the extracts filtered through the filter paper were removed in a rotary evaporator at 55° C for 15 minutes [13]. Stocks were prepared from the dried extracts at a concentration of 10 mg/mL(1:1 ratio of distilled water and DMSO) and used in activity studies.

2.2. Isolation of Gram Negative Coliforms from Wastewater

Water samples taken from the Karaman wastewater treatment plant effluent were brought to the laboratory in the cold chain and analyzed on the same day. 100 mL of the collected wastewater was filtered through cellulose nitrate filters with a pore size of 0.45 μ m using a membrane filtration system. To detect total coliform bacteria, the filter placed on Chromocult Coliform Agar (CCA)(Bioneks) medium was incubated at 37 \pm 0.5°C for 24 \pm 2 hours. After incubation, the bacteria growing on the petri dish were subjected to oxidation test [14]. For the oxidation (Merck 1.13300) test, a random colony thought to be coliform bacteria was selected from the colonies growing on CCA medium, and it was planted in Tryptic Soy Agar (Merck) and incubated at 37 \pm 0.5°C for 24 \pm 1 hours. 10 possible coliform bacteria were selected and isolated from the bacteria with negative oxidation results. Additionally, gram negativity was confirmed by gram staining.

2.3. Antibacterial Activity

In determining the antibacterial activity, 4 standard strains (*Escherichia coli* ATCC 8739, *Escherichia coli* ATCC 25922 *Salmonella typhimurium* ATCC 14028, *Salmonella abony* NCTC 6017) used from Sakarya University Microbiology laboratory and 4 coliform bacteria isolated from Karaman wastewater treatment facility (wastewater treatment plant) were used. In this study, the antibacterial activity of *C. sempervirens* leaf extract, amoxicillin trihydrate and leaf extract + amoxicillin trihydrate combinations was evaluated using the disc diffusion method.

2.3.1. Disc Diffusion Methods

First of all, the leaf extract prepared at a concentration of 5 mg/mL (1:1 ratio of distilled water and DMSO), 0.5 mg/mL amoxicillin trihydrate and the binary mixture were absorbed (20 μ L) into empty sterile discs (Himedia) with a diameter of 6 mm. Suspensions were prepared from 24-hour fresh bacterial cultures at a density of 0.5 McFarland. Then, bacteria were inoculated from these bacterial suspensions into Mueller Hinton Agar (Merck)

with sterile swabs and previously prepared sample-impregnated disks were placed. After 24 hours of incubation at $37\pm 0.5^{\circ}\text{C}$, the zone diameters formed in the petri dishes were measured in mm using a digital caliper [10]. Discs loaded with 50% DMSO (Merck) were used as negative control, and discs loaded with gentamicin (Oxoid) were used as positive control. The antimicrobial activity test was performed three times under aseptic conditions and the diameter of inhibition zone measured was the average of the three replicates.

3. RESULTS AND DISCUSSION

Gram-negative bacteria are more resistant than Gram-positive bacteria due to their unique morphological

Table 1. Inhibition zone diameters of extracts and amoxicillin trihydrate

Test bacteria	Inhibition Zones(mm)(\pm SD)			
	Extract	Amoxicillin trihydrate	Extract+ amoxicillin trihydrate	Negative control
<i>E. coli</i> ATCC 25922	9 \pm 0.1	28.3 \pm 0.7	28.3 \pm 0.6	-
<i>E. coli</i> ATCC 8739	-	18 \pm 1.0	19 \pm 0.1	-
<i>S. abony</i> NCTC 6017	-	23.7 \pm 0.6	23.5 \pm 0.3	-
<i>S. typhimurium</i> ATCC 14028	-	25.6 \pm 0.2	27 \pm 0.1	-
Coliform-1	-	8 \pm 0.2	8 \pm 0.1	-
Coliform-2	9 \pm 0.1	36 \pm 0.3	37.5 \pm 0.3	-
Coliform-3	10 \pm 0.3	31.5 \pm 0.1	32.7 \pm 0.6	-
Coliform-4	8 \pm 0.3	22 \pm 0.1	22.3 \pm 0.1	-

Amoxicillin, which is among the beta-lactams that constitute the largest antibiotic group, is used in veterinary medicine as well as being frequently used in human treatment. Amoxicillin trihydrate created an inhibition zone diameter of 23.7 mm in *S. abony*, 25.6 mm in *S. typhimurium*, 8 mm in Coliform-1, 36 mm in Coliform-2, 31.5 mm in Coliform-3, and 22 mm in Coliform-4. Standard strains, except *E. coli* ATCC 8739, were found to be highly sensitive to the antibiotic amoxicillin trihydrate. While amoxicillin trihydrate created an 18 mm inhibition zone in *E. coli* ATCC 8739, it created a 28 mm inhibition zone in *E. coli* ATCC 25922. There are many studies showing differences in the antibacterial activity of different strains of the same bacteria. In a study evaluating the antibacterial effect of cystatin on three *E. coli* strains, it was reported that cystatin showed different effects in the three strains [16]. In a study examining the activity of *C. sempervirens* leaf extracts, it was reported that the ethanolic extract created an 8 mm inhibition zone on *E. coli* ATCC 35218 [17]. Similarly, Mogna et al. [18] reported in their study that probiotic bacteria exhibited different antibacterial activities on *E. coli* strains (ATCC 8739, ATCC 10536, ATCC 35218 and ATCC 25922).

structure and cause morbidity and mortality worldwide. Various strategies have been reported to combat and control resistant Gram-negative bacteria, such as the development of adjuvants to antimicrobial agents, structural modification of existing antibiotics, investigation of new mechanisms of action, etc. [15].

In our study, the antibacterial activity results of *C. sempervirens* leaf extract and amoxicillin trihydrate combinations on gram-negative coliform bacteria isolated from wastewater environment and *Escherichia coli* ATCC 8739, *Escherichia coli* ATCC 25922 *Salmonella typhimurium* ATCC 14028, *Salmonella abony* NCTC 6017 bacteria used as standard strain are given in Table 1.

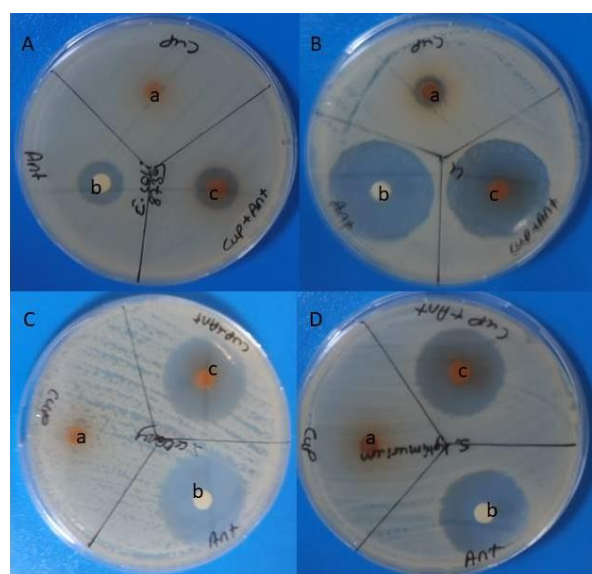


Figure 1. Antibacterial activity of samples (a=leaf extract, b= amoxicillin trihydrate, c) leaf extract + amoxicillin trihydrate) against (A= *E. coli* ATCC 8739, B=Coliform-3, C= *S. abony*, D= *S. typhimurium*).

In our study, we isolated fecal indicator bacteria (coliform bacteria) from the Sakarya Karaman Wastewater Facility and evaluated the effect of amoxicillin trihydrate, and *C. sempervirens* extracts on these bacteria. Because most of this group of bacteria threaten public health. In addition, *E. coli* and other coliform bacteria can relatively easily incorporate resistance genes contained in plasmids. This may cause the spread of resistance in sensitive bacteria in Wastewater Treatment Plants [1,8]. The results obtained showed that Coliform-1 bacteria isolated from wastewater were resistant to the antibiotic amoxicillin

trihydrate, while other coliform bacteria were found to be sensitive. In particular, the fact that *C. sempervirens* leaf extract creates an inhibition zone of 9 mm in Coliform-2, 10 mm in Coliform-3 and 8 mm in Coliform-4 is important in terms of demonstrating that phytochemical resources can be used as antibacterial agents. Many studies in the literature show that antibiotic-resistant bacteria are present in drinking water, surface water, groundwater and wastewater along with antibiotics [19-21].

The effect of antibiotics on bacteria can be enhanced by their combined use with phytopharmaceuticals and modern drugs. It was also observed that different combinations could help reduce the emergence of resistant bacteria and drug toxicity [22]. As a result of combining two drugs or phytochemical products, there

may be a synergistic, additive or antagonistic effect on antibacterial activity, depending on the interaction between the drugs.

In our study, the contributions of the combined use of *C. sempervirens* leaf extract and the antibiotic amoxicillin trihydrate to the activity of the antibiotic are given in Figure 2. If the antibacterial activity of two agents used together is greater than the sum of the antibacterial activities of the individual agents, it shows a synergistic effect. While *C. sempervirens* leaf extract did not show activity on *S. typhimurium* and *E. coli* ATCC 8739 bacteria, the leaf extract used together with the antibiotic (amoxicillin trihydrate) showed a synergistic effect by increasing the existing activity of the antibiotic.

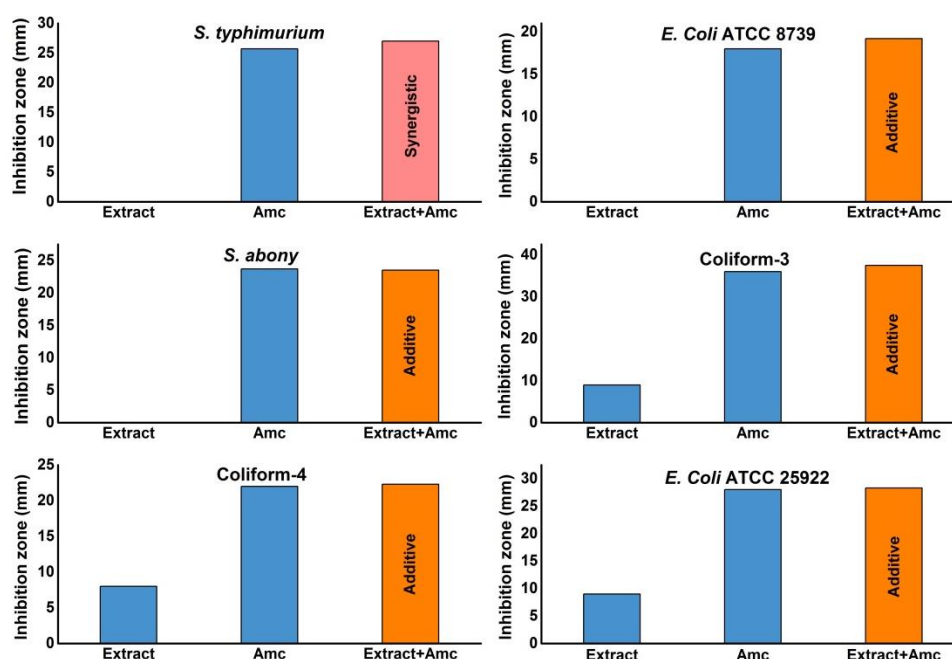


Figure 2. Antibacterial activity of combined use of amoxicillin trihydrate and *C. sempervirens* leaf extracts on bacteria

When *C. sempervirens* leaf extract was used together with the antibiotic amoxicillin trihydrate, it was observed that it contributed to the existing effect of the antibiotic on Coliform-3, Coliform-4, *E. coli* ATCC 25922 and *S. abony* bacteria. Studies in the literature have determined that *C. sempervirens* leaf extracts have antibacterial activity on many bacteria [23-25]. In our study, the effectiveness of *C. sempervirens* leaf extract on 3 of the 4 coliform bacteria isolated from wastewater emphasizes the importance of plant extracts against microbial resistance. In addition, our study provides important data to the literature by revealing that the use of *C. sempervirens* leaf extract together with amoxicillin trihydrate increases the antibacterial activity.

Our study confirmed that plants can indeed be a source of compounds that can potentiate the activity of antibiotics against bacterial pathogens. From studies in the literature, it was seen that synergistic interactions between plant extracts and antibiotics could support β -

lactamase inhibition, blocking drug flow, increasing permeability and antibacterial activity due to alternative mechanisms of action [26,27].

Acknowledgement

The authors would like to thank Dr. Sümeyye Çol and Ph.D. student Ayşe Gül Tekbaba and for their invaluable support

REFERENCES

- [1] Lépesová K, Olejníková P, Mackul'ak T, Tichý J, Birošová L. Annual changes in the occurrence of antibiotic-resistant coliform bacteria and enterococci in municipal wastewater. *Environ Sci Pollution Res*, 2019; 26,18470-18483.
- [2] Majumder A, Gupta AK, Ghosal PS, Varma M. A review on hospital wastewater treatment: A special emphasis on occurrence and removal of pharmaceutically active compounds, resistant

- microorganisms, and SARS-CoV-2. *J Environ Chem Engg*, 2021; 9(2): 104812.
- [3] Bouki C, Venieri D, Diamadopoulou E. Detection and fate of antibiotic resistant bacteria in wastewater treatment plants: a review. *Ecotoxicol Environ Safety*, 2013; 91: 1-9. <https://doi.org/10.1016/j.ecoenv.2013.01.016>
- [4] Kumar M, Ram B, Sewwandi H, Honda R, Chaminda T. Treatment enhances the prevalence of antibiotic-resistant bacteria and antibiotic resistance genes in the wastewater of Sri Lanka, and India. *Environ Res*, 2020;183: 109179
- [5] Yu Y, Wu G, Wang C, Lu N, Yuan X, Zhu X. Pollution characteristics of antibiotics and antibiotic resistance of coliform bacteria in the Yitong River, China. *Environ Monit Assess*, 2019;191, 1-13.
- [6] Le TH, Truong T, Tran LT, Nguyen DH, Pham TPT, Ng C. Antibiotic resistance in the aquatic environments: the need for an interdisciplinary approach. *Int J Environ Sci Technol*, 2023; 20(3): 3395-34.
- [7] Terreni M, Taccani M, Pregolato M. New antibiotics for multidrug-resistant bacterial strains: latest research developments and future perspectives. *Molecules*, 2021;26(9): 2671. <https://doi.org/10.3390/molecules26092671>
- [8] Berrazeg M, Diene SM, Medjahed L, Parola P, Drissi M, Raoult D. et al. New Delhi Metallo-beta-lactamase around the world: an Review using Google Maps. *Eurosurveillance*, 2014;19(20): 20809
- [9] Zagui, GS, De Andrade LN, Moreira NC, Silva TV, Machado GP, Da Costa Darini AL. et al. Gram-negative bacteria carrying β -lactamase encoding genes in hospital and urban wastewater in Brazil. *Environ Monit Assess*, 2020;192: 1-11.
- [10] Semerci AB, İnceçayır D, Konca T, Tunca H, Tunç K. Phenolic constituents, antioxidant and antimicrobial activities of methanolic extracts of some female cones of gymnosperm plant. *Indian J Biochem Biophys*, 2020;57(3): 298-303.
- [11] Al-Mijalli SH, El Hachlafi N, Jeddi M, Abdallah EM, Assaggaf H, Qasem A. et al. Unveiling the volatile compounds and antibacterial mechanisms of action of *Cupressus sempervirens* L., against *Bacillus subtilis* and *Pseudomonas aeruginosa*. *Biomed Pharmacot*, 2023;167: 115609.
- [12] Sriti J, Haj Salem M, Aidi Wannas W, Bachrouch O, Mejri H, Belloumi S. Antioxidant, antibacterial and insecticidal activities of cypress (*Cupressus sempervirens* L.) essential oil. *Int J Environ Health Res*. 2023;1-12.
- [13] Semerci AB, İnceçayır D, Sağıroğlu M, Tunç K. Antimicrobial activity of different flower extracts. *Curr Perspec Med Aromatic Plants*, 2019;2(1): 53-58.
- [14] TS EN ISO 9308-1 Su Kalitesi - E. coli ve Koliform Bakterilerin Tespiti ve Sayımı-Bölüm 1:Membran Süzme Yöntemi. 2004.
- [15] Breijyeh Z, Jubeh B, Karaman R. Resistance of gram-negative bacteria to current antibacterial agents and approaches to resolve it. *Molecules*, 2020;25(6): 1340.
- [16] Szpak M, Trziszka T, Polanowski A, Gburek J, Gołąb K, Juszczynska K. et al. Evaluation of the antibacterial activity of cystatin against selected strains of *Escherichia coli*. *Folia Biologica (Kraków)*, 2014;62(3): 187-192.
- [17] Anka L, Rammal H, Kobeissi A, Saab HB. Chemical composition and biological potentials of Lebanese *Cupressus sempervirens* L. leaves extracts. *J Med Plants Res*, 2020;14(6): 292-299.
- [18] Mogna L, Del Piano M, Deidda F, Nicola S, Soattini L, Debiaggi R. Assessment of the in vitro inhibitory activity of specific probiotic bacteria against different *Escherichia coli* strains. *J Clin Gastroenterol*, 2012;46: S29-S32.
- [19] Kumar A, Pal D. Antibiotic resistance and wastewater: Correlation, impact and critical human health challenges. *J Environ Chem Eng* 2018;6(1): 52-58. <https://doi.org/10.1016/j.jece.2017.11.059>.
- [20] Paulshus E, Kühn I, Möllby R, Colque P, O'Sullivan K, Midtvedt T. Diversity and antibiotic resistance among *Escherichia coli* populations in hospital and community wastewater compared to wastewater at the receiving urban treatment plant. *Water Res*, 2019;161: 232-241.
- [21] Smyth C, O'Flaherty A, Walsh F, Do TT. Antibiotic resistant and extended-spectrum β -lactamase producing faecal coliforms in wastewater treatment plant effluent. *Environ Pollution*, 2020; 262: 114244. <https://doi.org/10.1016/j.envpol.2020.114244>.
- [22] Bassolé IHN, Lamien-Meda A, Bayala B, Tirogo S, Franz C, Novak J. Composition and antimicrobial activities of *Lippia multiflora* Moldenke, *Mentha x piperita* L. and *Ocimum basilicum* L. essential oils and their major monoterpene alcohols alone and in combination. *Molecules*, 2010;15(11): 7825-7839.
- [23] Argui H, Youchret-Zalleza OB, Suner SC, Periz ÇD, Türker G, Ulusoy S. et al. Isolation, chemical composition, physicochemical properties, and antibacterial activity of *Cupressus sempervirens* L. essential oil. *J Essent Oil Bear Plants*, 2020;24(3): 439-452.
- [24] Sriti J, Haj Salem M, Aidi Wannas W, Bachrouch O, Mejri H, Belloumi S. et al. Antioxidant, antibacterial and insecticidal activities of cypress (*Cupressus sempervirens* L.) essential oil. *Int J Environ Health Res*, 2023;1-12.
- [25] Selim SA, Adam ME, Hassan SM, Albalawi AR. Chemical composition, antimicrobial and antibiofilm activity of the essential oil and methanol extract of the Mediterranean cypress (*Cupressus sempervirens* L.). *BMC complementary Alter Med*, 2014;14, 1-8.
- [26] Garvey MI, Rahman MM, Gibbons S, Piddock LJ. Medicinal plant extracts with efflux inhibitory activity against Gram-negative bacteria. *International journal of antimicrobial agents*, 2011;37(2):145-151.

- [27] Al-Alak SK, AL-Oqaili RMS, Mohammed BB, Abd-Alkhalik N. Antibacterial activity of *Hibiscus rosa-sinensis* extract and synergistic effect with amoxicillin against some human pathogens. *Am J Phytomed Clin Ther*, 2015;3(10): 020-027.

Inequalities For Strongly s -Convex Functions Via Atangana-Baleanu Fractional Integral Operators

Ebru YÜKSEL^{1*} 

¹ Ağrı İbrahim Çeçen University, Faculty of Science and Letters, Department of Mathematics, Ağrı, Türkiye
 Ebru YÜKSEL ORCID No: 0000-0001-7081-5924

*Corresponding author: eyuksel@agri.edu.tr

(Received: 24.01.2024, Accepted: 20.05.2024, Online Publication: 28.06.2024)

Keywords

Hermite-Hadamard inequality,
 Strongly s -convex function,
 Atangana-Baleanu fractional integral

Abstract: It is more convenient to use fractional derivatives and integrals to express and represent rapid changes than to use integer derivatives and integrals. For this reason, fractional analysis has been found worthy of study in many fields. In recent years, fractional derivatives and integrals have been discussed together with inequality theory and the studies have attracted attention. In this article, we discuss new Hermite-Hadamard type approximations for strongly s -convex functions with the help of Atangana-Baleanu fractional integral operators. Additionally, new upper bounds have been obtained using various auxiliary inequalities with the help of twice differentiable strongly convex functions.

Atangana-Baleanu Kesirli İntegral Operatörler Yardımıyla Güçlü s -Konveks Fonksiyonlar İçin Eşitsizlikler

49

Anahtar Kelimeler

Hermite-Hadamard eşitsizliği,
 Güçlü s -konveks fonksiyon,
 Atangana-Baleanu kesirli integral

Öz: Hızlı değişimleri ifade etmek ve temsil etmek için kesirli türev ve integraller kullanmak tamsayı mertebeden türev ve integralleri kullanmaktan daha uygun olmaktadır. Bu nedenle kesirli analiz birçok alanda çalışılmaya değer bulunmuştur. Son yıllarda da kesirli türev ve integraller eşitsizlik teorisiyle birlikte ele alınmış ve yapılan çalışmalar dikkat çekmiştir. Biz de bu makalede, Atangana-Baleanu kesirli integral operatörler yardımıyla güçlü s -konveks fonksiyonlar için Hermite-Hadamard tipli yeni tahminleri tartışıyoruz. Ayrıca, iki kez türevlenebilen güçlü konveks fonksiyonlar yardımıyla, çeşitli yardımcı eşitsizlikler kullanılarak yeni üst sınırlar elde edilmiştir.

1. INTRODUCTION

The discovery of mathematical inequalities in the twentieth century, leading to numerous new results and research problems, has contributed to the expansion of mathematics into different areas. Many studies, including various classical and new inequalities as well as many new applications and proof methods, have become the main resources for researchers [1,2]. Convex functions, which have a long history, began to find a place in mathematics as a result of the works of Hermite and Hadamard in the late 19th century. Convex functions increased their recognition with Jensen's systematic studies in 1905-1906, became an independent field of mathematical analysis and continued to develop rapidly. This rapid development can be attributed to the inclusion of applications of convex functions in many areas of mathematical analysis and the close relationship between the theory of convex functions and inequality theory [3,4]. The fact that inequalities and convex functions are not

only significant in mathematics but also in other branches of science has made these topics a focused point for researchers, leading to numerous ongoing studies in these areas.

The Hermite-Hadamard inequality plays an important and magnificent role in the literature and is stated as follows [5].

If $Q: \mathfrak{I} \subseteq \mathfrak{R} \rightarrow \mathfrak{R}$ is convex in \mathfrak{I} for $\xi_1, \xi_2 \in \mathfrak{I}$ and $\xi_1 < \xi_2$, then

$$Q\left(\frac{\xi_1 + \xi_2}{2}\right) \leq \frac{1}{\xi_2 - \xi_1} \int_{\xi_1}^{\xi_2} Q(x) dx \leq \frac{Q(\xi_1) + Q(\xi_2)}{2} \quad (1)$$

This inequality specifies the lower and upper bounds of the integral mean value of a convex function. In the last two decades, many studies have been published by

mathematicians regarding its generalizations and extensions.

Fractional calculus is a branch of mathematical analysis that encompasses applications and research involving arbitrary order derivatives and integrals [6,7]. In this respect, the concepts of fractional derivative and fractional integral differ from classical derivative and classical integrals and are also more comprehensive than these concepts.

The main objective of this study is to obtain new Hermite-Hadamard inequalities for Atangana-Baleanu fractional integrals. Twice differentiable strongly s -convex functions are employed to achieve the results, and new inequalities are demonstrated by parameter substitutions. It can be easily observed that the results of this study are a generalization of the existing similar results in the literature.

Definition 1: [8] A function such that $Q: \mathfrak{I} \rightarrow \mathfrak{R}$, $\mathfrak{I} \subset \mathfrak{R}$ is called convex function if

$$Q(\tau\xi_1 + (1-\tau)\xi_2) \leq \tau Q(\xi_1) + (1-\tau)Q(\xi_2) \quad (2)$$

for all $\xi_1, \xi_2 \in \mathfrak{I}$ and $\tau \in [0,1]$.

In 1966, Polyak introduced the class of strongly convex functions and made a contribution to convex analysis.

Definition 2: [9] A function such that $Q: \mathfrak{I} \rightarrow \mathfrak{R}$, $\mathfrak{I} \subset \mathfrak{R}$ is called strongly convex function with modulus $\rho > 0$, if

$$Q(\tau\xi_1 + (1-\tau)\xi_2) \leq \tau Q(\xi_1) + (1-\tau)Q(\xi_2) - \rho\tau(1-\tau)(\xi_1 - \xi_2)^2 \quad (3)$$

for all $\xi_1, \xi_2 \in \mathfrak{I}$ and $\tau \in [0,1]$.

Definition 3: [9] A function such that $Q: \mathfrak{I} \rightarrow \mathfrak{R}$, $\mathfrak{I} \subset \mathfrak{R}$ is called strongly s -convex function with modulus $\rho > 0$, if

$$Q(\tau\xi_1 + (1-\tau)\xi_2) \leq \tau^s Q(\xi_1) + (1-\tau)^s Q(\xi_2) - \rho\tau(1-\tau)(\xi_1 - \xi_2)^2 \quad (4)$$

for all $\xi_1, \xi_2 \in \mathfrak{I}$ and $\tau \in [0,1]$.

Fractional analysis has become a new field, laying the foundation for solving certain differential equation problems. Studies involving Riemann-Liouville fractional derivatives and integrals have begun, and it remains a popular field with ongoing research today [10,11,12,13]. Depending on the type of problem, there are multiple definitions to obtain the best solution. Grünwald-Letnikov, Weyl, Marchaud, Hadamard, Erdélyi-Kober, Riezs, Chen, Caputo, Osler, Khalil, Fabrizio, Atangana, Baleanu have made significant contributions to this

process. In this study, we will focus on Atangana-Baleanu fractional integrals.

In 2015, Caputo and Fabrizio introduced a new definition for the fractional derivative, which Caputo defined in 1967, in order to eliminate the singularity of the kernel function by using the exponential function. In 2017, Abdeljawad and Baleanu presented the Caputo-Fabrizio fractional integral associated with this fractional derivative as following.

Definition 4: [14] A function such that $Q \in H^1(0, \xi_2)$ is called left and right side of Caputo-Fabrizio fractional integral, if

$$\left({}^{CF}I_{\xi_1}^{\psi}\right)Q(x) = \frac{1-\psi}{B(\psi)}Q(x) + \frac{\psi}{B(\psi)}\int_{\xi_1}^x Q(y)dy \quad (5)$$

and

$$\left({}^{CF}I_{\xi_2}^{\psi}\right)Q(x) = \frac{1-\psi}{B(\psi)}Q(x) + \frac{\psi}{B(\psi)}\int_x^{\xi_2} Q(y)dy \quad (6)$$

where $\xi_2 > \xi_1$, $\psi \in [0,1]$ and $B(\psi)$ is normalization function.

In 2016, Atangana and Baleanu presented a new derivative operator and associated integral operator containing the Mittag-Leffler function in its kernel. The Mittag-Leffler function offers a more reasonable option than a power law in explaining the physical phenomena around us. This has made the Atangana-Baleanu fractional operator more powerful and flexible. Therefore, many researchers have shown great interest in using this operator [15,16,17,18,19].

Definition 5: [20,21] A function such that $Q \in H^1(0, \xi_2)$ is called left and right side of Atangana-Baleanu fractional integral, if

$$\left({}^{AB}I_{\xi_1}^{\psi}\right)Q(x) = \frac{1-\psi}{B(\psi)}Q(x) + \frac{\psi}{B(\psi)\Gamma(\psi)}\int_{\xi_1}^x Q(\tau)(x-\tau)^{\psi-1}d\tau \quad (7)$$

and

$$\left({}^{AB}I_{\xi_2}^{\psi}\right)Q(x) = \frac{1-\psi}{B(\psi)}Q(x) + \frac{\psi}{B(\psi)\Gamma(\psi)}\int_x^{\xi_2} Q(\tau)(\tau-x)^{\psi-1}d\tau \quad (8)$$

where $\xi_2 > \xi_1$, $\psi \in [0,1]$ and $B(\psi)$ is normalization function.

The next section focuses on establishing new Hermite-Hadamard type inequalities for Atangana-Baleanu fractional integrals involving twice differentiable strongly s -convex functions. To obtain these inequalities Hölder,

Power-Mean, Young and Hölder-İşcan inequalities were used.

2. MAIN RESULTS

To prove our main results, we consider the following Lemma given by Set *et al.* in [19].

Lemma 1:[19] $Q: [\xi_1, \xi_2] \rightarrow \mathfrak{R}$ be differentiable mapping on (ξ_1, ξ_2) with $\xi_1 < \xi_2$. Then the following identity is valid for Atangana-Baleanu fractional integral operators

$$\begin{aligned} & \left({}^{AB}I_{\xi_1}^{\psi} \right) Q(x) + \left({}^{AB}I_{\xi_2}^{\psi} \right) Q(x) \\ & - \frac{(x - \xi_1)^{\psi} Q(\xi_1) + (\xi_2 - x)^{\psi} Q(\xi_2)}{B(\psi)\Gamma(\psi)} \\ & - \frac{2(1-\psi)Q(x)}{B(\psi)} \\ & = \frac{(x - \xi_1)^{\psi+1}}{(\psi+1)B(\psi)\Gamma(\psi)} Q'(\xi_1) \\ & + \frac{(x - \xi_1)^{\psi+2}}{(\psi+1)B(\psi)\Gamma(\psi)} \int_0^1 (1-\tau)^{\psi+1} Q''(\tau x + (1-\tau)\xi_1) d\tau \\ & - \frac{(\xi_2 - x)^{\psi+1}}{(\psi+1)B(\psi)\Gamma(\psi)} Q'(\xi_2) \\ & + \frac{(\xi_2 - x)^{\psi+2}}{(\psi+1)B(\psi)\Gamma(\psi)} \int_0^1 \tau^{\psi+1} Q''(\tau \xi_2 + (1-\tau)x) d\tau \end{aligned} \tag{9}$$

where $\psi \in [0,1]$, $x \in [\xi_1, \xi_2]$ and Γ is Gamma function.

Theorem 1: Suppose that $Q: [\xi_1, \xi_2] \rightarrow \mathfrak{R}$ be a twice differentiable mapping on (ξ_1, ξ_2) with $\xi_1 < \xi_2$ and $L[\xi_1, \xi_2]$. If $|Q''|$ is strongly s -convex on $[\xi_1, \xi_2]$, for some $s \in (0,1]$ with modulus $\rho > 0$ then following inequalities hold

$$\begin{aligned} & \left| \left({}^{AB}I_{\xi_1}^{\psi} \right) Q(x) + \left({}^{AB}I_{\xi_2}^{\psi} \right) Q(x) \right. \\ & \left. - \frac{(x - \xi_1)^{\psi} Q(\xi_1) + (\xi_2 - x)^{\psi} Q(\xi_2)}{B(\psi)\Gamma(\psi)} \right| \end{aligned} \tag{10}$$

$$\begin{aligned} & - \frac{(x - \xi_1)^{\psi+1} Q'(\xi_1) - (\xi_2 - x)^{\psi+1} Q'(\xi_2)}{(\psi+1)B(\psi)\Gamma(\psi)} - \frac{2(1-\psi)Q(x)}{B(\psi)} \Big| \\ & \leq \frac{(x - \xi_1)^{\psi+2}}{(\psi+1)B(\psi)\Gamma(\psi)} \\ & \times \left[|Q''(x)|\beta(2+\psi, 1+s) + \frac{|Q''(\xi_1)|}{\psi+s+2} - \frac{\rho(x - \xi_1)^2}{\psi^2 + 7\psi + 12} \right] \\ & + \frac{(\xi_2 - x)^{\psi+2}}{(\psi+1)B(\psi)\Gamma(\psi)} \\ & \times \left[|Q''(x)|\beta(2+\psi, 1+s) + \frac{|Q''(\xi_2)|}{\psi+s+2} - \frac{\rho(\xi_2 - x)^2}{\psi^2 + 7\psi + 12} \right] \end{aligned}$$

where $\psi \in [0,1]$, $x \in [\xi_1, \xi_2]$, Γ is Gamma function and β is Beta function.

Proof: Taking modulus on both sides of Lemma 1, we have

$$\begin{aligned} & \left| \left({}^{AB}I_{\xi_1}^{\psi} \right) Q(x) + \left({}^{AB}I_{\xi_2}^{\psi} \right) Q(x) \right. \\ & \left. - \frac{(x - \xi_1)^{\psi} Q(\xi_1) + (\xi_2 - x)^{\psi} Q(\xi_2)}{B(\psi)\Gamma(\psi)} \right. \\ & \left. - \frac{(x - \xi_1)^{\psi+1} Q'(\xi_1) - (\xi_2 - x)^{\psi+1} Q'(\xi_2)}{(\psi+1)B(\psi)\Gamma(\psi)} - \frac{2(1-\psi)Q(x)}{B(\psi)} \right| \\ & \leq \frac{(x - \xi_1)^{\psi+2}}{(\psi+1)B(\psi)\Gamma(\psi)} \times \int_0^1 (1-\tau)^{\psi+1} |Q''(\tau x + (1-\tau)\xi_1)| d\tau \\ & + \frac{(\xi_2 - x)^{\psi+2}}{(\psi+1)B(\psi)\Gamma(\psi)} \times \int_0^1 \tau^{\psi+1} |Q''(\tau \xi_2 + (1-\tau)x)| d\tau \end{aligned}$$

By using strongly s -convexity of $|Q''|$, it yields

$$\begin{aligned} & \left| \left({}^{AB}I_{\xi_1}^{\psi} \right) Q(x) + \left({}^{AB}I_{\xi_2}^{\psi} \right) Q(x) \right. \\ & \left. - \frac{(x - \xi_1)^{\psi} Q(\xi_1) + (\xi_2 - x)^{\psi} Q(\xi_2)}{B(\psi)\Gamma(\psi)} \right. \\ & \left. - \frac{(x - \xi_1)^{\psi+1} Q'(\xi_1) - (\xi_2 - x)^{\psi+1} Q'(\xi_2)}{(\psi+1)B(\psi)\Gamma(\psi)} - \frac{2(1-\psi)Q(x)}{B(\psi)} \right| \\ & \leq \frac{(x - \xi_1)^{\psi+2}}{(\psi+1)B(\psi)\Gamma(\psi)} \\ & \times \left(\int_0^1 (1-\tau)^{\psi+1} \right) \\ & \times \left(\tau^s |Q''(x)| + (1-t)^s |Q''(\xi_1)| - \rho \tau(1-\tau)(x - \xi_1)^2 \right) d\tau \\ & + \frac{(\xi_2 - x)^{\psi+2}}{(\psi+1)B(\psi)\Gamma(\psi)} \\ & \times \left(\int_0^1 \tau^{\psi+1} \right) \\ & \times \left(\tau^s |Q''(\xi_2)| + (1-t)^s |Q''(x)| - \rho \tau(1-\tau)(\xi_2 - x)^2 \right) d\tau. \end{aligned}$$

By calculating the above integrals, the proof is completed.

Corollary 1: When we choose $s = 1$, Theorem 1 yields the following result for Atangana-Baleanu fractional operator

$$\begin{aligned} & \left| \left({}^{AB}I_{\xi_1}^{\psi} \right) Q(x) + \left({}^{AB}I_{\xi_2}^{\psi} \right) Q(x) \right. \\ & \left. - \frac{(x - \xi_1)^{\psi} Q(\xi_1) + (\xi_2 - x)^{\psi} Q(\xi_2)}{B(\psi)\Gamma(\psi)} \right. \\ & \left. - \frac{(x - \xi_1)^{\psi+1} Q'(\xi_1) - (\xi_2 - x)^{\psi+1} Q'(\xi_2)}{(\psi + 1)B(\psi)\Gamma(\psi)} - \frac{2(1 - \psi)Q(x)}{B(\psi)} \right| \\ & \leq \frac{(x - \xi_1)^{\psi+2}}{(\psi + 1)B(\psi)\Gamma(\psi)} \\ & \times \left[\frac{|Q''(x)|}{(\psi + 2)(\psi + 3)} + \frac{|Q''(\xi_1)|}{\psi + 3} - \frac{\rho(x - \xi_1)^2}{\psi^2 + 7\psi + 12} \right] \\ & + \frac{(\xi_2 - x)^{\psi+2}}{(\psi + 1)B(\psi)\Gamma(\psi)} \\ & \times \left[\frac{|Q''(x)|}{(\psi + 2)(\psi + 3)} + \frac{|Q''(\xi_2)|}{\psi + 3} - \frac{\rho(\xi_2 - x)^2}{\psi^2 + 7\psi + 12} \right]. \end{aligned} \tag{11}$$

Corollary 2: In Theorem 1, if we choose $x = \frac{\xi_1 + \xi_2}{2}$, we have

$$\begin{aligned} & \left| \left({}^{AB}I_{\xi_1}^{\psi} \right) Q\left(\frac{\xi_1 + \xi_2}{2}\right) + \left({}^{AB}I_{\xi_2}^{\psi} \right) Q\left(\frac{\xi_1 + \xi_2}{2}\right) \right. \\ & \left. - \frac{(\xi_2 - \xi_1)^{\psi}}{2^{\psi} B(\psi)\Gamma(\psi)} (Q(\xi_1) + Q(\xi_2)) \right. \\ & \left. - \frac{(\xi_2 - \xi_1)^{\psi+1}}{2^{\psi+1} (\psi + 1)B(\psi)\Gamma(\psi)} (Q'(\xi_1) - Q'(\xi_2)) \right. \\ & \left. - \frac{2(1 - \psi)Q\left(\frac{\xi_1 + \xi_2}{2}\right)}{B(\psi)} \right| \\ & \leq \frac{(\xi_2 - \xi_1)^{\psi+2}}{2^{\psi+2} (\psi + 1)B(\psi)\Gamma(\psi)} \\ & \times \left[2 \left| Q''\left(\frac{\xi_1 + \xi_2}{2}\right) \right| \beta(2 + \psi, 1 + s) \right. \\ & \left. + \frac{|Q''(\xi_1)| + |Q''(\xi_2)|}{\psi + s + 2} - \frac{\rho\left(\frac{\xi_2 - \xi_1}{2}\right)^2}{2(\psi^2 + 7\psi + 12)} \right] \end{aligned} \tag{12}$$

Theorem 2: Suppose that $Q: [\xi_1, \xi_2] \rightarrow \mathfrak{R}$ be a twice differentiable mapping on (ξ_1, ξ_2) with $\xi_1 < \xi_2$ and

$L[\xi_1, \xi_2]$. If $|Q''|^{\eta}$ is strongly s -convex on $[\xi_1, \xi_2]$, for some $s \in (0, 1]$ with modulus $\rho > 0$ then following inequalities hold,

$$\begin{aligned} & \left| \left({}^{AB}I_{\xi_1}^{\psi} \right) Q(x) + \left({}^{AB}I_{\xi_2}^{\psi} \right) Q(x) \right. \\ & \left. - \frac{(x - \xi_1)^{\psi} Q(\xi_1) + (\xi_2 - x)^{\psi} Q(\xi_2)}{B(\psi)\Gamma(\psi)} \right. \\ & \left. - \frac{(x - \xi_1)^{\psi+1} Q'(\xi_1) - (\xi_2 - x)^{\psi+1} Q'(\xi_2)}{(\psi + 1)B(\psi)\Gamma(\psi)} - \frac{2(1 - \psi)Q(x)}{B(\psi)} \right| \\ & \leq \frac{(x - \xi_1)^{\psi+2}}{(\psi + 1)B(\psi)\Gamma(\psi)} \\ & \times \left[\left(\frac{1}{\psi\mu + \mu + 1} \right)^{\frac{1}{\mu}} \right. \\ & \times \left(\frac{1}{s + 1} \left(|Q''(x)|^{\eta} + |Q''(\xi_1)|^{\eta} - \frac{\rho(x - \xi_1)^2}{6} \right)^{\frac{1}{\eta}} \right) \\ & \left. + \frac{(\xi_2 - x)^{\psi+2}}{(\psi + 1)B(\psi)\Gamma(\psi)} \right. \\ & \times \left[\left(\frac{1}{\psi\mu + \mu + 1} \right)^{\frac{1}{\mu}} \right. \\ & \times \left(\frac{1}{s + 1} \left(|Q''(x)|^{\eta} + |Q''(\xi_2)|^{\eta} - \frac{\rho(\xi_2 - x)^2}{6} \right)^{\frac{1}{\eta}} \right) \end{aligned} \tag{13}$$

where $\psi \in [0, 1]$, $x \in [\xi_1, \xi_2]$, $\mu^{-1} + \eta^{-1} = 1$, $\eta > 1$, Γ is Gamma function and β is Beta function.

Proof: From Lemma 1 and applying Hölder inequality, we have

$$\begin{aligned} & \left| \left({}^{AB}I_{\xi_1}^{\psi} \right) Q(x) + \left({}^{AB}I_{\xi_2}^{\psi} \right) Q(x) \right. \\ & \left. - \frac{(x - \xi_1)^{\psi} Q(\xi_1) + (\xi_2 - x)^{\psi} Q(\xi_2)}{B(\psi)\Gamma(\psi)} \right. \\ & \left. - \frac{(x - \xi_1)^{\psi+1} Q'(\xi_1) - (\xi_2 - x)^{\psi+1} Q'(\xi_2)}{(\psi + 1)B(\psi)\Gamma(\psi)} - \frac{2(1 - \psi)Q(x)}{B(\psi)} \right| \end{aligned}$$

$$\begin{aligned} &\leq \frac{(x - \xi_1)^{\psi+2}}{(\psi+1)B(\psi)\Gamma(\psi)} \\ &\times \int_0^1 (1-\tau)^{\psi+1} |Q''(\tau x + (1-\tau)\xi_1)| d\tau \\ &+ \frac{(\xi_2 - x)^{\psi+2}}{(\psi+1)B(\psi)\Gamma(\psi)} \\ &\times \int_0^1 \tau^{\psi+1} |Q''(\tau\xi_2 + (1-\tau)x)| d\tau \\ &\leq \frac{(x - \xi_1)^{\psi+2}}{(\psi+1)B(\psi)\Gamma(\psi)} \\ &\times \left[\left(\int_0^1 (1-\tau)^{(\psi+1)\mu} d\tau \right)^{\frac{1}{\mu}} \left(\int_0^1 |Q''(\tau x + (1-\tau)\xi_1)|^\eta d\tau \right)^{\frac{1}{\eta}} \right] \\ &+ \frac{(\xi_2 - x)^{\psi+2}}{(\psi+1)B(\psi)\Gamma(\psi)} \\ &\times \left[\left(\int_0^1 \tau^{(\psi+1)\mu} d\tau \right)^{\frac{1}{\mu}} \left(\int_0^1 |Q''(\tau\xi_2 + (1-\tau)x)|^\eta d\tau \right)^{\frac{1}{\eta}} \right]. \end{aligned}$$

Using strongly $s -$ convexity, we conclude

$$\begin{aligned} &\int_0^1 |Q''(\tau x + (1-\tau)\xi_1)|^\eta d\tau \\ &\leq \frac{|Q''(x)|^\eta + |Q''(\xi_1)|^\eta}{s+1} - \frac{\rho(x - \xi_1)^2}{6} \\ &\int_0^1 |Q''(\tau\xi_2 + (1-\tau)x)|^\eta d\tau \\ &\leq \frac{|Q''(x)|^\eta + |Q''(\xi_2)|^\eta}{s+1} - \frac{\rho(\xi_2 - x)^2}{6}. \end{aligned}$$

By a simple computation, we get desired result.

Corollary 3: Under the assumption of Theorem 2 with $s = 1$, we obtain

$$\begin{aligned} &\left| \left({}^{AB}I_\psi^\psi \right) Q(x) + \left({}^{AB}I_{\xi_2}^\psi \right) Q(x) \right. \\ &\quad - \frac{(x - \xi_1)^\psi Q(\xi_1) + (\xi_2 - x)^\psi Q(\xi_2)}{B(\psi)\Gamma(\psi)} \\ &\quad - \frac{(x - \xi_1)^{\psi+1} Q'(\xi_1) - (\xi_2 - x)^{\psi+1} Q'(\xi_2)}{(\psi+1)B(\psi)\Gamma(\psi)} \\ &\quad \left. - \frac{2(1-\psi)Q(x)}{B(\psi)} \right| \\ &\leq \frac{(x - \xi_1)^{\psi+2}}{(\psi+1)B(\psi)\Gamma(\psi)} \\ &\times \left[\left(\frac{1}{\psi\mu + \mu + 1} \right)^{\frac{1}{\mu}} \left(\frac{|Q''(x)|^\eta + |Q''(\xi_1)|^\eta}{2} - \frac{\rho(x - \xi_1)^2}{6} \right)^{\frac{1}{\eta}} \right] \end{aligned} \tag{14}$$

$$\begin{aligned} &+ \frac{(\xi_2 - x)^{\psi+2}}{(\psi+1)B(\psi)\Gamma(\psi)} \\ &\times \left[\left(\frac{1}{\psi\mu + \mu + 1} \right)^{\frac{1}{\mu}} \left(\frac{|Q''(x)|^\eta + |Q''(\xi_2)|^\eta}{2} - \frac{\rho(\xi_2 - x)^2}{6} \right)^{\frac{1}{\eta}} \right]. \end{aligned}$$

Corollary 4: In Theorem 2, by setting $x = \frac{\xi_1 + \xi_2}{2}$, we get

$$\begin{aligned} &\left| \left({}^{AB}I_{\xi_1}^\psi \right) Q\left(\frac{\xi_1 + \xi_2}{2}\right) + \left({}^{AB}I_{\xi_2}^\psi \right) Q\left(\frac{\xi_1 + \xi_2}{2}\right) \right. \\ &\quad - \frac{(\xi_2 - \xi_1)^\psi}{2^\psi B(\psi)\Gamma(\psi)} (Q(\xi_1) + Q(\xi_2)) \\ &\quad - \frac{(\xi_2 - \xi_1)^{\psi+1}}{2^{\psi+1}(\psi+1)B(\psi)\Gamma(\psi)} (Q'(\xi_1) - Q'(\xi_2)) \\ &\quad \left. - \frac{2(1-\psi)Q\left(\frac{\xi_1 + \xi_2}{2}\right)}{B(\psi)} \right| \\ &\leq \frac{(\xi_2 - \xi_1)^{\psi+2}}{2^{\psi+2}(\psi+1)B(\psi)\Gamma(\psi)} \times \left(\frac{1}{\psi\mu + \mu + 1} \right)^{\frac{1}{\mu}} \\ &\times \left[\left(\frac{1}{s+1} \left(|Q''\left(\frac{\xi_1 + \xi_2}{2}\right)|^\eta + |Q''(\xi_1)|^\eta \right) - \frac{\rho(\xi_2 - \xi_1)^2}{24} \right)^{\frac{1}{\eta}} \right. \\ &\quad \left. + \left(\frac{1}{s+1} \left(|Q''\left(\frac{\xi_1 + \xi_2}{2}\right)|^\eta + |Q''(\xi_2)|^\eta \right) - \frac{\rho(\xi_2 - \xi_1)^2}{24} \right)^{\frac{1}{\eta}} \right]. \end{aligned} \tag{15}$$

Theorem 3: Suppose that $Q: [\xi_1, \xi_2] \rightarrow \mathfrak{R}$ be a twice differentiable mapping on (ξ_1, ξ_2) with $\xi_1 < \xi_2$ and $L[\xi_1, \xi_2]$. If $|Q''|^\eta$ is strongly $s -$ convex on $[\xi_1, \xi_2]$, for some $s \in (0, 1]$ with modulus $\rho > 0$ then following inequalities hold,

$$\begin{aligned} &\left| \left({}^{AB}I_\psi^\psi \right) Q(x) + \left({}^{AB}I_{\xi_2}^\psi \right) Q(x) \right. \\ &\quad - \frac{(x - \xi_1)^\psi Q(\xi_1) + (\xi_2 - x)^\psi Q(\xi_2)}{B(\psi)\Gamma(\psi)} \end{aligned} \tag{16}$$

$$\begin{aligned} & \left| \frac{(x-\xi_1)^{\psi+1} Q'(\xi_1) - (\xi_2-x)^{\psi+1} Q'(\xi_2)}{(\psi+1)B(\psi)\Gamma(\psi)} - \frac{2(1-\psi)Q(x)}{B(\psi)} \right| \\ & \leq \frac{(x-\xi_1)^{\psi+2}}{(\psi+1)B(\psi)\Gamma(\psi)} \left(\frac{\eta-1}{\eta(\psi+2)-\mu(\psi+1)-1} \right)^{1-\frac{1}{\eta}} \\ & \quad \times \left[|Q''(x)|^\eta \beta(1+s, 1+\mu+\psi\mu) + \frac{|Q''(\xi_1)|^\eta}{1+s+\mu+\psi\mu} \right. \\ & \quad \left. - \frac{\rho(x-\xi_1)^2}{(2+\mu+\psi\mu)(3+\mu+\psi\mu)} \right]^{\frac{1}{\eta}} \\ & + \frac{(\xi_2-x)^{\psi+2}}{(\psi+1)B(\psi)\Gamma(\psi)} \left(\frac{\eta-1}{\eta(\psi+2)-\mu(\psi+1)-1} \right)^{1-\frac{1}{\eta}} \\ & \quad \times \left[|Q''(x)|^\eta \beta(1+s, 1+\mu+\psi\mu) + \frac{|Q''(\xi_2)|^\eta}{1+s+\mu+\psi\mu} \right. \\ & \quad \left. - \frac{\rho(\xi_2-x)^2}{(2+\mu+\psi\mu)(3+\mu+\psi\mu)} \right]^{\frac{1}{\eta}} \end{aligned}$$

where $\psi \in [0,1]$, $x \in [\xi_1, \xi_2]$, $\mu^{-1} + \eta^{-1} = 1$, $\eta \geq \mu > 1$, Γ is Gamma function and β is Beta function.

Proof: From Lemma 1 and applying Hölder inequality, we have

$$\begin{aligned} & \left| \left({}^{AB}I_{\xi_1}^\psi \right) Q(x) + \left({}^{AB}I_{\xi_2}^\psi \right) Q(x) \right. \\ & \quad \left. - \frac{(x-\xi_1)^\psi Q(\xi_1) + (\xi_2-x)^\psi Q(\xi_2)}{B(\psi)\Gamma(\psi)} \right. \\ & \quad \left. - \frac{(x-\xi_1)^{\psi+1} Q'(\xi_1) - (\xi_2-x)^{\psi+1} Q'(\xi_2)}{(\psi+1)B(\psi)\Gamma(\psi)} \right. \\ & \quad \left. - \frac{2(1-\psi)Q(x)}{B(\psi)} \right| \\ & \leq \frac{(x-\xi_1)^{\psi+2}}{(\psi+1)B(\psi)\Gamma(\psi)} \times \int_0^1 (1-\tau)^{\psi+1} |Q''(\tau x + (1-\tau)\xi_1)| d\tau \\ & \quad + \frac{(\xi_2-x)^{\psi+2}}{(\psi+1)B(\psi)\Gamma(\psi)} \times \int_0^1 \tau^{\psi+1} |Q''(\tau\xi_2 + (1-\tau)x)| d\tau \\ & \leq \frac{(x-\xi_1)^{\psi+2}}{(\psi+1)B(\psi)\Gamma(\psi)} \\ & \quad \times \left[\left(\int_0^1 (1-\tau)^{(\psi+1)\left(\frac{\eta-\mu}{\eta-1}\right)} d\tau \right)^{1-\frac{1}{\eta}} \right. \\ & \quad \left. \times \left(\int_0^1 (1-\tau)^{(\psi+1)\mu} |Q''(\tau x + (1-\tau)\xi_1)|^\eta d\tau \right)^{\frac{1}{\eta}} \right] \end{aligned}$$

$$\begin{aligned} & + \frac{(\xi_2-x)^{\psi+2}}{(\psi+1)B(\psi)\Gamma(\psi)} \times \left[\left(\int_0^1 \tau^{(\psi+1)\left(\frac{\eta-\mu}{\eta-1}\right)} d\tau \right)^{1-\frac{1}{\eta}} \right. \\ & \quad \left. \times \left(\int_0^1 \tau^{(\psi+1)\mu} |Q''(\tau\xi_2 + (1-\tau)x)|^\eta d\tau \right)^{\frac{1}{\eta}} \right]. \end{aligned}$$

By using strongly s -convexity of $|Q''|^\eta$ and by simple computation, the proof is completed.

Corollary 5: Under the assumption of Theorem 3 with $s = 1$, we obtain

$$\begin{aligned} & \left| \left({}^{AB}I_{\xi_1}^\psi \right) Q(x) + \left({}^{AB}I_{\xi_2}^\psi \right) Q(x) \right. \\ & \quad \left. - \frac{(x-\xi_1)^\psi Q(\xi_1) + (\xi_2-x)^\psi Q(\xi_2)}{B(\psi)\Gamma(\psi)} \right. \\ & \quad \left. - \frac{(x-\xi_1)^{\psi+1} Q'(\xi_1) - (\xi_2-x)^{\psi+1} Q'(\xi_2)}{(\psi+1)B(\psi)\Gamma(\psi)} \right. \\ & \quad \left. - \frac{2(1-\psi)Q(x)}{B(\psi)} \right| \\ & \leq \frac{(x-\xi_1)^{\psi+2}}{(\psi+1)B(\psi)\Gamma(\psi)} \left(\frac{\eta-1}{\eta(\psi+2)-\mu(\psi+1)-1} \right)^{1-\frac{1}{\eta}} \\ & \quad \times \left[|Q''(x)|^\eta \beta(2, 1+\mu+\psi\mu) + \frac{|Q''(\xi_1)|^\eta}{2+\mu+\psi\mu} \right. \\ & \quad \left. - \frac{\rho(x-\xi_1)^2}{(2+\mu+\psi\mu)(3+\mu+\psi\mu)} \right]^{\frac{1}{\eta}} \\ & \quad + \frac{(\xi_2-x)^{\psi+2}}{(\psi+1)B(\psi)\Gamma(\psi)} \left(\frac{\eta-1}{\eta(\psi+2)-\mu(\psi+1)-1} \right)^{1-\frac{1}{\eta}} \\ & \quad \times \left[|Q''(x)|^\eta \beta(2, 1+\mu+\psi\mu) + \frac{|Q''(\xi_2)|^\eta}{2+\mu+\psi\mu} \right. \\ & \quad \left. - \frac{\rho(\xi_2-x)^2}{(2+\mu+\psi\mu)(3+\mu+\psi\mu)} \right]^{\frac{1}{\eta}}. \end{aligned} \tag{17}$$

Corollary 6: In Theorem 3, by setting $x = \frac{\xi_1 + \xi_2}{2}$, we get

$$\begin{aligned} & \left| \left({}^{AB}I_{\xi_1}^\psi \right) Q\left(\frac{\xi_1 + \xi_2}{2}\right) + \left({}^{AB}I_{\xi_2}^\psi \right) Q\left(\frac{\xi_1 + \xi_2}{2}\right) \right. \\ & \quad \left. - \frac{(\xi_2 - \xi_1)^\psi}{2^\psi B(\psi)\Gamma(\psi)} (Q(\xi_1) + Q(\xi_2)) \right| \end{aligned} \tag{18}$$

$$\begin{aligned} & \frac{(\xi_2 - \xi_1)^{\psi+1}}{2^{\psi+1}(\psi+1)B(\psi)\Gamma(\psi)}(Q'(\xi_1) - Q'(\xi_2)) \\ & \left| \frac{2(1-\psi)Q\left(\frac{\xi_1 + \xi_2}{2}\right)}{B(\psi)} \right| \\ & \leq \frac{(\xi_2 - \xi_1)^{\psi+2}}{2^{\psi+2}(\psi+1)B(\psi)\Gamma(\psi)} \left(\frac{\eta-1}{\eta(\psi+2) - \mu(\psi+1) - 1} \right)^{1-\frac{1}{\eta}} \\ & \times \left[\left(\left| Q''\left(\frac{\xi_1 + \xi_2}{2}\right) \right|^{\eta} \beta(1+s, 1+\mu+\psi\mu) \right. \right. \\ & \left. \left. + \frac{|Q''(\xi_1)|^{\eta}}{1+s+\mu+\psi\mu} - \frac{\rho(\xi_2 - \xi_1)^2}{(2+\mu+\psi\mu)(3+\mu+\psi\mu)} \right)^{\frac{1}{\eta}} \right. \\ & \left. + \left(\left| Q''\left(\frac{\xi_1 + \xi_2}{2}\right) \right|^{\eta} \beta(1+s, 1+\mu+\psi\mu) \right. \right. \\ & \left. \left. + \frac{|Q''(\xi_2)|^{\eta}}{1+s+\mu+\psi\mu} - \frac{\rho(\xi_2 - \xi_1)^2}{(2+\mu+\psi\mu)(3+\mu+\psi\mu)} \right)^{\frac{1}{\eta}} \right]. \end{aligned}$$

Theorem 4: Suppose that $Q: [\xi_1, \xi_2] \rightarrow \mathfrak{R}$ be a twice differentiable mapping on (ξ_1, ξ_2) with $\xi_1 < \xi_2$ and $L[\xi_1, \xi_2]$. If $|Q''|^{\eta}$ is strongly s -convex on $[\xi_1, \xi_2]$, for some $s \in (0, 1]$ with modulus $\rho > 0$ then following inequalities hold,

$$\begin{aligned} & \left| \left({}^{AB}I_{\xi_1}^{\psi} \right) Q(x) + \left({}^{AB}I_{\xi_2}^{\psi} \right) Q(x) \right. \\ & \left. - \frac{(x - \xi_1)^{\psi} Q(\xi_1) + (\xi_2 - x)^{\psi} Q(\xi_2)}{B(\psi)\Gamma(\psi)} \right. \\ & \left. - \frac{(x - \xi_1)^{\psi+1} Q'(\xi_1) - (\xi_2 - x)^{\psi+1} Q'(\xi_2)}{(\psi+1)B(\psi)\Gamma(\psi)} \right. \\ & \left. - \frac{2(1-\psi)Q(x)}{B(\psi)} \right| \\ & \leq \frac{(x - \xi_1)^{\psi+2}}{(\psi+1)B(\psi)\Gamma(\psi)} \left(\frac{1}{\psi+2} \right)^{\frac{1}{\mu}} \\ & \times \left(\left| Q''(x) \right|^{\eta} \beta(1+s, 2+\psi) + \frac{|Q''(\xi_1)|^{\eta}}{\psi+s+2} - \frac{\rho(x - \xi_1)^2}{\psi^2 + 7\psi + 12} \right)^{\frac{1}{\eta}} \\ & + \frac{(\xi_2 - x)^{\psi+2}}{(\psi+1)B(\psi)\Gamma(\psi)} \left(\frac{1}{\psi+2} \right)^{\frac{1}{\mu}} \\ & \times \left(\left| Q''(x) \right|^{\eta} \beta(1+s, 2+\psi) + \frac{|Q''(\xi_2)|^{\eta}}{\psi+s+2} - \frac{\rho(\xi_2 - x)^2}{\psi^2 + 7\psi + 12} \right)^{\frac{1}{\eta}} \end{aligned} \tag{19}$$

where $\psi \in [0, 1]$, $x \in [\xi_1, \xi_2]$, $\eta \geq 1$, Γ is Gamma function and β is Beta function.

Proof: From Lemma 1 and using the power mean inequality, we obtain

$$\begin{aligned} & \left| \left({}^{AB}I_{\xi_1}^{\psi} \right) Q(x) + \left({}^{AB}I_{\xi_2}^{\psi} \right) Q(x) \right. \\ & \left. - \frac{(x - \xi_1)^{\psi} Q(\xi_1) + (\xi_2 - x)^{\psi} Q(\xi_2)}{B(\psi)\Gamma(\psi)} \right. \\ & \left. - \frac{(x - \xi_1)^{\psi+1} Q'(\xi_1) - (\xi_2 - x)^{\psi+1} Q'(\xi_2)}{(\psi+1)B(\psi)\Gamma(\psi)} \right. \\ & \left. - \frac{2(1-\psi)Q(x)}{B(\psi)} \right| \\ & \leq \frac{(x - \xi_1)^{\psi+2}}{(\psi+1)B(\psi)\Gamma(\psi)} \times \int_0^1 (1-\tau)^{\psi+1} \left| Q''(\tau x + (1-\tau)\xi_1) \right| d\tau \\ & + \frac{(\xi_2 - x)^{\psi+2}}{(\psi+1)B(\psi)\Gamma(\psi)} \times \int_0^1 \tau^{\psi+1} \left| Q''(\tau \xi_2 + (1-\tau)x) \right| d\tau \\ & \leq \frac{(x - \xi_1)^{\psi+2}}{(\psi+1)B(\psi)\Gamma(\psi)} \\ & \times \left[\left(\int_0^1 (1-\tau)^{(\psi+1)} d\tau \right)^{\frac{1}{\mu}} \right. \\ & \times \left. \left(\int_0^1 (1-\tau)^{(\psi+1)} \left| Q''(\tau x + (1-\tau)\xi_1) \right|^{\eta} d\tau \right)^{\frac{1}{\eta}} \right] \\ & + \frac{(\xi_2 - x)^{\psi+2}}{(\psi+1)B(\psi)\Gamma(\psi)} \\ & \times \left[\left(\int_0^1 \tau^{(\psi+1)} d\tau \right)^{\frac{1}{\mu}} \left(\int_0^1 \tau^{(\psi+1)} \left| Q''(\tau \xi_2 + (1-\tau)x) \right|^{\eta} d\tau \right)^{\frac{1}{\eta}} \right]. \end{aligned}$$

Since $|Q''|^{\eta}$ is strongly s -convex, by a simple computation, we have

$$\begin{aligned} & \left| \left({}^{AB}I_{\xi_1}^{\psi} \right) Q(x) + \left({}^{AB}I_{\xi_2}^{\psi} \right) Q(x) \right. \\ & \left. - \frac{(x - \xi_1)^{\psi} Q(\xi_1) + (\xi_2 - x)^{\psi} Q(\xi_2)}{B(\psi)\Gamma(\psi)} \right. \\ & \left. - \frac{(x - \xi_1)^{\psi+1} Q'(\xi_1) - (\xi_2 - x)^{\psi+1} Q'(\xi_2)}{(\psi+1)B(\psi)\Gamma(\psi)} \right. \\ & \left. - \frac{2(1-\psi)Q(x)}{B(\psi)} \right| \\ & \leq \frac{(x - \xi_1)^{\psi+2}}{(\psi+1)B(\psi)\Gamma(\psi)} \\ & \times \left[\left(\int_0^1 (1-\tau)^{(\psi+1)} d\tau \right)^{\frac{1}{\mu}} \times \left(\int_0^1 (1-\tau)^{(\psi+1)} \right. \right. \end{aligned}$$

$$\begin{aligned} & \times \left(\tau^s |Q''(x)|^\eta + (1-\tau)^s |Q''(\xi_1)|^\eta - \rho\tau(1-\tau)(x-\xi_1)^2 \right) d\tau \Bigg]^{\frac{1}{\eta}} \\ & + \frac{(\xi_2-x)^{\psi+2}}{(\psi+1)B(\psi)\Gamma(\psi)} \\ & \times \left[\left(\int_0^1 (\tau)^{(\psi+1)} d\tau \right)^{\frac{1}{\mu}} \times \left(\int_0^1 (\tau)^{(\psi+1)} \right. \right. \\ & \times \left. \left. \left(\tau^s |Q''(\xi_2)|^\eta + (1-\tau)^s |Q''(x)|^\eta - \rho\tau(1-\tau)(\xi_2-x)^2 \right) d\tau \right)^{\frac{1}{\eta}} \right] \\ & \leq \frac{(\xi_2-\xi_1)^{\psi+2}}{2^{\psi+2}(\psi+1)B(\psi)\Gamma(\psi)} \times \left(\frac{1}{\psi+1} \right)^{\frac{1}{\mu}} \\ & \times \left[\left(\left| Q'' \left(\frac{\xi_1+\xi_2}{2} \right) \right|^\eta \beta(1+s, 2+\psi) \right. \right. \\ & \left. \left. + \frac{|Q''(\xi_1)|^\eta}{\psi+s+2} - \frac{\rho(\xi_2-\xi_1)^2}{4(\xi^2+7\xi+12)} \right)^{\frac{1}{\eta}} \right. \\ & \left. + \left(\left| Q'' \left(\frac{\xi_1+\xi_2}{2} \right) \right|^\eta \beta(1+s, 2+\psi) \right. \right. \\ & \left. \left. + \frac{|Q''(\xi_2)|^\eta}{\psi+s+2} - \frac{\rho(\xi_2-\xi_1)^2}{4(\xi^2+7\xi+12)} \right)^{\frac{1}{\eta}} \right]. \end{aligned}$$

This completes the proof.

Corollary 7: Under the assumption of Theorem 4 with $s = 1$, we obtain

$$\begin{aligned} & \left| \left({}^{AB}I_{\xi_1}^\psi \right) Q(x) + \left({}^{AB}I_{\xi_2}^\psi \right) Q(x) \right. \\ & \left. - \frac{(x-\xi_1)^\psi Q(\xi_1) + (\xi_2-x)^\psi Q(\xi_2)}{B(\psi)\Gamma(\psi)} \right. \\ & \left. - \frac{(x-\xi_1)^{\psi+1} Q'(\xi_1) - (\xi_2-x)^{\psi+1} Q'(\xi_2)}{(\psi+1)B(\psi)\Gamma(\psi)} \right. \\ & \left. - \frac{2(1-\psi)Q(x)}{B(\psi)} \right| \\ & \leq \frac{(x-\xi_1)^{\psi+2}}{(\psi+1)B(\psi)\Gamma(\psi)} \left(\frac{1}{\psi+2} \right)^{\frac{1}{\mu}} \\ & \times \left(\frac{|Q''(x)|^\eta}{(\psi+2)(\psi+3)} + \frac{|Q''(\xi_1)|^\eta}{\psi+3} - \frac{\rho(x-\xi_1)^2}{\psi^2+7\psi+12} \right)^{\frac{1}{\eta}} \\ & + \frac{(\xi_2-x)^{\psi+2}}{(\psi+1)B(\psi)\Gamma(\psi)} \left(\frac{1}{\psi+2} \right)^{\frac{1}{\mu}} \\ & \times \left(\frac{|Q''(x)|^\eta}{(\psi+2)(\psi+3)} + \frac{|Q''(\xi_2)|^\eta}{\psi+3} - \frac{\rho(\xi_2-x)^2}{\psi^2+7\psi+12} \right)^{\frac{1}{\eta}}. \end{aligned} \tag{20}$$

Corollary 8: In Theorem 4, if we choose $x = \frac{\xi_1+\xi_2}{2}$, we have

$$\begin{aligned} & \left| \left({}^{AB}I_{\xi_1}^\psi \right) Q \left(\frac{\xi_1+\xi_2}{2} \right) + \left({}^{AB}I_{\xi_2}^\psi \right) Q \left(\frac{\xi_1+\xi_2}{2} \right) \right. \\ & \left. - \frac{(\xi_2-\xi_1)^\psi}{2^\psi B(\psi)\Gamma(\psi)} (Q(\xi_1) + Q(\xi_2)) \right. \\ & \left. - \frac{(\xi_2-\xi_1)^{\psi+1}}{2^{\psi+1}(\psi+1)B(\psi)\Gamma(\psi)} (Q'(\xi_1) - Q'(\xi_2)) \right. \\ & \left. - \frac{2(1-\psi)Q \left(\frac{\xi_1+\xi_2}{2} \right)}{B(\psi)} \right| \end{aligned} \tag{21}$$

Theorem 5: Suppose that $Q: [\xi_1, \xi_2] \rightarrow \mathfrak{R}$ be a twice differentiable mapping on (ξ_1, ξ_2) with $\xi_1 < \xi_2$ and $L[\xi_1, \xi_2]$. If $|Q''|^\eta$ is strongly s -convex on $[\xi_1, \xi_2]$, for some $s \in (0, 1]$ with modulus $\rho > 0$ then following inequalities hold,

$$\begin{aligned} & \left| \left({}^{AB}I_{\xi_1}^\psi \right) Q(x) + \left({}^{AB}I_{\xi_2}^\psi \right) Q(x) \right. \\ & \left. - \frac{(x-\xi_1)^\psi Q(\xi_1) + (\xi_2-x)^\psi Q(\xi_2)}{B(\psi)\Gamma(\psi)} \right. \\ & \left. - \frac{(x-\xi_1)^{\psi+1} Q'(\xi_1) - (\xi_2-x)^{\psi+1} Q'(\xi_2)}{(\psi+1)B(\psi)\Gamma(\psi)} \right. \\ & \left. - \frac{2(1-\psi)Q(x)}{B(\psi)} \right| \\ & \leq \frac{(x-\xi_1)^{\psi+2}}{(\psi+1)B(\psi)\Gamma(\psi)} \left[\left(\frac{1}{\mu(\psi\mu+\mu+1)} \right) \right. \\ & \left. + \frac{1}{\eta} \left(\frac{1}{s+1} (|Q''(x)|^\eta + |Q''(\xi_1)|^\eta) - \frac{\rho(x-\xi_1)^2}{6} \right) \right] \\ & + \frac{(\xi_2-x)^{\psi+2}}{(\psi+1)B(\psi)\Gamma(\psi)} \left[\left(\frac{1}{\mu(\psi\mu+\mu+1)} \right) \right. \\ & \left. + \frac{1}{\eta} \left(\frac{1}{s+1} (|Q''(x)|^\eta + |Q''(\xi_2)|^\eta) - \frac{\rho(\xi_2-x)^2}{6} \right) \right] \end{aligned} \tag{22}$$

where $\psi \in [0, 1]$, $x \in [\xi_1, \xi_2]$, $\mu^{-1} + \eta^{-1} = 1$, $\eta > 1$, Γ is Gamma function and β is Beta function.

Proof: By using Lemma 1 and Young inequality, we obtain

$$\begin{aligned} & \left| \left({}^{AB}I_{\xi_1}^\psi \right) Q(x) + \left({}^{AB}I_{\xi_2}^\psi \right) Q(x) \right. \\ & \left. - \frac{(x-\xi_1)^\psi Q(\xi_1) + (\xi_2-x)^\psi Q(\xi_2)}{B(\psi)\Gamma(\psi)} \right. \\ & \left. - \frac{(x-\xi_1)^{\psi+1} Q'(\xi_1) - (\xi_2-x)^{\psi+1} Q'(\xi_2)}{(\psi+1)B(\psi)\Gamma(\psi)} \right. \\ & \left. - \frac{2(1-\psi)Q(x)}{B(\psi)} \right| \\ & \leq \frac{(x-\xi_1)^{\psi+2}}{(\psi+1)B(\psi)\Gamma(\psi)} \times \int_0^1 (1-\tau)^{\psi+1} |Q''(\tau x + (1-\tau)\xi_1)| d\tau \\ & + \frac{(\xi_2-x)^{\psi+2}}{(\psi+1)B(\psi)\Gamma(\psi)} \times \int_0^1 \tau^{\psi+1} |Q''(\tau\xi_2 + (1-\tau)x)| d\tau \\ & \leq \frac{(x-\xi_1)^{\psi+2}}{(\psi+1)B(\psi)\Gamma(\psi)} \\ & \times \left[\frac{1}{\mu} \left(\int_0^1 (1-\tau)^{(\psi+1)\mu} d\tau \right) + \frac{1}{\eta} \left(\int_0^1 |Q''(\tau x + (1-\tau)\xi_1)|^\eta d\tau \right) \right] \\ & + \frac{(\xi_2-x)^{\psi+2}}{(\psi+1)B(\psi)\Gamma(\psi)} \\ & \times \left[\frac{1}{\mu} \left(\int_0^1 \tau^{(\psi+1)\mu} d\tau \right) + \frac{1}{\eta} \left(\int_0^1 |Q''(\tau\xi_2 + (1-\tau)x)|^\eta d\tau \right) \right]. \end{aligned}$$

By using strongly s -convexity of $|Q''|^\eta$ and by simple computation, the proof is completed.

Corollary 9: Under the assumption of Theorem 5 with $s = 1$, we obtain

$$\begin{aligned} & \left| \left({}^{AB}I_{\xi_1}^\psi \right) Q(x) + \left({}^{AB}I_{\xi_2}^\psi \right) Q(x) \right. \tag{23} \\ & \left. - \frac{(x-\xi_1)^\psi Q(\xi_1) + (\xi_2-x)^\psi Q(\xi_2)}{B(\psi)\Gamma(\psi)} \right. \\ & \left. - \frac{(x-\xi_1)^{\psi+1} Q'(\xi_1) - (\xi_2-x)^{\psi+1} Q'(\xi_2)}{(\psi+1)B(\psi)\Gamma(\psi)} \right. \\ & \left. - \frac{2(1-\psi)Q(x)}{B(\psi)} \right| \\ & \leq \frac{(x-\xi_1)^{\psi+2}}{(\psi+1)B(\psi)\Gamma(\psi)} \\ & \times \left[\left(\frac{1}{\mu(\psi\mu + \mu + 1)} \right) + \frac{(|Q''(x)|^\eta + |Q''(\xi_1)|^\eta)}{2\eta} - \frac{\rho(x-\xi_1)^2}{6\eta} \right] \\ & + \frac{(\xi_2-x)^{\psi+2}}{(\psi+1)B(\psi)\Gamma(\psi)} \\ & \times \left[\left(\frac{1}{\mu(\psi\mu + \mu + 1)} \right) + \frac{(|Q''(x)|^\eta + |Q''(\xi_2)|^\eta)}{2\eta} - \frac{\rho(\xi_2-x)^2}{6\eta} \right]. \end{aligned}$$

Corollary 10: In Theorem 5, by setting $x = \frac{\xi_1 + \xi_2}{2}$, we get

$$\begin{aligned} & \left| \left({}^{AB}I_{\xi_1}^\psi \right) Q\left(\frac{\xi_1 + \xi_2}{2}\right) + \left({}^{AB}I_{\xi_2}^\psi \right) Q\left(\frac{\xi_1 + \xi_2}{2}\right) \right. \tag{24} \\ & \left. - \frac{(\xi_2 - \xi_1)^\psi}{2^\psi B(\psi)\Gamma(\psi)} (Q(\xi_1) + Q(\xi_2)) \right. \\ & \left. - \frac{(\xi_2 - \xi_1)^{\psi+1}}{2^{\psi+1}(\psi+1)B(\psi)\Gamma(\psi)} (Q'(\xi_1) - Q'(\xi_2)) \right. \\ & \left. - \frac{2(1-\psi)Q\left(\frac{\xi_1 + \xi_2}{2}\right)}{B(\psi)} \right| \\ & \leq \frac{(x-\xi_1)^{\psi+2}}{(\psi+1)B(\psi)\Gamma(\psi)} \left[\left(\frac{1}{\mu(\psi\mu + \mu + 1)} \right) \right. \\ & \left. + \frac{1}{\eta} \left(\frac{1}{s+1} \left(|Q''\left(\frac{\xi_1 + \xi_2}{2}\right)|^\eta + |Q''(\xi_1)|^\eta \right) - \frac{\rho(\xi_2 - \xi_1)^2}{24} \right) \right] \\ & + \frac{(\xi_2-x)^{\psi+2}}{(\psi+1)B(\psi)\Gamma(\psi)} \left[\left(\frac{1}{\mu(\psi\mu + \mu + 1)} \right) \right. \\ & \left. + \frac{1}{\eta} \left(\frac{1}{s+1} \left(|Q''\left(\frac{\xi_1 + \xi_2}{2}\right)|^\eta + |Q''(\xi_2)|^\eta \right) - \frac{\rho(\xi_2 - \xi_1)^2}{24} \right) \right]. \end{aligned}$$

Theorem 6: Suppose that $Q: [\xi_1, \xi_2] \rightarrow \mathfrak{R}$ be a twice differentiable mapping on (ξ_1, ξ_2) with $\xi_1 < \xi_2$ and $L[\xi_1, \xi_2]$. If $|Q''|^\eta$ is strongly s -convex on $[\xi_1, \xi_2]$, for some $s \in (0, 1]$ with modulus $\rho > 0$ then following inequalities hold,

$$\begin{aligned} & \left| \left({}^{AB}I_{\xi_1}^\psi \right) Q(x) + \left({}^{AB}I_{\xi_2}^\psi \right) Q(x) \right. \tag{25} \\ & \left. - \frac{(x-\xi_1)^\psi Q(\xi_1) + (\xi_2-x)^\psi Q(\xi_2)}{B(\psi)\Gamma(\psi)} \right. \\ & \left. - \frac{(x-\xi_1)^{\psi+1} Q'(\xi_1) - (\xi_2-x)^{\psi+1} Q'(\xi_2)}{(\psi+1)B(\psi)\Gamma(\psi)} \right. \\ & \left. - \frac{2(1-\psi)Q(x)}{B(\psi)} \right| \\ & \leq \frac{(x-\xi_1)^{\psi+2}}{(\psi+1)B(\psi)\Gamma(\psi)} \\ & \times \left[\left(\frac{1}{\psi\mu + \mu + 2} \right)^\frac{1}{\mu} \right. \end{aligned}$$

$$\begin{aligned} & \times \left[\left(\frac{|Q''(x)|^\eta + |Q''(\xi_1)|^\eta}{s^2 + 3s + 2} - \frac{\rho(x - \xi_1)^2}{12} \right)^{\frac{1}{\eta}} \right. \\ & \quad \left. + \left(\frac{1}{(\psi\mu + \mu + 1)(\psi\mu + \mu + 2)} \right)^{\frac{1}{\mu}} \right. \\ & \quad \times \left[\left(\frac{|Q''(x)|^\eta}{s + 2} + \frac{|Q''(\xi_1)|^\eta}{s^2 + 3s + 2} - \frac{\rho(x - \xi_1)^2}{12} \right)^{\frac{1}{\eta}} \right. \\ & \quad \left. + \frac{(\xi_2 - x)^{\psi+2}}{(\psi + 1)B(\psi)\Gamma(\psi)} \right. \\ & \quad \times \left[\left(\frac{1}{(\psi\mu + \mu + 1)(\psi\mu + \mu + 2)} \right)^{\frac{1}{\mu}} \right. \\ & \quad \times \left. \left. \left(\frac{|Q''(x)|^\eta + |Q''(\xi_2)|^\eta}{s^2 + 3s + 2} - \frac{\rho(\xi_2 - x)^2}{12} \right)^{\frac{1}{\eta}} \right. \right. \\ & \quad \left. \left. + \left(\frac{1}{\psi\mu + \mu + 2} \right)^{\frac{1}{\mu}} \right. \right. \\ & \quad \left. \left. \times \left[\left(\frac{|Q''(\xi_2)|^\eta}{s + 2} + \frac{|Q''(x)|^\eta}{s^2 + 3s + 2} - \frac{\rho(\xi_2 - x)^2}{12} \right)^{\frac{1}{\eta}} \right] \right] \right] \end{aligned}$$

where $\psi \in [0, 1]$, $x \in [\xi_1, \xi_2]$, $\eta = \frac{\mu}{\mu - 1}$, $\mu > 1$, Γ is Gamma function and B is Beta function.

Proof: By using Lemma 1 and Hölder-İşcan inequality, we obtain

$$\begin{aligned} & \left| \left({}^{AB}I_{\xi_1}^\psi \right) Q(x) + \left({}^{AB}I_{\xi_2}^\psi \right) Q(x) \right. \\ & \quad \left. - \frac{(x - \xi_1)^\psi Q(\xi_1) + (\xi_2 - x)^\psi Q(\xi_2)}{B(\psi)\Gamma(\psi)} \right. \\ & \quad \left. - \frac{(x - \xi_1)^{\psi+1} Q'(\xi_1) - (\xi_2 - x)^{\psi+1} Q'(\xi_2)}{(\psi + 1)B(\psi)\Gamma(\psi)} \right. \\ & \quad \left. - \frac{2(1 - \psi)Q(x)}{B(\psi)} \right| \\ & \leq \frac{(x - \xi_1)^{\psi+2}}{(\psi + 1)B(\psi)\Gamma(\psi)} \times \int_0^1 (1 - \tau)^{\psi+1} |Q''(\tau x + (1 - \tau)\xi_1)| d\tau \\ & \quad + \frac{(\xi_2 - x)^{\psi+2}}{(\psi + 1)B(\psi)\Gamma(\psi)} \times \int_0^1 \tau^{\psi+1} |Q''(\tau\xi_2 + (1 - \tau)x)| d\tau \end{aligned}$$

$$\begin{aligned} & \leq \frac{(x - \xi_1)^{\psi+2}}{(\psi + 1)B(\psi)\Gamma(\psi)} \\ & \quad \times \left[\left(\int_0^1 (1 - \tau)^{(\psi+1)\mu+1} d\tau \right)^{\frac{1}{\mu}} \left(\int_0^1 (1 - \tau) |Q''(\tau x + (1 - \tau)\xi_1)|^\eta d\tau \right)^{\frac{1}{\eta}} \right. \\ & \quad \left. + \left(\int_0^1 \tau (1 - \tau)^{(\psi+1)\mu} d\tau \right)^{\frac{1}{\mu}} \left(\int_0^1 \tau |Q''(\tau x + (1 - \tau)\xi_1)|^\eta d\tau \right)^{\frac{1}{\eta}} \right] \\ & \quad + \frac{(\xi_2 - x)^{\psi+2}}{(\psi + 1)B(\psi)\Gamma(\psi)} \\ & \quad \times \left[\left(\int_0^1 (1 - \tau) \tau^{(\psi+1)\mu} d\tau \right)^{\frac{1}{\mu}} \left(\int_0^1 (1 - \tau) |Q''(\tau\xi_2 + (1 - \tau)x)|^\eta d\tau \right)^{\frac{1}{\eta}} \right. \\ & \quad \left. + \left(\int_0^1 \tau^{(\psi+1)\mu+1} d\tau \right)^{\frac{1}{\mu}} \left(\int_0^1 \tau |Q''(\tau\xi_2 + (1 - \tau)x)|^\eta d\tau \right)^{\frac{1}{\eta}} \right]. \end{aligned}$$

By using strongly s -convexity of $|Q''|^\eta$ and by computing the above integrals, we have desired result.

Corollary 11: Under the assumption of Theorem 6 with $s = 1$, we obtain

$$\begin{aligned} & \left| \left({}^{AB}I_{\xi_1}^\psi \right) Q(x) + \left({}^{AB}I_{\xi_2}^\psi \right) Q(x) \right. \\ & \quad \left. - \frac{(x - \xi_1)^\psi Q(\xi_1) + (\xi_2 - x)^\psi Q(\xi_2)}{B(\psi)\Gamma(\psi)} \right. \\ & \quad \left. - \frac{(x - \xi_1)^{\psi+1} Q'(\xi_1) - (\xi_2 - x)^{\psi+1} Q'(\xi_2)}{(\psi + 1)B(\psi)\Gamma(\psi)} \right. \\ & \quad \left. - \frac{2(1 - \psi)Q(x)}{B(\psi)} \right| \\ & \leq \frac{(x - \xi_1)^{\psi+2}}{(\psi + 1)B(\psi)\Gamma(\psi)} \\ & \quad \times \left[\left(\frac{1}{\psi\mu + \mu + 2} \right)^{\frac{1}{\mu}} \left(\frac{|Q''(x)|^\eta + |Q''(\xi_1)|^\eta}{6} - \frac{\rho(x - \xi_1)^2}{12} \right)^{\frac{1}{\eta}} \right. \\ & \quad \left. + \left(\frac{1}{(\psi\mu + \mu + 1)(\psi\mu + \mu + 2)} \right)^{\frac{1}{\mu}} \right. \\ & \quad \times \left[\left(\frac{|Q''(x)|^\eta}{3} + \frac{|Q''(\xi_1)|^\eta}{6} - \frac{\rho(x - \xi_1)^2}{12} \right)^{\frac{1}{\eta}} \right. \\ & \quad \left. + \frac{(\xi_2 - x)^{\psi+2}}{(\psi + 1)B(\psi)\Gamma(\psi)} \right. \\ & \quad \times \left[\left(\frac{1}{(\psi\mu + \mu + 1)(\psi\mu + \mu + 2)} \right)^{\frac{1}{\mu}} \right. \\ & \quad \left. \times \left(\frac{|Q''(x)|^\eta + |Q''(\xi_2)|^\eta}{6} - \frac{\rho(\xi_2 - x)^2}{12} \right)^{\frac{1}{\eta}} \right] \right] \end{aligned} \tag{26}$$

$$+ \left(\frac{1}{\psi\mu + \mu + 2} \right)^{\frac{1}{\mu}} \left[\frac{|Q''(\xi_2)|^n}{3} + \frac{|Q''(x)|^n}{6} - \frac{\rho(\xi_2 - x)^2}{12} \right]^{\frac{1}{n}} \Bigg].$$

Corollary 12: In Theorem 6, by setting $x = \frac{\xi_1 + \xi_2}{2}$, we get

$$\begin{aligned} & \left| \left({}^{AB}I_{\xi_1^+}^{\psi} \right) Q \left(\frac{\xi_1 + \xi_2}{2} \right) + \left({}^{AB}I_{\xi_2^-}^{\psi} \right) Q \left(\frac{\xi_1 + \xi_2}{2} \right) \right. \\ & - \frac{(\xi_2 - \xi_1)^{\psi}}{2^{\psi} B(\psi) \Gamma(\psi)} (Q(\xi_1) + Q(\xi_2)) \\ & - \frac{(\xi_2 - \xi_1)^{\psi+1}}{2^{\psi+1} (\psi+1) B(\psi) \Gamma(\psi)} (Q'(\xi_1) - Q'(\xi_2)) \\ & \left. - \frac{2(1-\psi) Q \left(\frac{\xi_1 + \xi_2}{2} \right)}{B(\psi)} \right| \\ & \leq \frac{(\xi_2 - \xi_1)^{\psi+2}}{2^{\psi+2} (\psi+1) B(\psi) \Gamma(\psi)} \left[\left(\frac{1}{\psi\mu + \mu + 2} \right)^{\frac{1}{\mu}} \right. \\ & \times \left(\left(\left| Q'' \left(\frac{\xi_1 + \xi_2}{2} \right) \right|^n + |Q''(\xi_1)|^n \right) \frac{1}{s^2 + 3s + 2} - \frac{\rho(\xi_2 - \xi_1)^2}{48} \right)^{\frac{1}{n}} \\ & + \left(\frac{1}{(\psi\mu + \mu + 1)(\psi\mu + \mu + 2)} \right)^{\frac{1}{\mu}} \\ & \times \left(\frac{1}{s+2} \left| Q'' \left(\frac{\xi_1 + \xi_2}{2} \right) \right|^n + \frac{|Q''(\xi_1)|^n}{s^2 + 3s + 2} - \frac{\rho(\xi_2 - \xi_1)^2}{48} \right)^{\frac{1}{n}} \\ & + \left(\frac{1}{(\psi\mu + \mu + 1)(\psi\mu + \mu + 2)} \right)^{\frac{1}{\mu}} \\ & \times \left(\left(\left| Q'' \left(\frac{\xi_1 + \xi_2}{2} \right) \right|^n + |Q''(\xi_2)|^n \right) \frac{1}{s^2 + 3s + 2} \right. \\ & \left. - \frac{\rho(\xi_2 - \xi_1)^2}{48} \right)^{\frac{1}{n}} \\ & + \left(\frac{1}{\psi\mu + \mu + 2} \right)^{\frac{1}{\mu}} \\ & \times \left(\frac{|Q''(\xi_1)|^n}{s+2} + \frac{1}{s^2 + 3s + 2} \left| Q'' \left(\frac{\xi_1 + \xi_2}{2} \right) \right|^n \right. \\ & \left. - \frac{\rho(\xi_2 - \xi_1)^2}{48} \right)^{\frac{1}{n}} \Bigg]. \end{aligned}$$

3. DISCUSSION AND CONCLUSION

In this study, new integral inequalities for strongly convex functions have been obtained with the help of Atangana-Baleanu fractional integral operators. Additionally, new upper bounds have been obtained by applying different types of auxiliary inequalities. It has also been observed that some of these results are generalizations of inequalities previously obtained in the literature. Researchers interested in this subject can produce new identities and obtain different types of strongly convex function classes, as well as generalize the results with strongly convex function classes by using inequalities in the literature.

REFERENCES

- [1] Hardy GH, Littlewood JE, Pólya G. Inequalities. Cambridge, England: Cambridge University Press, 1952.
- [2] Mitrinović DS. Analytic Inequalities. Berlin, New York, Heidelberg: Springer-Verlag, 1970.
- [3] Pečarić JE. Convex functions: inequalities. Serbocroatian, Beograd: 1987.
- [4] Niculescu CP, Persson LE. Convex functions and their applications. United States of America: Springer, 2006.
- [5] Hadamard, J. Étude sur les propriétés des fonctions entières en particulier d'une fonction considérée par Riemann. J. Math. Pures. Appl. 1893, 58, 171-215.
- [6] Oldham KB, Spanier J. The fractional calculus. New York: Academic Press, 1974.
- [7] Podlubny, I. Fractional differential equations: an introduction to fractional derivatives, fractional differential equations to methods of their applications. Academic Press, 1998.
- [8] Pečarić JE, Prochan F, Tong, Y. Convex functions, partial orderings and stactical applications, Academic Press, New York, USA, 1992.
- [9] Polyak BT. Existence theorems and convergence of minimizing sequences in extremum problems with restrictions, Soviet Math. Dokl. 7, 1966, 72-75.
- [10] Sarikaya MZ, Set E, Yaldiz H, Basak N. Hermite-Hadamard's inequalities for fractional integrals and related fractional inequalities. Mathematical and Computer Modelling, 2013; vol. 57, 2403-2407.
- [11] Set E, Akdemir AO, Özdemir ME. Simpson type integral inequalities for convex functions via Riemann-Liouville integrals. Filomat 2017;31(14):4415-20.
- [12] Sarikaya MZ, Yildirim H. On Hermite-Hadamard type inequalities for Riemann-Liouville fractional integrals. Miskolc Math. Notes 2017, 17, 1049-1059.
- [13] Akdemir AO, Aslan S, Dokuyucu MA, Çelik E. Exponentially Convex Functions on the Coordinates and Novel Estimations via Riemann-Liouville Fractional Operator. Journal of Function Spaces, 2023.
- [14] Abdeljawad T, Baleanu D. On fractional derivatives with exponential kernel and their discrete versions. Rep Math Phys 2017;80(1):11-27.

- [15] Ardic MA, Akdemir AO, Önalın HK. Integral inequalities for differentiable s -convex functions in the second sense via Atangana-Baleanu fractional integral operators. *Filomat* 2023, 37, 6229–6244.
- [16] Kızıl Ş, Ardiç MA. Inequalities for strongly convex functions via Atangana-Baleanu Integral Operators. *Turkish J Sci.* 2021, 6, 96–109.
- [17] Ahmad, H, Tariq, M, Sahoo, SK, Askar S, Abouelregal AE, Khedher KM. Refinements of Ostrowski Type Integral Inequalities Involving Atangana-Baleanu Fractional Integral Operator. *Symmetry* 2021; 13, (11) 2059.
- [18] Çelik B, Özdemir ME, Akdemir AO, Set E. Integral inequalities for some convexity classes via Atangana-Baleanu Integral Operators. *Turkish Journal of Inequalities*, 5(2) (2021), 82-92.
- [19] Karaođlan A, Çelik B, Set E, Akdemir AO. On New Inequalities Involving AB-fractional Integrals for Some Convexity Classes. *Fundamentals of Contemporary Mathematical Sciences*, 2(2) (2021), 127-145.
- [20] Abdeljawad T, Baleanu D. Integration by parts and its applications of a new nonlocal fractional derivative with Mittag-Leffler nonsingular kernel. *J Nonlin- ear Sci Appl* 2017;10:1098–107.
- [21] Atangana A, Baleanu D. New fractional derivatives with non-local and non-sin-gular kernel, theory and application to heat transfer model. *Therm Sci* 2016;20(2):763–9.
- [22] Set E, Butt SI, Akdemir AO, Karaođlan A, Abdeljawad T. New integral inequalities for differentiable convex functions via Atangana–Baleanu fractional integral operators. *Chaos Solitons Fractals* 2021;143:110554.
- [23] Aslan S, Akdemir AO. New estimations for quasi-convex functions and $((h, m))$ -convex functions with the help of Caputo-Fabrizio fractional integral operators. *Electronic Journal of Applied Mathematics* 2023; 1(3), 38-46.
- [24] Akdemir AO, Aslan S, Ekinci A. Novel approaches for s -convex functions via Caputo-Fabrizio fractional integrals. *Proceeding of IAM*, 2022; 11(1), 3-16.

Refractive Index Sensor Based on Terahertz Metamaterial Absorber with High Sensitivity and Quality Factor for Sensing Applications

Ahmet TEBER^{1*} 

¹ Bayburt University, Department of Electrical and Energy, Bayburt, Türkiye
Ahmet TEBER ORCID No: 0000-0002-7361-2302

*Corresponding author: ahmetteber@bayburt.edu.tr

(Received: 30.12.2023, Accepted: 24.05.2024, Online Publication: 28.06.2024)

Keywords
Absorber,
Polarization-
independent,
Refractive-
index,
Sensing,
Sensor

Abstract: This research describes and assesses a terahertz metamaterial absorber (TMA) with a simple and easy-to-produce structure consisting of gold-silicon (optical)-gold design as a refractive index sensing. Due to the high field limitation in the detection regime, electromagnetic (EM) wave's absorption reaches 99.40% at a frequency of 3.719 THz, including a significant quality factor (Q-Factor) of 65.77 and a figure of merit, FoM, of 21.49. The TMA has a remarkable sensitivity of 1.215 THz/RIU and can be used as a refractive index sensor (RIS). The proposed metamaterial absorber-based sensor is susceptible to refractive index changes (1.00 to 1.05) in the surrounding medium. For the physical absorption mechanism, the fundamental absorption peak is mainly due to the simultaneous occurrence of electric and magnetic dipole resonances. The proposed absorber has the feature of being an excellent RIS due to its sensing and detection applications.

Algılama Uygulamaları için Yüksek Hassasiyet ve Kalite Faktörüne Sahip Terahertz Metamalzeme Soğurucu Tabanlı Kırılma İndeks Sensörü

Anahtar Kelimeler
Soğurma,
Polarizasyon-
bağımsız,
Kırılma-
indeksi,
Algılama,
Sensör

Öz: Bu araştırma, kırılma indisi algılaması olarak altın-silikon (optik)-altın tasarımından oluşan basit ve üretimi kolay bir yapıya sahip terahertz metamalzeme soğurucuyu (TMA) tanımlamakta ve değerlendirmektedir. Tespit rejimindeki yüksek alan sınırlaması nedeniyle, elektromanyetik (EM) dalganın emilimi, 65,77'lik önemli bir kalite faktörü (Q-Faktörü) ve 21,49'luk bir başarı rakamı olan FoM dahil olmak üzere, 3,719 THz frekansta %99,40'a ulaşır. TMA, 1,215 THz/RIU'luk makul bir hassasiyet sergileyen bir kırılma indisi sensörü (RIS) olarak kullanılabilir. Metamalzeme soğurucu tabanlı sensör, çevredeki ortamdaki kırılma indisi değişikliklerine (1,00 ila 1,05) karşı hassastır. Soğurma mekanizması için, temel soğurma zirvesi esas olarak elektrik ve manyetik dipol rezonanslarının eşzamanlı oluşumundan kaynaklanmaktadır. Önerilen soğurucu, algılama ve tespit uygulamaları nedeniyle mükemmel bir RIS olma özelliğine sahiptir.

1. INTRODUCTION

Since materials extracted from nature rarely interact with terahertz (THz) frequencies, artificial metamaterials are critical in interacting with electromagnetic (EM) waves at THz frequencies. Thanks to their exclusive features, such as excellent absorption/transmission and stealth, metamaterials reveal an extensive range of potential uses, such as sensors [1-6], absorbers [7-9], and imaging [10-12]. It has excellent potential in chemistry and medicine, such as biomolecular sensing, metamaterial devices, and diagnostic devices for cancer and infectious diseases. Metamaterial structures attract the attention of researchers due to their new and distinctive properties,

which are very difficult to obtain by natural means, their excellent performance, especially in sensing, and their broad application capabilities.

In a TMA structure, absorption performances (peaks) can be adjusted by altering certain structural parameters. Thus, TMAs can be sensors in numerous applications [13-16]. Biosensors [17-19] and temperature sensors [20,21] are designed as sensing applications. It is also clear that thickness and temperature sensing are not the only areas of use of terahertz metamaterials. In this regard, the use of TMAs in sensing the refractive index of the medium surrounding the sensor is available in the literature. In studies on detecting the refractive index (RI) of the encircling medium, quality factor (Q-factor),

a figure of merit (FoM), refractive index range under examination, and step size (refractive index unit) are important parameters. Table 1 lists some studies in the literature based on these parameters.

Table 1. A comparison of the reported absorbers and the suggested TMA's sensing parameters

Reference	Q-factor	FoM	RI's Range	Step Size (RIU)	Band Type
[1]	22.05	2.94	$\eta=1.0-1.39$	0.05	Single
[22]	32.167	6.015	$\eta=1.1-1.90$	0.20	Single
[23]	132.05	8.887	$\eta=1.0-1.10$	0.02	Multi
[24]	N/A	N/A	$\eta=1.0-2.00$	0.2	Multi
[25]	7.036	2.67	$\eta=1.0-1.80$	0.2	Single
[26]	8.5	0.85	$\eta=1.0-2.00$	0.2	Multi
[27]	5.5	0.4	$\eta=1.0-1.40$	0.1	Single
[28]	35.36	94.05	$\eta=1.0-1.05$	0.01	Single
[29]	296.3	229	$\eta=1.0-1.10$	0.02	Dual
The Proposed Study	65.77	21.49	$\eta=1.0-1.05$	0.01	Single

It is essential to highlight some critical studies in the literature where the refractive index changes of the encircling medium are sensitive. As of 2019, a metamaterial absorber design with a near-perfect absorption response for terahertz sensing applications was projected and analyzed with a sensitivity of 300GHz/RIU [1]. In studies on biomedical samples, the refractive index of most models is between 1.3 and 1.39, and the sensor reported in the author's study has high sensitivity for biomedical applications. An ultrathin multiband TMA was proposed in another study [23]. Simulation results reported near-perfect absorption (in the frequency range of 4.5 THz-6.0 THz). The authors also analyzed the impact of changes in the refractive index of the medium surrounding the absorber on the detection performances and implications of the analyte's thickness. They reported a sensitivity of 471 GHz/RIU in a narrow refractive index range ($\eta=1.0-1.1$), noting that the presented absorber has potential applications in photodetectors, multispectral, biosensors, and imaging. In another study [28], a stainless-steel metamaterial absorber operating at THz was demonstrated. In this study, unlike metamaterial absorbers created with a sandwich structure (metal/dielectric/metal), they are made entirely of stainless-steel materials that do not contain a sandwich structure (metal metamaterial and substrate material). Thus, the authors reduced costs by aiming to simplify the production process. According to their results, by achieving a relatively high-quality factor ($Q = 35.36$) and a sensitivity of $74.18 \mu\text{m}/\text{RIU}$ based on the wavelength of resonance frequency, they presented sensor studies with a very high sensitivity compared to their counterparts. A dual-band TMA has been demonstrated by Wang et al. [29] Although the quality factor (6.9156) was too low in the first double-band absorption peak, they obtained a quality factor of approximately 296.3 in the second peak. It is also highlighted that the RIS exhibits a sensitivity of 1900GHz/RIU for the second resonance peak.

We present a simple and easy-to-fabricate terahertz metamaterial absorber with a gold-silicon (optical)-gold sandwich structure for terahertz sensing applications.

Taking the studies given as a reference, we chose a smaller step size (0.01) of the refractive index of the medium surrounding the sensor. We offer an excellent RIS for sensing and detection applications with an acceptable high sensitivity compared to its counterparts, 1215GHz/RIU, and a high-quality factor ($Q=65.77$). The study's organization can be given as follows: first, the structural design of the proposed RIS is presented in the next section, and then the simulation results are reported in Section 3. Then, the polarization dependence of the proposed RIS is examined. A detailed discussion of the appearance of absorption peaks concerning refractive index changes is presented using the available scatter plots. A parametrical analysis is additionally performed to verify the selection of parameters, and lastly, the absorption mechanism is addressed by simulating the electric, magnetic field, and surface current distributions.

2. METHODS AND DESIGNATION

2.1. Absorption Method and Designation of Proposed Structure

The metasurface consisting of gold (Au), which has a four-armed structure and an electrical conductivity (σ) of $4.561e7 \text{ S/m}$, forms the upper part of the sandwich structure. The first of the arms was created as a rectangular structure with width w and length R along the y -axis. Afterward, this rectangular structure was moved away from the origin point by g . An arm of the unit cell was created by removing two identical triangular structures from the upper edges of the rectangular structure. After completing three more identical components to this arm, they were positioned on the silicon (optical) substrate material with 45-degree angle increments clockwise. The base surface of the substrate material was covered entirely with Gold (Au) to obtain a sandwich structure (Figure 1).

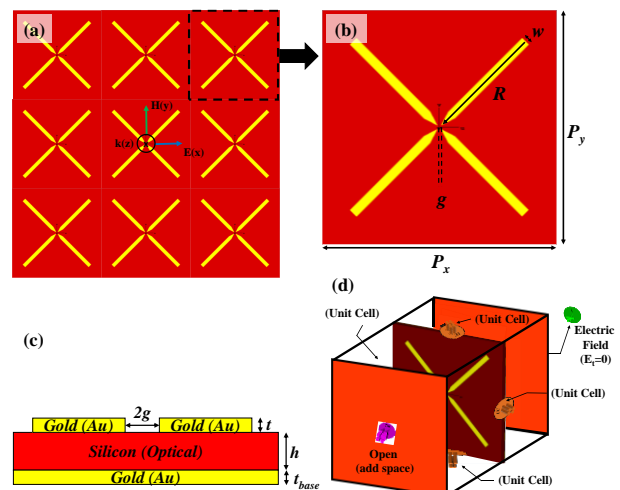


Figure 1. (a) Array of unit cell, (b) bird's eye view with design parameters, (c) lateral view, and (d) simulation medium

Silicon (optical) material, selected from the CST Microwave Studio program library and containing data in the 350-1500THz frequency band with a 10th-order model with a dispersive epsilon value and a magnetic permeability of 1, was used as the substrate material

[30]. The design parameters are shown in Figure 1b, and the unit cell structure is depicted in lateral design views (Figure 1c). Furthermore, the design parameters in micrometers, resulting in the best absorption peak, are listed in Table 2. In order to conduct simulations, the suggested sensor creation is configured as metal-substrate-metal. The layered structure's upper surface has been covered with lossy Au, which has an electrical conductivity of $\sigma = 4.561 \times 10^7$ S/m and a thickness of $0.1 \mu\text{m}$, regardless of frequency. In the simulations, the bottom surface of the DBMA structure is covered with the same metal, which has a thickness of $0.4 \mu\text{m}$. The finite Integration technique (FIT) was used for absorption performance simulations of the designed absorber. The unit cell receives illumination at normal incidence from a planar electromagnetic (EM) wave, where the x-axis represents the electric field (E-field) during the simulations. Perfectly matched layers are applied along the z-axis, and periodic boundary conditions are utilized in the x- and y-directions. (Figure 1d).

Table 2. Design parameters of the best performing TMA

g	h	$P_x=P_y$	R	t	t_{base}	w
1	4.5	100	52	0.1	0.4	4

Metamaterial surfaces absorb EM waves based on the theory of impedance matching. Part of the EM waves will be transmitted, and some will be reflected when they reach the metamaterial absorber surface. Hence, it follows that in order to guarantee optimal absorption, the transmission and reflection coefficients must be as low as feasible. For the best absorption results, the free space wave and the metal array's surface impedance must coincide. The following formula provides the metamaterial's absorption rate when there is a matching impedance between the air and the absorber [31]:

$$A(\omega) = 1 - R(\omega) - T(\omega) = 1 - |S_{11}(\omega)|^2 - |S_{21}(\omega)|^2 \quad (1)$$

$A(\omega)$ implies absorption, while $R(\omega)$ and $T(\omega)$ represent reflection and transmission, respectively. As known, $S_{11}(\omega)$ and $S_{21}(\omega)$ (as a function of frequency scattering parameters) obtained from the simulations yield $R(\omega)$ and $T(\omega)$, respectively. Simultaneous reflection and transmission coefficients can achieve the highest possible absorption rate. The thickness of the metallic surface on the substrate is such that $T(\omega) = 0$, which means that the incoming wave cannot be transmitted. The rate of reflection is the primary factor influencing the metamaterial absorber's absorption property. Perfect absorption is attained in these circumstances, with a reflectance of about zero (R). Thus, the absorption formula, which is independent of the transmission parameter and solely reliant on reflection, can be stated as follows:

$$A(\omega) = 1 - R(\omega) = 1 - |S_{11}(\omega)|^2 \quad (2)$$

3. RESULTS AND DISCUSSION

3.1. Outcomes

Simulations using CST Microwave Studio (2023) were used to determine the absorption and assess the scattering characteristics (S_{11} and S_{21}). Figure 2 displays the results that were achieved. The normalized input impedance of the proposed TMA is obtained with the following formula:

$$Z = \pm \sqrt{\frac{(1 + S_{11})^2 - S_{21}^2}{(1 - S_{11})^2 - S_{21}^2}} \quad (3)$$

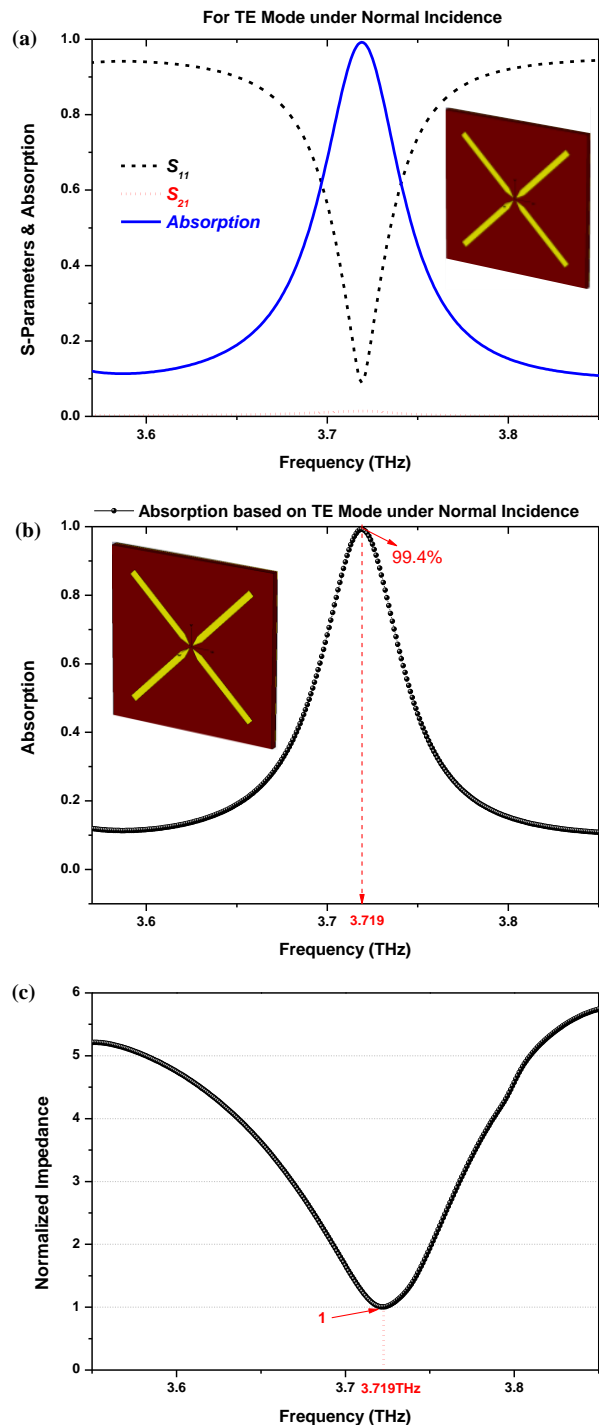


Figure 2. (a) S-parameters, (b) absorption spectra under normal oblique incidence angle, and (c) normalized impedance

A nearly perfect absorption at the operating frequency region can be achieved when the impedance matches between free space and a metamaterial absorber. It is valid if the normalized impedance of the free space (Z) is equal to 1 and equal to the normalized input impedance of the absorber. From Figure 2c, it is obviously seen that the condition of $Z = Z_0 = 1$ is obtained at the resonance frequency of 3.719 THz. The absorption is 99.4% when the surrounding medium's refractive index is the same as the free space's refractive index ($\eta = 1$).

The absorption peak of 99.4% at 3.719 THz was obtained at the normal polarization angle (0 deg.) of incidence. To check the suitability of the proposed RIS for practical applications, it is plotted for various polarization angles from 0° to 90° in 15° increments, taking into account the normal incidence of the incident plane wave, as shown in Figure 3. All absorption resonance points have a high absorption rate of over 99.4%. In addition, there is no significant change in the absorption resonance points in the spectrum when the polarization angle rises significantly, showing that the presented absorber sensor is not sensitive to polarization and is suitable for practical applications [32]. It should be noted that this is an expected result due to the symmetrical structure of the geometry. In addition, it was observed that the absorber presented was sensitive depending on the oblique angle of incidence. Assuming that the angle of incidence is not vital for sensor applications, the absorption results based on the oblique incidence are not included here.

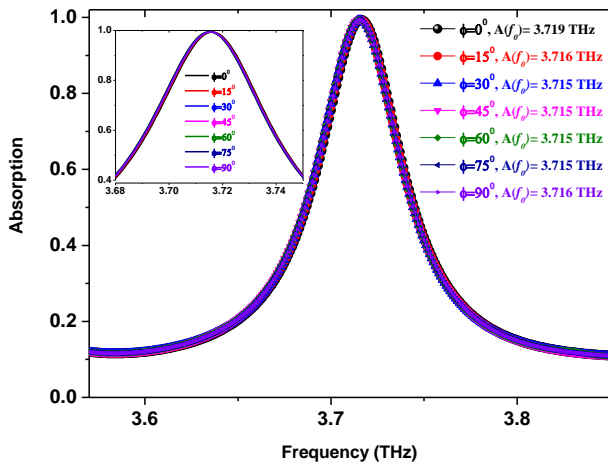


Figure 3. Absorption of the proposed sensor on different polarization angle

In sensing applications, the sensor is considered to be entirely surrounded by the encircling medium. When the medium thickness is much larger than the consistent length of the light wave arriving at the sensor, this thickness can be considered infinite [33]. The variation of absorption peaks according to the refractive index ' η ' is given in Figure 4. There is a significant shift in the absorption peaks in the refractive index of the medium surrounding the sensor. The shift feature shows that the proposed absorber (PA) has acceptable high absorption peaks even with a slight change of 0.01 in the refractive index. Thus, it shows that the PA acts as an outstanding

RIS. Additionally, the peak values of the absorption peaks according to the η changes are given in Table 3.

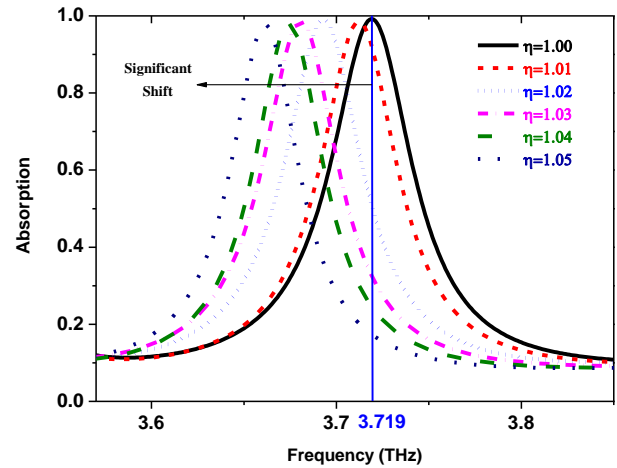


Figure 4. The absorption distributions of the proposed design based on changes in refractive index (η) of the encircling medium

Table 3. The absorption percentages based on the η , refractive index of the encircling medium

Refractive Index (η)	1.00	1.01	1.02	1.03	1.04	1.05
Absorption	99.20	98.60	99.00	98.77	98.00	97.75

By observing simulation results from Figure 2b, 99.2% absorption rate was reached by the structure at a narrow absorption peak located at 3.719 THz. As is well-known, the quality (Q-) factor can be determined from the equation of $Q = f / \text{FWHM}$ [33], where FWHM is defined as the full width at half maximum and f is the resonance frequency of EM waves. The FWHM of the PA is found to be 0.06264 THz, while the resonance frequency of EM waves is 3.719 THz. According to the quality factor formula, the Q is obtained as 65.77.

In Figure 5, the resonance frequencies (f_0) as a function of the η are analyzed to understand the sensing performance according to the narrow absorption properties. The provided structure broadens the detecting region to obtain a noticeable sensing impact and reinforces the coupling of EM waves to produce a significant absorption effect. The obtained data from the resonant frequencies versus the refractive index is plotted with the linear fit of the data in Figure 5. The relationship between the resonant frequencies and the refractive index is determined by linear fitting as given in the equation of $f_0 = -1.2\eta + 4.922$.

Sensitivity is a critical factor to consider when assessing a sensor's ability to sense. As shown below, the ratio of the evolution in the resonance frequency (f_r) to the change of refractive index (η) can be used to determine sensitivity (S)[28]:

$$S = \frac{\Delta f_r}{\Delta \eta} \tag{4}$$

where Δf_r and $\Delta \eta$ are the changes in the resonant frequency values and the refractive index, respectively. Thus, the sensitivity of the proposed RIS is approximately 1215 GHz/RIU.

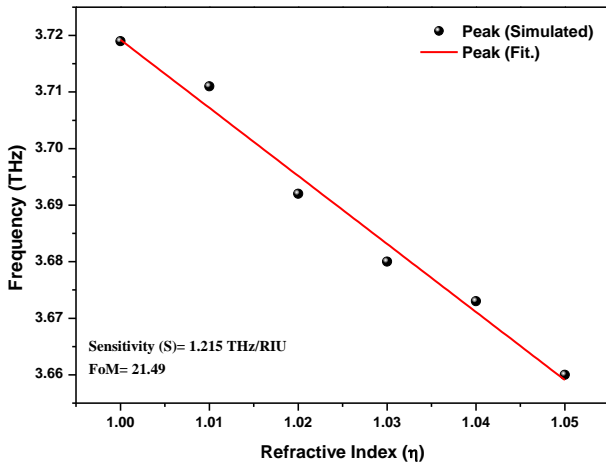


Figure 5. (a) The simulated resonant frequency distributions versus the refractive index (the red line shows the functions of the linear fit of the distributed data)

The ratio of sensitivity to FWHM of the absorber, called FoM, is another crucial parameter used to compare the detection performances of designed sensors. In our design, FoM was found to be 21.49. The high-quality factor, sensitivity as well as high FoM value make our design a high-quality RIS [33].

$$FoM = \frac{S}{FWHM} \quad (5)$$

A parametrical investigation is provided in Figure 6 to justify the design parameters. From Figure 6a-c, the geometric parameters of the metasurface structure were analyzed at different values to obtain the best optimum absorption results.

The best optimal results are given above in Table 1. Finally, the proposed structure was designed in diagonal two-arm shapes to simulate absorption. As can be seen from Figure 6d, the best absorption results are possible when a symmetrical structure is obtained. To vividly understand the physical mechanism of the absorption generated by the PA, the electric and magnetic field distributions at the frequency ($f_r=3.719$ THz) corresponding to the absorption peak are calculated, respectively. While Figure 7a represents the electric field distribution on the upper surface (xoy-plane) of the presented absorber structure, Figure 7b shows the magnetic field distribution on the upper surface of the presented absorber. Figure 7c and d show the electric and magnetic field distributions in the xoz-plane, respectively. Figure 7a shows strong electric field distribution with regional charge accumulation in the absorber structure's arms. It can be concluded that the local charge accumulation in the arms leads to the fundamental dipole's excitation. It means that there exists a robust electrical resonance [28].

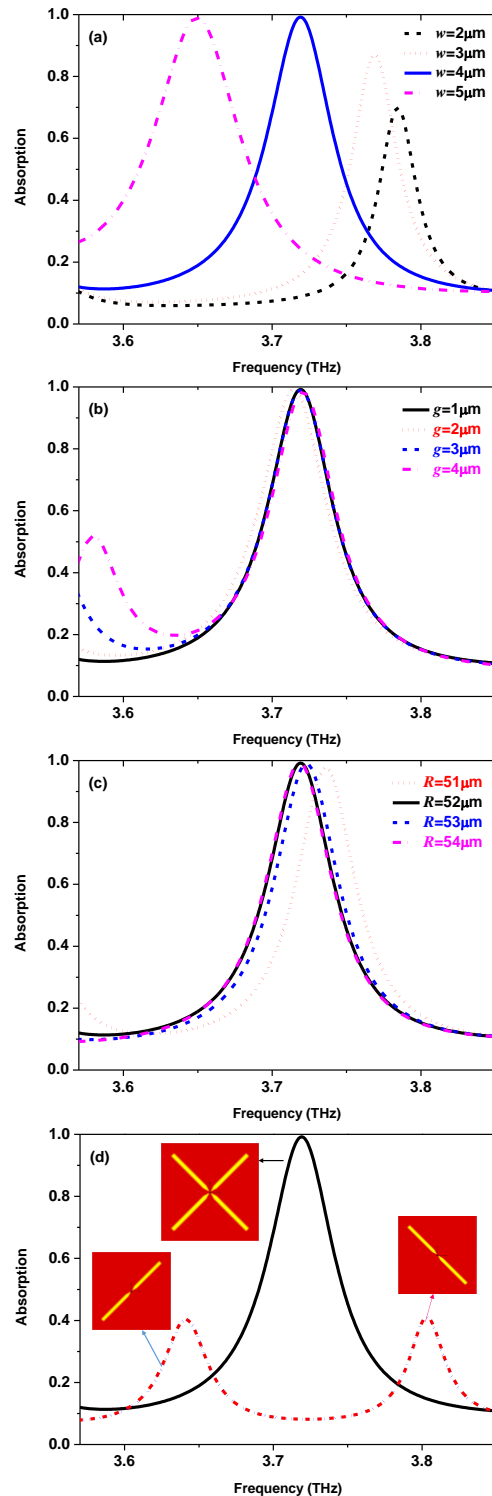


Figure 6. Parametric analysis based on (a) the width of each resonator, (b) the gap between resonators, (c) the length of each resonator, and (d) the number of resonators

From Figures 7b and d, the opposing charges formed between the metallic structure on the upper surface of the absorber structure and the layer on the lower surface (see Figures 3 and f) excite the magnetic dipole [34]. It is seen that a substantial magnetic field increase occurs in the center of the structure. Briefly, the occurrence of the fundamental absorption peak is facilitated by the simultaneous activation of electric and magnetic dipole resonances.

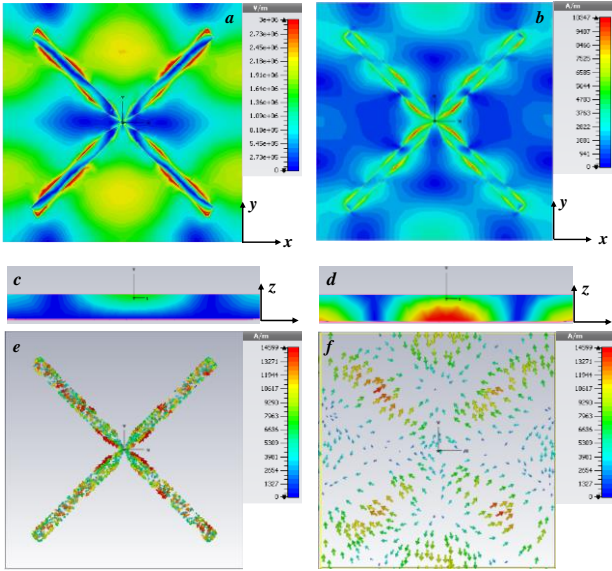


Figure 7. (a,b) Electric and magnetic field on xoy-plane, respectively, (c,d) electric and magnetic field on xoz-plane, respectively, (e) surface current distributions on the top surface, and (f) surface current distributions on the bottom surface

3.2. Equivalent Electrical Circuit Model

A method of quasi-static estimation to figure the equivalent circuit model of frequency selective surfaces (FSS) and metamaterial structures is known as an equivalent circuit approach. In this approach, the interaction of EM waves in infinite periodic arrays is assumed as an EM wave along a transmission line to present an array. This approach approximately transforms a metamaterial structure into an equivalent electrical circuit [35]. Using this technique, an equivalent circuit of the proposed TMA has been designed and simulated using the advanced design systems (ADS) [36]. A single port is assigned, considering zero transmission coefficient in the equivalent circuit because of the metal-backed design. Each arrow component of the PA has been considered an LC circuit, which has been parallelly connected, assigned as L_1C_{1a} through L_4C_{4a} , with a series of capacitors, assigned as C_1 through C_4 (Fig. 8a,b). The capacitors C_{1a} through C_{4a} represent the capacitance formed between the arrow-shaped metal metasurface structures and the ground plane, while the capacitors C_1 through C_4 display the capacitance formed between the arrow components. The calculated input impedance from the equivalent circuit of the PA is revealed in Eq. (5), while the impedance of Z_4 is defined as $[j\omega L_4 + 1/j\omega C_{4a}] // (1/j\omega C_4)$. The input impedance value obtained using Equation 5 is obtained with $\text{Re}(Z)=371.94$ ohm and $\text{Imag}(Z)=0.00175$ values at 3.719THz resonance frequency. Based on this, it is understood that mismatching is achieved between the input impedance of the metasurface and the free-space impedance.

$$Z = \left[\left(\left(\left(\left(\left(Z_4 + \frac{1}{j\omega C_3} \right) // Z_3 \right) + \frac{1}{j\omega C_2} \right) // Z_2 \right) + \frac{1}{j\omega C_1} \right) // Z_1 \right] \quad (6)$$

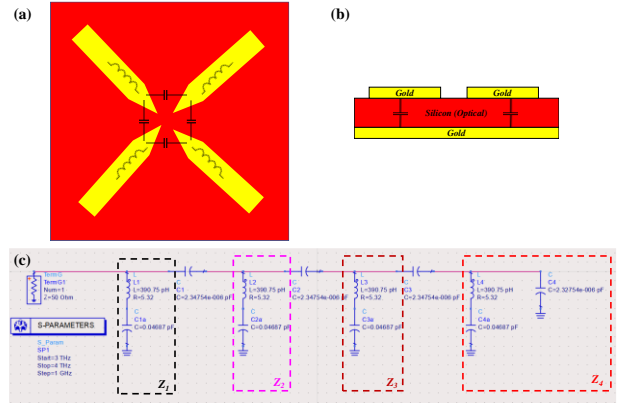


Figure 8. The equivalent electrical circuit diagram on (a) top surface view, (b) lateral view, and (c) the equivalent circuit of the PA with the values of the components in detail

For each identical component, the inductance and capacitance values formed between these structures and the ground plane are calculated as follows [37-39]:

$$L = 2 \times 10^{-4} l \left[\ln \left(\frac{l}{w+t} \right) + 1.193 + 0.02235 \left(\frac{w+t}{l} \right) \right] \quad (7)$$

$$C = 1 / (2\pi f_0)^2 L \quad (8)$$

The S-parameter simulation of the equivalent circuit was chosen in the same range as the frequency range in the CST simulations. The results of the S_{11} parameter, as a function of frequency, are plotted in Fig. 8c using the electromagnetic simulation and the equivalent electrical circuit simulation. The results are in good agreement shown in Figure 9.

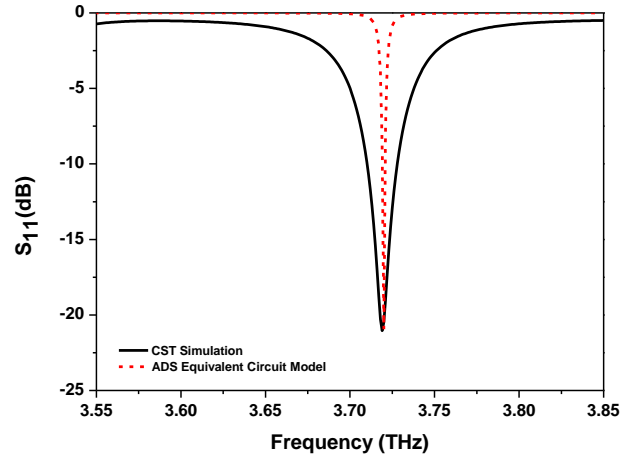


Figure 9. Comparison EM and equivalent electrical circuit simulation

4. CONCLUSION

This theoretical study presents a single-band THz metamaterial absorber in the THz regime that can be used as an outstanding refractive index sensor. An EM and equivalent electrical circuit simulations are compared regarding the S_{11} reflection coefficient (in dB-scale), resulting in a good agreement of findings by CST microwave studio and ADS. The proposed absorber is highly sensitive to changes in the surrounding medium's refractive index and has a polarization-independent property. From the analysis and the findings obtained, it is understood that this study demonstrates the theoretical feasibility and superior sensing performance. Theoretical findings show that the absorber-based sensor achieves a narrow peak absorption level of 99.20% at 3.719 THz. Geometric parameters can specifically be used to adjust the absorption. Further analysis reveals that electrical and magnetic resonances made the intended structure's efficient absorption possible. The absorber shows significant variations in the 3.719 THz resonance frequency for different refractive indexes (0.01 steps size in the range of 1-1.05), and the sensitivity of the sensor is 1215GHz/RIU while the Q quality factor is 65.77 and the FoM is 21.49. Our work uses the designed terahertz metamaterial absorber as a refractive index sensor (RIS) to detect the change in the refractive index of different media.

Acknowledgement

This research has been supported by Bayburt University Scientific Research Projects Coordination Department, Project Number:2023/69002-04.

REFERENCES

- [1] Saadeldin AS, Hameed MF, Elkaramany EM, Obayya SS. Highly sensitive terahertz metamaterial sensor. *IEEE Sensors Journal*. 2019 May 22;19(18):7993-9.
- [2] Zhang Z, Ding H, Yan X, Liang L, Wei D, Wang M, Yang Q, Yao J. Sensitive detection of cancer cell apoptosis based on the non-bianisotropic metamaterials biosensors in terahertz frequency. *Optical Materials Express*. 2018 Mar 1;8(3):659-67.
- [3] Palermo G, Lio GE, Esposito M, Ricciardi L, Manoccio M, Tasco V, Passaseo A, De Luca A, Strangi G. Biomolecular sensing at the interface between chiral metasurfaces and hyperbolic metamaterials. *ACS applied materials & interfaces*. 2020 Jun 18;12(27):30181-8.
- [4] He X, Li S, Yang X, Shi S, Wu F, Jiang J. High-sensitive dual-band sensor based on microsize circular ring complementary terahertz metamaterial. *Journal of Electromagnetic Waves and Applications*. 2017 Jan 2;31(1):91-100.
- [5] Geng Z, Zhang X, Fan Z, Lv X, Chen H. A route to terahertz metamaterial biosensor integrated with microfluidics for liver cancer biomarker testing in early stage. *Scientific reports*. 2017 Nov 27;7(1):16378.
- [6] Li Y, Chen X, Hu F, Li D, Teng H, Rong Q, Zhang W, Han J, Liang H. Four resonators based high sensitive terahertz metamaterial biosensor used for measuring concentration of protein. *Journal of Physics D: Applied Physics*. 2019 Jan 2;52(9):095105.
- [7] Park JW, Vu DL, Zheng HY, Rhee JY, Kim KW, Lee YP. THz-metamaterial absorbers. *Advances in Natural Sciences: Nanoscience and Nanotechnology*. 2013 Jan 18;4(1):015001.
- [8] Shrekenhamer D, Montoya J, Krishna S, Padilla WJ. Four-color Metamaterial absorber THz spatial light modulator. *Advanced Optical Materials*. 2013 Dec;1(12):905-9.
- [9] Zhu J, Ma Z, Sun W, Ding F, He Q, Zhou L, Ma Y. Ultra-broadband terahertz metamaterial absorber. *Applied Physics Letters*. 2014 Jul 14;105(2).
- [10] Grant J, Escorcia-Carranza I, Li C, McCrindle IJ, Gough J, Cumming DR. A monolithic resonant terahertz sensor element comprising a metamaterial absorber and micro-bolometer. *Laser & Photonics Reviews*. 2013 Nov;7(6):1043-8.
- [11] Carranza IE, Grant J, Gough J, Cumming DR. Metamaterial-based terahertz imaging. *IEEE Transactions on Terahertz Science and Technology*. 2015 Aug 21;5(6):892-901.
- [12] Duan G, Schalch J, Zhao X, Li A, Chen C, Averitt RD, Zhang X. A survey of theoretical models for terahertz electromagnetic metamaterial absorbers. *Sensors and Actuators A: Physical*. 2019 Mar 1;287:21-8.
- [13] Anik MH, Mahmud S, Mahmood KS, Isti MI, Talukder H, Biswas SK. Numerical investigation of a gear-shaped triple-band perfect terahertz metamaterial absorber as biochemical sensor. *IEEE Sensors Journal*. 2022 Aug 8;22(18):17819-29.
- [14] Cheng D, He X, Huang X, Zhang B, Liu G, Shu G, Fang C, Wang J, Luo Y. Terahertz biosensing metamaterial absorber for virus detection based on spoof surface plasmon polaritons. *International Journal of RF and Microwave Computer-Aided Engineering*. 2018 Sep;28(7):e21448.
- [15] Shen S, Liu X, Shen Y, Qu J, Pickwell-MacPherson E, Wei X, Sun Y. Recent advances in the development of materials for terahertz metamaterial sensing. *Advanced Optical Materials*. 2022 Jan;10(1):2101008.
- [16] Banerjee S, Dutta P, Basu S, Mishra SK, Appasani B, Nanda S, Abdulkarim YI, Muhammadsharif FF, Dong J, Jha AV, Bizon N. A New Design of a Terahertz Metamaterial Absorber for Gas Sensing Applications. *Symmetry*. 2022 Dec 22;15(1):24.
- [17] Mehrotra P. Biosensors and their applications—A review. *Journal of oral biology and craniofacial research*. 2016 May 1;6(2):153-9.
- [18] Liu J, Fan L, Su J, Yang S, Luo H, Shen X, Ding F. Study on a terahertz biosensor based on graphene-metamaterial. *Spectrochimica Acta Part A: Molecular and Biomolecular Spectroscopy*. 2022 Nov 5;280:121527.
- [19] Guo W, Zhai L, El-Bahy ZM, Lu Z, Li L, Elnaggar AY, Ibrahim MM, Cao H, Lin J, Wang B. Terahertz metamaterial biosensor based on open

- square ring. *Advanced Composites and Hybrid Materials*. 2023 Jun;6(3):92.
- [20] Jianjun L, Lanlan F. Development of a tunable terahertz absorber based on temperature control. *Microwave and Optical Technology Letters*. 2020 Apr;62(4):1681-5.
- [21] Zou H, Cheng Y. Design of a six-band terahertz metamaterial absorber for temperature sensing application. *Optical Materials*. 2019 Feb 1;88:674-9.
- [22] Banerjee S, Nath U, Jha AV, Pahadsingh S, Appasani B, Bizon N, Srinivasulu A. A terahertz metamaterial absorber based refractive index sensor with high quality factor. In 2021 13th International Conference on Electronics, Computers and Artificial Intelligence (ECAI) 2021 Jul 1 (pp. 1-4). IEEE.
- [23] Bai J, Shen W, Wang S, Ge M, Chen T, Shen P, Chang S. An ultra-thin multiband terahertz metamaterial absorber and sensing applications. *Optical and Quantum Electronics*. 2021 Sep;53(9):506.
- [24] Yahiaoui R, Tan S, Cong L, Singh R, Yan F, Zhang W. Multispectral terahertz sensing with highly flexible ultrathin metamaterial absorber. *Journal of Applied Physics*. 2015 Aug 28;118(8).
- [25] Singh R, Cao W, Al-Naib I, Cong L, Withayachumnankul W, Zhang W. Ultrasensitive terahertz sensing with high-Q Fano resonances in metasurfaces. *Applied Physics Letters*. 2014 Oct 27;105(17).
- [26] Li Y, Chen X, Hu F, Li D, Teng H, Rong Q, Zhang W, Han J, Liang H. Four resonators based high sensitive terahertz metamaterial biosensor used for measuring concentration of protein. *Journal of Physics D: Applied Physics*. 2019 Jan 2;52(9):095105.
- [27] Shen F, Qin J, Han Z. Planar antenna array as a highly sensitive terahertz sensor. *Applied optics*. 2019 Jan 20;58(3):540-4.
- [28] Yu J, Lang T, Chen H. All-metal terahertz metamaterial absorber and refractive index sensing performance. *Photonics*. 2021 May 14;8(5): 164.
- [29] Wang BX, He Y, Lou P, Xing W. Design of a dual-band terahertz metamaterial absorber using two identical square patches for sensing application. *Nanoscale Advances*. 2020;2(2):763-9.
- [30] Palik ED, editor. *Handbook of optical constants of solids*. Academic press; 1998.
- [31] Kong X, Jiang S, Kong L, Wang Q, Hu H, Zhang X, Zhao X. Transparent metamaterial absorber with broadband radar cross-section (RCS) reduction for solar arrays. *IET Microwaves, Antennas & Propagation*. 2020 Oct;14(13):1580-6.
- [32] Shen X, Cui TJ, Zhao J, Ma HF, Jiang WX, Li H. Polarization-independent wide-angle triple-band metamaterial absorber. *Optics express*. 2011 May 9;19(10):9401-7.
- [33] Banerjee S, Nath U, Dutta P, Jha AV, Appasani B, Bizon N. A theoretical terahertz metamaterial absorber structure with a high quality factor using two circular ring resonators for biomedical sensing. *Inventions*. 2021 Nov 2;6(4):78.
- [34] Guddala S, Kumar R, Ramakrishna SA. Thermally induced nonlinear optical absorption in metamaterial perfect absorbers. *Applied Physics Letters*. 2015 Mar 16;106(11).
- [35] Zhao M, Xu J, Zhao J. Design and analysis of dual-band FSS based on equivalent circuit. *International Journal of RF and Microwave Computer-Aided Engineering*. 2022 Dec;32(12):e23405.
- [36] Keysight Headquarters [Internet], Available from: <https://www.keysight.com/us/en/products/software/pathwave-design-software/pathwave-advanced-design-system.html>
- [37] Islam MS, Samsuzzaman M, Beng GK, Misran N, Amin N, Islam MT. A gap coupled hexagonal split ring resonator based metamaterial for S-band and X-band microwave applications. *IEEE Access*. 2020 Apr 6;8:68239-53.
- [38] Singh AK, Abegaonkar MP, Koul SK. Dual-and triple-band polarization insensitive ultrathin conformal metamaterial absorbers with wide angular stability. *IEEE Transactions on Electromagnetic Compatibility*. 2018 Jun 20;61(3):878-86.
- [39] Hakim ML, Alam T, Islam MT, Alsaif H, Soliman MS. Polarization-independent fractal square splits ring resonator (FSSRR) multiband metamaterial absorber/artificial magnetic conductor/sensor for Ku/K/Ka/5G (mm-Wave) band applications. *Measurement*. 2023 Mar 31;210:112545.

Persulfate Assisted Sonocatalytic Process for the Degradation of Reactive Yellow 145 Dye in Aqueous Solution

Özkan GÖRMEZ^{1*} 

¹Mersin University, Science Faculty, Chemistry Department, Mersin, Türkiye
Özkan GÖRMEZ ORCID No: 0000-0002-1360-9275

*Corresponding author: ozkan.grmz@gmail.com

(Received: 17.11.2023, Accepted: 28.05.2024, Online Publication: 28.06.2024)

Keywords

Wastewater treatment, Sonocatalytic process, Box-Behnken Design, Azo dyes

Abstract: Pollutants resulting from industrial wastewater significantly threaten environmental health. Purification of wastewater, especially from the synthetic dye industry, is of great importance for the protection of aquatic systems. Advanced oxidation processes (AOPs), which are among the methods used in wastewater treatment in recent years, provide effective degradation of persistent organic pollutants with the help of radical species produced from oxidants used in the experimental environment.

In this study, the removal of synthetically prepared reactive yellow 145 (RY145) dye solution by the sonocatalytic method, one of the AOPs, in the presence of $(\text{Mn}_{0.37}\text{Fe}_{0.63})_2\text{O}_3$ catalyst and using persulfate as oxidant was examined. Characterization of the $(\text{Mn}_{0.37}\text{Fe}_{0.63})_2\text{O}_3$ catalyst synthesized by the sol-gel method was carried out by XRD, SEM and EDS techniques. While persulfate concentration (5-10 mM), time (2-5 h) and catalyst dosage (0.25-0.75 g L⁻¹) were determined as experimental parameters for the oxidation of RY145 dye, Box-Behnken design was preferred for modeling the experimental study. In experimental studies, the maximum %TOC removal was calculated as 92.98% after 5 h at 10 mM PS and 0.75 g L⁻¹ catalyst dosage.

69

Reaktif Sarı 145 Boyasının Sulu Çözeltisinin Persülfat Destekli Sonokatalitik Proses ile Degradasyonu

Anahtar Kelimeler

Atık su arıtımı, Sonokatalitik proses, Box-Behnken Tasarımı, Azo boyar maddeler

Öz: Endüstriyel atık sulardan kaynaklanan kirleticiler çevre sağlığını önemli ölçüde tehdit etmektedir. Özellikle boya endüstrisinden kaynaklanan atık suların arıtılması, sucul sistemlerin korunması açısından büyük önem taşımaktadır. Atıksu arıtımında son yıllarda kullanılan yöntemler arasında yer alan ileri oksidasyon prosesleri (AOP'ler), deney ortamında kullanılan oksidanlardan üretilen radikal türler yardımıyla kalıcı organik kirleticilerin etkin bir şekilde parçalanmasını sağlamaktadır.

Bu çalışmada, reaktif sarı 145 (RY145) boyası içeren sentetik olarak hazırlanmış atık suyun, $(\text{Mn}_{0.37}\text{Fe}_{0.63})_2\text{O}_3$ katalizörü varlığında ve oksidant olarak persülfat kullanılarak AOP tekniklerinden biri olan sonokatalitik yöntemle giderimi incelenmiştir. Sol-jel yöntemiyle sentezlenen $(\text{Mn}_{0.37}\text{Fe}_{0.63})_2\text{O}_3$ katalizörünün karakterizasyonu XRD, SEM ve EDS teknikleriyle gerçekleştirilmiştir. RY145 boyasının oksidasyonunda deneysel parametreler olarak persülfat konsantrasyonu (5-10 mM), süre (2-5 saat) ve katalizör dozajı (0,25-0,75 g L⁻¹) belirlenirken, deneysel çalışmanın modellenmesinde Box-Behnken tasarımı tercih edilmiştir. Deneysel çalışmalarda 10 mM PS ve 0,75 g L⁻¹ katalizör dozajında 5 saat sonra maksimum %TOC giderimi %92,98 olarak hesaplanmıştır.

1. INTRODUCTION

In parallel with the development of industry, it has become necessary to develop methods for the effective

treatment of toxic compounds that cause environmental pollution without being released into natural water cycles [1]. Various synthetic dyes used in textile factories may cause changes in the oxygen content and temperature of

the water as a result of mixing with water, as well as causing a significant environmental hazard due to toxic species released as a result of hydrolysis, oxidation and/or other bio-chemical reactions of these dyes [2-4]. Therefore, effective methods must be applied to remove dyes from the aquatic environment. The processes applied to remove azo dyes from aqueous solutions are divided into three parts. These are respectively (i) physical; (ii) biological and (iii) chemical methods. Physical methods are generally based on the mass transfer mechanism or simple separation of dyes from aqueous solutions. Biological techniques require the use of microorganisms in the degradation process of azo dyes. In chemical methods, azo dyes are converted into degradation products by using various chemicals and theories. Physical methods are mainly classified as adsorption, filtration, ion exchange, coagulation, sedimentation and membrane separation. Chemical methods are generally grouped under Advanced oxidation techniques. Advanced oxidation techniques include many techniques such as Fenton and Fenton-based methods, Electro-oxidation, Ozonation, sonolysis, photolysis, and photocatalysis [5].

Reactive dyes included in synthetic textile dyes can be covalently bonded to the fiber structure thanks to the sulfonic group in their molecules and are highly water-soluble structures [3,6]. Another classification for synthetic dyes is azo dyes. Azo dyes have azo groups (-N=N-) in a complex aromatic structure. The deep color of these dyes is due to the azo group, and the color may disappear with the degradation of this group [7-9]. Reactive yellow 145 (RY145) dye, which contains azo group and monochlorotriazine, is generally used in cotton dyeing [6,10] and various physical and chemical techniques have been used to remove this dye from wastewater. To adsorption-based removal of RY145, various adsorbents such as watermelon seeds [6], KOH-activated biochar [11], eggshell waste [12], soybean hull [13], MnO_x - CeO_2 [6], zero-valent iron/(Fe-Mn) binary oxide/bentonite nanocomposite [14] have been used previous studies. Although the adsorption method is low-cost and simple operation, it cannot completely eliminate the pollutant. Recently, advanced oxidation methods based on reactive oxygen species (ROS) formation, especially hydroxyl radical ($\cdot OH$), have been used in the oxidation of refractory organic pollutants that cannot be completely removed in biological treatment, such as textile dyestuffs [15]. In previous studies, Ni_3O_4 - Co_3O_4/Al_2O_3 [8], Co-Fe BTC/graphitic carbon nitride [16], nano CuO [17], nano- TiO_2 [18], Al_2O_3/ZrO_2 [19], $Co_{1-x}Zn_xFe_2O_4$ nanodot coated with polyaniline [20], α - $Fe_2O_3@C@SiO_2/TiO_2$ [21] nanocomposite etc. photocatalysts were developed for the oxidation of the synthetic aqueous solution of RY145 dye and their effectiveness in photocatalytic oxidation was examined. In recent years, applications of sulfate radical-based processes have attracted attention. Sulfate radical ($SO_4^{\cdot -}$) formation is produced as a result of thermal, UV and metal ions (metal oxides) supported activations for the homolytic breaking of the peroxide (O-O) bond of persulfate (PS) and peroxymonosulfate (PMS) structures. Since hydroxyl ($\cdot OH$, $E^0=2.80$ V vs SCE), and sulfate radicals ($SO_4^{\cdot -}$, $E^0= 2.5$ - 3.1 V vs SCE) have very high

oxidation potential, they react with organic pollutants non-selectively and at very high rates [22].

Sonochemical degradation (sonolysis) is used in support of other AOPs as well as being used alone. Applications based on sonolysis include sonocatalysis [23], sono/Fenton [24], sonication-ozonation [25], sonophotocatalysis [26], sonoelectrochemical oxidation [27] processes. Acoustic cavitation occurs due to compression and rarefaction cycles caused by ultrasonic emissions during sonolysis. The positive pressure caused by a large number of cavitation bubbles causes local high temperatures (5000 K) and high pressures (500 atm) in the solution, like a microreactor. Among the ROS formed in these local regions, there are also significant amounts of hydroxyl radicals [28-30]. Although, the most important disadvantages of the sonolysis process seem to be relatively long process time and energy consumption, the use of different catalysts and oxidants that have emerged recently are effective in solving these problems [31].

Bixbyite ($Fe,Mn)_2O_3$ and hematite ($Fe_{2-x}Mn_xO_3$), which are manganese iron oxide structures, are stable phases at low temperatures, whereas the spinel phase ($Fe,Mn)_3O_4$ shows stability at higher temperatures [32]. It is also possible to obtain mixtures of these phase types at intermediate temperatures [33,34]. There may be different Mn/Fe molar ratios in the bixbyite structure depending on the synthesis conditions. The bixbyite-manganese iron oxide structure has been mostly studied as an oxygen storage material. Manganese iron oxide structures in bixbyite phase are mechanically durable and inexpensive oxygen-carrier materials that are suitable for chemical looping with oxygen uncoupling (CLOU) in the air reactor [33]. These types of storage materials undergo a reversible redox reaction with oxygen.

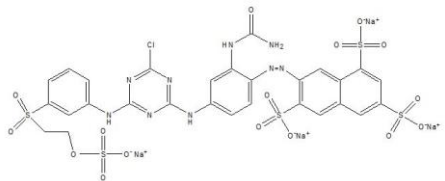
In this study, persulfate-assisted sonocatalytic oxidation of RY145 dye using manganese iron oxide ($Mn_{0.37}Fe_{0.63})_2O_3$ catalyst was examined. The effects of persulfate concentration, time and catalyst dosage on the oxidation of RY145 dye were examined using the response surface method and Box-Behnken design (BBD), and the optimum conditions were determined.

2. MATERIAL AND METHOD

2.1. Materials

Reactive yellow 145 (RY145) was supplied from EKSOY Company (Adana, Türkiye) (Table 1). Potassium persulfate ($K_2S_2O_8$), citric acid ($C_6H_8O_7$), $Mn(NO_3)_2 \cdot 4H_2O$, and $Fe(NO_3)_3 \cdot 9H_2O$ were purchased from Merck.

Table 1. Structure and properties of RY145 dye [35].

Properties of RY145	
Structure	
Molecular Formula	C ₂₈ H ₂₀ ClN ₉ Na ₄ O ₁₆ S ₅
Molecular Weight	1026.25 g mol ⁻¹
CAS Registry Number	93050-80-7
Water solubility	80 g L ⁻¹

2.2. Method

2.2.1. Synthesis of catalyst

In the synthesis of manganese^{III}-iron^{III} oxide ((Mn_{0.37}Fe_{0.63})₂O₃) structures, the sol-gel method was used to prepare Fe:Mn molar ratios of 1.7:1. Briefly, metal salts containing 0.17 mol Fe³⁺ and 0.1 mol Mn²⁺ were mixed in deionized pure water until completely dissolved. To this homogeneous mixture, 0.27 mol citric acid solution was added dropwise so that the metal ions: citric acid molar ratio was 1:1. It was waited in the magnetic stirrer at 70 °C until the gel formed, and then it was placed in a porcelain crucible and calcined at 700 °C for 5 h.

2.2.2. Sonocatalytic oxidation

The sonocatalytic experiments were carried out in capped pyrex glass bottles with a capacity of 150 mL. Catalyst and persulfate were added to 100 mL of 50 mg L⁻¹ RY145 solution and placed in an ultrasonic bath (Bandelin Sonorex, 84 W, 40 kHz). The temperature was kept constant at 30 °C by water circulation.

2.2.3. Experimental design

Box-Behnken design was used for the optimization study in the sonocatalytic oxidation of RY145 dyestuff. The most commonly used BBD for second order models in the surface method is a 3-level (-1, 0, +1) design. While persulfate (PS) concentration (X_1), time (X_2), and catalyst dosage (X_3) were selected as independent variables, TOC removal was followed as the dependent variable, that is the response (Y). The lowest (-1) and highest level (+1) ranges for the three independent variables were selected as 5-10 mM PS, 2-5 h, and 0.25-0.75 g L⁻¹ (Mn_{0.37}Fe_{0.63})₂O₃ catalyst (Table 2). The BBD with 3 independent variables (k) was created as a matrix of 17 runs (N) based on the $N=2k \times (k-1) + C_0$ formula (where C_0 is the number of central points) by the Design-Expert

11 program. The equation of quadratic equation showing the correlation between the independent variables and the response is as follows (Equation (1)).

$$Y = \beta_0 + \sum_{i=1}^k \beta_i X_i + \sum_{i=1}^k \beta_{ii} X_i^2 + \sum_i \sum_j \beta_{ij} X_i X_j + \varepsilon \quad (1)$$

where, X_i and X_j point out the independent variables, ε represents the random error, β_0 , β_i , β_{ii} and β_{ij} are the constant coefficient, the linear coefficient, the quadratic coefficient and the interaction coefficient, respectively.

2.2.4. Determination of total organic carbon content

Total organic carbon (TOC) contents of the samples taken were determined using the Merck TOC cell test. After the samples were heated at 120 °C for 2 h and were left for 1 h to cool. Afterwards, TOC content was measured with a Spectroquant NOVA 30 model photometer (Merck).

2.2.5. Characterization of catalyst

Crystal structure analysis of manganese iron oxide was performed by X-Ray powder Diffractometry (XRD, Rigaku SmartLab model) using Cu-K $\alpha_{1,2}$ radiation at 40 kV from 20° to 70° at the scan rate of 2°/min. Field Emission Scanning Electron Microscopy (Fe-SEM, Zeiss Supra 55) was used to determine the morphology of the catalyst using Pt coating. Also, surface element distribution was examined with the Energy Dispersive Spectrometry (SEM-EDS) system.

3. RESULTS AND DISCUSSION

3.1. Characterization of Manganese Iron Oxide

The SEM images of the (Mn_{0.37}Fe_{0.63})₂O₃ catalyst is given in Figure 1a, b. It is similar to the literature in terms of morphological structure [34]. Moreover, the elemental composition and atomic distribution of the manganese iron oxide catalyst are depicted in the EDS spectrum in Figure 1c.

According to the XRD pattern given in Figure 1d, the presence of specific diffraction peaks (ICDD PDF-2, 01-071-0637) belonging to the cubic bixbyite ((Mn,Fe)₂O₃) manganese iron oxide structure is seen due to, as well as the diffraction peaks of the hematite phase as an impurity [33]. Herein, XRD pattern supports bixbyite ((Mn_{0.37}Fe_{0.63})₂O₃) structure with 37% Mn and 63% Fe molar fraction. The lattice parameter of the synthesized magnesium iron oxide structure corresponds to $a = b = c = 9.41 \text{ \AA}$ and $\alpha = \beta = \gamma = 90^\circ$, and the formation of a strong cubic lattice structure is observed.

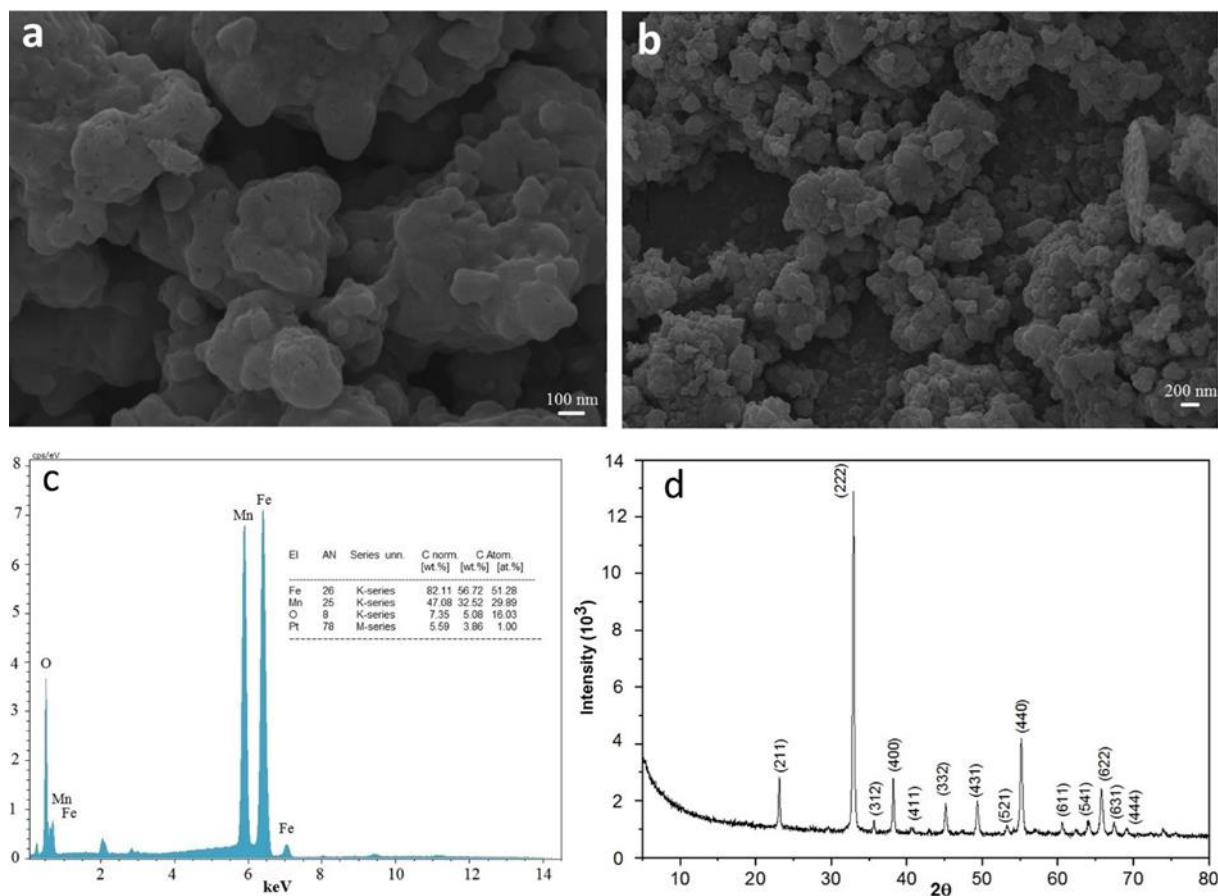


Figure 1. SEM images (a, b), EDS spectrum (c), and XRD pattern of catalyst (d).

3.2. Persulfate Assisted Sonocatalytic Oxidation of RY145

The effects of sonolysis (US), persulfate-assisted sonolysis (US/PS), sonocatalysis (US/Catalyst), and persulfate-assisted sonocatalysis (US/PS/Catalyst) processes on the oxidation of RY145 dye solution were monitored by the decrease in TOC content. While it was observed that sonolysis alone and PS-assisted sonolysis methods were not effective on TOC removal, 18% and 58% TOC removal was achieved with sonocatalytic and PS-assisted sonocatalytic methods, respectively. The combination of sonolysis with other systems creates a synergistic effect for radical formation and oxidation of organic pollutants. In sonolysis applications, especially magnetic catalysts can be distributed more homogeneously in the solution, thus increasing the effective surface area.

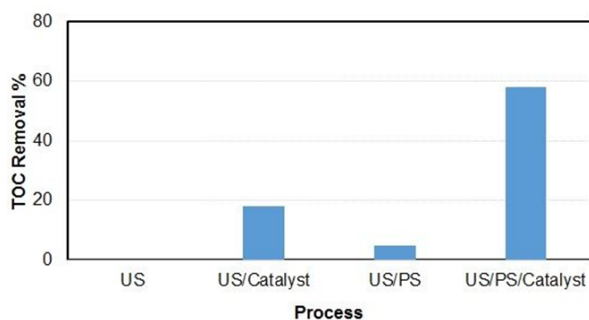
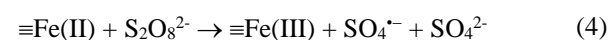
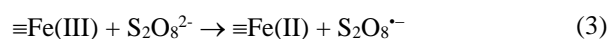
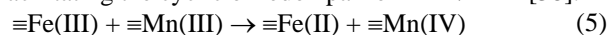


Figure 2. TOC removal of RY145 solution at different processes (Catalyst: 0.25 g L⁻¹, PS: 5 mM, t= 3.5 h).

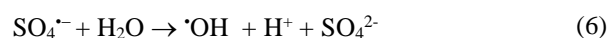
In order for the sulfate radical to form through heat activation, the temperature must be between 40-120 °C, because to break of peroxide (O-O) bond requires 140 - 213.3 kJ mol⁻¹ a thermal activation energy [36]. Whereas, persulfate activation is carried out with transition metal ions and the formation of sulfate radical is achieved by Equations (2-4) at moderate temperatures [37].



Herein, the higher standard redox potential of Fe³⁺/Fe²⁺ ($E^\circ = 0.77$ V vs SHE) allows for the oxidation of Mn³⁺ to Mn⁴⁺ ($E^\circ = 0.15$ V) as giving Equation (5) and results in facilitating the cyclic of redox pair of Mn⁴⁺/Mn³⁺ [38].



At all pH values, the formation of hydroxyl radicals may occur as a result of the reaction of the sulfate radical with water due to Equation (6) [39]. For this reason, it would be more accurate to accept the presence of both hydroxyl and sulfate radicals in the bulk solution.



The effects of persulfate, catalyst concentration and time on the sonocatalytic oxidation of RY145 solution at close to room temperature were examined using the Box-Behnken design, the experimental matrix and results are given in Table 2.

Table 2. BBD matrix for RY145 oxidation.

Run no	X_1 PS (mM)	X_2 Time (h)	X_3 Catalyst (g L ⁻¹)	TOC Removal (%)
1	5 (-1)	5 (+1)	0.50 (0)	76.82
2	15 (+1)	3.5 (0)	0.25 (-1)	66.23
3	5 (-1)	3.5 (0)	0.75 (+1)	73.72
4	15 (+1)	3.5 (0)	0.75 (+1)	81.25
5	10 (0)	2 (-1)	0.25 (-1)	59.33
6	10 (0)	3.5 (0)	0.50 (0)	82.12
7	5 (-1)	2 (-1)	0.50 (0)	51.82
8	10 (0)	3.5 (0)	0.50 (0)	84.28
9	10 (0)	5 (+1)	0.75 (+1)	92.98
10	10 (0)	3.5 (0)	0.50 (0)	79.02
11	10 (0)	2 (-1)	0.75 (+1)	70.33
12	10 (0)	3.5 (0)	0.50 (0)	85.36
13	5 (-1)	3.5 (0)	0.25 (-1)	58.54
14	10 (0)	5 (+1)	0.25 (-1)	81.62
15	15 (+1)	2 (-1)	0.50 (0)	62.61
16	10 (0)	3.5 (0)	0.50 (0)	82.26
17	15 (+1)	5 (+1)	0.50 (0)	88.21

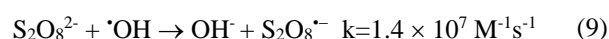
In ANOVA, the F -value (40.69) and p -value (<0.0001) of the proposed quadratic model (Table 3) for the sonocatalytic oxidation of RY145 dye solution shows an excellent fit to the experimental results. The compatibility of the model with the experimental results was also supported by the correlation coefficient values, R^2 and adjusted R^2 , these values are 0.9812 and 0.9571, respectively. In the proposed quadratic model, the most effective terms according to their p -values (<0.05) are the linear (X_1 , X_2 , X_3) and quadratic (X_1^2 , X_2^2 , X_3^2) terms of the three independent variables. In contrast, the interactive effects of the independent variables do not have a significant effect on the TOC removal efficiency. When the polyfunctional Equation (7) of the quadratic model is examined, when linear terms have a positive effect, quadratic terms have a negative effect on the response. In other words, as all three independent variables increase up to a certain level, they have a positive effect on the response, but after the optimum point, their effect decreases or becomes constant (Figure 3).

Table 3. ANOVA results of BBD for sonocatalytic oxidation of RY145

Source	Sum of Squares	df	Mean Square	F value	P value	
Model	2163.18	9	240.35	40.69	< 0.0001	significant
X_1 -PS (mM)	174.85	1	174.85	29.60	0.0010	
X_2 -time (h)	1140.99	1	1140.99	193.18	< 0.0001	
X_3 -Catalyst (g L ⁻¹)	345.32	1	345.32	58.47	0.0001	
X_1X_2	0.0900	1	0.0900	0.0152	0.9052	
X_1X_3	0.0064	1	0.0064	0.0011	0.9747	
X_2X_3	0.0324	1	0.0324	0.0055	0.9430	
X_1^2	374.94	1	374.94	63.48	< 0.0001	
X_2^2	46.03	1	46.03	7.79	0.0268	
X_3^2	44.10	1	44.10	7.47	0.0292	
Residual	41.34	7	5.91			
Lack of Fit	17.74	3	5.91	1.00	0.4781	not significant
Pure Error	23.60	4	5.90			
Cor Total	2204.53	16				

$$\begin{aligned} \text{TOC Removal (\%)} = & 82.61 + 4.67X_1 + \\ & 11.94X_2 + 6.57X_3 + 0.15X_1X_2 - 0.04X_1X_3 \\ & + 0.09X_2X_3 - 9.44X_1^2 - 3.31X_2^2 - 3.24X_3^2 \end{aligned} \quad (7)$$

Figure 3 shows the interactive effects of PS concentration, catalyst dosage, and process time, which are effective in the PS-assisted sonocatalytic oxidation of RY145 dye, when a variable is kept constant. When Figure 3a is examined, it is seen that the processing time is an important parameter, and an effective TOC removal efficiency can be achieved especially after 4 h. A significant increase in TOC removal was observed when the PS oxidant concentration was increased up to 11 mM, but the efficiency started to decrease as it increased above 11 mM. When the PS concentration was 5 mM, TOC removal enhanced to 79%, whereas the PS concentration was increased to 11 and 15 mM the efficiency was observed as 94% and 89%, respectively. The reason for this result is that excess PS in the medium acts as a radical scavenger and consumes the radicals created during the process via Equations (8) and (9) [40].



In case the effect of catalyst dosage on TOC removal was examined in Figures 3b and 3c, 82% TOC removal was achieved with 0.25 g L⁻¹ catalyst at 5 h and 11 mM PS. Increasing the catalyst dosage to 0.6 g L⁻¹ increased TOC removal to 94% as it provided more active surfaces involved in radical formation. Keeping the catalyst dosage at 0.75 g L⁻¹ and determining TOC removal as 95% under the same conditions showed that there was no need to increase the catalyst dosage further.

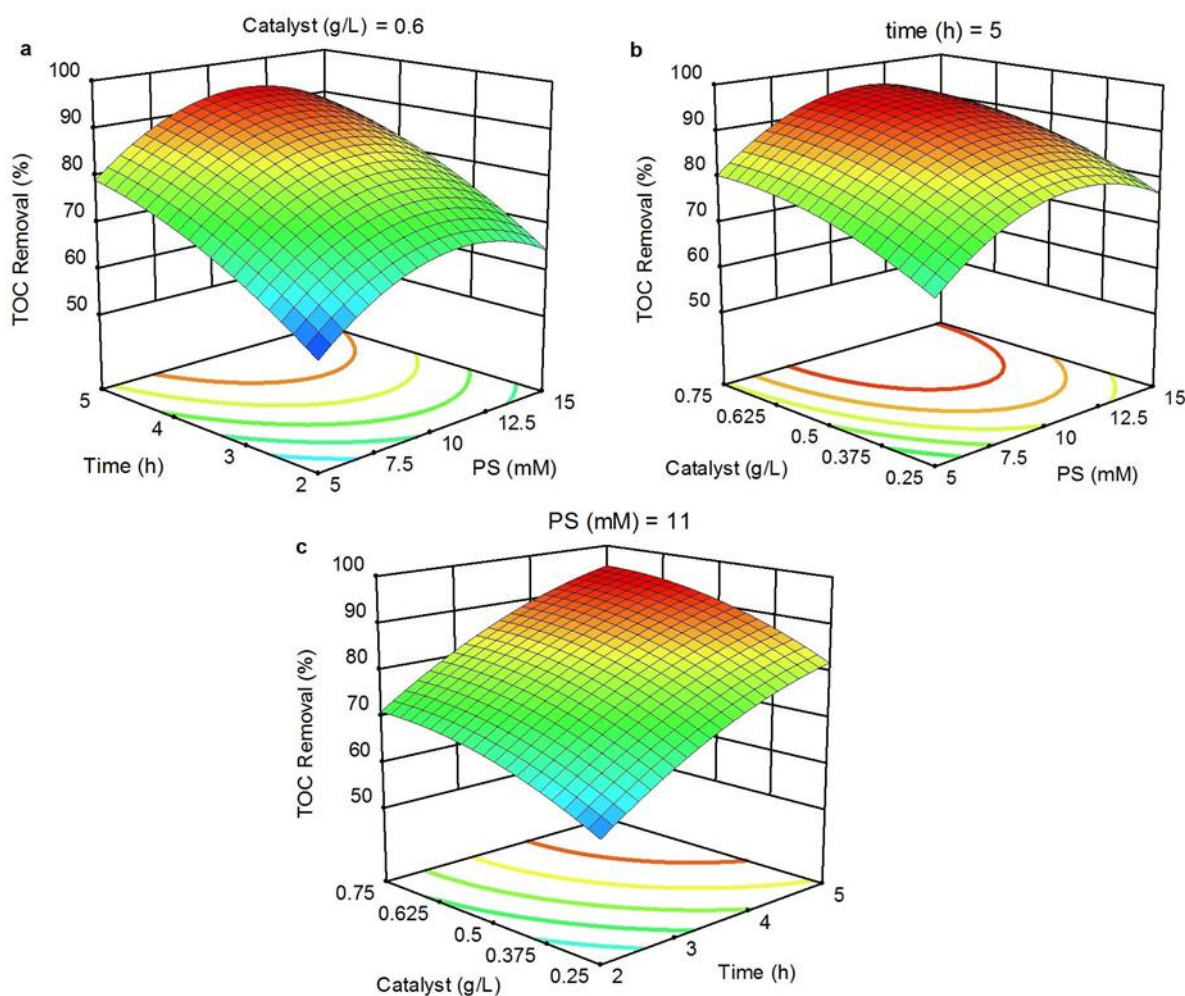


Figure 3. The effect of time and PS concentration (a), catalyst dosage and PS concentration (b), and catalyst dosage and time on TOC removal efficiency (pH 5.5).

According to the response surface method, the optimum conditions to achieve 95% TOC removal were determined as follows: 11 mM PS, 5 h process time, and 0.7 g L⁻¹ catalyst dosage. After the magnetic catalyst was collected with an external magnet and washed with ethanol and water, its reuse was tested for five runs, and 95% TOC removal was achieved in each cycle.

Mohammad et al. [8], reported that the color removal of 50 mg L⁻¹ RY145 aqueous solution was completed in 60 min at pH 3 with a catalyst dosage of 0.1 g L⁻¹ with the Ni₃O₄-Co₃O₄/Al₂O₃ photocatalyst. Nguyen et al. [17], achieved 99% color removal and 46% TOC removal for 50 mg/L of RY145 in 45 min by using bimetallic Co-Fe BTC/graphitic carbon nitride nanocomposite photocatalyst. Vu et al. [41], achieved 98% color removal of RY145 (100 mg L⁻¹) as a result of 60-min photocatalysis using the e-BTC/Graphene oxide (GO)-30 composite synthesized by microwave-assisted hydrothermal method. In the another study where Ag-Zn-BTC/GO composite was used as the photocatalyst, COD, BOD and TOC removals were reported as 80.06%, 81.66% and 56.13%, respectively, as a result of photocatalytic oxidation of 65 mg L⁻¹ RY145 aqueous solution for 35 min [42]. When the previous studies are examined, it can be seen that more emphasis is placed on color removal. In this study, 100%

color removal as well as 95% TOC removal for RY145 dye was achieved using the PS-assisted sonocatalytic method at 5 h.

4. CONCLUSION

In the study, experimental modeling was made with the Box-Behnken design, persulfate was used as the oxidant and (Mn_{0.37}Fe_{0.63})₂O₃ was used as the catalyst in the sonocatalytic degradation process of RY145 dye. The maximum TOC removal value during experimental studies was 92.98%. However, according to the second-order model obtained with the Box-Behnken design, the optimum conditions were determined as 11 mM PS, 5 h of processing time and 0.7 g L⁻¹ catalyst dosage, and the TOC removal value to be obtained under these conditions was calculated as 95%. It has been determined that (Mn_{0.37}Fe_{0.63})₂O₃ used as a catalyst can be easily separated from the experimental environment due to its magnetic properties and maintains its catalytic activity even when reused 5 times. The obtained ANOVA datas such as F-value, R² and Adj-R² of the applied quadratic model prove the high compatibility of the obtained results with each other. The quadratic equation obtained for the removal of RY145 dye in the study can be used as preliminary data in determining experimental conditions for similar studies

to be carried out in this field. Considering the whole study, it has been shown that AOPs techniques, whose effectiveness has been demonstrated in many studies, can be applied in perfect harmony with experimental modeling methods.

REFERENCES

- [1] Arefi-Oskoui S, Khataee A, Behrouz SJ, Vatanpour V, Gharamaleki SH, Orooji Y, et al. Development of MoS₂/O-MWCNTs/PES blended membrane for efficient removal of dyes, antibiotic, and protein. *Sep. Purif. Technol.* 2022;280:119822.
- [2] Deveci İ, Mercimek B. Performance of SiO₂/Ag Core/Shell particles in sonocatalytic degradation of Rhodamine B. *Ultrason. Sonochem.* 2019;51:197-205.
- [3] Miladinova PM, Lukanova VR. Investigations on the dyeing ability of some reactive triazine azo dyes containing tetramethylpiperidine fragment. *J. Chem. Technol. Metall.* 2017;52(1):3-12.
- [4] Karaman C, Karaman O, Show PL, Orooji Y, Karimi-Maleh H, Utilization of a double-cross-linked amino-functionalized three-dimensional graphene networks as a monolithic adsorbent for methyl orange removal: equilibrium, kinetics, thermodynamics and artificial neural network modeling. *Environ. Res.* 2021;207:112156.
- [5] Kamenicka B. Chemical degradation of azo dyes using different reducing agents: A review. *J. Water Process Engin.* 2024;61:105350.
- [6] Gharbani P. Modeling and optimization of Reactive Yellow 145 dye removal process onto synthesized MnOX-CeO₂ using response surface methodology. *Colloids and Surfaces A* 2018;548:191-7.
- [7] Benkaddour S., Slimani R, Hiyane H, El Ouahabi I, Hachoumi I, El Antri S, et al. Removal of reactive yellow 145 by adsorption onto treated watermelon seeds: Kinetic and isotherm studies. *Sustain. Chem. Pharm.* 2018;10:16–21.
- [8] Mohammad EJ, Lafta AJ, Kahdim SH. Photocatalytic removal of reactive yellow 145 dye from simulated textile wastewaters over supported (Co, Ni)₃O₄/Al₂O₃ co-catalyst. *Pol. J. Chem. Technol.* 2016;18(3):1-9.
- [9] Raval NP, Shah PU, Shah NK. Malachite green “a cationic dye” and its removal from aqueous solution by adsorption. *Appl. Water Sci.* 2017;7:3407-3445.
- [10] Khurana I, Saxena A, Bharti, Khurana, JM, Rai PK. Removal of dyes using graphene-based composites: a review. *Water Air Soil Poll.* 2017;228:180-197.
- [11] Ullah F, Ji G, Irfan M, Gao Y, Shafiq F, Sun Y. Adsorption performance and mechanism of cationic and anionic dyes by KOH activated biochar derived from medical waste pyrolysis. *Environ. Pollut.* 2022;314:120271.
- [12] Ofudje EA, Sodiya EF, Ibadin FH, Ogundiran AA, Alayande SO, Osideko OA. Mechanism of Cu²⁺ and reactive yellow 145 dye adsorption onto eggshell waste as low-cost adsorbent. *Chem. Ecol.* 2021;37(3), 268-289.
- [13] Giordano EDV, Brassesco ME, Camiscia P, Picó GA, Valetti NW. A new alternative and efficient low-cost process for the removal of reactive dyes in textile wastewater by using soybean hull as adsorbent. *Water Air Soil Poll.* 2021;232:165.
- [14] Lam PV, Duong NB, Bich PTN, Trang, QTT. Adsorption removal of Reactive Yellow 145 dye from aqueous solution using novel nZVI/(Fe–Mn) binary oxide/bentonite nanocomposite. *Desalin. Water Treat.* 2022;280:168-176.
- [15] Khataee A, Gholami P, Vahid B, Joo SW. Heterogeneous sono-Fenton process using pyrite nanorods prepared by non-thermal plasma for degradation of an anthraquinone dye. *Ultrason. Sonochem.* 2016;32:357-370.
- [16] Nguyen MB, Sy DT, Thoa VTK, Hong NT, Doan HV. Bimetallic Co-Fe-BTC/CN nanocomposite synthesised via a microwave-assisted hydrothermal method for highly efficient Reactive Yellow 145 dye photodegradation. *J. Taiwan Inst. Chem. Eng.* 2022;140:104543.
- [17] Ebrahimzadeh-Rajaei G. Removal of reactive yellow 145 dye from aqueous solution by photocatalytic and sonocatalytic degradation in the presence of CuO nanocatalyst. *Theor. Found. Chem. Eng.* 2022;56:1088–1099.
- [18] Aksu M, Hasa M, Tanattı NP, Erden B, Katircioğlu Sınmaz G, Boysan F, et al. Assessment of photocatalytic n-TiO₂/UV and n-TiO₂/H₂O₂/UV methods to treat DB 86, RY 145 and AV 90 dye mix containing wastewater. *Desalin. Water Treat.* 2022;266:226-235.
- [19] Yaghoubi A, Ramazani A, Fardood ST. Synthesis of Al₂O₃/ZrO₂ nanocomposite and the study of its effects on photocatalytic degradation of Reactive Blue 222 and Reactive Yellow 145 dyes. *Chemistry Select* 2020;5:9966-9973.
- [20] Bashar MA, Molla MTH, Chandra D, Malitha MD, Islam MS, Rahman MS, et al. Hydrothermal synthesis of cobalt substitute zinc-ferrite (Co_{1-x}Zn_xFe₂O₄) nanodot, functionalised by polyaniline with enhanced photocatalytic activity under visible light irradiation. *Heliyon* 2023;9(4): e15381.
- [21] Mousavi SE, Younesi H, Bahramifar N, Tamunaidu P, Karimi-Maleh H. A novel route to the synthesis of α-Fe₂O₃@C@SiO₂/TiO₂ nanocomposite from the metal-organic framework as a photocatalyst for water treatment. *Chemosphere* 2022;297:133992.
- [22] Brillas E. Removal of insecticides from waters and soils by sulfate radical-based advanced oxidation processes. *Appl. Res.* 2023; e202300055.
- [23] Karaca S, Çakmak Önal E, Açıslı Ö, Khataee A. A literature review of ultrasound technology and its application in wastewater disinfection. *Mater. Chem. Phys.* 2021;260:124125.
- [24] Dindarsafa M, Khataee A, Kaymak B, Vahid B, Karimi A, Rahmani, A. Heterogeneous sono-Fenton-like process using martite nanocatalyst prepared by high energy planetary ball milling for treatment of a textile dye. *Ultrason. Sonochem.* 2017;34:389-399.
- [25] Wang B, Shi W, Zhang H, Ren HY, Xiong MY. Promoting the ozone-liquid mass transfer through external physical fields and their applications in

- wastewater treatment: A review. *J. Environ. Chem. Eng.* 2021;9(5):106115.
- [26] Joseph CG, Puma GL, Bono A, Krishnaiah D. Sonophotocatalysis in advanced oxidation process: A short review. *Ultrason. Sonochem.* 2009;16(5):583–589.
- [27] Ojo BO, Arotiba OA, Mabuba N. Sonoelectrochemical oxidation of sulfamethoxazole in simulated and actual wastewater on a piezopolarizable FTO/BaZr_xTi_(1-x)O₃ electrode: reaction kinetics, mechanism and reaction pathway studies. *RSC Adv.* 2022;12:30892-30905.
- [28] Liu P, Wu Z, Abramova AV, Cravotto G. Sonochemical processes for the degradation of antibiotics in aqueous solutions: A review. *Ultrason. Sonochem.* 2021;74:105566.
- [29] Yap HC, Pang YL, Lim S, Abdullah AZ, Ong HC, Wu CH. A comprehensive review on state-of-the-art photo-, sono-, and sonophotocatalytic treatments to degrade emerging contaminants. *Int. J. Environ. Sci. Technol.* 2019;16:601-628.
- [30] Sathishkumar P, Mangalaraja RV, Anandan S. Review on the recent improvements in sonochemical and combined sonochemical oxidation processes—A powerful tool for destruction of environmental contaminants. *Renew. Sust. Energ. Rev.* 2016;55:426–454.
- [31] Akdağ S, Rad TZ, Keyikoğlu R, Orooji Y, Yoon Y, Khataee A. Peroxydisulfate-assisted sonocatalytic degradation of metribuzin by La-doped ZnFe layered double hydroxide. *Ultrason. Sonochem.* 2022;91:106236.
- [32] Kjellqvist L, Selleby M. Thermodynamic assessment of the Fe-Mn-O system. *J. Phase Equilib. Diffus.* 2010;31:113-134.
- [33] Azimi G, Leion H, Rydén M, Mattisson T, Lyngfelt A. Investigation of different Mn–Fe oxides as oxygen carrier for Chemical-Looping with Oxygen Uncoupling (CLOU). *Energy and Fuels* 2013;27(1):367-377.
- [34] Wokon M, Kohzer A, Linder M. Investigations on thermochemical energy storage based on technical grade manganese-iron oxide in a lab-scale packed bed reactor. *Sol. Energy* 2017;153:200-214.
- [35] World dye variety [Cited 2023 Nov 15] Available from: (<https://www.worlddyevariety.com/reactive-dyes/reactive-yellow-145.html>).
- [36] Wang J, Wang S. Activation of persulfate (PS) and peroxymonosulfate (PMS) and application for the degradation of emerging contaminants. *Chem. Eng. J.* 2018;334:1502-1517.
- [37] Liu H, Bruton TA, Li W, Buren JV, Prasse C, Doyle FM, et al. Oxidation of benzene by persulfate in the presence of Fe(III)- and Mn(IV)-containing oxides: Stoichiometric efficiency and transformation products. *Environ. Sci. Technol.* 2016;50:890–898.
- [38] Deng Q, Zhang X, Chang L, Chai H, Huang Y. The MOF/LDH derived heterostructures Co₃O₄/MnCo₂O₄ composite for enhanced degradation of levofloxacin by peroxymonosulfate activation. *Sep. Purif. Technol.* 2022;294:121182.
- [39] Liang C, Wang ZS, Bruell CJ. Influence of pH in persulfate oxidation of TCE at ambient temperatures. *Chemosphere.* 2007;66(1):106-113.
- [40] Ren W, Huang X, Wang L, Liu X, Zhou Z, Wang Y., et al. Degradation of simazine by heat-activated peroxydisulfate process: A coherent study on kinetics, radicals and models. *Chem. Eng. J.* 2021;426:131876.
- [41] Vu HT, Nguyen MB, Vu TM, Le GH, Pham TTT, Nguyen TD, et al. Synthesis and application of novel nano Fe-BTC/GO composites as highly efficient photocatalysts in the dye degradation. *Topics in Catalysis* 2020;63:1046–1055.
- [42] Nguyen MB, Le GH, Nguyen TD, Nguyen QK, Pham TTT, Lee T, et al. Bimetallic Ag-Zn-BTC/GO composite as highly efficient photocatalyst in the photocatalytic degradation of reactive yellow 145 dye in water. *J. Hazard. Mater.* 2021;420:126560.

Experimental Investigation of Photovoltaic Panel Surface Temperatures and Electricity Production in Summer

Perihan ÇULUN^{1*} 

¹Bingöl University, Engineering and Architecture Faculty, Mechanical Engineering Department, Bingöl, Türkiye
Perihan ÇULUN ORCID No: 0000-0002-1797-9695

*Corresponding author: pculun@bingol.edu.tr

(Received: 28.02.2024, Accepted: 08.06.2024, Online Publication: 28.06.2024)

Keywords
Photovoltaic
panel,
Electricity,
Temperature,
PCM,
TEC,
PV Cooling

Abstract: Due to the efficiency drops in solar panels at temperatures above 25°C, various panel surface temperature reduction studies are ongoing. Phase change materials can cool surfaces without needing an external energy source, but their performance varies depending on seasonal temperatures. Within the scope of this study, instantaneous panel surface temperatures in August were evaluated to present the panel temperature value of the summer months in Bingöl. Along with panel surface temperature values, instantaneous voltage, current, power, and efficiency results were also evaluated. According to the temperature measurement results made with thermocouples, the average and local maximum temperature on the front surface of the panel was 55°C, and 65°C respectively. On the other hand, according to the thermal camera measurement, it was understood that there was no homogeneous temperature distribution throughout the panel and the temperature value increased to 85°C in some local areas. It has been understood that this temperature value is far from the panel operating conditions, therefore it is essential to cool the panels with appropriate phase change materials.

77

Yaz Aylarında Fotovoltaik Panel Yüzey Sıcaklıkları ve Elektrik Üretiminin Deneysel İncelenmesi

Anahtar Kelimeler
Fotovoltaik
panel,
Elektrik,
Sıcaklık,
PCM,
TEC,
PV Soğutma

Öz: Güneş panellerinde 25 °C'nin üzerindeki yüzey sıcaklıklarda verim düşüşleri nedeniyle panel yüzey sıcaklığının düşürülmesi üzerine çeşitli çalışmalar devam etmektedir. Faz değiştiren malzemeler harici bir enerji kaynağına ihtiyaç duymadan yüzeyleri soğutabilir, ancak performansları mevsim sıcaklıklarına bağlı olarak değişir. Bu çalışma kapsamında Bingöl ilinde yaz aylarına ait panel sıcaklık değerini ortaya koymak amacıyla Ağustos ayı anlık panel yüzey sıcaklıkları değerlendirilmiştir. Panel yüzey sıcaklık değerlerinin yanı sıra anlık gerilim, akım, güç ve verim sonuçları da değerlendirilmiştir. Termokuplular ile yapılan sıcaklık ölçüm sonuçlarına göre panelin ön yüzeyinde ortalama ve yerel maksimum sıcaklık sırasıyla 55 °C ve 65 °C olarak tespit edilmiştir. Öte yandan termal kamera ölçümüne göre panel genelinde homojen bir sıcaklık dağılımının olmadığı ve bazı yerel bölgelerde sıcaklık değerinin 85 °C'ye kadar çıktığı anlaşılmıştır. Bu sıcaklık değerinin panel standart çalışma şartlarından çok uzak olduğu, dolayısıyla panellerin uygun faz değiştirici malzemelerle soğutulmasının önemli olduğu anlaşılmıştır.

1. INTRODUCTION

Solar energy systems are examined in two parts: collector applications, thermal systems, and photovoltaic panel (PV) applications, which produce electrical energy. Although the efficiency of solar thermal systems is known to be around 60%, the efficiency of PV panels is low, it changes between 12-20% [1,2]. PV efficiency depends on

the panel material, panel type, weather conditions, solar incidence angle, panel surface temperature, etc. Due to the heat-absorbing feature of the panel material, most of the radiation also causes the panel to heat up. According to some studies, it is said that approximately 80% of the solar radiation coming to the panel unit surface cannot be converted into electrical energy, and this causes the panel temperature to increase [3]. Also, it has been observed that

as solar radiation increases during the day, panel temperature and panel efficiency increase together. However, it is known that increasing panel temperature negatively affects most parameters of the panel and ultimately decreases panel efficiency [4]. So the amount of electricity produced by photovoltaic panels is directly proportional to solar radiation and inversely proportional to the panel surface temperature. It is known that the surface temperature of a panel can rise to 40°C above the environmental temperature, depending on the solar radiation on the surface [5,6]. Although it depends on the environment where the experiment is performed, the monocrystalline panel surface temperature can increase from 51.8°C to 88.2°C [7]. In another study, it was mentioned that the temperature in the uncooled panel was 95 °C, while the temperature in the cooled panel was 55 °C [8]. According to some studies, if the surface temperature is reduced by 1 °C, PV panel efficiency increases by 0.5% or 0.65% [9]. In a study conducted in an area where solar radiation is 901 W/m², it is mentioned that a 7.28% efficiency increase was achieved by reducing the panel surface temperature by 4.7 °C [10]. This means there was a 1.6% increase in panel efficiency with a 1°C temperature drop. In another similar study, a 7.3% efficiency increase was achieved with a 2.4°C temperature drop in the region where solar radiation was 100-1120 W/m² [11]. Therefore, a 3% increase in efficiency was achieved with a 1°C temperature drop. According to these results, the increase in panel efficiency at a 1°C temperature drop also depends on solar radiation. In other words, in case of a 1°C temperature drop in regions with higher solar radiation, the increase in panel efficiency will also be higher. Bahaidarah et al., [12] mention that if there is a 20% decrease in panel surface temperature, there will be a 9% increase in electrical efficiency. According to the electrical data graphs in the study by Kane et al., [13], it shows that the change in the panel surface temperature from 25°C to 75°C and the change in the environmental temperature from 25°C to 35°C will cause a 20%-27% change in the panel electrical efficiency.

The best efficiency in solar panels is achieved when the surface temperature is 25°C at 1000W/m² solar radiation, which is the panel's standard operating condition [14]. Today, it is known that even the best panels have a maximum efficiency of 17-18%, whereas monocrystalline panel efficiencies are generally between 12-15% [15]. It is also stated in literature studies that panel efficiency can reach up to 26% depending on the panel material [16]. With the increase in panel temperature, panel open circuit voltage, filling factor, panel output power decrease, and short circuit current increases [16,17]. Although the short circuit current (I_{sc}) increases slightly, the open circuit voltage (V_{oc}) decreases more obviously with the increase in panel temperature [18], so the maximum power and efficiency of the panel decrease significantly [14, 19].

In his study, Yılancı [14] mentions an approximately 20% increase in panel efficiency with appropriate thermoelectric cooling. Considering these situations, it is understood that an efficiency increase of approximately 20-30% will be achieved by reducing the panel

temperature from 50 °C to 40 °C in the summer months when solar radiation is at its highest. Therefore, it is predicted that panel efficiency will increase by up to 50% with good cooling. There are studies stating that PV/T systems will always produce more electricity, the payback period will be shorter, and their lifespan will be longer than the PV system [20]. It is also possible to store energy as electricity or heat in PV/T systems. Kabul and Duran [8] achieved a 7% increase in efficiency and a 31% increase in power by reducing the panel surface temperature by using cold water in the PV/T study. It has been determined that if nanofluid water is used instead of pure water in PV/T systems, much better cooling will be achieved on the panel surface, hot water can be obtained and the electrical output power will be 51% higher [21]. Gürbüz et al. [22] by using commercial-type phase change material (RT55) for cooling purposes, a maximum power of 31.5W was achieved in a 40W power PV/T panel with 424 × 674 × 25 dimensions and 36° angle. The necessity of cooling PV and PV/T modules due to high summer temperatures is established in much literature [23]. Kerem et al. [17] stated in their study at Osmaniye Korkut Ata University that the panel efficiency increased by 14% as a result of cooling the panel surface with cold water. It is understood that effective surface cooling of PV panels is very important in terms of efficiency.

Panel active cooling systems require pumps, compressors, etc. Since they use energy-consuming devices, they reduce the efficiency of the entire system. Passive cooling systems developed as an alternative to these can provide a lower cost of energy produced in the long run, as there are no energy-consuming devices. Passive cooling systems, which are more economical and state-of-the-art, are under development. Phase change materials are being tested within the scope of passive cooling systems. However, since phase change materials (PCM) have different melting/freezing temperatures and the daily/annual operating conditions of solar panels constantly change, PCMs to be used in passive cooling systems must be carefully selected. It will not be possible to use the system actively in the long term with a randomly selected phase change material. To select appropriate phase change materials, it is necessary to know the long-term operating conditions of PV panels in different regions. Particularly local solar radiation and panel temperature data will be of great importance in the studies to be carried out. With the use of relevant comprehensive data, more appropriate PCM selection and passive cooling system designs will be useful for a longer period. In this sense, instantaneous and average experimental/numerical data are to be obtained for each region to be used for proper PCM selections.

It is also possible to passively cool PV panels by using a thermoelectric generator. There are studies in this field using thermoelectric coolers (TEC), which have the same operating principle as thermoelectric generators [24, 25]. However, if a thermoelectric cooler is used in panel cooling, electricity will be consumed, but if a thermoelectric generator (TEG) is used instead, no additional electrical energy will be used, and additional electrical energy will be produced from the heat of the hot

panel. This will increase the total efficiency of the PV/TEG system. So is of great importance to determine the surface temperatures of panels in different regions and different climatic conditions to design good systems, whether it is a PV/PCM or PV/TEG system, which can be called panel passive cooling systems.

In this study, panel surface temperatures, panel power, and efficiency were investigated in the high-temperature month of August in Bingöl province, to serve as a reference for future studies on panel cooling. For this purpose, data obtained from the panel's front and back surfaces were evaluated. The panel temperatures to be obtained for Bingöl province within the scope of our study will be of great importance for suitable designs in suitable PV/TEG or PV/PCM passive cooling systems.

2. MATERIAL AND METHOD

Bingöl province, located in the northern hemisphere of the world, is surrounded by Muş in the east, Erzurum and Erzincan in the north, Tunceli and Elazığ in the west, and Diyarbakır in the south (Figure 1a). Bingöl borders are between 41 - 20 and 39 - 56 eastern longitudes and 39 - 31 and 36 - 28 northern latitudes. High temperatures in Bingöl start in mid-June and last until mid-September. The average daily high temperature on these dates is above 28°C. The hottest months in the Bingöl region are July and August. In these months, the average high temperature is 33°C, the low temperature is 19°C, and maximum temperatures can reach 40°C [26]. Bingöl's annual sunshine duration is 2719 hours, and as seen from Bingöl's solar map (Figure 1b) annual average solar radiation is around 1650 kWh/m².

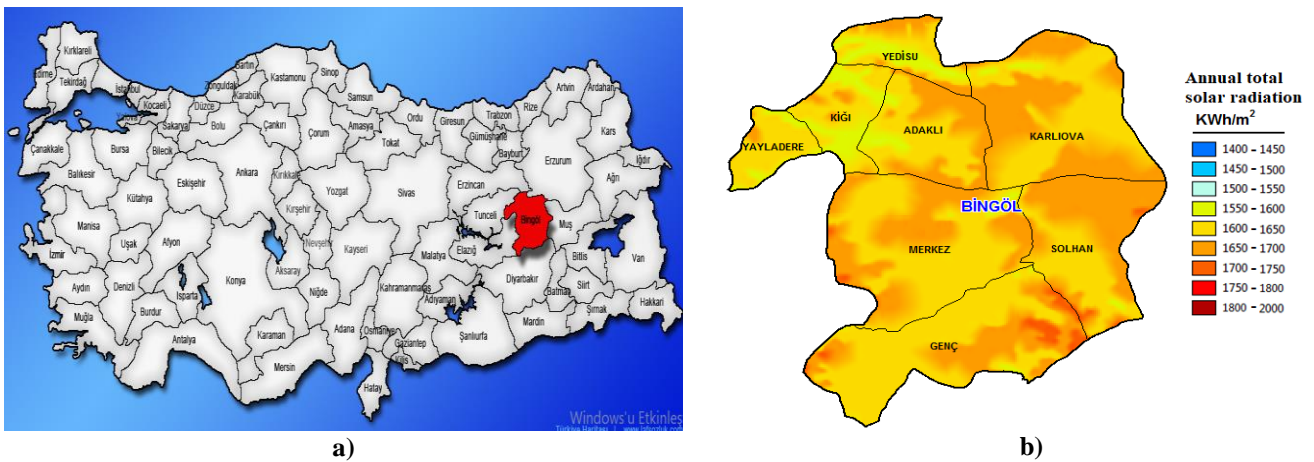


Figure 1. a) The location of Bingöl on the map of Turkey b) Solar radiation map of Bingöl (GEPA)[27]

Turkey Solar Energy Atlas [27] data were taken as the basis for solar radiation values. Accordingly, Figure 2a shows the amounts of solar radiation in Bingöl province by month, and Figure 2b shows the daily sunshine distribution for months. Here, the daily average amount of solar radiation is 5.81 kWh/m²-day, and the average daily sunshine duration is 10.7 hours for August. In the light of these data, the total solar radiation (E) incident on the panel surface is equal to the product of the solar radiation falling on the panel unit area (I) and the panel effective surface area (A_p) and can be calculated with equation number 1 [16, 28]. The electrical efficiency (η) of a panel shows the ratio of the maximum electrical energy (P_{max})

obtained from the panel to the total solar radiation (E) incident on the panel surface [16, 28]. Panel efficiency can be calculated with Equation 2. In Equation 2 and Equation 3 I_{max}, V_{max}, I_{sc}, V_{oc}, and FF indicate the maximum current, maximum voltage, short circuit current, open circuit voltage, and fill factor, respectively. In the study, instantaneous electricity and temperature data were taken throughout the day in August, one of the hottest months of the year. According to meteorological data, on the relevant date (26 August - 3 September 2023), the related Bingöl outdoor temperature is between 30-31°C and the average wind speed is 7m/s.

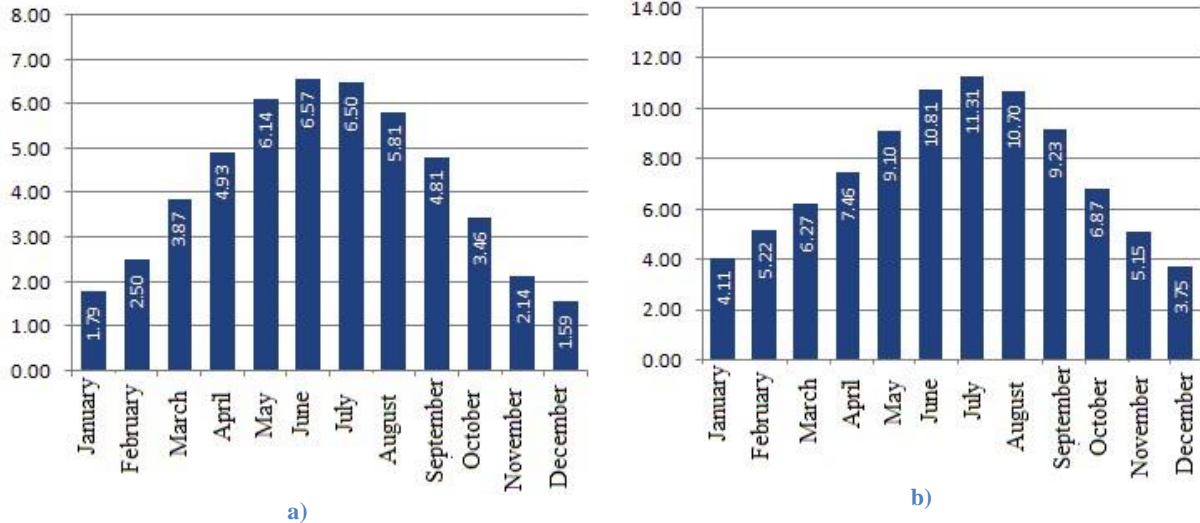


Figure 2. a) Global radiation values (kWh/m²-day) of Bingöl, b) The daily sunshine duration of Bingöl(hour)(GEPA)[27]

$$E = IxA_p \quad (1)$$

$$\eta = \frac{P_{max}}{E} = \frac{I_{max}V_{max}}{IxA_p} = \frac{I_{sc}xV_{oc}xFF}{IxA_p} \quad (2)$$

$$FF = \frac{I_{max}V_{max}}{I_{sc}xV_{oc}} \quad (3)$$

Two identical panels with 25W power were used to investigate panel production power, efficiency, and panel surface temperatures. The monocrystalline panel, whose properties are given in Table 1, was preferred because it is the most preferred in Turkey and has higher efficiency than polycrystalline [29].

Table 1. Panel label data

Rated Power (P _m)	25W
Type	Monocrystal
Total Number of Cells (N _s)	36
Open Circuit Voltage (V _{oc})	24.84V
Max. Voltage (V _{mp})	20.70V
Short Circuit Current (A _{sc})	1.27A
Max. Current (A _{mp})	1.21A
Max. System Voltage (V)	1000V
Module Dimensions (mm) Panel efektifif alanı(A _p)	362*433*20 0.157m ²
Weight (kg)	1.68

Instantaneous voltage and current values were noted with a digital voltmeter/amperimeter. 10 LED lamps with a power of 1.5W and 1 single lamp with a power of 10W were used to create resistance to read the current and voltage values through the system (Figure 3, Table 2). As seen in Figure 3, temperature data were taken with digital thermometers at a total of 6 points on both panels, 4 points on the front surface of the panel (T₁, T₂, T₃, T₄), 2 points on the back surface of the panel (T₅, T₆). Ambient

temperature (T_o) was also measured for accurate evaluation of panel surface temperatures. Surface temperatures were measured with the help of k-type thermocouples in the 2-channel CEM DT 612 model thermometer and the 4-channel CEM DT 3891G model digital thermometer (Table 2). Temperature data were taken with the thermal camera also to see local temperature changes.

Table 2. Information of devices used

Instrument name	Measurement range	working environment conditions	Error rate
Digital manual-type thermometer With 2 two input signals	-50°C ÷ 1300°C	0°C ÷ 50°C	±2.2°C or ±0.75%
Digital manual type thermometer with 4 input signals	-50 ÷ 1370°C	0°C ÷ 75°C	± 0,15 % K type ± 2 % Infrared
Voltmeter /amper meter	Dc 4.5-100V Dc 0.00-10.00A	-10°C ÷ 65°C	± 1%
Thermal Camera	-30 ÷ 750°C	-15 ÷ 50°C	
Resistance	10 of 1.5W led lamps +10W single lamp		

A thermal camera, whose detailed specifications are given in Table 2, was used to see local temperature fluctuations on the surface. The data were taken at 15-minute intervals during the daytime between 10:30 and 16:30 when solar radiation is at its highest.

A 45° tilt angle was used in this study as the best data was obtained at the related angle according to our previous study[29]. It is known that the highest efficiency is achieved in regions located in the northern hemisphere if the solar panels are directed toward the south. In this regard, the panels are oriented towards the south(Figure 4). The experimental setup was installed in an environment where there was no shadow factor between the specified measurement times.

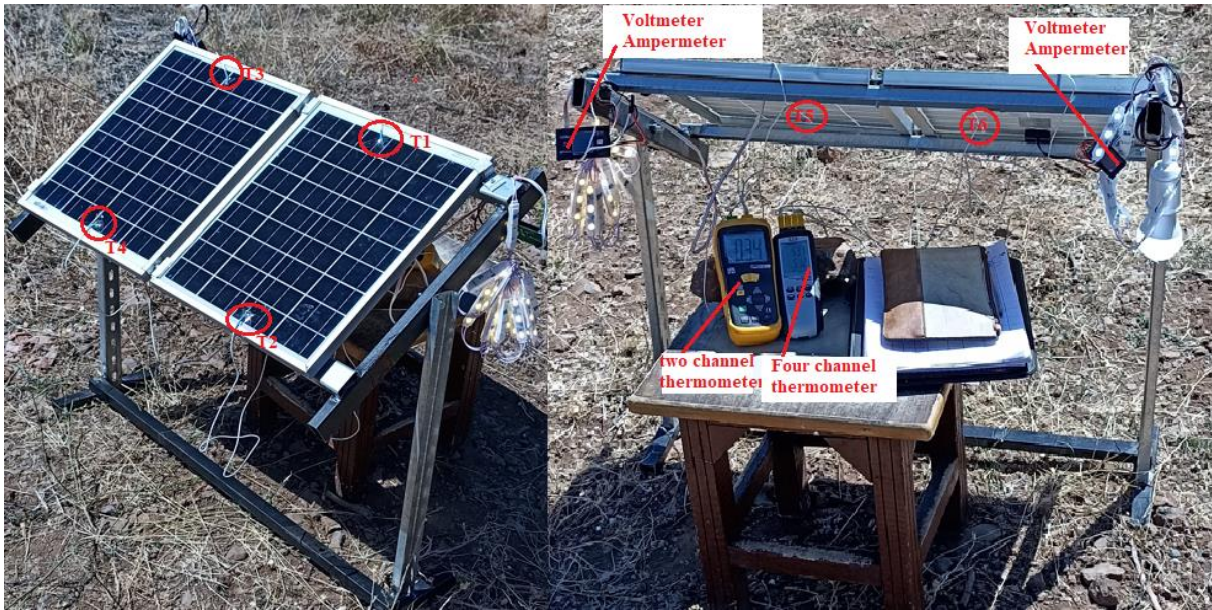


Figure 3. Experimental setup

3. RESULTS

The changes in panel surface instantaneous temperature (T_{ps}) data taken in different weeks in August according to time (h) are presented in Figure 5. As seen in the figure, digital temperature measurements were taken from two points on the back surface of the panel and four points on the front surface of the panel, measured with an interval of 15 minutes. According to the results, the front surface temperatures of the panel (T_1 , T_2 , T_3 , and T_4) were generally higher than back surface temperatures (T_5 , and T_6) with a difference of 10°C . It has been understood that a temperature difference of 10°C between the front and back surfaces of the panel is compatible with the literature

[28]. According to the temperature measurement results made with thermocouples, the average temperature on the front surface of the panel was 55°C , local maximum temperature also reached 65°C . From the relevant graph, it can be read that all panel front temperatures are above 45°C . The average temperature value of the back surface was calculated as 45°C . It is also possible to read similar results from the instantaneous temperature graph (Figure 5). According to Figure 5, it is seen that the panel front surface temperature data is much higher than the environmental temperature ($> T_0 = 35^{\circ}\text{C}$) throughout the day, and the panel back temperatures T_5 and T_6 are close to the environmental temperature.



Figure 5. Instant temperature graphs, a) First day, b) Second day, c) Third day, d) Fourth-day data

According to the data taken from another day, it is seen that the panel minimum surface temperature is around 30°C throughout the day, the average temperature is around 40-45°C, and the maximum surface temperature rises to 80°C at 12:30 (Figure 7b). Therefore, due to their ability to absorb and retain heat, panel temperatures can reach up to 80-85°C (Figure 6c and Figure 7b). However, according to both meteorological data and also according to Figure 5b, and Figure 5c, the average temperature value of the surrounding environment (T_o) on the relevant date is 30-36°C.

Thermal camera images were taken from the panel's front surface every two hours. Thermal images of the panel pair, whose real images are shown in Figure 3 and Figure 4, and corresponding clocks, are presented in Figure 6 and Figure 7. The images more clearly reveal a non-uniform temperature distribution on the panel surfaces. Although the panels are identical in Figure 6, at different times (11:30, 12:30, 13:30, 14:30), a higher temperature region was detected in the second panel. It is thought that the relevant temperature difference is due to the insufficient orientation of the panel towards the south. It can be said that this situation is related to the Azimuth angle not being adjusted properly. As it is known, while the panels are oriented exactly to the south, they can lean a little east or a little west. This can be possible by adjusting the Azimuth angle professionally. According to the images, higher temperature regions were seen in the upper region

of both panels. During the day, the minimum temperature value is approximately 40°C (Figure 6c, Figure 6d), the minimum average temperature is approximately 45°C, and the maximum temperature is up to 85°C (Figure 6c). In similar literature studies, it was understood that the average solar radiation value was 1100W/m² between 11:00 and 13:00 hours, and the panel temperature was around 110°C [30].

It is also stated in the literature that the monocrystalline panel surface temperature can increase from 51.8°C to 88.2°C, depending on the environment temperature in which the experiment is performed [7]. In the study conducted for Isparta province, it was mentioned that the temperature in the uncooled panel was 95 °C, while the average temperature in the cooled panel was 55 °C [8]. If the panel surface temperature value of Bingöl is high like this, located in the northern hemisphere of Turkey, it is clear that these temperatures will be even higher in the southern provinces such as Antalya, Şanlı Urfa etc. So it is essential to cool the solar power systems to be installed in the relevant regions with appropriate cooling methods, both to increase their electrical efficiency and make the panels last longer. Since the high temperatures the panels are exposed to will deteriorate the structure of the panels, the panels will have a shorter lifespan and produce less electricity than expected.

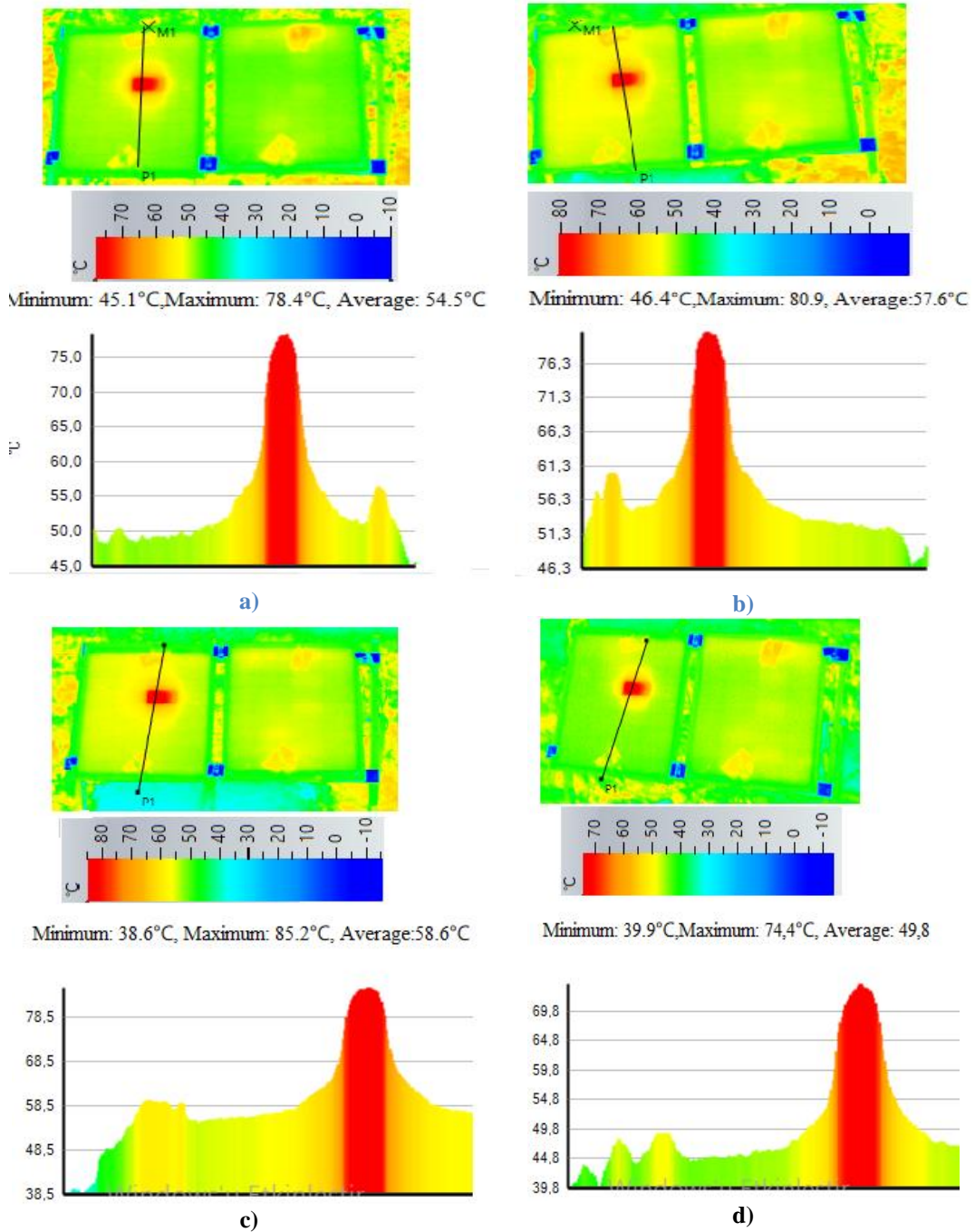


Figure 6. Thermal images of PV panel, a) at 11:30, b) at 12:30, c) at 13:30, d) at 14:30

Since high temperatures are a result of high solar radiation, high solar radiation increases both the panel surface temperature and electrical data. For example, according to the temperature data on the first day (Figure 5a), since the panel temperatures were not stable throughout the day, the electricity efficiency curve peaked in a narrower range (between 12.00 and 15.30) (Figure

8a). In Figure 5b, temperatures throughout the day (especially the panel front surface temperatures T_1 , T_2 , T_3 , and T_4 values) are more uniform and higher, and in parallel, the related electrical data is also higher (Figure 8b).

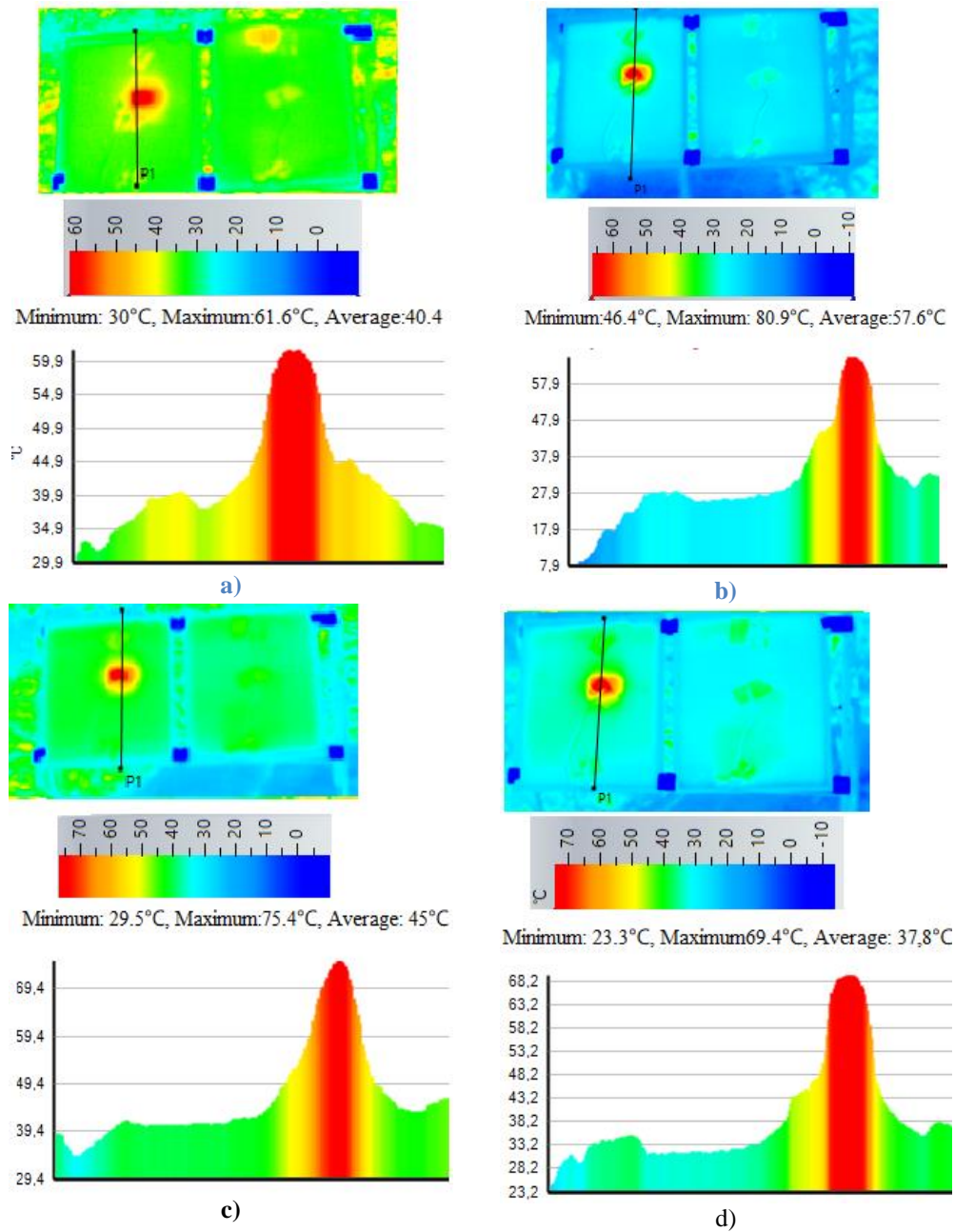


Figure 7. Thermal images of PV, a) at 10:30, b) at 12:30, c) at 14:30, d) at 15:30

The ideal panel temperature value should be 25°C according to literature research. According to the IEC 60904-3 [31] panel standard, it is stated that at 1000 W/m² radiation, which is the standard test conditions, the air mass flow rate is 1.5 and the relevant panel ideal temperature value is 25°C. Under the same radiation intensity, panel surface temperatures closest to 25°C will be the most efficient. In this regard, the high surface temperature of panels should be reduced with appropriate cooling methods. Therefore, if the surface temperature had been reduced with proper cooling on the second day, the efficiency would have been higher (Figure 5b and

Figure 8b). Various literature has stated that by reducing panel temperatures by applying appropriate cooling under the same radiation conditions, significant efficiency increases will be achieved and panel life will increase, as thermal stresses that will occur in the material will be prevented [15, 32, 33]. Figure 8 shows that panel power and efficiency values are at their highest during the 12:00-15:00 hours when the solar radiation value is highest. Parallel to this, panel front surface temperatures increase proportionally during the same hours. Therefore, in passive cooling designs can be developed especially for these noon hours.

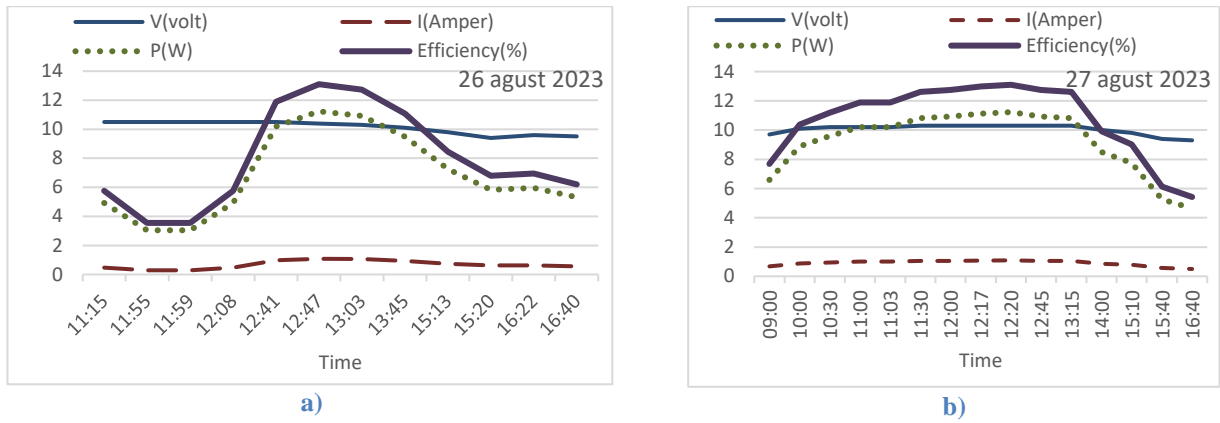


Figure 8. Instant electrical data, a) First day, b) Second day

Gürbüz et al. [22] by using commercial-type PCM (RT55) for cooling purposes in a 40W PV/T panel, a maximum power of 31.5W was achieved. Considering that the maximum electricity obtained without cooling in the 25W panel used in this study is around 11-12W (Figure 8a, Figure 8b), Gürbüz et al., [22] reported significant efficiency gains with panel cooling (FDM cooling) in the PV/T study. While an average of 20W electricity was expected to be obtained without cooling from a 40W panel, approximately 1.5 times higher electricity (31.5W) was obtained with the hot water obtained. If we make an evaluation from here, there is actually an increase in efficiency of at least 30% thanks to PCM. For example, in another study conducted for Pakistani climate conditions, it was mentioned that the breeding yield was increased by 29% with the organic PCM used [34]. Based on all these results, it is of great importance for the country's economies to carefully observe the increasing panel temperatures, especially in the summer months, and to carry out appropriate cooling processes. For panel passive cooling systems, especially those developed using PCM, to have relatively longer and wider usage areas, data on the outdoor temperatures where the panel is operated and the panel surface temperature will be needed. In this regard, the operating conditions of panels and relevant panel surface temperature data should be established throughout the country, especially in the summer months.

4. DISCUSSION AND CONCLUSION

Passive cooling systems that are more effective and more economical should be developed. So there is a need to select the appropriate phase change materials with suitable melting/freezing temperatures and to have specific passive cooling systems for certain climatic conditions and certain regions. To select appropriate phase change materials, it is necessary to know the long-term operating conditions of PV panels in different regions. Particularly local solar radiation and panel temperature data will be of great importance in the studies to be carried out. With the use of relevant comprehensive data, more appropriate phase change material selection and passive cooling system designs that will be useful for a longer period will be possible. In this sense, the instantaneous and average experimental and numerical data obtained for each region to be used in panel cooling studies are important in selecting the appropriate PCM.

According to the results of the 25W monocrystalline panel used in our study, panel efficiency values were found to be as low as 3% to 13%. Due to their heat-absorbing properties, solar panels absorb most of the solar energy as heat, approximately 80% or 60% [3, 16]. This causes the panel surface temperatures to warm up well above the ambient temperature. According to our study, data taken in August, one of the hottest months in Bingöl, the temperature value of the panel front surface was on average 10°C higher than the rear surface. On the other hands front surface temperature values can rise to a maximum of 85°C, especially during the noon hours (12:00-15:00), when solar radiation values are most intense, in parallel with the radiation intensity. In this regard, PCM material selection and system design accordingly can provide better performance, especially in passive cooling designs. For example, according to the thermal camera temperature results, the maximum temperature was 85°C on one day and 80°C on the other day. In this case, if higher efficiency will be obtained from the panel, especially at noon hours, PCM material with an average melting temperature of 50-65C can be used. Or, if it is desired to increase efficiency throughout the day, the PCM melting temperature can be selected lower a. Ccordint to average temperature of panel surface. For example, if the average temperature of the panel throughout the day is around 55-60C, it would be more appropriate to choose a PCM melting point of 40-45°C. Of course, these scenarios need to be tested in the field and more data must be obtained for different regions and different seasons. Different material performances can be tried in this range. Thus, material melting temperature selections can be made more accurately thanks to extensive panel surface temperature data.

Panel efficiency will be further increased if the panel temperature is reduced from 85°C to at least the environment temperature (40°C) with appropriate cooling methods within the relevant period. The panel temperature values obtained as a result of our study are of great importance for the selection of appropriate PCMs, especially in passive cooling, which is likely to be used in the future. In this regard, if the panel surface temperature has reached a maximum of 85°C in Bingöl province, these temperatures will be much higher in the southern provinces of Turkey. So cooling operations will be more meaningful as they will provide a higher efficiency

increase in southern regions. In northern regions where radiation is low, the application of passive cooling systems is more suitable in terms of system total cost and total efficiency. As can be seen, the widespread use of cooling PV panels, both passively and actively, will increase panel efficiency. In this respect, any progress in both active and passive cooling methods will be important. In active cooling/heating systems such as vapor compression cooling systems or heat pumps, additional electricity is consumed in the system because a pump or fan systems are used to circulate the intermediate fluid [35]. However, since there is no pump or fan in passive systems, there is no additional energy cost. In southern regions where radiation is higher, active or passive cooling systems may be preferred, but it would be more appropriate to choose passive systems as they are more economical in the long term [36]. In addition, studies on increasing the conductivity coefficient of PCM material continue in these studies. For example, there are studies using nanomaterials to increase the transmission coefficient of the PCM material in order to achieve higher efficiency in this field [37]. In addition, since PV panel cooling is costly, increasing panel applications that do not require cooling will be an important development. For example, it is possible to use PV panels more efficiently in moving vehicles. Since the PV cells to be used on the top, front, and sides of the vehicle will be exposed to airflow while in motion, they will be protected from overheating that will cause efficiency drops and there will be no need for panel cooling. In this regard, studies on the use of PV panels in moving objects such as vehicles should be accelerated. It would be beneficial for future panel cooling studies to be carried out in this direction. In addition, another way to reduce panel cooling system costs will of course be PV/T systems. The widespread use of PV/T panels on roofs is extremely important in terms of meeting building electricity and hot water needs more efficiently. As a matter of fact, in PV/T systems, the complete system will be much more efficient as the PV panel will be actively cooled thanks to the domestic water circulated behind the PV panel. As we mentioned in our previous study [37], under normal conditions, if the payback period of PV systems installed on the roof of a house is 6 years on average, if this system is designed as PV/T, this payback period will be approximately halved. It is clear that the dissemination of PV/T systems, especially in industry, will make a significant contribution to the economy. Because in the industrial area, there is a need for hot water, hot air, heat pump etc. It will be possible to meet the electricity needs with the electricity produced at high efficiency by using it for the needs and by actively cooling the PV system. In solar energy systems, PV/T systems should be considered first, depending on the facilities located in the installation area. It would be more logical to choose a PV/T system instead of classical PV in all regions that require hot water or hot air (such as a heat pump).

Acknowledgment

In the study, devices in the Mechanical Engineering department laboratory of Bingöl University Faculty of

Engineering and Architecture were used. Thanks to the Bingöl University for their relevant contributions.

REFERENCES

- [1] Tyagi VV, Rahim NA, Rahim NA, Jeyraj A, Selvaraj L. Progress in solar PV technology: Research and achievement. *Renewable and sustainable energy reviews*, 2013; 20: 443-461.
- [2] Sharma S, Jain KK, Sharma A. Solar cells: in research and applications a review. *Materials Sciences and Applications*, 2015; 6(12):1145.
- [3] Sun X, Dubey R, Chattopadhyay S, Khan MR, Chavali RV, Silverman, TJ, et al. A novel approach to thermal design of solar modules: Selective-spectral and radiative cooling. In *2016 IEEE 43rd Photovoltaic Specialists Conference (PVSC), 2016*; 3584-3586). IEEE.
- [4] Sudhakar P, Kumaresan G, Velraj R. Experimental analysis of solar photovoltaic unit integrated with free cool thermal energy storage system. *Solar Energy*, 2017; 158: 837-844.
- [5] Makki A, Omer S, Sabir H. Advancements in hybrid photovoltaic systems for enhanced solar cell performance. *Renewable and sustainable energy reviews*, 2015; 41: 658-684.
- [6] Sheik MA, Aravindan MK, Cuce E, Dasore A, Rajak U, Shaik S, et al. A comprehensive review on recent advancements in cooling of solar photovoltaic systems using phase change materials. *International Journal of Low-Carbon Technologies*, 2022; 17: 768-783.
- [7] Khanna S, Sundaram S, Reddy KS, Mallick TK. Performance analysis of perovskite and dye-sensitized solar cells under varying operating conditions and comparison with monocrystalline silicon cell. *Applied Thermal Engineering*, 2017; 127: 559-565.
- [8] Kabul A, Duran F. Isparta ilinde fotovoltaik/termal (PV/T) hibrit sistemin performansı. *Tr. Doğa ve Fen Derg.*, 2014; 12 (2):68 -75.
- [9] Klugmann-Radziemska E, Wcisło-Kucharek P. Photovoltaic module temperature stabilization with the use of phase change materials. *Solar Energy*, 2017; 150: 538-545.
- [10] Luo Z, Huang Z, Xie, N, Gao X, Xu, T, Fang Y. Numerical and experimental study on temperature control of solar panels with form-stable paraffin/expanded graphite composite PCM. *Energy Convers. Manage.*, 2017; 149: 416-423.
- [11] Indartono YS, Suwono A, Pratama FY. Improving photovoltaic performance by using yellow petroleum jelly as phase change material. *Int. J. Low-Carbon Technol.*, 2016; 11 (3): 333-337.
- [12] Bahaidarah H, Subhan A, Gandhidasan P, Rehman S. Performance evaluation of a PV (photovoltaic) module by back surface water cooling for hot climatic conditions. *Energy*, 2013; 59: 445-453.
- [13] Kane A, Verma V, Singh B. Optimization of thermoelectric cooling technology for an active cooling of photovoltaic panel. *Renewable and Sustainable Energy Reviews*, 2017; 75: 1295-1305.

- [14] Shastry DM, Arunachala UC. Thermal management of photovoltaic module with metal matrix embedded PCM. *Journal of Energy Storage*, 2020; 28: 101312.
- [15] Yılcancı A. Performance analysis of a photovoltaic panel cooled by thermoelectric effect. *Journal of the Faculty of Engineering and Architecture of Gazi University*, 2020; 35(2), 619-634.
- [16] Pathak SK, Sharma PO, Goel V, Bhattacharyya S, Aybar HŞ, Meyer JP. A detailed review on the performance of photovoltaic/thermal system using various cooling methods. *Sustainable Energy Technologies and Assessments*, 2022; 51: 101844.
- [17] Kerem A, Atik M, Bayram A. Fotovoltaik (PV) panel sisteminde yüzey soğutma işleminin elektrik üretimine etkisinin deneysel incelenmesi. *International Journal of Engineering Research and Development*, 2020; 12(2), 565 -578.
- [18] Rezvanpour M, Borooghani D, Torabi F, Pazoki M. Using CaCl₂· 6H₂O as a phase change material for thermo-regulation and enhancing photovoltaic panels' conversion efficiency: Experimental study and TR-NSYS validation. *Renewable Energy*, 2020; 146: 1907-1921.
- [19] Dwivedi P, Sudhakar K, Soni A, Solomin E, Kirpichnikova I. Advanced cooling techniques of PV modules: A state of art. *Case studies in thermal engineering*, 2020; 21: 100674.
- [20] Sohani A, Cornaro C, Shahverdiyan MH, Pierro M, Moser D, Nižetić S & Doranehgard M H. Building integrated photovoltaic/thermal technologies in Middle Eastern and North African countries: Current trends and future perspectives. *Renewable and Sustainable Energy Reviews*, 2023; 182, 113370.
- [21] Ahmadiou LA, Najafi G, Loni R, Kasaeian A, Mamat R, Ghazali MF, et al. Experimental investigation of PV/T and thermoelectric systems using CNT/water nanofluids. *Applied Thermal Engineering*, 2023; 227: 120350.
- [22] Gürbüz H, Demirtürk S, Akçay H, Topalcı Ü. Experimental investigation on electrical power and thermal energy storage performance of a solar hybrid PV/T-PCM energy conversion system. *Journal of Building Engineering*, 2023;69:106271.
- [23] Su Y, Zhang Y, Shu L. Experimental study of using phase change material cooling in a solar tracking concentrated photovoltaic-thermal system. *Solar Energy*, 2018; 159: 777-785.
- [24] Gillott M, Jiang L, Riffat S. An investigation of thermoelectric cooling devices for small-scale space conditioning applications in buildings. *International Journal of Energy Research*, 2010; 34(9): 776-786.
- [25] Kandry H, Ennawaoui C, El Ballouti A, Malki Z, El Jouad M, Balhamri A, et al. Optimized photovoltaic panels power using cooling system based thermoelectric materials. *Materials Today: Proceedings*, 2022; 66: 479-483.
- [26] Çulun P, Varolgüneş FK, Gonca Ö, Kılınç C. Thermal Comfort Comparison of Different Dwelling Typologies. *İDEALKENT*, 2022;13(38): 2677-2701.
- [27] GEPA [Internet] [cited 2023 March 3] Available from: <https://gepa.enerji.gov.tr/MyCalculator/pages/12.aspx>
- [28] Yıldırım E, Aktacir MA. Investigation of azimuth and tilt angle effects on building integrated photovoltaic systems. *Journal of the Faculty of Engineering and Architecture of Gazi University*, 2019;34(2): 609-619.
- [29] Işık SK, Çulun P. Experimental Investigation Of Photovoltaic Panel Performance In Bingol Province For Different Parameters. *Türk Doğa ve Fen Dergisi*, 2023; 12(2): 68-75.
- [30] Soliman AM. A numerical investigation of PVT system performance with various cooling configurations. *Energies*, 2023;16(7): 3052.
- [31] Standard IEC 60904-3, International Electrotechnical Commission, "Standard IEC 60904-3: photovoltaic devices," Part 3: measurement principal for terrestrial photovoltaic (PV) solar devices with reference spectral irradiance data, 1987.
- [32] Looser R, Vivar M, Everett V. Spectral characterisation and long-term performance analysis of various commercial Heat Transfer Fluids (HTF) as Direct-Absorption Filters for CPV-T beam-splitting applications. *Applied energy*, 2014; 113: 1496-1511.
- [33] Hamada AT, Sharaf OZ, Orhan MF A novel photovoltaic/thermal (PV/T) solar collector based on a multi-functional nano-encapsulated phase-change material (nano-ePCM) dispersion. *Energy Conversion and Management*, 2023; 280:116797.
- [34] Durez, A., Sohail, M. U., Ali, M., & Khan, U. A. (2024). Thermal analysis and efficiency enhancement of solar modified PV panels through organic PCM under climate conditions of Pakistan. *Mehran University Research Journal of Engineering and Technology*, 43(1), 97-110.
- [35] Der, O., Alqahtani, A. A., Marengo, M., & Bertola, V. (2021). Characterization of polypropylene pulsating heat stripes: Effects of orientation, heat transfer fluid, and loop geometry. *Applied Thermal Engineering*, 184, 116304.
- [36] Kameswara Rao, D., Sudhakar Reddy, K., & Subba Rao, V. V. (2024). Influence on solar PV performance integrated with heat sinks and nano-enhanced phase change material. *Proceedings of the Institution of Mechanical Engineers, Part E: Journal of Process Mechanical Engineering*, 09544089241253149.
- [37] Çulun P, Kılıçkap IS, Recent Developments in Cooling of Photovoltaic Solar Panels, *Gece Akademi, Çankaya/ANKARA*, 2023; 113-136

Evaluation of the Effect of Different Extraction Temperatures on the Synthesis of Silver Nanoparticles from *Ocimum basilicum* (Basil) Plant

İlkay Ünal^{1*} , Burcu Aydoğdu² 

¹ Munzur University, Faculty of Fine Arts, Design and Architecture Education, Department of Gastronomy and Culinary Arts, Tunceli, Turkey

² Munzur University Faculty of Engineering, Department of Mechanical Engineering, Tunceli, Turkey

İlkay ÜNAL ORCID No: 0000-0002-1587-4187
Burcu AYDOĞDU ORCID No: : 0000-0002-3309-1995

*Corresponding author: ilkayunal@munzur.edu.tr

(Received: 18.03.2024, Accepted: 09.06.2024, Online Publication: 28.06.2024)

Keywords
Green
synthesis,
Extraction,
*Ocimum
basilicum*,
Silver
nanoparticle

Abstract: The eco-friendly green synthesis of silver nanoparticles (AgNPs) using *Ocimum basilicum* (basil) extract at varying extraction temperatures (40, 60, 80, and 100°C) was investigated to determine the optimal conditions for nanoparticle formation. Analysis methods such UV-Vis spectrophotometry, Fourier Transform Infrared Spectroscopy (FTIR), X-ray Diffraction (XRD), and Transmission Electron Microscopy (TEM) confirmed the crystalline, spherical nature of AgNPs and identified phytochemicals acting as capping and reducing agents. Notably, it was found that the extraction temperature influenced both the DPPH radical scavenging activity and the structural properties of AgNPs. TEM analysis revealed that higher extraction temperatures led to increased nanoparticle formation efficiency but also resulted in wider size distribution. The crystallite sizes of AgNPs synthesized at different extraction temperatures were determined to be 12.45 nm, 18.77 nm, 17.76 nm, and 16.03 nm, respectively, using the Scherrer equation. The hydrodynamic sizes of the AgNPs ranged between 158.1 and 333.7 nm. The study highlights the critical role of extraction temperature in the synthesis process, proposing 40°C as the optimal temperature for achieving efficient and environmentally friendly synthesis of AgNPs with enhanced biological activities.

Ocimum basilicum (Fesleğen) Bitkisinin Farklı Ekstraksiyon Sıcaklıklarının Gümüş Nanopartikül Sentezine Etkisinin Değerlendirilmesi

**Anahtar
Kelimeler**
Yeşil sentez,
Ekstraksiyon,
*Ocimum
basilicum*,
Gümüş
nanopartikül

Öz: *Ocimum basilicum* (fesleğen) özütü kullanılarak çeşitli ekstraksiyon sıcaklıklarında (40, 60, 80, ve 100°C) çevre dostu yeşil sentez yöntemi ile gümüş nanopartikülleri (AgNPs) sentezi araştırıldı. Nanopartikül oluşumunun optimal koşullarını belirlemek için UV-Vis spektrofotometri, Fourier Dönüşümlü Kızılötesi Spektroskopisi (FTIR), X-ışını Kırınımı (XRD) ve Geçirimli Elektron Mikroskobu (TEM) gibi analiz yöntemleri kullanıldı. Bu yöntemlerle AgNPs'lerin kristalin ve küresel yapısı doğrulanmış ve kaplama ile indirgeyici ajan olarak hareket eden fitokimyasallar tespit edilmiştir. Özellikle, ekstraksiyon sıcaklığının hem DPPH radikal süpürme aktivitesini hem de AgNPs'nin yapısal özelliklerini etkilediği bulunmuştur. TEM analizi, daha yüksek ekstraksiyon sıcaklıklarının nanopartikül oluşum verimliliğinin artmasına yol açtığını ancak aynı zamanda daha geniş boyut dağılımına yol açtığını ortaya çıkardı. Farklı ekstraksiyon sıcaklıklarında sentezlenen AgNPs'lerin kristalit boyutları Scherrer denklemi kullanılarak sırasıyla 12.45 nm, 18.77 nm, 17.76 nm ve 16.03 nm olarak hesaplanmıştır. AgNPs'nin hidrodinamik boyutlarının 158.1 ile 333.7 nm arasında değişmiştir. Çalışma, ekstraksiyon sıcaklığının sentez sürecindeki kritik rolünü vurgulayarak, gelişmiş biyolojik aktivitelere sahip AgNP'lerin verimli ve çevre dostu sentezini için 40 °C'yi en uygun ekstraksiyon sıcaklığı olarak önermektedir.

1. INTRODUCTION

Nanotechnology is an interdisciplinary field of research and innovation taht focused on building constructing materials and devices at the atomic and molecular scale, typically within the size range of one nanometer (one billionth of a meter, or 10^{-9} meters) [1]. Nanoparticles are recognized as essential building blocks within nanotechnology, holding the potential to revolutionize a broad spectrum of applications [2]. These miniature particles, with sizes ranging from 1 to 100 nanometers (nm), exhibit unique physical, chemical, and biological properties that differ significantly from those of bulk materials. Due to their small size, nanoparticles possess a high surface area to volume ratio, resulting in heightened reactivity and interaction with biological systems [3]. Nanoparticles, which include metallic (such as gold, silver, and platinum), metal oxide (including titanium dioxide, zinc oxide, and iron oxide), quantum dots, carbon-based (fullerenes, carbon nanotubes, graphene), ceramic, polymeric, and lipid-based varieties, offer a diverse range of applications from catalysis, medical imaging, and drug delivery to cosmetics, electronics, energy solutions, and pharmaceuticals, due to unique properties like conductivity, optical characteristics, mechanical strength, and magnetic or electronic behaviour [5]. Silver nanoparticles (AgNPs), among others, exhibit a multitude of biological properties that render them promising candidates for a variousbiomedical applications. Their diverse properties include antimicrobial activity against a broad spectrum of pathogens, including bacteria, fungi and viruses [5]. AgNPs exert their antimicrobial effect through diverse mechanisms, such as disrupting of microbial cell membranes, interfering with key cellular processes and including oxidative stress leading to cell death [6]. In addition, silver nanoparticles exhibit remarkable anti-inflammatory properties by modulating the production of pro-inflammatory cytokines and attenuating the activation of inflammatory cascades. This anti-inflammatory effect is promising for the treatment of various inflammatory conditions, thus promoting tissue repair and wound healing [7].

Silver nanoparticles can be synthesized by various methods, including physical (plasma spraying, thermal reduction and electrospinning under inert gas atmosphere), chemical (chemical reduction, sol-gel method, microemulsion) and biological (plant extracts, microorganisms, proteins or polysaccharides) methods [8]. The use of plant extracts in the biological synthesis of AgNPs has gained significant attention for several reasons. Plant extracts contain bioactive molecules such

as phenolic compounds, flavonoids, alkaloids and terpenoids, which can serve as reducing agents, stabilizing agents and capping agents during the synthesis process. These compounds facilitate the reduction of silver ions into silver nanoparticles. Additionally, the use of plant extracts offers a green and eco-friendly approach to nanoparticle synthesis compared to conventional chemical methods, which often involve the use of hazardous chemicals and harsh conditions. The green synthesis route using plant extracts not only reduces the environmental impact but also eliminates the need for energy-intensive processes, making it a sustainable and cost-effective alternative [9]. However, there are some important points to consider when synthesizing nanoparticles from plant extract. The conditions of plant extraction in nanoparticle synthesis crucial, given the pivotal as both reducing and stabilizing agents in the green synthesis process [10]. The extraction method and conditions—including temperature, time, and pH—must be optimized to maximize the extraction of active compounds without degrading their properties, as these factors directly impact the nucleation, growth, and morphology of the nanoparticles [11]. Among them, extraction temperature is a critical parameter in the process of extracting phytochemicals from plant materials, as it directly influences the efficiency, yield, and quality of the extracted compounds. Furthermore, the temperature at which phytochemicals are extracted significantly affects their antioxidant capacity, notably their effectiveness in DPPH radical scavenging activity, which in turn influences the biosynthesis and functional quality of nanoparticles derived from these extracts. This underscores the interconnected impact of extraction temperature on both the phytochemical yield and the subsequent synthesis of biologically active nanoparticles [12]. Higher temperatures generally increase the solubility of phytochemicals in solvents, allowing for more efficient extraction, yet there is a risk of thermal degradation of heat-sensitive compounds [13]. Many different temperatures are used in plant extraction. Previous studies on the synthesis of AgNP using plant extract are shown in Table 1. This paper presents a comprehensive study on the synthesis of AgNPs using *Ocimum basilicum* extract at different extraction temperature (40, 60, 80 and 100 °C). This research investigates the influence of temperature variations on synthesis efficiency and the properties of produced nanoparticles by harnessing the natural reducing and stabilizing properties of plant extract. Biosynthesized AgNPs were characterized using UV-Vis spectrophotometer, FT-IR, XRD, and TEM analysis. The 2,2 diphenyl-1-picrylhydrazyl (DPPH) radical scavenging activity of each extract was determined

Table 1. Green synthesis of silver nanoparticles using plant extracts

Plants	Extraction temp. (°C)	Extraction time	Sahape-Size	References
<i>Allium cepa L</i>	25	4h	Cubic-150-200 nm	[14]
<i>C. prophetarum</i>	80	3h	Polymorphic-below 150 nm	[15]
<i>Tectona grandis</i> seed	80	20 min	Oval,spherical-10–30 nm	[16]
<i>Sambucus ebulus</i>	55	4h	Spherical-18.6 nm	[17]
<i>Moringa oleifera</i>	100	30 min	Spherical-10-25nm	[18]
<i>Selaginella myosurus</i>	80	5 min	Spherical-15-95nm	[19]
<i>Guettarda speciosa</i>	60	30 min	Spherical-30-35 nm	[20]

2. MATERIAL AND METHOD

2.1. Materials

Silver nitrate (AgNO_3 , 99.8%), ethanol ($\text{C}_2\text{H}_6\text{O}$), and DPPH (2,2-diphenyl-1-picrylhydrazyl) were purchased from Sigma-Aldrich. The plant materials required for the synthesis were sourced from the area's Marketplace

2.2. Preparation Process of The Herbal Extracts

10 grams of the dried plant were weighed and added to 100 mL of pure water. Based on the extraction temperatures most commonly used in the literature, it was allowed to stand for 1 hour at 40, 60, 80, and 100°C. After the extraction process, the mixture was allowed to cool to room temperature. Subsequently, the samples were filtered and stored at 4°C [21].

2.3. Biosynthesis of AgNPs

100 mL of 0.01 M silver nitrate solution was prepared in four separate beaker 10 mL of plant extract was gradually added to each. The mixture was left to react for 24 hours. At the end of the reaction time, the samples were centrifuged at 10,000 rpm. The pellet was washed several times with ethanol to remove impurities. It was then left to dry at 50 °C in the oven [18].

2.4. DPPH Radical Scavenging Assays

The DPPH (2,2-diphenyl-1-picrylhydrazyl) assay relies on the reduction of the DPPH radical (a stable free radical with a violet colour) in the presence of a hydrogen-donating antioxidant, leading to a colour change from violet to yellow. The DPPH free radical scavenging capacity was applied with some modifications to the Molyneux (2004) method [22]. Initially, the plant was extracted at 40, 60, 80 and 100 °C for 1 hour. The measured 0.1 mL extract was then transferred into a clean test tube and ethanol was added to bring the total volume of the solution up to 3 mL. 1 mL of 10^{-4} M DPPH (2,2-diphenyl-1-picrylhydrazyl) solution was added and the mixture was vortexed, followed by incubation for 30 minutes at room temperature in the dark. Absorbance were measured against ethanol at 517 nm with a UV-Vis spectrophotometer (UV-1601, Shimadzu, Kyoto, Japan). Measurements were made in three replicates. Results are given as percentage of DPPH radical scavenging. % inhibition was calculated with the following formula:

$$\%Inhibition = \frac{(Abscontrol - Abssample)}{Abscontrol} \times 100$$

2.5. Characterization Analysis

Morphological structure was examined using transmission electron microscopy (TEM, Hitachi HighTech HT7700). Crystal structure was evaluated with an X-ray diffractometer (XRD, PANalytical Empyrean), across a range of 2θ angles from 20° to 80°. Functional groups responsible for NP reduction and stability were identified through Fourier transform infrared

spectroscopy (FTIR, Bruker VERTEX 70v). Zeta potential and hydrodynamic size distribution were measured using a Malvern Zetasizer Nano ZSP. DPPH scavenging activity of the extracts was measured using UV-Vis spectrophotometer (1601, Shimadzu, Kyoto, Japan).

3. RESULTS AND DISCUSSION

3.1. Colour Change Observation

The synthesis of AgNPs utilizing plant extracts was visually monitored. Initially, the solution displayed a brownish-purple to purple colour, indicating of the presence of plant extracts alone. Upon the addition of silver ions, a gradual color transition from gray to gray-brown was observed, signifying the formation of AgNPs [23] (Fig 1). This colour change serves as a qualitative indicator of silver nanoparticle formation, attributable to the SPR effect of AgNPs [24].

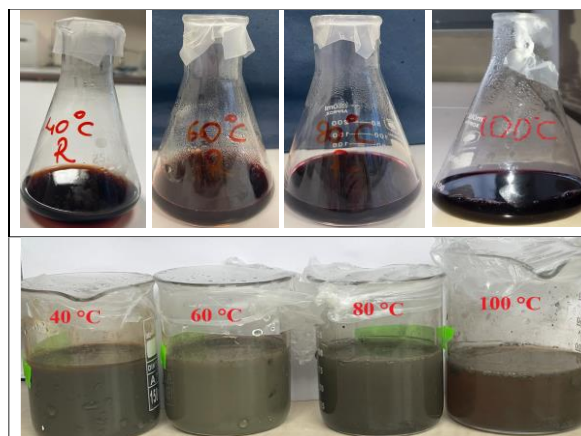


Figure 1. Plant extracted at different temperatures (40, 60, 80 and 100 °C and AgNP formation (reaction time 24 hours)

3.2. DPPH Radical Scavenging Results

In Figure 2, percentage the %inhibition values are presented depending on the extraction temperature. It was observed that DPPH radical scavenging activity increased with higher extraction temperatures. The % inhibition values at 40, 60, 80 and 100 °C were found to be 33%, 39%, 59% and 74.5%, respectively. The extraction of compounds from plants and their subsequent antioxidant activity are significantly influenced by temperature. Higher temperatures usually increase the solubility of many compounds, including antioxidants, in the solvent. Elevated temperatures enhance the efficiency of the extraction process as they can dissolve and extract more compounds from the plant material by breaking down the cell walls, thereby releasing more phytochemicals into the extraction solvent.

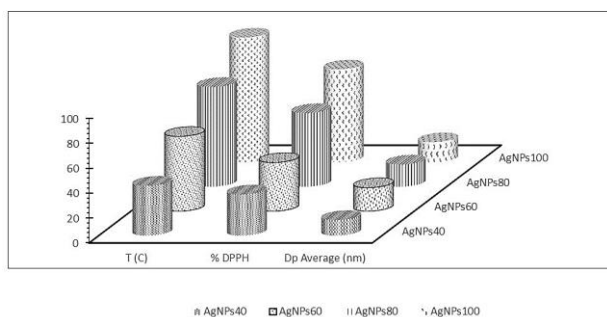


Figure 2. DPPH radical scavenging activity of basil extracted at different temperatures

3.3. TEM Results

TEM analysis enabled a detailed investigation of morphological, structural, and dimensional characteristics of the nanoparticle (NP) samples. The findings revealed a predominance of spherical nanoparticles, with sizes primarily ranging from 5 to 100 nanometers (Fig 3). A wide size distribution is generally observed in nanoparticle synthesis using plant extracts. This variability can be attributed to the diverse bioactive compounds present in plant extracts, each with its own unique reducing capacities. As a result, nanoparticles of various sizes and shapes are formed. Dhir et al. (2024) and Iravani (2011) have noted that the use of plant extracts in NP synthesis leads to wide variations in size distribution [25-26]. Additionally, it was also noted that nanoparticles tended to agglomerate. A significant finding was that the efficiency of nanoparticle formation was positively influenced by higher extraction temperatures, indicating the crucial role of thermal conditions in the synthesis and properties of nanoparticles. TEM has led to significant insights into the influence of crystalline structures within individual particles on TEM image contrast. It has been observed that particles containing multiple AgNPs crystallites exhibit a significantly higher degree of electron scattering than particles with a single crystalline structure. This enhanced scattering effect is attributed to the presence of multiple interfaces and boundaries within the particle resulting from the aggregation of different crystallites. Consequently, such particles appear darker in TEM images as the electron beam is more obstructed when passing through the particle [27].

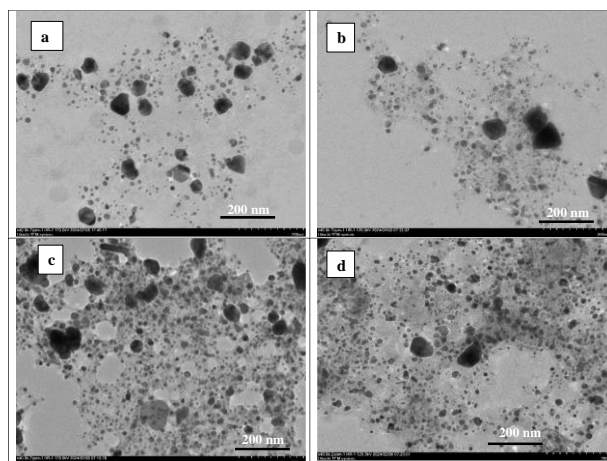


Figure 3. TEM image of AgNPs synthesis from different extraction temperature a) 40 °C b) 60 °C c) 80 °C d) 100 °C

3.4. XRD Results

The crystalline structure of AgNPs was characterized using X-ray diffraction (XRD) analysis. The obtained XRD pattern is presented in Figure 4. The diffraction peaks observed at 2θ values are indexed to the (111), (200), (220), and (311) planes, respectively, of face-centered cubic (fcc) silver, according to the standard Joint Committee on Powder Diffraction Standards (JCPDS) file No. 04-0783 [28]. These peaks confirm the crystalline nature of the synthesized silver nanoparticles. A high XRD peak intensity has been observed in the AgNPs synthesized from the plant extract obtained at 40 and 60 °C. This indicates that these nanoparticles possess a more regular crystalline structure [29]. The additional peaks indicated by asterisks in the XRD pattern may suggest the crystallization of a bio-organic phase on the surface of the AgNPs [30]. The average crystallite size was calculated using the Scherrer equation;

$$D = \frac{K\lambda}{\beta \cos \theta}$$

where: D is the mean size of the crystallites (often in nanometers), K is the shape factor (a dimensionless constant, typically taken as about 0.9), λ is the wavelength of the X-ray radiation (in meters), β is the full width at half maximum (FWHM) of the peak in radians, θ is the Bragg angle (in radians). AgNP synthesis conducted with extracts obtained at 40, 60, 80, and 100°C, the crystallite sizes were calculated to be 12.45, 18.77, 17.76, and 16.03 nm, respectively. The results suggest that the controlled synthesis parameters significantly influence the crystallite size, thereby impacting the physical and chemical properties of the materials.

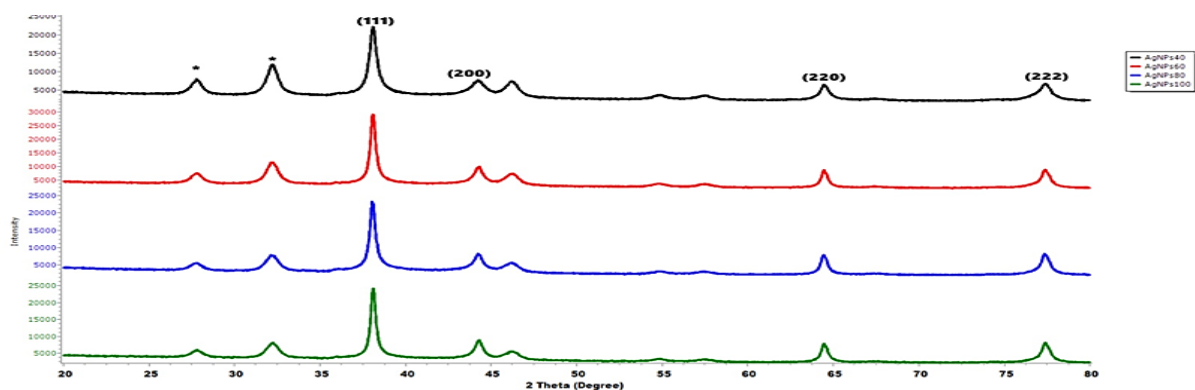


Figure 4. XRD graph of AgNPs (black line 40 °C, red line 60 °C, blue line 80 °C, green line 100 °C)

3.5. FT-IR Results

FTIR spectroscopy was utilized to identify the functional groups present on the surface of the synthesized AgNPs and to elucidate the mechanism behind the reduction of silver ions to AgNPs using plant extract. The FTIR spectra were recorded in the range of 4000-400 cm^{-1} (Fig 5). The presence of a peak in the 2928 cm^{-1} region signifies C-H stretching vibrations, indicating aliphatic hydrocarbons' presence. This could relate to fatty acids or other hydrocarbon chains in the plant extract, possibly playing a role in stabilizing the silver nanoparticles. A strong peak around 1650 cm^{-1} , indicative of C=O stretching vibrations typical of carbonyl groups in carboxylic acids, esters, and amides, suggests that compounds with carbonyl groups.

emphasizing the potential of phytochemicals as dual-functioning reducing and capping agents in the environmentally friendly production of nanoparticles.

3.6. Hydrodynamic Size and Zeta Potential Results

The analysis of hydrodynamic size and zeta potential provides crucial insights into the physical stability and surface charge characteristics of nanoparticles. The hydrodynamic size, determined through dynamic light scattering (DLS) techniques, provides information on the effective diameter of nanoparticles in a suspension, reflecting both the core particle size and any surface-bound layers or molecules [34]. The results from this analysis indicated that the nanoparticles had an average

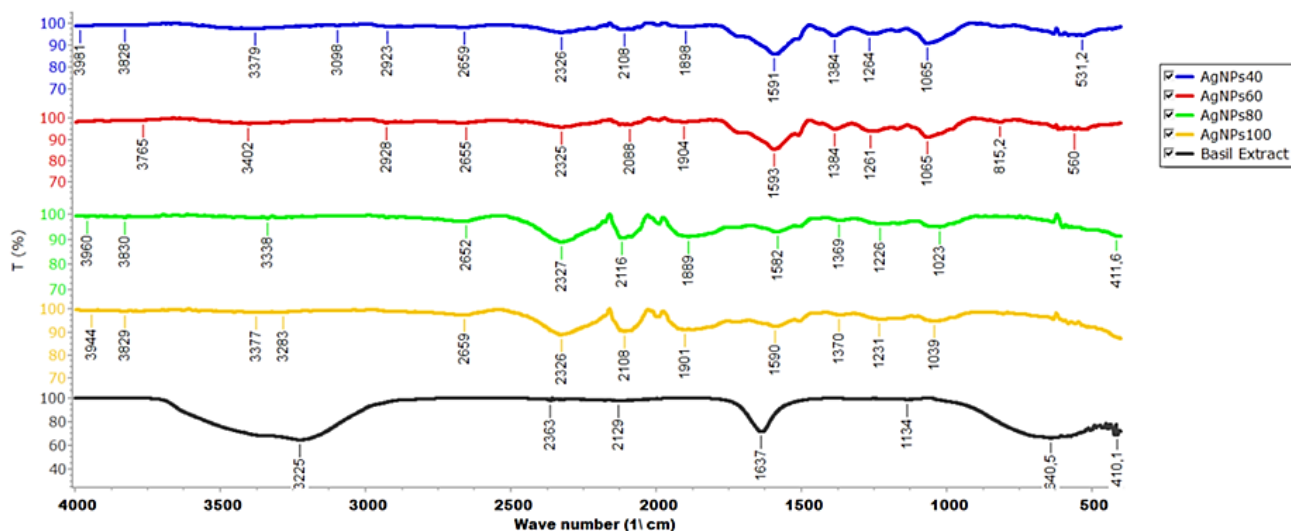


Figure 5. FTIR spectrum of Basil extract and synthesized AgNPs

The peak at around 1591 cm^{-1} can indicate C=C stretching vibrations, and it may also correspond to N-H bending vibrations in amides of the aromatic rings. The peak at $\sim 1370 \text{ cm}^{-1}$ indicates C-N stretching from amines, and the peak at $\sim 1040\text{-}1070 \text{ cm}^{-1}$, showing C-O stretching, suggests the plant extract's nitrogen compounds aid in the synthesis and stabilization of AgNPs [31-33]. The FTIR results suggest that the phytochemicals present in the plant extract, such as phenolics, alcohols, aliphatic compounds, proteins, and nitrogen-containing compounds, play a crucial role in the bioreduction of silver ions to nanoparticles and their subsequent stabilization. These findings offer valuable insight into the green synthesis of AgNPs using plant extracts,

hydrodynamic diameter within the range of 158.1 and 333.7 (Fig 6 and Table 2). Nanoparticles synthesized with extracts prepared at 80 °C have shown a wide size distribution. The polydispersity index (PDI) quantifies the distribution of particle sizes within a sample [35]. It provides insight into the uniformity of the particles, with a lower PDI indicating a more uniform size distribution. While nanoparticles synthesized with extracts prepared at 80 °C had high PDI values, the lowest PDI was observed at 60 °C. High temperatures can increase the solubility of bioactive components in plant materials [36-37]. With increasing solubility, more reducing agent passes into solution, which can lead to the formation of a denser nanoparticle. Higher temperatures may enhance the

solubility of phytochemicals in the extract, leading to a more rapid reduction of silver ions and accelerated growth of nanoparticles. This rapid growth can result in larger nanoparticles.

Table 2. Zeta potential, size and PDI values of synthesized AgNPs

Samples	Temperature (°C)	Z-Ave. size (nm)	PdI	Zeta potential (mV)	Mobility (µmcm/Vs)	Conductivity (mS/cm)
AgNPs40	25	158,1	0,263	-21,5	-1,686	0,00729
AgNPs60	25	230,4	0,233	-25,7	-2,014	0,012
AgNPs80	25	333,7	0,401	-21,6	-1,692	0,0142
AgNPs100	25	294,9	0,27	-16,2	-1,27	0,00587

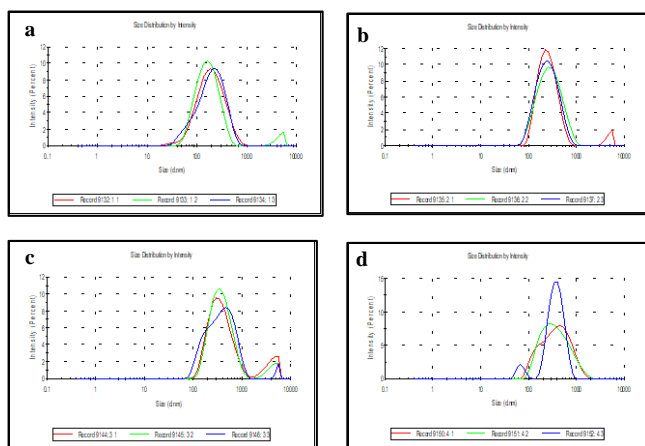


Figure 6. Hydrodynamic size distribution of AgNPs a) 40 °C b) 60 °C c) 80 °C d)100 °C

4. DISCUSSION

This study investigated the impact of different extraction temperatures (40°, 60, 80, and 100°C) on the eco-friendly synthesis of silver nanoparticles (AgNPs) using *Ocimum basilicum* (basil) extract. It was observed that higher extraction temperatures increased DPPH activity likely due to increasing the solubility of phytochemicals in basil extract. However, despite the higher efficiency in nanoparticle formation, higher extraction temperatures led to larger size distribution, lower stability, and aggregation. The study underscores the critical influence of extraction temperature in the synthesis process, proposing 40°C as the optimal temperature for achieving efficient and environmentally friendly synthesis of AgNPs with enhanced biological activities.

Acknowledgement

This research did not receive any funding. We acknowledge the author for their contributions

REFERENCES

[1] Bayda S, Adeel M, Tuccinardi T, Cordani M, Rizzolio F. The history of nanoscience and nanotechnology: From chemical-physical applications to nanomedicine. *Molecules*. 2020;25(1):1–15.

[2] Maity D, Sahoo SR, Saha S. Synthesis and Characterization of Nanomaterials for Electrochemical Sensors. *ACS Symp Ser*.

2023;1437:193–222.

[3] Khan Y, Sadia H, Ali Shah SZ, Khan MN, Shah AA, Ullah N, Khan MI. Classification, synthetic, and characterization approaches to nanoparticles, and their applications in various fields of nanotechnology: A review. *Catalysts*. 2022;12(11), 1386.

[4] Altammar KA. A review on nanoparticles: characteristics, synthesis, applications, and challenges. *Front Microbiol*. 2023;14(April):1–20.

[5] Burduşel AC, Gherasim O, Grumezescu AM, Mogoantă L, Ficaï A, Andronescu E. Biomedical applications of silver nanoparticles: An up-to-date overview. *Nanomaterials*. 2018;8(9):1–25.

[6] Xu L, Wang YY, Huang J, Chen CY, Wang ZX, Xie H. Silver nanoparticles: Synthesis, medical applications and biosafety. *Theranostics*. 2020;10(20):8996–9031.

[7] Wong KKY, Cheung SOF, Huang L, Niu J, Tao C, Ho CM, Tam PK. Further evidence of the anti-inflammatory effects of silver nanoparticles. *ChemMedChem*. 2009;4(7):1129–35.

[8] Ren Y yu, Yang H, Wang T, Wang C. Bio-synthesis of silver nanoparticles with antibacterial activity. *Mater Chem Phys [Internet]*. 2019;235(November 2016):121746.

[9] Marslin G, Siram K, Maqbool Q, Selvakesavan RK, Kruszka D, Kachlicki P, Franklin G. Secondary metabolites in the green synthesis of metallic nanoparticles. *Materials (Basel)*. 2018;11(6):1–25.

[10] Thatyana M, Dube NP, Kemboi D, Manicum ALE, Mokgalaka-Fleischmann NS, Tembu J V. Advances in Phytonanotechnology: A Plant-Mediated Green Synthesis of Metal Nanoparticles Using *Phyllanthus* Plant Extracts and Their Antimicrobial and Anticancer Applications. *Nanomaterials*. 2023;13(19).

[11] Wirwis A, Sadowski Z. Green Synthesis of Silver Nanoparticles: Optimizing Green Tea Leaf Extraction for Enhanced Physicochemical Properties. *ACS Omega*. 2023;8(33):30532–49.

[12] Baliyan S, Mukherjee R, Priyadarshini A, Vibhuti A, Gupta A, Pandey RP, Chang CM. Determination of Antioxidants by DPPH Radical Scavenging Activity and Quantitative Phytochemical Analysis of *Ficus religiosa*. *Molecules*. 2022;27(4).

[13] Awad AM, Kumar P, Ismail-Fitry MR, Jusoh S, Ab Aziz MF, Sazili AQ. Green extraction of bioactive compounds from plant biomass and their application in meat as natural antioxidant. *Antioxidants*. 2021;10(9):1–39.

[14] Abdellatif AAH, Mahmood A, Alsharidah M, Mohammed HA, Alenize SK, Bouazzaoui A, Abdulla MH Bioactivities of the Green Synthesized Silver Nanoparticles Reduced Using *Allium cepa* L Aqueous Extracts Induced Apoptosis in Colorectal Cancer Cell Lines. *J Nanomater*. 2022; (1), 1746817.

[15] HemLata, Meena PR, Singh AP, Tejavath KK. Biosynthesis of Silver Nanoparticles Using *Cucumis prophetarum* Aqueous Leaf Extract and Their Antibacterial and Antiproliferative Activity against Cancer Cell Lines. *ACS Omega*. 2020;5(10):5520–8.

- [16] Rautela A, Rani J, Debnath (Das) M. Green synthesis of silver nanoparticles from *Tectona grandis* seeds extract: characterization and mechanism of antimicrobial action on different microorganisms. *J Anal Sci Technol*. 2019;10(1).
- [17] Karan T, Gonulalan Z, Erenler R, Kolemen U, Eminagaoglu O. Green synthesis of silver nanoparticles using *Sambucus ebulus* leaves extract: Characterization, quantitative analysis of bioactive molecules, antioxidant and antibacterial activities. *J Mol Struct [Internet]*. 2024;1296(P1):136836. Available from: <https://doi.org/10.1016/j.molstruc.2023.136836>
- [18] Asif M, Yasmin R, Asif R, Ambreen A, Mustafa M, Umbreen S. Green Synthesis of Silver Nanoparticles (AgNPs), Structural Characterization, and their Antibacterial Potential. Dose-Response. 2022;20(1):1–11.
- [19] Kedi PBE, Meva FE, Kotsedi L, Nguemfo EL, Zangueu CB, Ntounda AA, Maaza M. Eco-friendly synthesis, characterization, in vitro and in vivo anti-inflammatory activity of silver nanoparticle-mediated *Selaginella myosurus* aqueous extract. *Int J Nanomedicine*. 2018;13:8537–48.
- [20] Deivanathan SK, Prakash JTJ. Green synthesis of silver nanoparticles using aqueous leaf extract of *Guettarda Speciosa* and its antimicrobial and anti-oxidative properties. *Chem Data Collect [Internet]*. 2022;38(January):100831. Available from: <https://doi.org/10.1016/j.cdc.2022.100831>
- [21] Unal İ, Egri S, Ates M. Green Synthesis (*Paeonia kesrouanensis*) of Silver Nanoparticles and Toxicity Studies in *Artemia salina*. *Bull Environ Contam Toxicol*. 2022;109(6):1150–4.
- [22] Molyneux P. The Use Of The Stable Free Radical Diphenylpicryl-hydrazyl (DPPH) For Estimating Anti-oxidant Activity. *Songklanakarin J Sci Technol*. 2004;26(May):1–10.
- [23] Ali K, Ahmed B, Dwivedi S, Saquib Q, Al-Khedhairy AA, Musarrat J. Microwave accelerated green synthesis of stable silver nanoparticles with *Eucalyptus globulus* leaf extract and their antibacterial and antibiofilm activity on clinical isolates. *PLoS One*. 2015;10(7):1–20.
- [24] Rodríguez-Serrano C, Guzmán-Moreno J, Ángeles-Chávez C, Rodríguez-González V, Juan Ortega-Sigala J, Ramírez-Santoyo RM, Vidales-Rodríguez LE. Biosynthesis of silver nanoparticles by *Fusarium scirpi* and its potential as antimicrobial agent against uropathogenic *Escherichia coli* biofilms. *PLoS One*. 2020;15(3):1–20.
- [25] Dhir R, Chauhan S, Subham P, Kumar S, Sharma P, Shidiki A, Kumar G. Plant-mediated synthesis of silver nanoparticles: unlocking their pharmacological potential—a comprehensive review. *Front Bioeng Biotechnol*. 2023;11(January):1–24.
- [26] Irvani S. Green synthesis of metal nanoparticles using plants. *Green Chem*. 2011;13(10):2638–50.
- [27] Mourdikoudis S, Pallares RM, Thanh NTK. Characterization techniques for nanoparticles: Comparison and complementarity upon studying nanoparticle properties. *Nanoscale*. 2018;10(27):12871–934.
- [28] Abdi V, Sourinejad I, Yousefzadi M, Ghasemi Z. Biosynthesis of Silver Nanoparticles from the Mangrove *Rhizophora mucronata*: Its Characterization and Antibacterial Potential. *Iran J Sci Technol Trans A Sci [Internet]*. 2019;43(5):2163–71. Available from: <https://doi.org/10.1007/s40995-019-00739-9>
- [29] Mamdooh NW, Naeem GA. The effect of temperature on green synthesis of silver nanoparticles. *AIP Conf Proc*. 2022;2450(July).
- [30] Vanaja M, Annadurai G. *Coleus aromaticus* leaf extract mediated synthesis of silver nanoparticles and its bactericidal activity. *Appl Nanosci*. 2013;3(3):217–23.
- [31] Gnanajobitha G, Annadurai G, Kannan C. Green synthesis of silver nanoparticle using *Elettaria cardamomom* and assesment of its antimicrobial activity. *Int J Pharma Sci Res(IJPSR) [Internet]*. 2012;3(3):323–30. Available from: <http://www.ijpsr.info/docs/IJPSR12-03-03-011.pdf>
- [32] Ghaseminezhad SM, Hamedi S, Shojaosadati SA. Green synthesis of silver nanoparticles by a novel method: Comparative study of their properties. *Carbohydr Polym [Internet]*. 2012;89(2):467–72. Available from: <http://dx.doi.org/10.1016/j.carbpol.2012.03.030>
- [33] Khan MZH, Tareq FK, Hossen MA, Roki MNAM. Green synthesis and characterization of silver nanoparticles using *Coriandrum sativum* leaf extract. *J Eng Sci Technol*. 2018;13(1):158–66.
- [34] Kato H, Nakamura A, Takahashi K, Kinugasa S. Accurate Size and Size-Distribution Determination of Polystyrene Latex Nanoparticles in Aqueous Medium Using Dynamic Light Scattering and Asymmetrical Flow Field Flow Fractionation with Multi-Angle Light Scattering. *Nanomaterials*. 2012; 2(1):15-30.
- [35] Danaei M, Dehghankhold M, Ataei S, Hasanzadeh Davarani F, Javanmard R, Dokhani A, Mozafari MR. Impact of particle size and polydispersity index on the clinical applications of lipidic nanocarrier systems. *Pharmaceutics*. 2018;10(2):1–17.
- [36] Gil-Martín E, Forbes-Hernández T, Romero A, Cinciosi D, Giampieri F, Battino M. Influence of the extraction method on the recovery of bioactive phenolic compounds from food industry by-products. *Food Chem*. 2022;378.
- [37] Antony A, Farid M. Effect of Temperatures on Polyphenols during Extraction. *Appl Sci*. 2022;12(4).

Optimization of Medium Components for Enhanced Expression of Recombinant Human Vascular Endothelial Growth Factor (VEGF₁₆₅) in *Kluyveromyces lactis* GG799

Hülya KUDUĞ CEYLAN^{1*}, Cafer MEYDAN², Ayşe NALBANTSOY², Murat ELİBOL²

¹ Tokat Gaziosmanpaşa University, Faculty of Pharmacy, Department of Basic Pharmaceutical Sciences, Tokat, Türkiye

² Ege University, Faculty of Engineering, Department of Bioengineering, İzmir, Türkiye

Hülya KUDUĞ CEYLAN ORCID No: 0000-0003-0365-2760

Cafer MEYDAN ORCID No: 0000-0001-6201-4860

Ayşe NALBANTSOY ORCID No: 0000-0002-9108-4451

Murat ELİBOL ORCID No: 0000-0002-6756-6290

*Corresponding author: hulya.kudug@gop.edu.tr

(Received: 28.04.2024, Accepted: 10.06.2024, Online Publication: 28.06.2024)

Keywords

Vascular endothelial growth factor (VEGF₁₆₅), *Kluyveromyces lactis*, Biomass optimization, Recombinant protein, Response Surface Methodology

Abstract: Vascular endothelial growth factor (VEGF₁₆₅) is a vital biomarker linked to diverse physiological processes and pathological conditions like cancer, owing to its pivotal role in angiogenesis. Therefore, an efficient method to obtain recombinant VEGF₁₆₅ in high yield is required. This study focused on optimizing a medium to enhance the biomass of *Kluyveromyces lactis* (*K. lactis*) GG799 cells that express recombinant VEGF₁₆₅. Through screening various media components, galactose, tryptone, and yeast extract were identified as the most effective components. Using the Box–Behnken design, the medium components were optimized, resulting in a notable 31% increase in biomass concentration. The optimized medium, comprising 45 g L⁻¹ galactose, 30 g L⁻¹ tryptone, and 5 g L⁻¹ yeast extract, achieved biomass productivity (P) of 0.26 gDCW L⁻¹ h⁻¹. Additionally, the expression of VEGF₁₆₅ reached 1024.09 µg per L of the culture medium, representing a 1.27-fold increase compared to the unoptimized medium. These results imply that the proposed optimized medium can serve as a model for a process development strategy, providing a foundation for obtaining elevated yields of other recombinant proteins in *K. lactis*.

Rekombinant İnsan Vasküler Endotelial Büyüme Faktörü (VEGF₁₆₅)'nün *Kluyveromyces lactis* GG799'da Geliştirilmiş Ekspresyonu İçin Ortam Bileşenlerinin Optimizasyonu

Anahtar Kelimeler

Vasküler endotelial büyüme faktörü (VEGF₁₆₅), *Kluyveromyces lactis*, Biyokütle optimizasyonu, Rekombinant protein, Yanıt Yüzey Metodu

Öz: Vasküler endotelial büyüme faktörü (VEGF₁₆₅), anjiyogenezdeki rolünden dolayı çeşitli fizyolojik süreçler ve kanser gibi patolojik hastalıklar ile ilişkili önemli bir biyobelirteçtir. Bu nedenle, yüksek verimde rekombinant VEGF₁₆₅ elde etmek için etkili bir yöntem gereklidir. Bu çalışmada, *Kluyveromyces lactis* (*K. lactis*) GG799 hücrelerinde rekombinant VEGF₁₆₅ ekspresyonunu artırmak amacıyla büyüme ortamının optimize edilmesi amaçlanmıştır. Farklı ortam bileşenlerinin taranması sonucunda galaktoz, tripton ve maya ekstraktı en etkili bileşenler olarak belirlenmiştir. Box-Behnken tasarımı kullanılarak seçilen ortam bileşenleri optimize edilmiş ve biyokütle konsantrasyonunda %31'lik kayda değer bir artış sağlanmıştır. 45 g L⁻¹ galaktoz, 30 g L⁻¹ tripton ve 5 g L⁻¹ maya ekstraktı içeren optimize ortam ile 0,26 gDCW L⁻¹ h⁻¹ biyokütle üretkenliğine (P) ulaşılmıştır. Ayrıca VEGF₁₆₅ ekspresyonu, optimize edilmemiş ortama kıyasla 1,27 kat artışla 1024,09 µg L⁻¹ değerine ulaşmıştır. Elde edilen sonuçlar, önerilen optimize edilmiş ortamın *K. lactis*'te diğer rekombinant proteinlerin üretimine yönelik proses geliştirme stratejisi olarak bir model olabileceğini göstermektedir.

1. INTRODUCTION

Growth factors, which are biologically active molecules regulating cellular responses by binding to specific receptors on target cells, are essential for cellular regulation. Among these factors, Vascular Endothelial Growth Factor (VEGF) is a pivotal determinant, influencing both cell growth and survival, particularly in stimulating blood vessel formation through vasculogenesis and angiogenesis [1,2]. Although endothelial cells are the primary target of VEGF, its effects extend to various other cell types. VEGF plays a critical role in vascular development, contributing significantly to developmental processes and physiological homeostasis. Moreover, VEGF is vital for various physiological functions, including wound healing, regulation of the menstrual cycle, bone formation, hematopoiesis, and neural development [3–6]. Beyond its role in normal physiological processes, VEGF exerts pathogenic effects on tumor growth and metastasis by influencing vascular permeability and neoangiogenesis (neovascularization). Additionally, VEGF contributes to the progression of non-malignant diseases such as rheumatoid arthritis [7], psoriasis [8], diabetes, and neovascular eye diseases [9].

The VEGF family encompasses a group of proteins, including VEGF-A, B, C, D, E, and placenta growth factor (PlGF), regulated by three well-known receptors (VEGFR-1, VEGFR-2, and VEGFR-3) [10]. Initially identified as a vascular permeability factor (VPF) [11], VEGF-A, commonly referred to as VEGF, undergoes alternative splicing, resulting in various isoforms such as VEGF₁₆₅, VEGF₁₂₁, VEGF₁₈₉, and VEGF₂₀₆ in humans [12]. Among these isoforms, VEGF₁₆₅ holds particular significance and has been a focal point of extensive research, especially in the context of tumor development [13]. Functionally potent in tumor vascularization, VEGF₁₆₅ influences endothelial cell migration, proliferation, and tube formation. [14]. Structurally, VEGF₁₆₅ is a disulfide-linked homodimeric protein consisting of two monomers with a 165-amino acid polypeptide chain and a molecular weight of 38.2 kDa [15].

Recombinant DNA technology is a cornerstone of synthetic biology, particularly in the production of pharmaceutical proteins. The importance of recombinant therapeutic proteins in treating various diseases is steadily increasing, making them indispensable in the biotechnology market. Among the host systems utilized, yeasts are prominently featured for their numerous advantages in producing recombinant pharmaceuticals [16]. The main capacity of yeast is its sustained growth under straightforward media conditions in bioreactors. Yeasts excel in sustained growth under simple media conditions in bioreactors, and their amenability to genetic modification enhances their suitability as an ideal host system for pharmaceutical protein production [17]. *Kluyveromyces lactis* (*K. lactis*) emerges as one of the most promising yeast hosts for recombinant protein production due to its numerous advantages, including rapid growth, effective secretion levels, suitability for

high cell density fermentation, low-cost culture media requirements, and ease of genetic manipulation compared to other yeast hosts. The industrial applications of *K. lactis* began with its use as a source of the enzyme lactase and later expanded into a protein supplement in foods. Notably, the production of bovine chymosin, the first recombinant protein from *K. lactis*, marked a significant milestone. Since then, numerous heterologous proteins have been recombinantly secreted from *K. lactis*. The GRAS (Generally Recognized as Safe) FDA status of these recombinant proteins underscores their safety and suitability for applications in both the food and pharmaceutical industries [18]. However, like all expression systems, certain process parameters must be optimized to ensure the successful expression of a protein in *K. lactis* and to increase production capacity before industrial-scale production for commercialization. For example, the impact of culture conditions and medium composition has been extensively studied to enhance the system's performance for higher biomass and protein titers. Previous studies have highlighted the crucial role played by medium components and their composition in both cell growth and protein expression levels [19–21].

As a result, medium optimization has emerged as a critical step in enhancing protein yield for industrial production. Traditional optimization, characterized by its time-consuming nature and neglecting factor interactions, has increasingly given way to statistical methods [22,23]. Response Surface Methodology (RSM) stands out as a valuable tool that integrates mathematical and statistical techniques to determine the optimal values of multiple variables in biochemical processes and has been widely adopted in recent years [24]. In this study, we aimed to optimize the medium components to maximize the biomass of *K. lactis*, thereby enhancing the expression of recombinant VEGF₁₆₅. *K. lactis* was selected as the ideal host organism due to its capacity to achieve high cell densities and consistent reproducibility at an industrial scale. Initial screening studies investigated the effect of various carbon, nitrogen, and extract sources on biomass production. Subsequently, the most effective components were optimized using RSM based on a full factorial central composite design (CCD).

2. MATERIAL AND METHOD

2.1. Reagents, Strains, and Growth Medium

All the chemicals were purchased from Sigma–Aldrich (St. Louis, MO, USA) and Merck (Merck Millipore, Darmstadt, Germany). Ni-NTA agarose resin was purchased from Qiagen (Hilden, Germany), 1000 kDa MWCO cellulose acetate dialysis membrane was purchased from Spectrum Laboratories (California, USA), 3,3',5,5'-tetramethylbenzidine (TMB) (Acros Organics, Belgium) and Pierce™ BCA Protein Assay Kit was purchased from Thermo Fisher Scientific (Waltham, MA, USA). The ELISA washing buffer (PBST) consisted of 0.1 M PBS pH 7.2 containing 0.15M NaCl and 0.05% Tween 20, while the coating buffer was a 50 mM carbonate buffer, pH 9.6. The ELISA maxisorp immunoplate (96 flat-bottomed wells) was purchased

from Nunc (Roskilde, Denmark). Recombinant *K. lactis* strain GG799 (New England BioLabs, Massachusetts, USA) was previously constructed by inserting the human VEGF₁₆₅ cDNA (GenBank accession no. AF486837.1) into the *XhoI* and *EcoRI* sites of the pKLAC2 vector under the control of the *LAC4* promoter [25]. The recombinant strain was cultivated on YCB plates (3% 1 M Tris-HCl pH 7.4, 1.17% YCB, and 2% agar) containing 5 mM acetamide and preserved at -80°C as a glycerol stock. Furthermore, YPLac (1% yeast extract, 2% peptone, and 4% lactose) (pH 7.4) served as the unoptimized medium for the expression performance of recombinant VEGF₁₆₅, allowing for comparison with the optimized medium. Optimization experiments at the shaking flask level were conducted in triplicate, and ELISA was performed in triplicate for each sample to determine the VEGF₁₆₅ concentration.

2.2. Expression and Purification of Recombinant Human VEGF₁₆₅

The inoculum was prepared by transferring a single colony of recombinant *K. lactis* GG799 from YCB plates into 25 mL of YPLac medium, followed by incubation at 30°C at 250 rpm for 72 h. This pre-culture was then inoculated at a 1:100 ratio into a 2 L Erlenmeyer shaking flask containing 300 mL of YPLac for the VEGF₁₆₅ expression. After 72 hours of incubation, the supernatant containing the secreted recombinant VEGF₁₆₅ was collected by centrifugation at 5000 rpm for 5 minutes at room temperature to facilitate protein purification. For VEGF₁₆₅ purification, the supernatant was precipitated with a 60% ammonium sulfate solution in an ice bath for an hour, followed by centrifugation at 12000 rpm for 20 minutes. The protein pellet was then solubilized in 100 mM phosphate buffer (pH 7.4). Subsequently, a polycarbonate column containing Ni-NTA Agarose resin (Qiagen, Hilden, Germany) for affinity chromatography was washed with 100 mM phosphate buffer (pH 7.4). The protein solution was applied to the column, and the target protein was eluted from the column in fractions with 100 mM phosphate buffer containing 300 mM imidazole. The eluted VEGF₁₆₅ solution was dialyzed against 20 mM pH 7.4 HEPES buffer using a 1000 kDa MWCO cellulose acetate dialysis membrane (Spectrum Laboratories, California, USA) at $+4^{\circ}\text{C}$ overnight on a magnetic stirrer. The resulting pure VEGF₁₆₅, obtained from the unoptimized medium, was used as the standard protein for the ELISA. The concentration of VEGF₁₆₅ was determined using the 'Pierce™ BCA Protein Assay Kit'.

2.3. Quantification of VEGF₁₆₅ by Direct ELISA

A direct ELISA protocol, adapted from methods outlined by Abcam (Cambridge, UK) with some modifications. VEGF₁₆₅, purified from recombinant *K. lactis* GG799, served as the standard protein solution, prepared as previously described. Samples and dilutions of the standards were prepared using a coating buffer. Maxisorp 96-well plates were coated overnight at 4°C with $100\ \mu\text{L}$ well⁻¹ of either sample or standard. After four washes with $200\ \mu\text{L}$ well⁻¹ of PBST, the wells were blocked with $100\ \mu\text{L}$ of 2% w/v BSA in PBST for 2 h at room temperature.

Following a rewashing step, the plates were incubated with $100\ \mu\text{L}$ well⁻¹ of HRP-conjugated anti-6X His tag antibody (Cat. No. ab1187; Abcam, UK), diluted to 1:5000 in PBS, for 1 h at room temperature in the dark. After another round of washing, $100\ \mu\text{L}$ of TMB substrate solution was added to each well for colorimetric development. The reaction was stopped by the addition of $25\ \mu\text{L}$ well⁻¹ stop solution (4M H₂SO₄) and absorbances were measured at 450 nm using the Multiskan™ FC Microplate Photometer (Thermo Fisher Scientific, USA). The VEGF₁₆₅ concentrations of the samples were calculated using the VEGF₁₆₅ standard curve following the manufacturer's protocol.

2.4. Growth Profile of *K. lactis* Cells

To assess the kinetics of VEGF₁₆₅ production, transformed *K. lactis* cells were inoculated into flasks containing 300 ml of YPLac (pH 7.4) medium and cultivated at 30°C with agitation at 250 rpm for 72 h. At predetermined intervals during the incubation, the biomass of *K. lactis* cells and the concentration of VEGF₁₆₅ were measured. Simultaneously, optical density, lactose consumption, and ethanol production were continually monitored. For dry cell weight (DCW) determination, 2 mL of culture broth samples were vacuum-filtered on pre-weighed filters (Whatman GF/C™). After two rinses with 5 mL distilled water, the filter papers were dried at 65°C for 24 hours and reweighed. Culture samples underwent ELISA analysis to quantify the secreted VEGF₁₆₅ protein. Lactose and ethanol levels in the culture medium were detected using the HPLC Dionex Ultimate 3000 system (Thermo Fisher Scientific, MA, USA) equipped with the HyperREZ XP Carbohydrate H⁺ column.

2.5. Screening of Different Medium Components

To evaluate the impact of various medium components on the biomass production of recombinant *K. lactis*, cultures were conducted in 250 mL shake flasks containing 50 mL of the initial basal medium in triplicate. The basal medium composition mirrored that of YPLac, with each flask supplemented with $40\ \text{g L}^{-1}$ of a carbon source, $20\ \text{g L}^{-1}$ of a nitrogen source, and $10\ \text{g L}^{-1}$ of an extract component. The cultures were then incubated for 72 hours at 30°C and 250 rpm. Eight carbon sources-lactose, glucose, starch, molasses, glycerol, acetic acid, sucrose, and galactose-were tested at an initial concentration of $40\ \text{g L}^{-1}$. Similarly, eight nitrogen sources-bacteriological peptone, meat peptone, casein peptone, urea, ammonium sulfate, diammonium sulfate, tryptone, and glycine-were examined at an initial concentration of $20\ \text{g L}^{-1}$. Additionally, three different extracts-yeast, malt, and meat extract-were chosen as additional nutritional sources and screened at an initial concentration of $10\ \text{g L}^{-1}$.

2.6. Box Behnken Design

Response surface methodology (RSM) was employed to optimize the medium components for the *K. lactis* cell biomass production. The experimental design utilized the Box-Behnken design within the Design Expert 13.0.0

program (Stat-Ease Inc., Minneapolis, USA). Overall, Box-Behnken design is characterized by a three-level second-order spherical design and offers several advantages compared to other designs. It allows the determination of significant factors using a limited number of runs and offers enhanced flexibility in selecting designs for a specified number of factors. In this study, the aim of using Box-Behnken design was to determine the optimal concentrations of galactose, tryptone, and yeast extract—identified as carbon, nitrogen, and extract sources, respectively—based on earlier screening.

Table 1. The central composite experimental design with coded values of variables.

Symbol	Independent variable name	Level		
		-1	0	1
A	Galactose (g L ⁻¹)	20	40	60
B	Tryptone (g L ⁻¹)	10	20	30
C	Yeast extract (g L ⁻¹)	5	10	15

A total of 17 experiments, encompassing all combinations of the three variables, were conducted with five replicates at the center point. This experimental setup aimed to fit a second-order polynomial model for each of the three independent variables, each at three levels. Additionally, the expression was carried out in 250 mL shake flasks filled with 100 mL of the medium in triplicate, incubated for 72 hours at 30°C and 250 rpm. Table 1 provides details on the normalized variables at levels of -1 (representing the lower value of the experimental conditions used), +1 (representing the higher value of the experimental conditions), and 0 (representing the central point condition) in the central composite design. For further clarity, Table 2 presents the experimental design with the terms in codes and their actual values within the specified range of variables.

Table 2. The central composite design of independent variables

Run	Coded value			Actual value		
	A	B	C	A	B	C
1	0	+1	+1	40	30	15
2	+1	-1	0	60	10	10
3	-1	0	-1	20	20	5
4	0	0	0	40	20	10
5	-1	0	-1	20	20	15
6	0	0	0	40	20	10
7	0	+1	-1	40	30	5
8	0	-1	+1	40	10	15
9	+1	0	+1	60	20	15
10	+1	+1	0	60	30	10
11	0	0	0	40	20	10
12	0	0	0	40	20	10
13	-1	-1	0	20	10	10
14	+1	0	-1	60	20	5
15	-1	+1	0	20	30	10
16	0	-1	-1	40	10	5
17	0	0	0	40	20	10

2.7. Statistical Analysis

The dry cell weight of the transformant *K. lactis* cells was taken as the response to be influenced by the four variables. The relationship between the response and the variables can be described by the second-order polynomial equation given as (1):

$$Y = \beta_0 + \sum \beta_i \chi_i + \sum \beta_{ij} \chi_i \chi_j + \sum \beta_{ii} \chi_i^2 \quad (1)$$

where Y represents the response variable (in this case, the dry cell weight of the transformant *K. lactis* cells); β_0 represents the constant value; β_i , β_{ij} and β_{ii} represent the regression coefficients, χ_i and χ_j represent the independent variables in coded values. Analysis of variance (ANOVA) was used to obtain the second-order polynomial equation for all response variables. The significance of the model equation was assessed using the F-test. The quality of fit of the polynomial model equation was determined by the coefficient of determination (R^2) and adjusted R^2 .

3. RESULTS

3.1. Process Kinetics of the Expression of VEGF₁₆₅ from *K. lactis*

The growth curve of *K. lactis* GG799 cultivated on YPLac medium with an initial lactose concentration of 40 g L⁻¹ was monitored over 120 hours. Samples were collected at intervals during this duration. Figure 1 presents the time course of changes in key growth parameters, including dry cell weight, optical density, lactose consumption, and ethanol production in shake flask fermentation. The graph illustrates that the strain *K. lactis* GG799 efficiently utilizes lactose as a carbon source for growth, with rapid consumption observed. Moreover, the strain expresses the gene encoding VEGF₁₆₅ under the *LAC4* promoter, inducible by lactose [26]. The results suggest the strain's ability to utilize lactose for both growth and the expression of the target gene, showcasing its potential for biotechnological applications. Figure 1 also indicates that VEGF₁₆₅ production in shake flask cultures parallels cell growth until reaching the stationary phase at 72 hours. Concurrently, ethanol production peaks at 24 hours (2.49 g L⁻¹) and is nearly completely consumed. Notably, the culture exhibits a distinct exponential growth phase, with a maximum specific growth rate of 0.24 h⁻¹ and a doubling time of 22 hours.

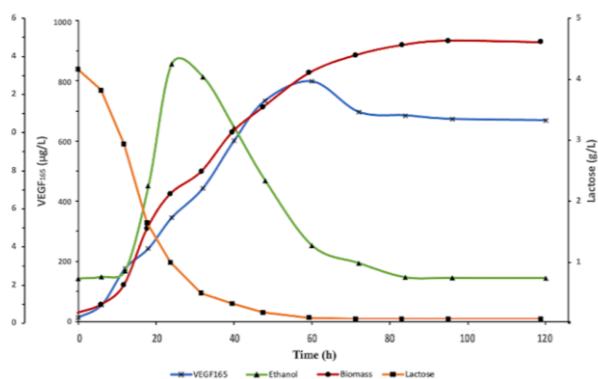


Figure 1. Production of recombinant VEGF₁₆₅ and cell growth profile of *K. lactis* GG799 in shake flask

3.2. Effect of Different Medium Components on Biomass and VEGF₁₆₅ Production

As an initial screening step before further optimization, various broth media in shake flasks containing different medium components were employed to investigate the effects on *K. lactis* cell growth and VEGF₁₆₅ expression. Figure 2 illustrates the impact of eight tested carbon sources added to the basal medium at 40 g L⁻¹. While glucose and glycerol exhibited favorable outcomes for biomass production, galactose emerged as a particularly notable carbon source, resulting in 1.58 ± 0.013 μg L⁻¹ of VEGF₁₆₅ production. Lactose and starch, also showed significant VEGF₁₆₅ production, yielding 0.99 ± 0.011 and 0.83 ± 0.014 μg L⁻¹, respectively. This result is consistent with many reports in the literature on recombinant protein production in *K. lactis* based on the use of galactose and lactose as carbon sources [27–29]. Indeed, galactose exhibited the highest biomass production among the tested carbon sources, yielding 15.98 ± 0.587 g L⁻¹. This was notably higher compared to both the control lacking any carbon source and the other carbon sources tested.

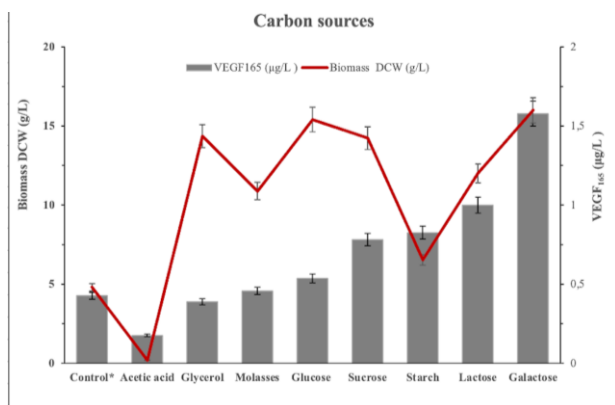


Figure 2. Effect of carbon sources on the biomass of *K. lactis* and VEGF₁₆₅ production. *Control culture without any carbon source

In this study, the influence of eight nitrogen sources on VEGF₁₆₅ production was investigated by supplementing them to a basal medium at a concentration of 20 g L⁻¹. The results, illustrated in Figure 3, revealed notable variations in both biomass and VEGF₁₆₅ production. Among the nitrogen sources examined, tryptone demonstrated the most favorable outcomes, yielding the highest biomass production at 16.18 ± 0.213 g L⁻¹. Additionally, tryptone also resulted in the highest VEGF₁₆₅ production at 0.99 ± 0.052 μg L⁻¹. Other nitrogen sources such as bacteriological peptone, casein peptone, and meat peptone showed similar VEGF₁₆₅ production levels, with yields of 0.86 ± 0.019, 0.87 ± 0.005, and 0.89 ± 0.028 μg L⁻¹, respectively. These findings highlight the impact of different nitrogen sources on both biomass and VEGF₁₆₅ production, offering valuable insights for the optimization of culture conditions in *K. lactis* to enhance recombinant protein expression.

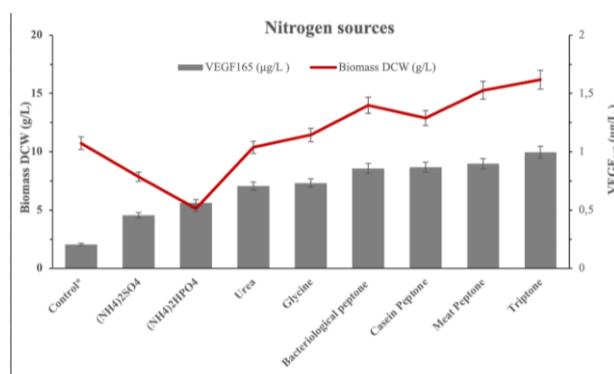


Figure 3. Effect of nitrogen sources on the biomass of *K. lactis* and VEGF₁₆₅ production. *Control culture without any nitrogen source

In this study, three extract components—malt, meat, and yeast extract—were evaluated as an additional nutritional resource in the growth medium to assess their effects on *K. lactis* biomass and VEGF₁₆₅ production. As depicted in Figure 4, the maximum VEGF₁₆₅ production of 0.68 ± 0.017 μg L⁻¹ and the highest biomass production of 16.18 ± 0.758 g L⁻¹ were achieved when yeast extract (10 g L⁻¹) was utilized. These results from the initial screening experiment highlight the significant impact of different medium components on both the biomass production of *K. lactis* and VEGF₁₆₅ production. Consequently, galactose, tryptone, and yeast extract were selected as the medium components for further optimization experiments.

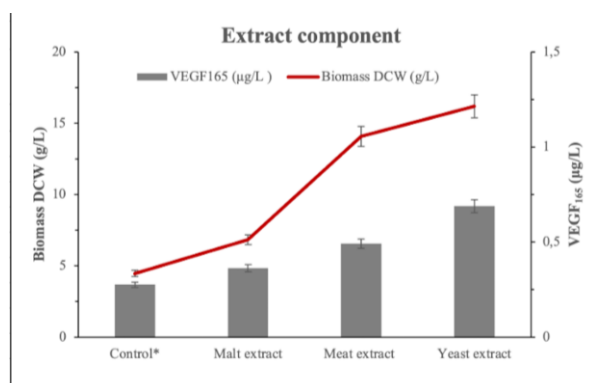


Figure 4. Effect of extract components on the biomass of *K. lactis* and VEGF₁₆₅ production. *Control culture without any extract component

3.3. Optimization of *K. lactis* Biomass using Response Surface Methodology

The objective of this study was to optimize the screened variables for biomass production to maximize VEGF₁₆₅ production, employing the Box-Behnken design. Experiments were conducted with compositions specified in Table 3. Following the screening experiments, three culture medium components—galactose, tryptone, and yeast extract—were selected for further evaluation in flask culture based on the experimental design. The relationship between the examined significant variables and biomass concentration, chosen as the response, was established using Response Surface Methodology (RSM). A central composite design (CCD) involving seventeen experiments, including 5 replicates of the central point, was executed. The observed and predicted responses, represented by dry cell weight values, for the 30

experiments are presented in Table 3. Utilizing the Box-Behnken experimental design, a wide range of biomass production in *K. lactis* GG799 was observed, ranging from 8.74 ± 0.22 to 17.52 ± 0.95 g L⁻¹. Comparing these experiments, the medium containing 20 g L⁻¹ galactose, 10 g L⁻¹ tryptone, and 10 g L⁻¹ yeast extract exhibited the

lowest biomass production at 8.74 g L⁻¹. Conversely, the highest biomass response of 17.52 g L⁻¹ was achieved in a medium containing 40 g L⁻¹ galactose, 20 g L⁻¹ tryptone, and 10 g L⁻¹ yeast extract.

Table 3. Central composite design and with actual and predicted response of biomass production with the independent variable values. Values are means of triplicates \pm SD.

Run	Factors			Response Biomass (g L ⁻¹)	
	A	B	C	Actual	Predicted
1	40	30	15	17.12 \pm 0.68	17.03
2	60	10	10	14.68 \pm 0.60	14.55
3	20	20	5	11.61 \pm 1.04	11.25
4	40	20	10	16.33 \pm 0.45	15.86
5	20	20	15	11.30 \pm 0.08	11.26
6	40	20	10	17.52 \pm 0.95	15.86
7	40	30	5	15.94 \pm 0.37	16.17
8	40	10	15	15.04 \pm 0.50	14.81
9	60	20	15	17.18 \pm 0.42	17.54
10	60	30	10	16.94 \pm 1.50	16.67
11	40	20	10	15.87 \pm 0.61	15.86
12	40	20	10	14.97 \pm 0.75	15.86
13	20	10	10	8.74 \pm 0.22	9.01
14	60	20	5	15.08 \pm 1.00	15.11
15	20	30	10	11.93 \pm 1.07	12.06
16	40	10	5	13.14 \pm 0.4	13.23
17	40	20	10	14.63 \pm 0.67	15.86

By applying the response surface, the following second-order regression equation explained the biomass as the interactions of the three culture medium components were yielded and is presented in the following equation:

$$Y_{\text{biomass}} = 15,86 + 2,54A + 1,29B + 0,6096C - 0,2330AB + 0,6035AC - 0,1813BC - 2,15A^2 - 0,6348B^2 + 0,0840C^2 \quad (2)$$

where Y is the response (biomass) and; A, B, and C are galactose, tryptone, and yeast extract respectively. Plus (+) and minus (-) symbols represent positive and negative effects on the response, respectively.

The effect of three independent factors on *K. lactis* GG799 biomass production was assessed using the analysis of variance (ANOVA) as detailed in Table 4. F-test, comparing the mean square regression to the mean square residual (12.19), indicates the significance of the process model with $p < 0.05$. The lack of fit F-value of 0.15 means the lack of fit is not significant relative to pure

error. The goodness of fit of the model is further evaluated using the R² coefficient (R² value), which stands at 0.94, explaining 94% of the validity of the response. Additionally, the predicted R² of 0.8207 is in reasonable agreement with the adjusted R² of 0.8629.

Among the terms analyzed, A (galactose), B (tryptone), and A² (galactose squared) with p-values less than 0.05 are deemed significant model terms. In Table 4, it is evident that galactose and tryptone exerted a more substantial effect on biomass production, as indicated by their relatively high mean square values (51.55 and 13.33 g L⁻¹, respectively), compared to yeast extract (2.97 g L⁻¹). Specifically, galactose played a crucial role in inducing heterologous protein production and enhancing cell growth through the utilization of the *LAC4* promoter (*P_{LAC4}*). This promoter drives the expression of the *LAC4* gene, encoding native lactase (β -galactosidase). β -galactosidase is an integral component of the lactose-galactose regulon, enabling the organism to efficiently use lactose as a carbon and energy source [30].

Table 4. Analysis of variance results for the model for biomass production

Source	Sum of Squares	df	Mean Square	F-value	p-value	
Model	91.58	9	10.18	12.19	0.0017	Significant
A (galactose, g L ⁻¹)	51.55	1	51.55	61.74	0.0001	
B (tryptone, g L ⁻¹)	13.33	1	13.33	15.97	0.0052	
C (yeast extract, g L ⁻¹)	2.97	1	2.97	3.56	0.1011	
AB	0.22	1	0.22	0.26	0.6257	
AC	1.46	1	1.46	1.74	0.2281	
BC	0.13	1	0.13	0.16	0.7033	
A ²	19.54	1	19.54	23.41	0.0019	
B ²	1.70	1	1.70	2.03	0.1970	
C ²	0.03	1	0.03	0.036	0.8557	
Residual	5.84	7	0.83			
Lack of Fit	0.58	3	0.19	0.15	0.9279	Not significant
Pure Error	5.27	4	1.32			
Cor Total	97.43	16				

R²=0.94, Adjusted R²=0.8629, Prediction R²=0.8207, Adeq Precision=12.1756

Biomass production was predicted for various values of the tested variables, and the results are illustrated through three-dimensional response surface plots (Figure 5). The plots depict the response (biomass production) on the z-axis against any two independent variables. In Figure 5a, the 3D plot showcases the effects of galactose and tryptone concentrations on biomass production. The plot suggests that intermediate concentrations of galactose and tryptone result in a more pronounced increase in biomass production. Figure 5b highlights the interaction between

galactose and yeast extract. It becomes evident that at higher concentrations of both components, biomass production can be elevated. In Figure 5c, the plot reveals the relationship between yeast extract and tryptone concentrations, indicating that increased biomass is observed with the rising concentration of yeast extract and tryptone. These three-dimensional response surface plots offer valuable insights into the intricate relationships among the variables and their impact on biomass production.

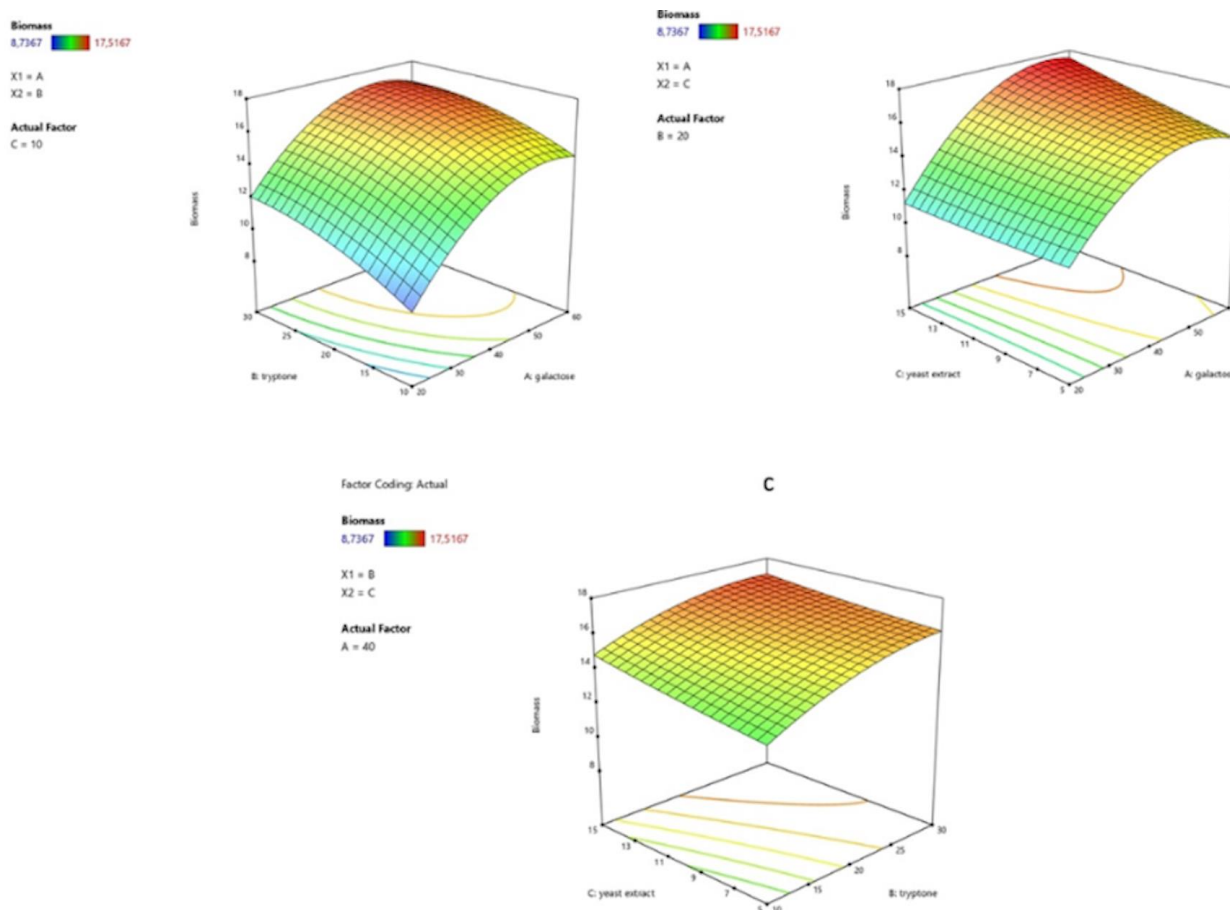


Figure 5. Three-dimensional response surface plot for *K. lactis* GG799 biomass production showing the interactive effects of (a) galactose and tryptone, (b) galactose and yeast extract, and (c) yeast extract and tryptone with the remaining factors held constant at the middle level of the Box-Behnken experimental design.

3.4. Model Diagnostics

To assess the adequacy of the model, the difference between observed values and calculated values obtained by the model, termed 'residuals,' was examined. The normal probability plot of 'studentized' residuals emerged as a crucial diagnostic tool for identifying and understanding systematic deviations from assumptions that errors are normally distributed and independent of each other [31]. As depicted in Figure 6, the graphical representation of residuals as a function of estimated values reveals that the errors of the biomass production models are scattered close to the diagonal line. This pattern implies that the model is a good fit and that the errors are normally distributed. The normal probability plot serves as a valuable validation tool, affirming the reliability of the model for predicting biomass production.

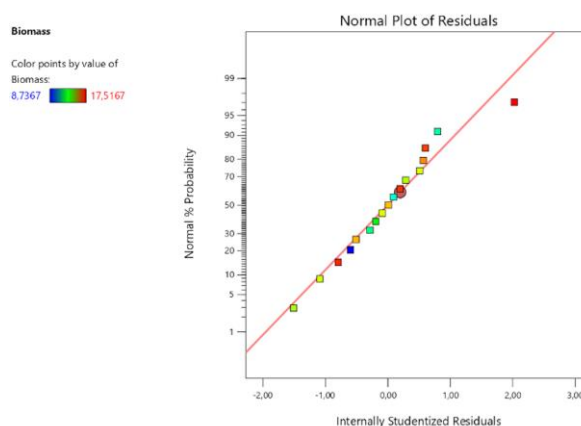


Figure 6. Normal (%) probability plot of the 'studentized' residuals for the model of biomass production

3.5. Validation of the Model

The model was optimized using the 'Point Optimization' of the Design Expert to achieve the maximum biomass production of *K. lactis* for recombinant VEGF₁₆₅. To validate the optimization, the criteria for biomass were set to 'maximize,' while galactose and tryptone were set to 'in range,' and yeast extract was set to 'minimize.' The level of yeast extract was minimized because it was identified as a non-significant model term with a p-value greater than 0.1. To verify the model, duplicate experiments were performed at the proposed optimum levels of the medium, comprising 45 g L⁻¹ galactose, 30 g L⁻¹ tryptone, and 5 g L⁻¹ yeast extract. The observed value for the biomass production was 18,65 g L⁻¹ and the predicted mean was 16.46. The 95% prediction interval ranged from 14.02 to 18.90. Additionally, in the same study, VEGF₁₆₅ concentration increased from 803.63 µg L⁻¹ to 1024.09 µg L⁻¹ after optimization, representing a 1.27-fold improvement. The biomass productivity (P), expressed in g of dry biomass per L of culture medium per h of cultivation time, reached 0.26 (g_{DCW} L⁻¹ h⁻¹) at the optimal levels. The excellent agreement between predicted and experimental biomass production after optimization reaffirms the validity of the screened medium components under the Box-Behnken experimental design.

4. DISCUSSION

The optimization of biomass production in *K. lactis* is paramount from an industrial perspective, as it significantly enhances the efficiency and feasibility of the processes involving recombinant protein production and other biotechnological applications. Numerous studies in the existing literature have emphasized maximizing *K. lactis* biomass production due to its inherent advantages, including, faster and cost-efficient recombinant protein production, scale-up potential, and enhanced productivity in terms of protein expression. This study delves into the impact of various growth medium components on the biomass production of *K. lactis* GG799. Subsequently, a statistical optimization approach was employed to augment the efficacy of the most impactful components.

Initially, the growth curve of *K. lactis* GG799 was studied over 120 hours, analyzing the key parameters, including dry cell weight, optical density, lactose consumption, and ethanol production in the growth medium YPLac, which includes lactose as a carbon source. Rapid lactose consumption was observed, facilitating both growth and the expression of the target gene VEGF₁₆₅ under the *LAC4* promoter (P_{LAC4}). The P_{LAC4} encodes native lactase, an essential part of the lactose-galactose regulon, enabling *K. lactis* to utilize lactose as a carbon and energy source [32]. Biomass production and VEGF₁₆₅ expression progressed in parallel progress until reaching the stationary phase at 72 hours. Subsequently, while the biomass continued to increase, the VEGF₁₆₅ expression remained constant. Within the initial 24 hours, most of the carbon source was consumed, and ethanol production peaked, gradually diminishing as ethanol was utilized as a substrate through the respire-fermentative metabolism of *K. lactis* [33]. The culture exhibited a distinct exponential growth phase,

resulting in a maximum specific growth rate of 0.24 h⁻¹ and a doubling time of 22 hours. This growth rate closely aligns with the 0.29 h⁻¹ reported by Toivari et al. (2013) for the same strain [34] and slightly exceeds the 0.16 h⁻¹ reported by Hun et al. (2013) for another strain (*K. lactis* NRRL Y-110) [27]. Furthermore, Boender et al. (2009) noted that a doubling time of 23.1 hours represents rapid growth for yeast in many natural environments [35].

Most studies on *K. lactis* growth have utilized complex media or glucose as a primary carbon source. However, this study diverges by screening eight carbon sources to determine the most effective components for biomass production and VEGF₁₆₅ expression. Both lactose and galactose serve as sugars capable of inducing expression under the *LAC4* promoter in *K. lactis*. It was reported that the transcription of *LAC4* can be induced 100-fold in the presence of lactose or galactose [36]. The screening assay highlights galactose and lactose stand out as carbon sources, yielding the highest expression of VEGF₁₆₅. Interestingly, the use of galactose notably enhances VEGF₁₆₅ production per unit of biomass compared to lactose. This suggests galactose supplementation exerts a more pronounced impact on the efficiency of VEGF₁₆₅ expression.

In the unoptimized medium, two nitrogen sources, peptone and yeast extract are present. To enhance biomass production and VEGF₁₆₅ expression, various nitrogen sources and extract components were screened. Among the nitrogen sources investigated tryptone yielded the most favorable outcomes, resulting in the highest biomass and VEGF₁₆₅ production, following bacteriological peptone and meat peptone. This suggests that in the metabolic process of tryptone in *K. lactis* GG799, utilization of the peptides and amino acids present in tryptone serves as the most effective nitrogen source, promoting growth and biomass production. Moreover, among the diverse extract components tested, yeast extract, rich in amino acids, peptides, vitamins, and minerals, emerged as the most potent supporter of *K. lactis* GG799 cell growth and proliferation.

This study aimed to optimize the screened variables for enhanced biomass production, with the ultimate goal of maximizing VEGF₁₆₅ production, employing the Box-Behnken design. The relationship between the three examined variables (galactose, tryptone, and yeast extract) and biomass concentration, chosen as the response, was established using RSM. The maximum biomass response of 17.52 g L⁻¹ was achieved in a medium comprising 40 g L⁻¹ galactose, 20 g L⁻¹ tryptone, and 10 g L⁻¹ yeast extract. The wide variation in biomass production, ranging from 8.74 ± 0.22 to 17.52 ± 0.95 g L⁻¹, underscores the significant influence of factors in recombinant protein production [37, 38]. The impact of the three independent factors on *K. lactis* GG799 biomass production was evaluated through ANOVA, revealing that the interaction between the variables significantly contributes to improving biomass production (p<0.05). Furthermore, the difference between the predicted and adjusted R² was less than 0.2, as expected for the fit statistic [39]. According to ANOVA, of the terms examined, A (galactose), B

(tryptone), and A2 (galactose squared) with p-values less than 0.05 are considered significant model terms. Galactose and tryptone had a more pronounced impact on biomass production, as reflected by their relatively high mean square compared to yeast extract. Additionally, the 3D plot illustrates the effects of galactose and tryptone concentrations on biomass production, suggesting that intermediate concentrations of galactose and tryptone lead to a more notable increase in biomass production. Also, the graphical representation of residuals as a function of estimated values indicates that the errors adhere to a normal distribution, affirming the good fit of the proposed model. The positive and negative contributions of the coefficients signify that any increase in medium components results in a statistically significant decrease or increase in biomass production, respectively. In equation (1), it is observed that the supplementation of galactose, tryptone, and yeast extract has a positive effect. The combined interaction of galactose and yeast extract (AC) has a positive effect on biomass production, while those of galactose and tryptone (AB) and tryptone and yeast extract (BC) are positive. However, the quadratic contribution of galactose and tryptone has a negative effect, while yeast extract shows a positive effect.

Under the experimental conditions considered in this study, the optimal medium composition predicted by

Design Expert software was determined to be 45 g L⁻¹ galactose, 30 g L⁻¹ tryptone, and 5 g L⁻¹ yeast extract. This resulted in biomass production of 18.65 g L⁻¹ and VEGF₁₆₅ production of 1024.09 µg L⁻¹. Notably, these values are approximately 1.31 and 1.27-fold higher than values obtained under unoptimized conditions, respectively. Despite the different medium compositions, the maximum biomass production obtained in this study (18.65 g L⁻¹) exceeded the values reported in the literature. For instance, Pandey and Veeranki [21] studied the optimization of human interferon-gamma by varying growth parameters and carbon source concentration and they observed the maximum biomass of *K. lactis* GG799 (15 g L⁻¹ dry cell weight) produced at a lactose concentration. In another study, Pandey et al. optimized the medium components for maximizing the biomass of recombinant *K. lactis*, resulting in a biomass production increased to 23.1 g L⁻¹, which was 1.5-fold higher as compared to the initial biomass value observed [20]. Zaharah et al. [38], developed a medium for recombinant endo-β-1,4-xylanase (Xyn2) production using *K. lactis* GG799, and the designed medium improved biomass output (5.67 g L⁻¹) and protein production by approximately 9 and 22%, respectively. Finally, Hun et al. investigated the effect of medium composition on the production of probiotic *K. lactis* NRRL Y-110 biomass, with maximal biomass of 6.32 g L⁻¹ yield obtained in shake flask cultivation [27].

Table 5. Comparison of results before and after optimization

Variable	Un-optimized medium		Optimized medium	
	g L ⁻¹		g L ⁻¹	
Medium components	Lactose	40	Galactose	45
	Peptone	20	Tryptone	30
	Yeast extract	10	Yeast extract	5
Biomass (g L ⁻¹)	14.22		18.65	
VEGF ₁₆₅ (µg L ⁻¹)	803.63		1024.09	
Biomass productivity (g _{DCW} L ⁻¹ h ⁻¹)	0.19		0.26	

5. CONCLUSION

In this study, we significantly enhanced the expression of recombinant human VEGF₁₆₅ by optimizing the biomass production of *K. lactis* through a statistical experimental design. Among the screened carbon, nitrogen, and extract components, galactose, tryptone, and yeast extract emerged as key factors leading to higher biomass production and increased VEGF₁₆₅ expression. Through the application of the Box-Behnken design, we achieved a remarkable increase in biomass production at the shake flask level compared to the initial production in the unoptimized growth medium. Concurrently, the expression level of recombinant VEGF₁₆₅ experienced a significant increase, surpassing 1 mg L⁻¹ with the optimized medium. These findings underscore the significant influence of medium components on both the growth of *K. lactis* GG799 and the production of recombinant VEGF₁₆₅. Nonetheless, the insights gained from this research have broader implications, offering potential relevance for the overexpression of other recombinant proteins utilized in various biotechnological applications. Furthermore, studies employing optimized media will advance the current understanding of the mechanism of heterologous

protein secretion by *K. lactis* and facilitate new strategies to enhance the production capabilities of these cells.

Acknowledgement

The authors thank the Ege University Scientific Research Projects Coordination Unit (Project Number: ONAP-2020-21791) for financial support.

REFERENCES

- [1] Apte RS, Chen DS, Ferrara N. VEGF in Signaling and Disease: Beyond Discovery and Development. *Cell*. 2019;176(6):1248-64.
- [2] Ferrara N, Kerbel RS. Angiogenesis as a therapeutic target. *Nature*. 2005;438:967-74.
- [3] Gerber HP, Vu TH, Ryan AM, Kowalski J, Werb Z, Ferrara N. VEGF couples hypertrophic cartilage remodeling, ossification and angiogenesis during endochondral bone formation. *Nat Med*. 1999;5:623-28.
- [4] Ferrara N, Carver-Moore K, Chen H, Dowd M, Lu L, O'Shea KS, et al. Heterozygous embryonic lethality

- induced by targeted inactivation of the VEGF gene. *Nature*. 1996;380:439-42.
- [5] Chintalgattu V, Nair DM, Katwa LC. Cardiac myofibroblasts: A novel source of vascular endothelial growth factor (VEGF) and its receptors Flt-1 and KDR. *J Mol Cell Cardiol*. 2003;35(3):277-86.
- [6] Reichardt LF, Tomaselli KJ. Extracellular matrix molecules and their receptors: Functions in neural development. *Annu Rev Neurosci*. 1991;14:531-70.
- [7] Lee SS, Joo YS, Kim WU, Min DJ, Min JK, Park SH, et al. Vascular endothelial growth factor levels in the serum and synovial fluid of patients with rheumatoid arthritis. *Clin Exp Rheumatol*. 2001;19:321-24.
- [8] Xia YP, Li B, Hylton D, Detmar M, Yancopoulos GD, Rudge JS. Transgenic delivery of VEGF to mouse skin leads to an inflammatory condition resembling human psoriasis. *Blood*. 2003;102(1):161-68.
- [9] Adamis AP, Shima DT. The Role of Vascular Endothelial Growth Factor in Ocular Health and Disease. *Retina*. 2005;25(2):111-18.
- [10] Dakowicz D, Zajkowska M, Mroczko B. Relationship between VEGF Family Members, Their Receptors and Cell Death in the Neoplastic Transformation of Colorectal Cancer. *Int J Mol Sci*. 2022;23(6):3375.
- [11] Dvorak HF, Nagy JA, Feng D, Brown LF, Dvorak AM. Vascular permeability factor/vascular endothelial growth factor and the significance of microvascular hyperpermeability in angiogenesis. In: Claesson-Welsh L, editor. *Vascular Growth Factors and Angiogenesis*. *Curr Top Microbiol Immunol*. Springer, Berlin, Heidelberg; 1999. p. 97-132.
- [12] Zhou Y, Zhu X, Cui H, Shi J, Yuan G, Shi S, et al. The Role of the VEGF Family in Coronary Heart Disease. *Front Cardiovasc Med*. 2021;8:738325.
- [13] Shen HL, Xu W, Wu ZY, Zhou LL, Qin RJ, Tang HR. Vector-based RNAi approach to isoform-specific downregulation of vascular endothelial growth factor (VEGF)165 expression in human leukemia cells. *Leuk Res*. 2007;31(4):515-21.
- [14] Papetti M, Herman IM. Mechanisms of normal and tumor-derived angiogenesis. *Am J Physiol Cell Physiol*. 2002;282(5):C947-70.
- [15] Vicari D, Foy KC, Liotta EM, Kaumaya PTP. Engineered Conformation-dependent VEGF Peptide Mimics Are Effective in Inhibiting VEGF Signaling Pathways. *J Biol Chem*. 2011;286(15):P13612-25.
- [16] Kim H, Yoo SJ, Kang HA, Alper EH. Yeast synthetic biology for the production of recombinant therapeutic proteins. *FEMS Yeast Res*. 2015;15(1):1-16.
- [17] Milton Vieira Gomes A, Souza Carmo T, Silva Carvalho L, Mendonça Bahia FI, Skorupa Parachin N. Comparison of Yeasts as Hosts for Recombinant Protein Production. *Microorganisms*. 2018;6(2):38.
- [18] Spohner SC, Schaum V, Quitmann H, Czermak P. *Kluyveromyces lactis*: An emerging tool in biotechnology. *J Biotechnol*. 2016;222:104-16.
- [19] Panuwatsuk W, Da Silva NA. Application of a gratuitous induction system in *Kluyveromyces lactis* for the expression of intracellular and secreted proteins during fed-batch culture. *Biotechnol Bioeng*. 2003;81:712-18.
- [20] Pandey R, Kumar N, Prabhu AA, Dasu Veeranki V. Application of medium optimization tools for improving recombinant human interferon gamma production from *Kluyveromyces lactis*. *Prep Biochem Biotechnol*. 2018;48(3):279-87.
- [21] Pandey R, Venkata &, Veeranki D, Dasu Veeranki V. Optimizing secretory expression of recombinant human interferon gamma from *Kluyveromyces lactis*. *Prep Biochem Biotechnol*. 2018;48(2):202-12.
- [22] Prabhu AA, Mandal B, Dasu VV. Medium optimization for high yield production of extracellular human interferon- γ from *Pichia pastoris*: A statistical optimization and neural network-based approach. *Korean J Chem Eng* 2017;34:1109-21.
- [23] Kumar S, Pakshirajan K, Venkata Dasu V. Development of medium for enhanced production of glutaminase-free l-asparaginase from *pectobacterium carotovorum* MTCC 1428. *Appl Microbiol Biotechnol*. 2009;84(3):477-86.
- [24] Gunst RF, Myers RH, Montgomery DC. Response Surface Methodology: Process and Product Optimization Using Designed Experiments. *Technometrics* 1996;38(3):285-86.
- [25] Kuduğ Ceylan H, Erden Tayhan S, Gökçe İ. Secretory Expression of Human Vascular Endothelial Growth Factor (VEGF165) in *Kluyveromyces lactis* and Characterization of Its Biological Activity. *Int J Pept Res Ther*. 2021;27:1989-2001.
- [26] Álvarez-Cao ME, Rico-Díaz A, Cerdán ME, Becerra M, González-Siso MI. Valuation of agro-industrial wastes as substrates for heterologous production of α -galactosidase. *Microb Cell Fact*. 2018;17:137.
- [27] C. Hun C, Sueb MS, Malek RA, Othman NZ, Elsayed EA, Ramili S, et al. Bioprocess Development for High Cell Mass Production of the Probiotic Yeast-*Kluyveromyces lactis*. *IOSR J Pharm Biol Sci*. 2013;8(3):49-59.
- [28] Rajoka MI, Khan S, Shahid R. Kinetics and regulation studies of the production of β -galactosidase from *Kluyveromyces marxianus* grown on different substrates. *Food Technol Biotechnol*. 2003;41:315-20.
- [29] Coelho Sampaio F, da Conceição Saraiva TL, Dumont de Lima e Silva G, Teles de Faria J, Grijó Pitangui C, Aliakbarian B, et al. Batch growth of *Kluyveromyces lactis* cells from deproteinized whey: Response surface methodology versus Artificial neural network-Genetic algorithm approach. *Biochem Eng J*. 2016;109:305-11.
- [30] Sheetz RM, Dickson RC. Lac4 is the structural gene for beta-galactosidase in *Kluyveromyces lactis*. *Genetics* <https://doi.org/10.1093/GENETICS/98.4.729>
- [31] Leardi R (2009) Experimental design in chemistry: A tutorial. *Anal Chim Acta*. 1981;98(4):729-45.
- [32] Colussi PA, Taron CH. *Kluyveromyces lactis* LAC4 promoter variants that lack function in bacteria but retain full function in *K. lactis*. *Appl Environ Microbiol*. 2005;71(11).

- [33] González-Siso MI, Freire-Picos MA, Ramil E, González-Domínguez M, Rodríguez Torres A, Cerdán ME. Respirofermentative metabolism in *Kluyveromyces lactis*: Insights and perspectives. *Enzyme and Microbial Technology* 2000;26(9-10):699-705.
- [34] Toivari M, Vehkomäki ML, Nygård Y, Penttilä M, Ruohonen L, Wiebe MG. Low pH d-xylonate production with *Pichia kudriavzevii*. *Bioresour Technol.* 2013;133:555-62.
- [35] Boender LGM, De Hulster EAF, Van Maris AJA, Daran-Lapujade PAS, Pronk JT. Quantitative physiology of *Saccharomyces cerevisiae* at near-zero specific growth rates. *Appl Environ Microbiol.* 2009;75(17):5607-14.
- [36] Dickson RC, Sheetz RM, Lacy LR. Genetic regulation: yeast mutants constitutive for beta-galactosidase activity have an increased level of beta-galactosidase messenger ribonucleic acid. *Mol Cell Biol.* 1981;1(11):1048-56.
- [37] Purama RK, Goyal A. Screening and optimization of nutritional factors for higher dextransucrase production by *Leuconostoc mesenteroides* NRRL B-640 using statistical approach. *Bioresour Technol.* 2008;99(15):7108-14.
- [38] Zaharah SF, Fuzi M, Razali F, Jamaliah, Jahim JM, Rahman RA, Illias RM. Simplified feeding strategies for the fed-batch cultivation of *Kluyveromyces lactis* GG799 for enhanced recombinant xylanase production. *Bioprocess Biosyst Eng.* 2014;37:1887-98.
- [39] Variyana Y, Muchammad RSC, Mahfud M. Box-behnken design for the optimization using solvent-free microwave gravity extraction of garlic oil from *Allium sativum* L. *IOP Conference Series: Materials Science and Engineering*, 2019;673.

Effect of cAMP-dependent Phosphodiesterase Activity on *NTH1* Gene Expression and Reserve Carbohydrate Metabolism

Tülay TURGUT GENÇ^{1*} 

¹ Çanakkale Onsekiz Mart University, Science Faculty, Biology Department, Çanakkale, Türkiye
ORCID No: 0000-0001-5074-3572

*Corresponding author: tturgutgenc@comu.edu.tr

(Received: 22.11.2023, Accepted: 10.06.2024, Online Publication: 28.06.2024)

Keywords

Heat stress,
Nitrogen
starvation,
PDE1,
PDE2,
*Saccharomyces
cerevisiae*,
Stress recovery

Abstract: The regulation of Protein kinase A signaling pathway is controlled by the cellular cAMP level. The level of cAMP in the cell is regulated by the enzymes adenylate cyclase, which synthesizes the cAMP from ATP, and cAMP phosphodiesterase, which degrades the cAMP to AMP. The *PDE1* and *PDE2* genes encode two phosphodiesterases with low and high affinity for cAMP, respectively. The *NTH1* gene encodes the neutral trehalase enzyme, which is responsible for stress-accumulated trehalose degradation, and its expression is regulated by PKA. The aim of this study was to examine the effect of *PDE1* and *PDE2* gene products on the expression of the *NTH1* gene and reserve carbohydrate metabolism in both stressful and restoring conditions. Thus, the expression of the *NTH1* was assessed under nitrogen starvation, heat stress, and recovery period by inserting the plasmid containing the *Nth1-LacZ* gene fusion into *pde1Δ*, *pde1Δ*, and wild-type yeast strains. The expression of the *NTH1* gene was shown to be lower than that of the wild-type under normal conditions, heat stress, nitrogen starvation, and also during the replenishment period in *pde1Δ* and *pde1Δ* yeast cells. The accumulation of trehalose and glycogen was shown to be dramatically enhanced in *pde1Δ* yeast cells. However, deletion of the *PDE2* gene did not lead to a significant change in trehalose and glycogen accumulation comparable to that found in the wild-type. These results indicate that the *PDE1* gene product, rather than *PDE2*, is required for the downregulation of reserve carbohydrate metabolism. Consequently, the Pde1 protein is considered to exert yet-unidentified regulatory control over the Pde2 protein.

cAMP-bağımlı Fosfodiesteraz Aktivitesinin *NTH1* Gen Ekspresyonu ve Depo Karbonhidrat Metabolizması Üzerine Etkisi

Anahtar

Kelimeler

Isı stresi,
Azot açlığı,
PDE1,
PDE2,
*Saccharomyces
cerevisiae*,
Stresten
kurtulma

Öz: Protein kinaz A sinyal yolağının düzenlenmesi hücrel cAMP seviyesi tarafından kontrol edilir. Hücredeki cAMP seviyesi ise, cAMP'yi ATP'den sentezleyen adenilat siklaz ve cAMP'yi AMP'ye indirgeyen cAMP fosfodiesteraz enzimleri tarafından düzenlenir. *PDE1* ve *PDE2* genleri, cAMP için düşük ve yüksek afiniteye sahip iki fosfodiesterazı kodlar. *NTH1* geni stres şartlarında biriktirilen trehalozun parçalanmasından sorumlu olan nötral trehalaz enzimini kodlar ve ekspresyonu PKA tarafından kontrol edilir. Bu çalışmada, stres koşullarında ve stres sonrasında, *PDE1* ve *PDE2* genlerinin *NTH1* gen ekspresyonu ve depo karbonhidrat metabolizması üzerine etkisinin belirlenmesi amaçlanmıştır. Bu nedenle *Nth1-LacZ* gen füzyonu taşıyan plazmid *pde1Δ*, *pde1Δ* ve yaban tip maya suşlarına transforme edilerek azot açlığında, ısı stresinde ve stres sonrasında *NTH1* gen ekspresyonu belirlendi. Normal koşullarda, ısı stresinde, azot açlığında ve stresten kurtulma sonrasında, *pde1Δ* ve *pde1Δ* maya hücrelerinde belirlenen *NTH1* gen ekspresyonunun yaban tipten daha düşük olduğu gözlemlendi. Trehaloz ve glikojen birikiminin *pde1Δ* maya hücrelerinde oldukça yüksek oranda arttığı gözlemlendi. Bununla birlikte, *PDE2* yokluğunun trehaloz ve glikojen birikiminde önemli bir değişikliğe yol açmadığı gözlemlendi. Bu sonuçlar, depo karbonhidrat metabolizmasının aşağı regülasyonu için *PDE2*'nin değil de *PDE1* gen ürününün gerekli olduğunu göstermektedir. Sonuç olarak, Pde1 proteininin, Pde2 proteini üzerinde henüz tanımlanamayan düzenleyici kontrol uyguladığı düşünülmektedir.

1. INTRODUCTION

The budding yeast *Saccharomyces cerevisiae* has the ability to respond to environmental alterations by using different sensing and signaling mechanisms. Depending on nutrient availability, yeast cells alter their gene expression patterns and related metabolic pathways. The stress response system is a good example of how to analyze these alterations in nutrient-deficient conditions. The stress tolerance of yeast cells begins to increase whenever they enter the stationary phase of growth, where essential nutrients are depleted [1, 2]. One of these signaling pathways is the RAS-cAMP-PKA pathway, which is involved in different stress responses such as oxidative stress, osmotic stress, and STRE-related stress. Protein kinase A (PKA) is a tetrameric protein that is composed of two regulatory subunits (encoded by *BCY1*) and two catalytic subunits (encoded by *TPK1*, *TPK2*, and *TPK3*) [2, 3]. The activity of PKA is regulated by the binding of cyclic AMP (cAMP) to Bcy1p, which results in the release of catalytic subunits. The level of cAMP in the cell is regulated by the activity of RAS-associated adenylate cyclase (encoded by *CYR1*) and cAMP phosphodiesterase (encoded by *PDE1* and *PDE2*) enzymes. The adenylate cyclase enzyme is responsible for the synthesis of cAMP from ATP, and the phosphodiesterase enzyme degrades the cAMP to AMP [4, 5].

The primary amino acid sequences of Pde1 and Pde2 cAMP phosphodiesterases are not similar. *PDE1* and *PDE2* genes were coded for 526 and 369 amino acids, respectively. Both phosphodiesterase enzymes have different affinities for cAMP. The monomeric Pde1p has low affinity for cAMP, with its Michaelis-Menten constant (K_m) changing between 20 and 250 μ M. The dimeric Pde2p has a high affinity for cAMP, with a K_m for cAMP of 170 nM. Pde1 protein has dual activity on the hydrolysis of both cAMP and cGMP with similar enzymatic efficiencies. Pde1p is required for lowering the concentration of intracellular cAMP levels upon the addition of glucose. In addition, Pde1p has a specific role in agonist-induced cAMP signaling in response to intracellular acidification. Pde2p is responsible for breaking down exogenous cAMP. Pde2p controls the basal cAMP level in the cell. Deletion of the *PDE2* gene causes the accumulation of cAMP and continuously active PKA, which results in irregularities in cell wall integrity and stress response pathways [5-7].

The level of the stress metabolite, trehalose, is controlled by cAMP in *S. cerevisiae* yeast cells. Trehalose accumulation starts in the diauxic phase and continues during the stationary phase in normal growth conditions. But in a stressful environment, trehalose is accumulated at the logarithmic phase. The stress-accumulated trehalose must be rapidly degraded whenever the stress is terminated. The level of trehalose in yeast cells is maintained by means of the TPS enzyme complex and the trehalase enzyme. The hydrolysis of trehalose is fulfilled by the neutral trehalase enzyme encoded by the *NTH1* gene. The promoter region of *NTH1* contains three STRE motifs that are the targets of transcriptional activator

proteins, Msn2 and Msn4. *NTH1* expression is induced by various stresses as well as by cAMP-dependent protein kinase [8]. Therefore, the inhibition of Msn2p and Msn4p activation via the highly activated RAS-cAMP-PKA pathway or some other interconnected pathways directly affects the stress response of the yeast *S. cerevisiae* [9-11].

We investigated the role of cAMP phosphodiesterases in *NTH1* gene expression and reserve carbohydrate deposits under nitrogen deficiency and heat stress. Our results indicated that the deletion of *PDE1* or *PDE2* genes downregulates *NTH1* gene expression both in normal growth conditions and stressful environments. In addition, the *PDE1* gene product may be involved in the downregulation of reserve carbohydrate metabolism.

2. MATERIAL AND METHOD

2.1. Yeast Strains and Plasmids

Yeast strains BY4741 (*Mata*, *his3 Δ 1*; *leu2 Δ 0*; *met15 Δ 0*; *ura3 Δ 0*) and mutant derivatives *pde1 Δ* (*Mata*, *his3 Δ 1*; *leu2 Δ 0*; *met15 Δ 0*; *ura3 Δ 0*; YGL248w::kanMX4) and *pde2 Δ* (*Mata*, *his3 Δ 1*; *leu2 Δ 0*; *met15 Δ 0*; *ura3 Δ 0*; YOR360c::kanMX4) were used in this study. The yeast strains were purchased from EUROSCARF (Frankfurt, Germany). *PDE1* and *PDE2* genes were completely replaced with the KanMX4 module in both *pde1 Δ* and *pde2 Δ* strains, respectively. The pNL1 plasmid, including the *Nth1-lacZ* gene fusion, was used to quantify the promoter activity of the *NTH1* gene. The other plasmid, including the *Suc2-lacZ* gene fusion, was used as a control.

S. cerevisiae strains were cultured in YPD medium (1% yeast extract, 2% peptone, and 2% glucose) for plasmid transformation. The plasmids were transformed into wild-type, *pde1 Δ* , and *pde2 Δ* yeast strains using a procedure as described previously [12]. Yeast cells were plated on Yeast Synthetic Minimal (YSM) medium without uracil (0.17% yeast nitrogen base (w/o amino acids and ammonium sulphate) + 0.5% ammonium sulphate + 20 mg L⁻¹ histidine + 60 mg L⁻¹ leucine + 20 mg L⁻¹ methionine) supplemented with 2% glucose and grown at 30 °C till well-grown transformant colonies were obtained.

2.2. Growth Conditions

Transformant yeast cells were grown overnight in YSM medium at 120 rpm and 30 °C. The overnight cultures were resuspended in fresh YSM culture and grown to an exponential phase under the same conditions. The yeast cultures were then separated into two groups, and one part of the culture was transferred directly to a 42 °C incubator without changing the other growth conditions. The second part was harvested, washed, refreshed in YSM culture supplemented with proline (0.1%), and then incubated at 30 °C. All yeast cultures were further incubated for four hours. At the end of incubation periods, half of the cultures were harvested and used for measurements of β -galactosidase activities, trehalose, and glycogen contents

of the yeast cells. The second half of the cultures grown at 42 °C were transferred to 30 °C for heat stress recovery, and 0.5% ammonium sulphate was added to rescue yeast cells from nitrogen starvation. Then all yeast cultures were grown at these conditions for further 4 hours.

2.3. Enzyme Assays

The harvested yeast cells were used for determining β -galactosidase activities as described previously [13]. Beta galactosidase units (U) were given in nanomoles of ONPG (o-Nitrophenyl β -D-Galactopyranoside) cleaved per minute per milligram of protein in permeabilized yeast cells. Trehalose and glycogen assays of yeast cells were determined as described previously [14]. The yeast transformants were removed, washed with ice-cold water, and then resuspended in 125 μ L of 0.25 M Na_2CO_3 and incubated at 95 °C for about 3 hours. Then 75 μ L of 1 M acetic acid and 300 μ L of 0.2 M sodium acetate, pH 5.2 were added and divided into two parts. One half of the cell mixture was incubated at 37 °C overnight in the presence of 3 mU trehalase enzyme (Sigma, T8778) for the trehalose assay. The second half of the suspension was incubated at 57 °C for overnight with continuous shaking in the presence of 70 U mg^{-1} amyloglucosidase enzyme from *Aspergillus niger* (Sigma, 10115) for the glycogen assay. The quantity of liberated glucose was measured enzymatically using the glucose oxidase-peroxidase system (GOD-POD assay) (Fluitest®-GLU, Biocon, Germany). The amounts of trehalose and glycogen in the yeast cells were calculated and expressed as micrograms of glucose equivalent per milligram of wet mass ($\mu\text{g mg}^{-1}$).

2.4. Statistical Analysis

The results were reported as the means \pm standard deviation (SD) of at least three independent transformants and three independent experiments. Data analysis was performed using GraphPad Prism software 5 (GraphPad Software Inc., La Jolla, USA). Differences were considered statistically significant when a P value was less than 0.05.

3. RESULTS AND DISCUSSION

3.1. Effects of Pde1 and Pde2 on *NTH1* Transcription

In order to determine the effects of low- and high-affinity cyclic AMP phosphodiesterases on regulation of *NTH1* gene transcription, Nth1-lacZ gene fusion was transformed into wild-type, *pde1 Δ* , and *pde2 Δ* strains. The expression of Nth1-lacZ gene fusion in wild-type, *pde1 Δ* , and *pde2 Δ* yeast cells was found to be 857.7 \pm 98.6 U, 437.2 \pm 40.5 U, and 226.3 \pm 27.3 U, respectively (Figure 1). The *NTH1* gene expression decreased 2-fold in the absence of Pde1 protein and 2-fold in the absence of Pde2 protein at normal growth conditions. This result indicated that the absence of PDE genes caused a significant reduction in *NTH1* transcription under normal growth conditions. Also, the promoter activation in *pde2 Δ* yeast cells was 2-fold lower than that in *pde1 Δ* yeast cells.

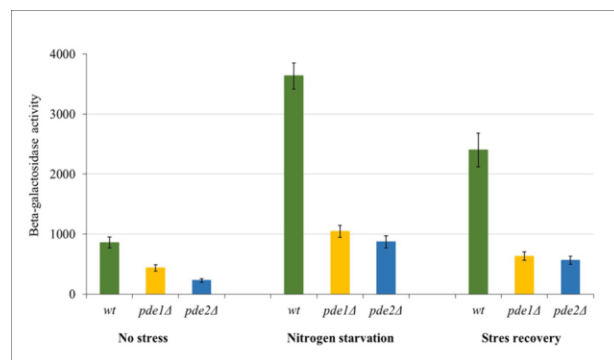


Figure 1. The effect of Pde1 and Pde2 proteins on the expression of *NTH1* gene during nitrogen starvation and recovery. For nitrogen starvation yeast cells transferred to 0.1% proline and for recovery 0.5% ammonium sulfate was added. Incubation period for nitrogen starvation and recovery period was 4 hours.

In glucose-grown yeast cells, PKA is activated through the RAS-cAMP pathway, depending on the cAMP concentration. High cAMP accumulation results in a continuously active PKA that phosphorylates Rim15, Yak1, and Msn2/4 and localizes them in the cytoplasm [2, 10, 15, 16]. Also, nuclear Msn2/4 proteins are phosphorylated by active Yak1 and Rim15 kinases from sites apart from the PKA phosphorylation site, and then they bind to the relevant stress elements (STRE sequences) and activate transcription. Therefore, in the absence of *PDE1* and *PDE2* gene products, continuously active PKA blocks Msn2/4 activation, resulting in reduced *NTH1* transcription in a stress-free environment. As a result, even under normal growth circumstances, cAMP phosphodiesterase enzyme activity is required for *NTH1* gene regulation. Furthermore, it was shown that the Pde2 protein exhibited greater efficacy in facilitating *NTH1* transcription compared to the Pde1 protein.

The exponentially growing yeast cells were transferred to the nitrogen starvation condition, and the promoter activations were determined (Figure 1). The expression of Nth1-lacZ gene fusion in the wild-type, *pde1 Δ* and *pde2 Δ* yeast cells was determined to be 3636.2 \pm 218.5 U, 1044.5 \pm 98.6 U, and 869.8 \pm 95.2 U, respectively. The promoter activity of wild-type yeast cells increased nearly 4-fold in nitrogen starvation. Similarly, when *pde1 Δ* and *pde2 Δ* mutant yeast cells were transferred to poor nitrogen sources, the expression level increased nearly 2-fold in *pde1 Δ* and 4-fold in *pde2 Δ* mutants. The *NTH1* transcription level in *pde1 Δ* and *pde2 Δ* yeast cells was 2-fold lower than in wild-type yeast cells under nitrogen starvation conditions. When the yeast cells shifted to a nitrogen-rich environment, Nth1-lacZ gene expression became 2400.4 \pm 278.6 U, 631.8 \pm 72.6 U, and 561.6 \pm 65.3 U in the wild-type, *pde1 Δ* , and *pde2 Δ* yeast cells, respectively. Although the *NTH1* promoter activity in wild-type and mutant yeast cells decreased nearly 2-fold after the replenishment period, it was still higher than in the normal growth condition. Yeast strains did not show a dramatic fall in *NTH1* gene expression after the 4-hour post-stress period, but it was observed that there was a gradual recovery of gene expression back to pre-stress patterns after 8 hours (data not given).

When heat stress was applied to yeast cells, Nth1-lacZ expression of wild-type, *pde1Δ*, and *pde2Δ* yeast cells was measured as 1789.6±214.6 U, 679.7±71.8 U, and 288.6±50.3 U, respectively (Figure 2). The shifting of wild-type and *pde2Δ* yeast cells to 42 °C increased the expression of Nth1-LacZ gene fusion nearly twofold. However, the shifting of *pde1Δ* yeast cells to heat stress did not cause a change in *NTH1* promoter activity. After the 4-hour recovery period, the *NTH1* promoter activities of wild-type (766.5±72.7 U) and *pde1Δ* yeast cells (458.3±62.8 U) were returned to the pre-stress level. Interestingly, in the absence of the *PDE2* gene, *NTH1* transcription was not affected during heat stress and stress recovery. Generally, *NTH1* transcription levels in *pde1Δ* and *pde2Δ* yeast cells became lower than wild-type yeast cells under both normal and stressful conditions. In addition, regulation of *NTH1* gene expression in stress conditions is faster than in stress recovery.

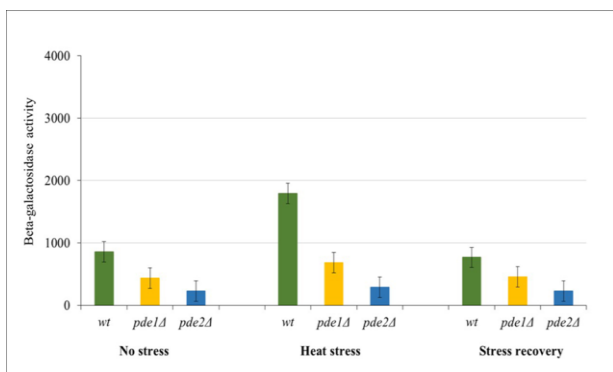


Figure 2. The effect of Pde1 and Pde2 proteins on the expression of *NTH1* gene during heat stress and recovery. For heat stress yeast cells transferred to 42 °C and for recovery yeast cells retreated to 30 °C. Incubation period for heat stress and recovery period was 4 hours.

The variable stress conditions activate Msn2/4 and Hsf1 transcription factors via different signaling pathways. Msn2/4 and Hsf1 transcription factors bind to the STRE sequences and heat shock elements (HSE), respectively. Msn2/4 transcription factors are localized both in the cytoplasm and nucleus, depending on environmental conditions [15]. The nuclear localization and activity of Msn2/4 proteins increase after nutrient starvation or other stress treatments [15-17]. Hsf1 transcription factor is localized in the nucleus and bound to HSE under normal growth conditions. The occupancy and activity of Hsf1 increase after heat shock treatment. The activity of Msn2/4 and Hsf1 transcription factors is regulated by different signaling pathways. Yak1 and Rim15 kinases are regulated by cAMP-dependent PKA and TOR (Target of Rapamycin) signaling pathways [18]. Rapamycin treatment or nitrogen starvation causes the inactivation of the TOR pathway, which results in the nuclear accumulation of Msn2/4 proteins and the localization of Yak1 and Rim15 kinases in the nucleus [2, 10, 16, 18, 19]. Thus, Yak1 kinase activates the nuclear Msn2/4 and Hsf1 proteins for binding to STRE and HSE sequences, respectively. Therefore, in our research, *NTH1* gene expression increased in wild-type yeast cells in response to nitrogen starvation and heat stress. The constitutive activation of the RAS/cAMP pathway blocks several rapamycin-induced responses, such as the activation of stress transcription [18, 20]. The high cAMP level in the

absence of cAMP phosphodiesterase enzyme activity caused constitutive activation of PKA and may have blocked STRE-mediated *NTH1* gene expression. Therefore, *NTH1* transcription in *pde1Δ* and *pde2Δ* yeast strains may have been lower than in wild-type yeast cells.

SUC2 gene expression is independent of stress regulation, so it was used as a control. The expression of *Suc2-lacZ* gene fusion at normal growth conditions was found to be 1.48±0.02 U, 1.12±0.02 U, and 1.53±0.03 U in wild-type, *pde1Δ*, and *pde2Δ* yeast strains, respectively. The *Suc2-lacZ* expressions in wild-type, *pde1Δ*, and *pde2Δ* yeast strains were found to vary between 1.88±0.01 U and 4.72±0.05 U during nitrogen starvation, heat stress, and replenishment periods.

3.2. Effects of Pde1 and Pde2 on Trehalose and Glycogen Accumulation

S. cerevisiae yeast cells accumulate trehalose and glycogen as an energy source when environmental conditions become unfavorable. The accumulation of both carbohydrates is regulated by different signaling pathways, such as the RAS/cAMP pathway, depending on the growth rate of yeast cells. Therefore, the effect of cAMP phosphodiesterase activity on reserve carbohydrate accumulation was determined in wild-type, *pde1Δ*, and *pde2Δ* yeast strains during the exponential phase. As expected, the trehalose level was 2-fold higher than the glycogen level in wild-type cells under normal growth conditions (Figure 3). In *pde1Δ* yeast cells, the level of trehalose was almost four times higher than the level of glycogen. However, the levels of trehalose and glycogen in *pde1Δ* yeast cells were 17-fold and 9-fold higher, respectively, than in wild-type cells. The trehalose level in *pde2Δ* yeast cells was nearly 2-fold higher than the glycogen level, and the level of these carbohydrates in *pde2Δ* yeast cells was similar to the wild-type level. Both trehalose and glycogen levels in the yeast cells were quite high in the presence of solo *PDE2* gene. But the presence of a solo *PDE1* gene (*pde2Δ*) or the presence of both *PDE1* and *PDE2* genes (wt) resulted in basal-level accumulation of these reserve carbohydrates. These results suggest that *PDE1* and *PDE2* gene products may be involved in down- and up-regulation of reserve carbohydrate metabolism, respectively.

It was previously reported that *PDE2* deletion did not result in a significant reduction in expected PKA-dependent phosphorylation events [21]. Furthermore, deletion of the *PDE1* gene results in significantly larger cAMP accumulation in response to glucose addition, whereas deletion of the *PDE2* gene results in low cAMP accumulation [22]. The phosphorylation of the Pde1 protein by PKA does not change its affinity for cAMP but may change its interaction with other proteins and subcellular localization [22]. The cAMP-phosphodiesterase Pde2 exhibits physical interaction with several stress-regulated transcription factors that are targeted by PKA [23]. The role of Pde2 is crucial in the proper initiation of Msn2/4 target genes [21]. Consequently, the Pde2 protein interacts with the Msn2/4 transcription factors, creating a stress signal that induces

the accumulation of reserve carbohydrates. High levels of trehalose and glycogen were therefore observed in *pde1Δ* mutant cells.

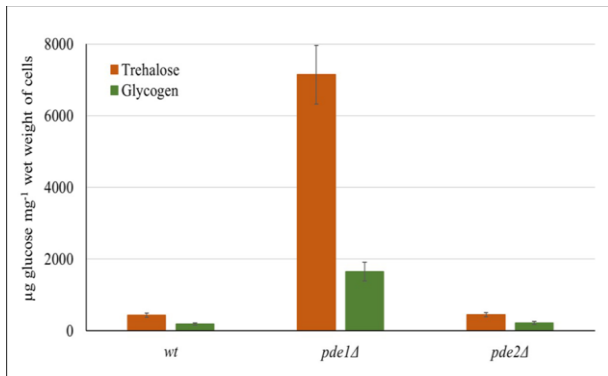


Figure 3. The effect of cAMP phosphodiesterase activity on trehalose and glycogen accumulations at normal growth condition.

In a recent study, the hyperactivation of the Ras/cAMP/PKA pathway in *pde2Δ* mutant cells resulted in decreased glycogen accumulation and thermotolerance in the pathogenic fungus *Candida auris* [24]. As a result, they suggested that *C. auris* primarily uses high-affinity phosphodiesterase (Pde2) as the primary regulator of the cAMP/PKA signaling pathway, with the low-affinity Pde1 enzyme playing a minor role. However, the low levels of trehalose and glycogen in the wild-type and *pde2Δ* yeast cells in this study show that the Pde1 protein can regulate the activity of the Pde2 protein under normal growth conditions via an unidentified mechanism. It has been reported that the creation of deterministic mathematical models of the PKA module and complete cAMP pathway reveals that Pde1p is more important than Pde2p for controlling the cAMP levels following glucose pulses, and the proportion of active PKA is not directly proportional to the cAMP level, allowing PKA to exert negative feedback by activating Pde1p [25]. Our findings suggest that, in addition to the enzymatic activity of Pde1, its regulatory role confers upon it a heightened significance comparable to that of the Pde2 protein.

3.3. Trehalose and Glycogen Accumulation Under Nitrogen Starvation and Recovery

In order to determine the effect of Pde1 and Pde2 on trehalose and glycogen accumulation, yeast cells were grown at a strong nitrogen source until the exponential stage and then transferred to a poor nitrogen source. Trehalose and glycogen levels increased 3-fold and 26-fold in wild-type yeast cells during nitrogen starvation, respectively (Figure 4). Glycogen accumulation during starvation was fourfold higher than the trehalose level in wild-type yeast cells. During starvation, half of the stored trehalose was broken down in *pde1Δ* yeast cells, resulting in a decline in the trehalose level, whereas the glycogen level increased two-fold. Trehalose level in *pde1Δ* yeast cells was still 3-fold higher than that of wild-type. The nitrogen deficiency induced trehalose and glycogen accumulation about 2-fold and 3-fold, respectively, in *pde2Δ* yeast cells. These results indicate that nitrogen starvation induces more glycogen accumulation than trehalose, both in wild-type and mutant yeast cells.

Additionally, *pde2Δ* yeast cells were more susceptible to nitrogen deficiency than *pde1Δ* yeast cells, which indicates that Pde2 protein has a more significant function than Pde1 protein in the regulation of reserve carbohydrate metabolism. It was previously shown that the deletion of the *PDE2* gene made cells sensitive to freeze-thawing and oxidative stress, whereas the deletion of the *PDE1* gene has no effect on cellular stress resistance [6]. Furthermore, it was shown that glycogen accumulation and stress tolerance were lower in *C. auris pde2Δ* cells compared to *Δpde1* mutant cells [24]. Since *pde2Δ* yeast cells accumulate fewer stress metabolites than *pde1Δ* yeast cells and are thus more sensitive to environmental stresses, our results are consistent with these findings.

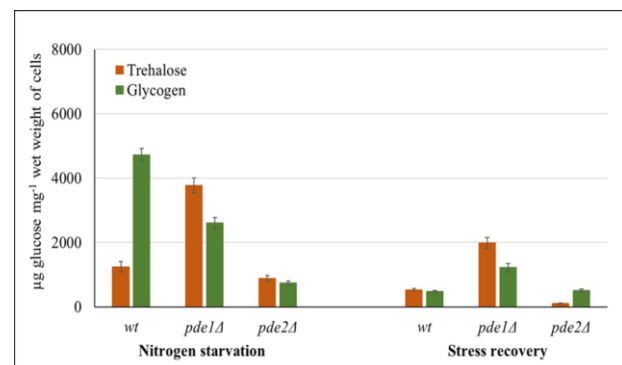


Figure 4. The effect of Pde1 and Pde2 proteins on trehalose and glycogen accumulation during nitrogen starvation and recovery. For nitrogen starvation yeast cells transferred to 0.1% proline and for recovery 0.5% ammonium sulfate was added. Incubation period for nitrogen starvation and recovery period was 4 hours.

Reserve carbohydrate accumulation was also analyzed during the 4 hours' recovery period. In wild-type and mutant yeast cells, starvation-induced trehalose and glycogen synthesis stopped during recovery. Within 4 hours, 57% of the accumulated trehalose and 90% of the accumulated glycogen were broken down into glucose and restored to normal growth conditions in wild-type yeast cells (Figure 4). In wild-type cells, the rate of glycogen breakdown was seen to be higher compared to that of trehalose. In the presence of a solo *PDE1* gene (*pde2Δ*), the levels of both trehalose and glycogen were shown to decrease by approximately 50% during the replenishing phase. In contrast to *pde1Δ* cells, *pde2Δ* cells showed 90% and 30% degradation in stress-induced accumulation of trehalose and glycogen, respectively. The rate of trehalose breakdown was shown to be faster in *pde2Δ* cells in comparison to both wild-type and *pde1Δ* cells.

Trehalose levels in *pde1Δ* cells were high under normal growth conditions, but when stress was applied, yeast cells immediately began to break it down and continued to do so even after the stress was removed. However, the accumulation of glycogen continued through the starvation period and was subsequently metabolized during the recovery phase. These findings indicate that the Pde2 protein plays a crucial role in the regulation of intracellular trehalose accumulation, both in normal and stressful environments.

3.4. Trehalose and Glycogen Accumulation During Heat Stress and Recovery

Intracellular trehalose levels are very low during normal growth conditions and increase during different stress conditions and heat shock. The heat shock treatment of yeast cells causes a decrease in the growth rate and the concomitant accumulation of reserve carbohydrates [26, 27]. Therefore, the effects of Pde1 and Pde2 proteins on reserve carbohydrate accumulation during heat shock and recovery were analyzed. When wild-type yeast cells grown under favorable growth conditions were shifted to 42 °C, the trehalose level increased 7-fold but the glycogen content remained unchanged (Figure 5). The reserve carbohydrate accumulations in *pde1Δ* cells decreased when exposed to heat shock, but they were still 2-fold and 12-fold higher than the trehalose and glycogen levels of wild-type cells, respectively. As opposed to *pde1Δ* yeast cells, trehalose and glycogen levels increased 3- and 2-fold in *pde2Δ* cells, respectively. During heat shock, the amount of trehalose in *pde2Δ* cells was 2-fold lower than in wild-type cells, whereas the amount of glycogen was 5-fold greater.

The glycogen accumulation exhibited an upward trend in *pde1Δ* and *pde2Δ* cells after heat stress, while remaining unchanged in wild-type cells. As in nitrogen starvation, trehalose continued to be synthesized in wild-type and *pde2Δ* cells during heat stress, but it was degraded in *pde1Δ* cells. These results indicate that both Pde1 and Pde2 activity are essential for the proper accumulation of trehalose and glycogen during nitrogen starvation and heat stress. Furthermore, in the presence of Pde2 protein (in *pde1Δ* cells), trehalose levels were very high in normal and stressful conditions. This finding suggests that the Pde2 protein is capable of initiating stress signaling pathways even in the absence of external stress. Consequently, it can be inferred that the *PDE1* gene product plays a crucial function in the regulation of PKA activity and, indirectly, in the regulation of Pde2 protein activity, thereby enabling the detection of stress signals.

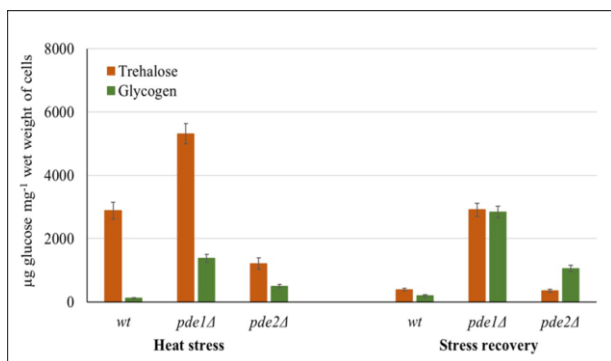


Figure 5. The effect of Pde1 and Pde2 proteins on trehalose and glycogen accumulation during heat stress and recovery. For heat stress yeast cells transferred to 42 °C and for recovery yeast cells retreated to 30 °C. Incubation period for heat stress and recovery period was 4 hours.

For recovery, yeast cells were transferred to 42 °C and incubated for 4 hours, then trehalose and glycogen levels were detected. Approximately 87% and 71% of stress-accumulated trehalose were hydrolyzed in wild-type and *Δpde2* yeast cells, respectively, during the recovery

period. (Figure 5). Interestingly, in *pde1Δ* cells, 50% of the stress-accumulated trehalose was degraded, whereas glycogen synthesis continued twofold throughout the replenishment period. It was shown that *pde2Δ* cells recovered to a similar extent as the wild-type, whereas *pde1Δ* failed to recover properly in terms of trehalose. Additionally, unlike wild-type yeast cells, *pde1Δ* and *pde2Δ* yeast cells continued to synthesize glycogen during the recovery phase. These results indicate that both *PDE1* and *PDE2* gene products are crucial for the regulation of trehalose and glycogen metabolism under normal circumstances, stress conditions, and replenishment.

It is known that low levels of cAMP and repression of cAMP-dependent protein phosphorylation show enhanced heat resistance in yeast strains [19]. The overexpression of *PDE2* genes showed enhanced heat resistance, whereas the overexpression of the Pde1 enzyme did not show a significant change in heat resistance compared with the control yeast strain [22]. The ability of *pde2Δ* yeast strains to survive in stress conditions such as heat stress and nitrogen starvation was decreased [28, 29]. In addition, deletion of the *PDE2* gene made cells sensitive to different stresses, whereas deletion of the *PDE1* gene did not affect cellular stress resistance [6]. Our results showed that the trehalose level in *pde1Δ* yeast cells was too high and did not change during stress or the recovery period compared to the wild-type. Consistent with these results, the *PDE2* gene product is essential for the accumulation of the stress metabolite trehalose, thus making the yeast cells more resistant to stress conditions. Interestingly, the level of glycogen in *pde1Δ* yeast cells decreased during heat stress and quietly resynthesized in the recovery period. Conversely, in *pde2Δ* yeast cells, glycogen synthesis was triggered during stress and the recovery period. Therefore, the *PDE2* gene product has a distinct regulatory role in glycogen metabolism, even if the exact mechanism is unknown yet.

Different external and internal factors affect the stress response production rate and the duration of the response in yeast cells. In the absence of cAMP phosphodiesterases, cAMP clearance is altered, affecting the overall timing of cellular decisions. Therefore, Pde1 and Pde2 proteins affecting stress response duration [22, 30]. The findings of our study indicate that Pde1 and Pde2 proteins also play a crucial role in the sensing and production of stress responses.

4. CONCLUSION

In yeast cells, PKA activity has been linked to a variety of cellular functions, including stress response. The activity of PKA is regulated by the cAMP level, which is controlled by adenylate cyclase and cAMP phosphodiesterase enzymes. *PDE1* and *PDE2* genes encode the low- and high-affinity cAMP phosphodiesterases, respectively. Inactivation of PKA activates the stress response pathways and causes the accumulation of storage carbohydrates, which leads to increased tolerance to diverse environmental stresses such as nutrient deficiency, oxidative stress, and heat stress.

The activation of PKA represses the expression of genes, including STRE sequences on their promoters. The genes involved in trehalose metabolism and glycogen synthesis include STRE elements on their promoters. The neutral trehalase enzyme, encoded by the *NTH1* gene, is responsible for the breakdown of stress-accumulated trehalose. In this study, the effect of Pde1 and Pde2 proteins on *NTH1* gene expression and storage carbohydrate accumulation was investigated at nitrogen starvation, heat stress, and during stress recovery. *NTH1* transcription levels in *pde1Δ* and *pde2Δ* yeast cells were lower than in wild-type yeast cells under normal conditions, nitrogen starvation, heat stress, and also during the recovery phase. In the absence of *PDE1* and *PDE2* gene products, the high cAMP level caused constitutive activation of PKA and may have blocked STRE-mediated *NTH1* gene expression. Both trehalose and glycogen levels in the yeast cells were quite high in *pde1Δ* cells at normal growth conditions. However, in *pde2Δ* yeast cells, the accumulation of trehalose and glycogen was at the level of wild-type cells. Under conditions of nitrogen deficiency, heat stress, and subsequent replenishment, the concentration of trehalose in *pde1Δ* cells remained higher than in *pde2Δ* and wild type cells. In addition, *pde2Δ* cells recovered to a similar extent as the wild-type, whereas *pde1Δ* cells failed to recover properly. The Pde2 protein may interact with Msn2/4, creating a long-lasting stress signal to induce the accumulation of reserve carbohydrates. So, *PDE1* is necessary for the downregulation of reserve carbohydrate metabolism, and/or Pde1 may regulate the activity of Pde2 via an unknown mechanism. These findings suggest that Pde1 and Pde2 proteins are essential for the regulation of trehalose and glycogen metabolism in both normal and stressful circumstances, as well as throughout the replenishment process.

Acknowledgement

The work is an outcome of research project number FHD-2017-1325 financed by the Scientific Research Coordination Unit of Çanakkale Onsekiz Mart University, Türkiye. We thank to Professor Jean Marie François for gift of LacZ fusion systems.

REFERENCES

- [1] Smets B, Ghillebert R, De Snijder P, Binda M, Swinnen E, De Virgilio C, et al. Life in the midst of scarcity: adaptations to nutrient availability in *Saccharomyces cerevisiae*. *Curr Genet*. 2010; 56(1):1-32.
- [2] Conrad M, Schothorst J, Kankipati HN, Van Zeebroeck G, Rubio-Teixeira M, Thevelein JM. Nutrient sensing and signaling in the yeast *Saccharomyces cerevisiae*. *FEMS Microbiol Rev*. 2014; 38(2):254-299.
- [3] Huang G, Huang Q, Wei Y, Wang Y, Du H. Multiple roles and diverse regulation of the Ras/cAMP/protein kinase A pathway in *Candida albicans*. *Mol Microbiol*. 2019; 111(1):6-16.
- [4] Bouchez C, Devin A. Mitochondrial biogenesis and mitochondrial reactive oxygen species (ROS): A complex relationship regulated by the cAMP/PKA signaling pathway. *cells*. 2019; 8(4):287.
- [5] Creamer DR, Hubbard SJ, Ashe MP, Grant CM. Yeast protein kinase A isoforms: A means of encoding specificity in the response to diverse stress conditions? *Biomolecules*. 2022; 12(7):958.
- [6] Park JI, Grant CM, Dawes IW. The high-affinity cAMP phosphodiesterase of *Saccharomyces cerevisiae* is the major determinant of cAMP levels in stationary phase: involvement of different branches of the Ras-cyclic AMP pathway in stress responses. *Biochem Biophys Res Commun*. 2005; 327(1):311-319.
- [7] McCormick K, Baillie GS. Compartmentalisation of second messenger signalling pathways. *Curr Opin Genet Dev*. 2014; 27:20-25.
- [8] Eleutherio E, Panek A, De Mesquita JF, Trevisol E, Magalhães R. Revisiting yeast trehalose metabolism. *Curr Genet*. 2015; 61(3):263-274.
- [9] Tisi R, Belotti F, Martegani E. Yeast as a model for Ras signalling. In: Trabalzini L, Retta S. editors. *Ras signaling methods and protocols*. 1st ed. Humana Press, Totowa, NJ. 2014, p. 359-390.
- [10] François JM, Walther T, Parrou JL. Genetics and regulation of glycogen and trehalose metabolism in *Saccharomyces cerevisiae*. In: Liu Z. editor. *Microbial stress tolerance for biofuels*. 1st ed. Springer Berlin, Heidelberg. 2012, p.29-55.
- [11] Yap CF, Garcia-Albornoz M, Jarnuczak AF, Hubbard SJ, Schwartz JM. Model parameterization with quantitative proteomics: Case study with trehalose metabolism in *Saccharomyces cerevisiae*. *Processes*. 2021; 9(1):139.
- [12] Genc TT. The SAGA complex is essential for the regulation of genes involved in yeast trehalose metabolism. *Trakya University Journal of Natural Sciences*. 2022; 23(2):167-176.
- [13] Trimborn L, Hoecker U, Ponnu J. A Simple quantitative assay for measuring β -Galactosidase activity using X-Gal in yeast-based interaction analyses. *Curr Protoc*. 2022; 2(5):e421.
- [14] Chen Y, Futcher B. Assaying glycogen and trehalose in yeast. *Bio-protocol*. 2017; 7(13):e2371.
- [15] Gorner W, Durchschlag E, Martinez-Pastor MT, Estruch F, Ammerer G, et al. Nuclear localization of the C₂H₂ zinc finger protein Msn2p is regulated by stress and protein kinase A activity. *Genes Dev*. 12(4):586-597.
- [16] Lee P, Kim MS, Paik SM, Choi SH, Cho BR, Hahn JS. Rim15-dependent activation of Hsf1 and Msn2/4 transcription factors by direct phosphorylation in *Saccharomyces cerevisiae*. *FEBS Lett*. 2013; 587(22):3648-3655.
- [17] Sweeney K, McClean MN. Transcription factor localization dynamics and DNA binding drive distinct promoter interpretations. *Cell Rep*. 2023; 42(5):112426.
- [18] Plank M. Interaction of TOR and PKA signaling in *S. cerevisiae*. *Biomolecules*. 2022; 12(2):210.
- [19] Ferguson SB, Anderson ES, Harshaw RB, Thate T, Craig NL, Nelson HC. Protein kinase A regulates constitutive expression of small heat-shock genes in an Msn2/4p-independent and Hsf1p-dependent

- manner in *Saccharomyces cerevisiae*. *Genetics*. 2005; 169(3):1203-1214.
- [20] Alfatah M, Wong JH, Krishnan VG, Lee YC, Sin QF, Goh CJH, et al. TORC1 regulates the transcriptional response to glucose and developmental cycle via the Tap42-Sit4-Rrd1/2 pathway in *Saccharomyces cerevisiae*. *BMC Biol*. 2021; 19(1):95.
- [21] Chasman D, Ho YH, Berry DB, Nemecek CM, MacGilvray ME, Hose J, et al. Pathway connectivity and signaling coordination in the yeast stress-activated signaling network. *Mol Syst Biol*. 2014; 10(11):759.
- [22] Ma P, Wera S, Van Dijck P, Thevelein JM. The PDE1-encoded low-affinity phosphodiesterase in the yeast *Saccharomyces cerevisiae* has a specific function in controlling agonist-induced cAMP signaling. *Mol Biol Cell*. 1999; 10(1):91-104.
- [23] MacGilvray ME, Shishkova E, Chasman D, Place M, Gitter A, Coon JJ, et al. Network inference reveals novel connections in pathways regulating growth and defense in the yeast salt response. *PLoS Comput Biol*. 2018; 13(5):e1006088.
- [24] Kim JS, Lee KT, Bahn YS. Deciphering the regulatory mechanisms of the cAMP/protein kinase A pathway and their roles in the pathogenicity of *Candida auris*. *Microbiol Spectr*. 2023; e0215223.
- [25] Williamson T, Schwartz JM, Kell DB, Stateva L. Deterministic mathematical models of the cAMP pathway in *Saccharomyces cerevisiae*. *BMC Syst Biol*. 2009; 16(3):70.
- [26] Paalman JW, Verwaal R, Slofstra SH, Verkleij AJ, Boonstra J, Verrips CT. Trehalose and glycogen accumulation is related to the duration of the G1 phase of *Saccharomyces cerevisiae*. *FEMS Yeast Res*. 2003; 3:261-268.
- [27] Eardley J, Timson DJ. Yeast Cellular Stress: Impacts on Bioethanol Production. *Fermentation*. 2020; 6: 109.
- [28] Jung WH, Warn P, Ragni E, Popolo L, Nunn CD, Turner MP, Stateva L. Deletion of *PDE2*, the gene encoding the high-affinity cAMP phosphodiesterase, results in changes of the cell wall and membrane in *Candida albicans*. *Yeast*. 2005; 22(4):285-294.
- [29] Jacquet B, Matifas A, Charvin G. A trade-off between stress resistance and tolerance underlies the adaptive response to hydrogen peroxide. *bioRxiv*. 2021; ffhal-03451307f.
- [30] Zaccolo M, Zerio A, Lobo MJ. Subcellular organization of the cAMP signaling pathway. *Pharmacol Rev*. 2021; 73(1):278-309.

A Study of Effects of Organic Origin Liquid Seaweed on Germination Radicle and Plumule Growth in Winter Cereal Genus

Ali Rahmi KAYA^{1*}, Mustafa YILDIRIM¹, Songül ÇİFTÇİ SAKİN¹

¹ Kahramanmaraş Sütçü İmam University, Faculty of Agriculture, Department of Field Crops, Kahramanmaraş, Türkiye

Ali Rahmi KAYA ORCID No: 0000-0003-0318-6034

Mustafa YILDIRIM ORCID No: 0000-0002-9523-4007

Songül ÇİFTÇİ SAKİN ORCID No: 0000-0002-5157-2709

*Corresponding author: alirahmikaya@ksu.edu.tr

(Received: 03.01.2023, Accepted: 12.06.2024, Online Publication: 28.06.2024)

Keywords

Dose,
Germination
index,
Germinated
seed,
Organic liquid
seaweed,
Cool season
cereals

Abstract: In this study, it was aimed to determine the effects of liquid seaweed on seed germination and radicle and plumule growth in some winter cereal species [Triticale (T), Barley (B) and Wheat (W)] were investigated. In the study, 6 different doses [Control (D0), 1000 ppm L⁻¹ (D1), 2000 ppm L⁻¹ (D2), 4000 ppm L⁻¹ (D3), 8000 ppm L⁻¹ (D4) and 16000 ppm L⁻¹ (D5)] of seaweed were used. Germination index, radicle and plumule fresh weight (g), radicle and plumule dry weight (g) and germinated seed number (number) were measured during the 14-day development period of cereal species at all seaweed doses. According to the study findings, apart from the "number of germinated seeds in cereal species" and "germination index in species x dose interaction"; significant differences were found between the average values of all the properties examined in the grain types, fertilizer doses and species x dose interactions. Wheat among cereals had the highest values concerning radicle dry weight and radicle fresh weight. D2 dose from the doses of seaweed fertilizer form has the highest values in germinated seed number, radicle dry weight, plumule dry weight, and radicle fresh weight, while D5 dose was the lowest. In terms of species x dose interaction, radicle fresh weight was found to be high in T x D1 interaction. Germinated seed number and plumule fresh weight were found to be high in H x D0 interaction. Germinated seed number and radicle dry weight were found to be high in W x D2 interaction. As a result, in the germination study with liquid seaweed, D2 dose for wheat, D1 and D2 doses for triticale, D0, D1 and D2 doses for barley were found as encouraging.

Farklı Organik Kökenli Sıvı Deniz Yosunu Dozlarının Serin İklim Tahıl Cinslerinde Çimlenme Radikula ve Plumula Gelişimi Üzerine Etkilerinin İncelenmesi

Anahtar Kelimeler

Çimlenme
indeksi,
Çimlenen
tohum,
Doz,
Serin iklim
tahılları,
Organik sıvı
deniz yosunu

Öz: Bu çalışmada, sıvı deniz yosununun bazı serin iklim tahıl cinslerinde [Tritikale (T), Arpa (B) ve Buğday (W)] tohum çimlenmesi ile radikula ve plumula gelişimi üzerine etkilerinin belirlenmesi amaçlanmıştır. Çalışmada 6 farklı dozda [Kontrol (D0), 1000 ppm L⁻¹ (D1), 2000 ppm L⁻¹ (D2), 4000 ppm L⁻¹ (D3), 8000 ppm L⁻¹ (D4) ve 16000 ppm L⁻¹ (D5)] deniz yosunu kullanılmıştır. Tahıl türlerinin 14 günlük büyümedöneminde tüm deniz yosunu dozlarında çimlenme indeksi, radikula ve plumula yaş ağırlığı (g), radikula ve plumula kuru ağırlığı (g) ve çimlenen tohum sayısı (adet) ölçülmüştür. Çalışma bulgularına göre, "tahıl türlerinde çimlenen tohum sayısı" ve "tür x doz interaksyonunda türler çimlenme indeksi" dışında; tahıl türleri, gübre dozları ve tür x doz interaksyonlarında incelenen tüm özelliklerin ortalama değerleri arasında önemli farklılıklar bulunmuştur. Tahıllar içinde buğday, radikula kuru ağırlığı ve radikula yaş ağırlığı en yüksek değerlere sahip olmuştur. Deniz yosunu gübre formunun dozlarından D2 dozu; çimlenen tohum sayısı, radikula kuru ağırlığı, plumula kuru ağırlığı ve radikula yaş ağırlığında en yüksek değerlere sahipken, D5 dozu en düşük olarak bulunmuştur. Tür x doz interaksyonu açısından radikula yaş ağırlığı T x D1 interaksyonunda yüksek bulunmuştur. H x D0 etkileşiminde çimlenen tohum sayısı ve plumula yaş ağırlığı yüksek bulunmuştur. G x D2 etkileşiminde çimlenen tohum sayısı ve radikula kuru ağırlığı yüksek bulunmuştur. Sonuç olarak, sıvı deniz yosunu ile çimlendirme çalışmasında buğday için D2 dozu, tritikale için D1 ve D2 dozları, arpa için D0, D1 ve D2 dozları teşvik edici bulunmuştur.

1. INTRODUCTION

Cereals in the Poaceae family are important cultural plants because they are mainly used as a source of carbohydrates and proteins in human and animal nutrition. In the structure of winter cereals, there is approximately 79.5% carbohydrates, 13.6% protein, 2.3% crude oil, 2.5% cellulose and 2.1% ash [1]. Therefore, it is an important food source for human and animal nutrition. Apart from human and animal nutrition, it has an important place in the country's economy since it is also used in industry with value-added products.

Winter and spring cereals have an important place for cultivation area and production in the world and Türkiye. Especially, the cultivation of spring cereals such as bread and durum wheat, barley, oat, rye and triticale cultivars are carried out intensively in Türkiye.

According to TURKSTAT [2], cereal sufficiency was 80.3% in 2021 in Türkiye. However, sufficiency in wheat was the highest with 87.3% and sufficiency in durum wheat with 151.8%. As of 2022, the cultivation area of wheat was 5423779 ha. Wheat production was 16000000 tons for grain and 310966 tons for green grass. In wheat yield, grain was 2930 kg ha⁻¹ and green grass was 18480 kg ha⁻¹. The cultivation area of barley was 3085617 ha in grain and 29273 ha in green grass. In addition, while the production of barley was 8100000 tons in grain and 482665 tons in green grass, its yield was 2630 kg ha⁻¹ for grain and 16520 kg ha⁻¹ for green grass. The cultivation area of triticale was 99640 ha for grain and 61919 ha for green grass. Triticale production was recorded as 320000 tons for grain and 1072635 tons for green grass, triticale yield was recorded as 3210 kg ha⁻¹ for grain and 17320 kg ha⁻¹ for green grass. Increasing the yield and quality values of winter cereals in proportion to the increasing population is important for more adequate and balanced nutrition for people and animals. Yield and quality vary according to the variety, environmental factors and agricultural methods applied. Türkiye, which is the gene center of many species, has the more importance for cereals. The existence of many registered cultivars, especially in the wheat, is an important place for Türkiye. However, the measures taken to protect and sustain it are not sufficient [3]. Fertilizer is one of the most important inputs in agricultural production, thus providing efficient and high-quality products and supporting the economic sustainability of agriculture [4]. Although there has been a significant increase in the use of chemical fertilizers and chemical pesticides by farmers to increase the fertility of the soil in parallel with the rapid increase in the world population after the Industrial Revolution [5], conventional agriculture in which excessive use of chemical fertilizers and pesticides is considered that it will not be sustainable due to cause problems such as deteriorates the soil organic matter, environmental and soil pollution, contributes to global warming, deterioration of the ecological balance and has problems with food security. [6,7]. For this reason, the necessity of alternative methods in agricultural production is

inevitable One way to eliminate the negative effects of chemical fertilizers, which are used intensively, is to use organic fertilizers more in agriculture. Organic-origin liquid seaweed fertilizer is one of the mentioned organic fertilizers. Organic fertilizers or fertilizer forms provide root development by increasing the oxygen content of the soil and its water-holding capacity and also protect the structure of the soil by decreasing salinity in the soil [8]. Seaweed, which is an organic fertilizer form, increases germination, helps root development, and prolongs the life of the plant by protecting plants against diseases and pests [9]. This study was carried out to determine the effects of liquid seaweed doses on germination, radicle and plumule growth in wheat, barley and triticale, which have an important place in terms of cultivation and production.

2. MATERIAL AND METHOD

In the study carried out, organic-origin liquid seaweed obtained from "Kristal AG Kimya Tarım Sanayi ve Ticaret Ltd. Şti." was used. Information on liquid seaweed is given below (Table 1).

Table 1. The organic-origin liquid seaweed fertilizer's content and amount

Seaweed Fertilizer Content	Amount
Organic Matter (%)	15.0
Organic Carbon (%)	10.0
Total Nitrogen (%)	1.0
Water-soluble Potassium Oxide (K ₂ O) (%)	2.0
Alginate Acid (%)	1.5
Gibberellic Acid (ppm)	0.4
pH	4.0-6.0

This study was carried out in the climate cabinet in the laboratory of Department of Field Crops, Faculty of Agriculture, Kahramanmaraş Sütçü İmam University in April 2021 in Türkiye. In the research, T (Triticale: Ayşehanım variety), B (2-row barley: Novosadski 565 variety), and W (Bread wheat: Balkoni variety), which are winter cereal species, were used as seeds.

In the research, organic-origin liquid seaweed fertilizer form was applied in 6 different ways as D0 (Control: tap water) and 5 doses (1000 ppm L⁻¹:D1, 2000 ppm L⁻¹:D2, 4000 ppm L⁻¹:D3, 8000 ppm L⁻¹:D4, 16000 ppm L⁻¹:D5) [8]. In the study, symbolizing the doses of the species is done by adding the symbol of the species to the beginning of the dose. For example, the 2000 ppm L⁻¹ (D2) dose of triticale (T) is symbolized as TD2. Tap water was used as a control and for the preparation of other doses. The experiment was carried out according to the randomized plot design with 3 replications. 120 mm petri dishes were used, the bottom of these petri dishes was covered with 2 layers of blotting paper, and then blotting papers were wetted with 12 ml of prepared solutions. 25 healthy seeds from each cereal species were subjected to surface sterilization in 5% NaOCl (sodium hypochlorite) solution for 5 minutes. The seeds

of the cereal species subjected to surface sterilization were washed in tap water and sown in petri dishes by adding different doses of solutions. Petri dishes were covered with parafilm (PM-992) to prevent evaporation of the applied solutions at different doses. Afterwards, it was left to germinate for 14 days in an incubator at 20 ± 2 °C. Measurements for germination and radicle and plumule growth were made on the 15th day.

In the experiment, in winter cereal species; properties such as germination index (GI), radicle fresh weight (RFW) (g), plumule fresh weight (PFW) (g), radicle dry weight (RDW) (g), plumule dry weight (PDW) (g) and germinated seed number (GSN) (number) were investigated. Images of the research are given below (Figure 1-6).



Figure 1. First and 6th dose of wheat (23.04.2021)



Figure 2. In barley 4th dose 1st and 3rd recurrence (01.05.2021)

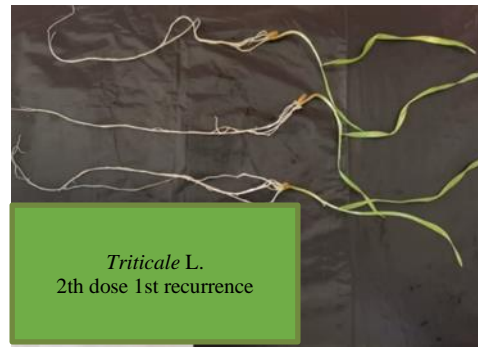


Figure 3. In triticale 2th dose 1st recurrence (06.05.2021)



Figure 4. In wheat 3. dose 1. Recurrence (06.05.2021)



Figure 5. In triticale 1. Döşe 1. recurrence (06.05.2021)

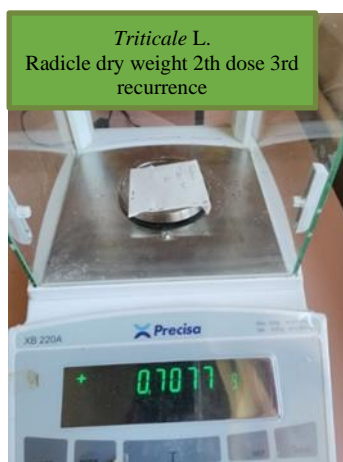


Figure 6. Radicle dry weight of triticale was measured in the laboratory (15th day after placing) (07.05.2021)

The germinated seed number from the examined traits was found by counting the germinated seeds from 25 seeds planted in the petri dish. Counts were made every 24 hours from the second day to the fourteenth day to find the germination index. Germination index (GI) values were calculated using the germinated seed number [10].

$$GI = \frac{\sum (Gi / Tt)}{Tt} \quad (1)$$

GI= Germination index, Gi= seed germinated number on the "t. day", Tt= day number of the "t. day"

Scales with a sensitivity of 0.001 grams were used to measure the radicle and plumule fresh weight. The radicle and plumule fresh weights were weighed. Then, the dry weight of radicula and plumula was calculated

when they reached constant temperature in the oven at 70 °C.

2.1. Statistical analysis of data

The statistical analysis of all data was made using the SAS (v. 9.0, 2002) statistical package programme according to the Completely Randomized Experimental Design. The mean of data was compared by least significant difference (LSD) multiple comparison test [10].

3. RESULTS AND DISCUSSION

The average values of the effects of different seaweed doses on the germination and seedling growth of wheat, barley and triticale seeds are given in Tables 2,3 and 4.

Table 2. Mean values of GSN, GI, RFW, PFW, RDW and PDW in organic-origin liquid seaweed doses.

Features	Doses (ppm L ⁻¹)										Dose average	LSD (0.05)
	D0	D1	D2	D3	D4	D5						
GSN (number)	25.00 a	25.00 a	24.78 a	24.44 a	23.00 b	23.00 b	24.20	0.830 **				
GI	18.41 b	19.89 a	18.94 ab	18.37 b	15.85 c	12.69 d	17.36	1.376 **				
RFW (g)	1.59 a	1.60 a	1.60 a	1.44 b	1.31 c	1.10 d	1.44	0.119 **				
PFW (g)	2.05 bc	1.95 c	2.10 ab	1.96 bc	2.21 a	1.78 d	2.01	0.142 **				
RDW (g)	0.10 b	0.07 d	0.17 a	0.04 e	0.09 c	0.04 e	0.09	0.009 **				
PDW (g)	0.11 b	0.11 b	0.13 a	0.11 b	0.11 b	0.12 b	0.12	0.009 **				

GSN: Germinated Seed Number, GI: Germination Index, RFW: Radicle Fresh Weight, PFW: Plumule Fresh Weight, RDW: Radicle Dry Weight, PDW: Plumule Dry Weight, Fertilizer Doses D0: Kontrol, D1: 1000 ppm L⁻¹, D2: 2000 ppm L⁻¹, D3: 4000 ppm L⁻¹, D4: 8000 ppm L⁻¹, D5: 16000 ppm L⁻¹, the same letters in each line are in the same group.

Table 3. Mean values of GSN, GI, RFW, PFW, RDW and PDW across species.

Features	Species (S)					S average	LSD (0.05) S
	T	B	W	S	S		
GSN (number)	24.61	24.00	24.00	24.20	-		
GI	19.48 a	14.60 c	18.00 b	17.36	0.97**		
RFW(g)	1.52 a	1.32 b	1.48 a	1.44	0.08**		
PFW(g)	2.05 a	2.11 a	1.86 b	2.01	0.10**		
RDW(g)	0.05 c	0.06 b	0.14 a	0.08	0.00**		
PDW (g)	0.12 b	0.13 b	0.10 a	0.12	0.00**		

T: Triticale, B: Barley, W: Wheat, GSN: Germinated Seed Number, GI: Germination Index RFW: Radicle Fresh Weight, PFW: Plumule Fresh Weight, RDW: Radicle Dry Weight, PDW: Plumule Dry Weight, CV: Coefficient of Variation, S: Species.

3.1. Germinated Seed Number (Number)

The results of variance analysis showed that although the difference between the doses (P<0.01) and species x dose interaction (P<0.05) were statistically significant for the germinated seed number, the difference between

cereal species was found to be insignificant (Table 2, Table 3, Table 4). It was determined that the doses of germinated seeds varied between 22.00 and 25.00. The highest germinated seed number was found in the doses D0, D1, D2 and D3 (25.00, 25.00, 24.78, and 24.44, respectively) doses, and the least germinated seeds were

in the D4 and D5 (23.00) doses. Among the doses, D4 and D5 seem to have a limiting effect on the germinated seed number (Table 2). It was determined that the germinated seed number of the species x dose interaction varied between 23.00 and 25.00. Within the species x dose interaction, the highest germinated seed number was in TD0, TD1, TD2, TD3, TD4, BD0, BD1, WD0, WD1, WD2, WD3 (25.00), followed by BD2 and BD3 (24.00) the least germinated seed number was obtained in BD4 and WD4 (22.00) (Table 4). Kaya and Erdönmez [8], in their research to determine the effect of 6 different doses (D0, D1, D2, D3, D4 and D5) of seaweed on soybean germination and seedling development; the highest germinated seed number was determined at a dose of 22.00 with D1 (1000 ppm L⁻¹), and the least germinated seed number at a fertilizer dose of 5.00 with D5 (16000 ppm L⁻¹). Kaya and Coşkun [11], in their research to determine the effect of 6 different doses (D0, D1, D2, D3, D4, D5) of liquid seaweed on rapeseed germination and seedling development; it was determined that the highest germinated seed number in the D0 application and D1 (23.78 pieces and 22.67 pieces, respectively), the least germinated seed number was 4.33 at D3, germination did not occur in D5. As seen in previous studies, the number of germinating seeds varies according to plant species.

3.2. Germination Index

According to the results of the analysis of variance; In terms of germination index, the difference between cereal types and doses was statistically significant ($P < 0.01$), while the difference between species x dose interaction was found to be insignificant (Table 2., Table 3., Table 4.). The germination index of cereal species varied between 14.60-19.48. Among the species, the highest germination index was found in the T type (19.48), and the lowest germination index was found in the B type (14.60) (Table 3). The germination index of the doses varied between 12.69-19.89. The highest germination index was observed in the D1 dose, and the lowest germination index was observed in the D5 dose (Table 2). D1 dose seems to be more encouraging in terms of germination index. The germination index of the species x dose interaction ranged from 11.64 to 22.00. Kaya and Erdönmez [8], who carried out to determine the effect of 6 different doses (D0, D1, D2, D3, D4 and D5) of seaweed on soybean germination and seedling development; reported that the highest germination index in the materials they applied seaweed at 6.39% to D1 dose, and the lowest germination index at 1.39% to D5 fertilizer dose. In the study, it was observed that the germination index decreased with the increase of the seaweed fertilizer dose, except for the D0 application, and this is consistent with our findings.

Table 4. Mean GSN, GI, RL, PL, SL and RFW values in the organic-origin liquid seaweed doses of species.

Species	Doses (ppm L ⁻¹)	GSN (Number)		GI	RFW (g)		PFW (g)		RDW (g)		PDW (g)	
T	D0	25.00	a	22.00	1.52	a-d	1.83	cd	0.09	bcd	0.10	def
	D1	25.00	a	22.00	1.87	a	2.14	abc	0.08	de	0.12	cde
	D2	25.00	a	19.92	1.74	ab	2.31	ab	0.06	ef	0.17	a
	D3	25.00	a	20.89	1.64	abc	2.20	abc	0.01	g	0.11	def
	D4	25.00	a	18.23	1.26	def	2.24	abc	0.05	ef	0.13	cd
	D5	23.00	ab	13.82	1.07	fg	1.60	de	0.04	fg	0.08	fg
B	D0	25.00	a	13.74	1.38	c-f	2.38	a	0.09	bcd	0.14	bc
	D1	25.00	a	16.67	1.29	def	1.93	cd	0.05	f	0.12	de
	D2	24.00	a	16.87	1.45	bcd	2.23	abc	0.04	f	0.16	a
	D3	24.00	a	15.09	1.23	def	1.62	de	0.03	fg	0.09	f
	D4	22.00	b	13.57	1.19	ef	2.20	abc	0.10	bc	0.10	ef
	D5	23.00	ab	11.64	1.40	cde	2.28	ab	0.05	f	0.16	ab
W	D0	25.00	a	19.47	1.86	a	1.94	cd	0.00	b	0.09	fg
	D1	25.00	a	21.01	1.63	abc	1.78	d	0.09	cd	0.09	f
	D2	25.00	a	20.02	1.61	abc	1.75	d	0.41	a	0.07	g
	D3	25.00	a	19.14	1.45	cd	2.05	bc	0.09	cd	0.13	cd
	D4	22.00	b	15.75	1.48	bcd	2.18	abc	0.10	bc	0.11	de
	D5	23.00	ab	12.61	0.82	g	1.46	e	0.04	f	0.12	de
Overall Average		24.22		17.36	1.44		2.01		0.08		0.12	
LSD (0.05) T x D		2.49*		-	0.36**		0.43**		0.03**		0.03**	
CV (%)		3.58		8.27	8.65		7.39		11.21		8.43	

T: Triticale, B: Barley, W: Wheat, GSN: Germinated Seed Number, GI: Germination Index, RFW: Radicle Fresh Weight, PFW: Plumule Fresh Weight, RDW: Radicle Dry Weight, PDW: Plumule Dry Weight, CV: Coefficient of Variation, D: Dose, Fertilizer Doses; D0: Control, D1: 1000 ppm L⁻¹, D2: 2000 ppm L⁻¹, D3: 4000 ppm L⁻¹, D4: 8000 ppm L⁻¹, D5: 16000 ppm L⁻¹. There is no statistical difference between the same capital letters in the same column. There is no statistical difference between the same lowercase letters in the same column.

3.3. Radicle Fresh Weight (g)

In the analysis of variance, the statistical difference ($P < 0.01$) between cereal types, doses and species x dose interaction was found to be very significant for radicle fresh weight (Table 2, Table 3 and Table 4.). The fresh radicle weight of the cereal species varied between 1.32 and 1.52 g. The highest radicle fresh weight was found in T and W types (1.52 and 1.48 g, respectively) among

cereal species, and the lowest radicle fresh weight was determined in B type (1.32 g).

It was observed that the doses ranged from 1.10 g to 1.60 g fresh weight of the radicle. While the highest radicle fresh weight was observed in the D1, D2 and D0 doses (1.60, 1.60 and 1.59 g, respectively) among the doses, the lowest radicle fresh weight was observed in the D5 dose.

It has been determined that D5 has a limiting effect on the fresh weight of the radicle within the doses. The radicle fresh weight of the species x dose interaction ranged from 0.82 g to 1.87 g. Among the species x dose interaction, the highest radicle fresh weight was found in TD1 and WD0 (1.87 and 1.86 g, respectively), while the lowest radicle fresh weight was found in WD5. Bat et al. [13] investigated the effects of seaweed doses (0, 2, 4 and 6 cc L⁻¹) applied in viols on echinacea plant under drought stress. As a result of the research, the highest radicle fresh weight of 5.93 g and 6 cc L⁻¹ seaweed dose was determined in the echinacea plant, and the lowest radicle fresh weight was 4.26 g at the control dose, and they reported that seaweed had a positive effect on the radicle fresh weight.

Kara et al. [12], investigated the effect of seaweed applications (control, 2, 4 and 6 cc L⁻¹) on salt stress (control, NaCl, KCl and CaCl₂) in echinacea plant. As a result of the research, they observed that the highest average radicle fresh weight was obtained from 4.35 g and 6 cc L⁻¹ seaweed dose, and the lowest average radicle fresh weight was obtained from 3.46 g and 2 cc L⁻¹ dose.

3.4. Plumule Fresh Weight (g)

In the analysis of variance, the difference ($P < 0.01$) between cereal types, doses and species x dose interaction in terms of plumule fresh weight was found to be statistically very significant (Tables 2, 3 and 4). The plumule fresh weight of the cereal species varied between 1.86 and 2.11 g. Among the species, the highest plumule fresh weight was obtained in B and T (2.11 and 2.05 g, respectively) species, and the lowest plumule fresh weight was obtained in W species (1.86 g).

It was determined that the fresh weight of the plumule of the doses varied between 1.78 and 2.21 g. The highest plumule fresh weight was observed in the D4 dose, and the lowest plumule fresh weight was observed in the D5 dose. It was observed that the species x dose interaction varied between 1.46-2.38 g plumule fresh weight. Among the species x dose interaction, the highest plumule fresh weight was found in BD0, and the lowest plumule fresh weight was found in WD5 (Table 4).

Bat et al. [13] investigated the effects of seaweed doses (0, 2, 4 and 6 cc L⁻¹) applied in viols on echinacea plant under drought stress. As a result of the research, the highest plumule fresh weight of 6.35 g and 6 cc L⁻¹ seaweed was observed in the echinacea plant, and the lowest plumule fresh weight was observed in the control application with 5.11 g. Steveni et al. [14] determined that the seedling weight increased by 56% to 63% in the application of seaweed material in winter barley. Kara et al. [12] investigated the effect of seaweed applications (control, 2, 4 and 6 cc L⁻¹) on salt stress (control, NaCl, KCl and CaCl₂) in echinacea plant. As a result of the research, they observed that the highest average plumule fresh weight was obtained from 3.38 g and 6 cc L⁻¹ seaweed dose, and the lowest average plumule fresh weight was obtained from 2.45 g and 2 cc L⁻¹ dose.

3.5. Radicle Dry Weight (g)

In the analysis of variance, the difference ($P < 0.01$) between cereal species, doses and species x dose interaction in terms of radicle dry weight was found to be statistically very significant (Table 2, Table 3 and Table 4.). The radicle dry weight of the cereal species ranged from 0.05 g to 0.14 g. Among the species, the highest radicle dry weight was found in the W type, and the lowest radicle dry weight was found in the T type (Table 3.). The radicle dry weight of the doses ranged from 0.04 g to 0.17 g. The highest radicle dry weight was found in the D2 dose, and the lowest radicle dry weight was determined in the D3 and D5 doses (Table 2). The radicle dry weight of the species x dose interaction ranged from 0.01 g to 0.41 g. Among the species x dose interaction, the highest radicle dry weight was observed in WD2, and the lowest radicle dry weight was observed in TD3 (Table 4). Bat et al. [13] investigated the effects of seaweed doses (0, 2, 4 and 6 cc L⁻¹) applied in viols on echinacea plant under drought stress. As a result of the research, the highest radicle dry weight of 1.04 g and 6 cc L⁻¹ seaweed was observed in the echinacea plant, and the lowest radicle dry weight was observed in the control application with 0.71 g. Kara et al. [12] investigated the effect of seaweed applications (control, 2, 4 and 6 cc L⁻¹) on salt stress (control, NaCl, KCl and CaCl₂) in echinacea plant.

As a result of the research, they observed that the highest average radicle dry weight was obtained with 0.81 g and 6 cc L⁻¹ seaweed dose, and the lowest average radicle dry weight was obtained in the control application with 0.58 g. Kaya and Coşkun [11], in their research to determine the effect of 6 different doses (D0, D1, D2, D3, D4, D5) of liquid seaweed on rapeseed germination and seedling development; found that the highest radicle dry weight was 1.914 mg with D4, the lowest radicle dry weight was 0.535 mg with D1, and germination did not occur at D5 dose.

3.6. Plumule Dry Weight (g)

In the analysis of variance, the difference ($P < 0.01$) between cereal types, doses and species x dose interaction in terms of plumule dry weight was found to be statistically very significant (Table 2, Table 3 and Table 4.). The plumule dry weight of the cereal species varied between 0.10-0.13 g. Among the species, the highest plumule dry weight was obtained in B species, and the lowest plumule dry weight was obtained in W species (Table 3.). The plumule dry weight of the doses ranged from 0.11 g to 0.13 g. Among the doses, the highest plumule dry weight was found in the D2 dose, and the lowest plumule dry weight was found in the D0, D1, D3, D4 (0.12 g) and D5 (0.12 g) doses (Table 2).

The plumule dry weight of the species x dose interaction ranged from 0.07 g to 0.17 g. Among the species x dose interaction, the highest plumule dry weight was found in TD2 and BD2 (0.17 and 0.16 g, respectively), and the lowest plumule dry weight was found in WD2 (Table 4.). Bat et al. [13] investigated the effects of seaweed

doses (0, 2, 4 and 6 cc L⁻¹) applied in violets on echinacea plant under drought stress. As a result of the research, the highest plumule dry weight of 1.21 g and 4 cc L⁻¹ seaweed was determined in the echinacea plant, and the lowest plumule dry weight was determined as 0.84 g in the control application. Kara et al. [12] investigated the effect of seaweed applications (control, 2, 4 and 6 cc L⁻¹) on salt stress (control, NaCl, KCl and CaCl₂) in echinacea plant. As a result of the research, they observed that the highest average plumule dry weight was obtained with 0.81 g and 6 cc L⁻¹ seaweed dose, and the lowest average plumule dry weight was obtained with 0.62 g in the control application. Kaya and Coşkun [11], in their research to determine the effect of 6 different doses (D0, D1, D2, D3, D4, D5) of liquid seaweed on rapeseed germination and seedling development; determined that the highest plumule dry weight was 7.880 mg with D2, the lowest plumule dry weight was 4.591 mg with D1, and germination did not occur at D5.

4. CONCLUSION

Germination studies on organic liquid seaweed and seeds of cereal species have not been very much. With this study, the effect of organic-origin liquid seaweed material on the germination and growth of radicle and plumule in cereal species will be determined and will guide many future studies.

In the study, it was observed that the data on the germination and radicle and plumule growth of the cereal species of seaweed doses were statistically significant. D2 (2000 ppm L⁻¹) dose gave the highest values in terms of germinated seed number, radicle dry weight, plumule dry weight and radicle fresh weight, while the D5 (16000 ppm L⁻¹) dose gave the lowest values. Among the cereal types, wheat reached the highest values for germination index, radicle fresh weight and plumule fresh weight.

As a result, the D2 (2000 ppm L⁻¹) dose of seaweed organic material is generally recommended for wheat from cereal species; while D1 (1000 ppm L⁻¹) and D2 (2000 ppm L⁻¹) dose in triticale; D2 (2000 ppm L⁻¹) dose are recommended as incentives in barley.

REFERENCES

- [1] Geçit HH, İkincikarakaya SÜ. Tarla Bitkileri. Tahıllar ve Baklagiller (Serin İklim Tahılları). Ankara University, Faculty of Agriculture Publications; 2011 No: 1588: p. 117-194.
- [2] TURKSTAT [Internet]. Turkish Statistical Institute (The production, production area, yield and sufficiency of cereals); 2023 [25.07.2023]. Available from: <https://biruni.tuik.gov.tr/medas/?kn=104&locale=tr/>
- [3] Altındal D, Akgün İ. Plant genetic resources and situation in cereals. Adnan Menderes University Journal of The Faculty of Agriculture. 2015; 12 (1):147-153.
- [4] Yılmaz H, Demircan V, Gül M. Determination of information sources of manufacturers in the use of chemical fertilizers and evaluation in terms of agricultural extension. Journal of Suleyman Demirel University Faculty of Agriculture. 2009;4(1): 31-44.
- [5] Shi J.. Decomposition rates and nutrient release of different cover crops in organic farm systems. The Graduate College at the University of Nebraska. 2013 p.1-73.
- [6] Gliessman SR. Agroecology: the ecology of sustainable food systems. 2nd Edition. CRC Press. Boca Raton; 2007.
- [7] Öztemiz S. Biological control in organic agriculture. Journal of GOU Faculty of Agriculture. 2008;25(2):19-27.
- [8] Kaya AR, Erdönmez HK. The effect of different origin fertilizer forms and doses on seed germination and seedling growth of soybean (*Glycine max. L. Merrill*). Turkish Journal of Nature and Science. 2020;9:73-79.
- [9] Hong YP, Chen CC, Cheng HL, Lin CH. Analysis of auxin and cytokinin activity of commercial aqueous seaweed extract. Gartenbauwissenschaft. 1995;60(4):191-194.
- [10] Wang YR, Yu L, Nan ZB, Liu YL. Vigor tests used to rank seed lot quality and predict field emergence in four forage species. Crop Science. 2004; 44 (2):535-541.
- [11] Kaya AR, Coşkun N. Effect of organic fertilizer forms and doses on the seed germination and seedling development of rapeseed (*Brassica napus L.*). Applied Ecology and Environmental Research. 2020;18(5):6813-6828.
- [12] Kara A, Tunçtürk M, Tunçtürk R. Effect of seaweed on growth parameters and total phenolic and antioxidant content of *Echinacea purpurea L.* under salt stress. Bahri Dağdaş Journal of Herbal Research. 2019;8(1):115-124.
- [13] Bat M, Tunçtürk R, Tunçtürk M. Kuraklık stresi altındaki ekinezya (*Echinacea purpurea L.*)' da deniz yosununun büyüme parametreleri, toplam fenolik ve antioksidan madde üzerine etkisi. Yüzüncü Yıl University Journal of Agricultural Sciences, 2019;29(3):496-505.
- [14] Steveni CM, Norrington-Davies J, Hankins SD. Effect of seaweed concentrate on hydroponically grown spring barley. Journal of Applied Phycology. 1992;4(2):173-180.

Superconductivity in Brain

Özden ASLAN ÇATALTEPE ^{1*} 

¹ İstanbul Gedik University, Engineering Faculty, Department of Mechatronics Engineering, İstanbul, Türkiye
Özden ASLAN ÇATALTEPE ORCID No: 0000-0003-4520-9839

*Corresponding author: ozden.aslan@gedik.edu.tr

(Received: 24.08.2023, Accepted: 05.04.2024, Online Publication: 28.06.2024)

Keywords

Superconductivity,
Quantum
entanglement,
Consciousness,
Empathy,
Brain

Abstract: In this article, the phenomenon of superconductivity in the brain has been examined based on some properties of superconductivity. The possibility of hydrogen-based compounds to be superconducting at ambient temperature and pressure has enabled an analogy to be established between superconductivity and living organisms including high ratio water in other words hydrogen. In this context, the superconductivity phenomenon occurring in microtubules structures in neurons in the brain has been studied and thus the quantum mechanical properties of the brain have been tried to be explained. Due to the behavior of acting like computer memory, the role of repairing deoxyribonucleic acid damage, property of giving the quantum mechanical behavior to the brain, microtubules are very interesting organelles. Hence superconductivity with its extraordinary properties such as the quantum entanglement and bosonic state etc. may be guide for human beings in the respect of long term memory, empathy and consciousness.

Beyindeki Süperiletkenlik

121

Anahtar Kelimeler

Süperiletkenlik,
Kuantum
Dolanıklık,
Bilinç,
Empati,
Beyin

Öz: Bu makalede beyindeki süperiletkenlik olgusu, süperiletkenliğin bazı özellikleri temel alınarak incelenmiştir. Hidrojen bazlı bileşiklerin ortam sıcaklığı ve basıncında süperiletken olma olasılığı, süperiletkenlik ile yüksek oranda su yani hidrojen içeren canlı organizmalar arasında bir analogi kurulmasına olanak sağlamıştır. Bu bağlamda, beyindeki nöronlarda bulunan mikrotübül yapılarında meydana gelen süperiletkenlik olgusu incelenmiş ve böylece beyin kuantum mekaniksel özellikleri açıklanmaya çalışılmıştır. Bilgisayar belleği gibi işlev görme davranışı, deoksiribonükleik asit hasarını onarmadaki rolü, beyne kuantum mekaniksel davranış kazandırma özelliği nedeniyle mikrotübüller çok ilginç organellerdir. Dolayısıyla süperiletkenlik kuantum dolaşıklığı ve bozonik durum gibi olağanüstü özellikleriyle uzun süreli hafıza, empati ve bilinç kavramları açısından insanlara yol gösterici olabilir.

1. INTRODUCTION

Superconductivity was discovered by Kamerlingh Onnes in 1911 at Leiden University in mercury at liquid helium temperature for the first time As the temperature decreases to a specific temperature value called as a critical transition temperature, T_c the resistance of the material disappears suddenly and superconductivity occurs in material [1]. Superconducting materials exhibit some interesting properties such as zero resistance below T_c , Meissner effect [2,3], Josephson junction tunneling [4], Bose-Einstein Condensation [5,6], quantum gravity [7,8] quantum entanglement [9], etc. These properties belonging of the superconductivity are of the collective behaviors of the superconducting material. First, general properties of a superconducting material have been

summarized in the article and then the phenomenon of superconductivity in living organisms especially in brain is examined from literature in detail. Then the analogy between superconductivity and brain has been made and investigated in the terms of consciousness, memory etc. Also, the study has tried to determine the relationships between some characteristics properties of human brain and quantum mechanics by guiding of superconductivity.

2. THE SOME CRUCIAL PROPERTIES OF SUPERCONDUCTORS

The most known property of the superconductivity is the zero resistivity of material under the critical transition temperature, T_c , as shown in Figure 1. This fundamental property of the superconductivity was discovered for

mercury by Kammerlingh Onnes in 1911 for the first time [1].

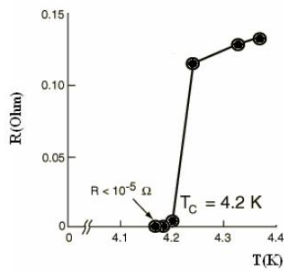


Figure 1. Discovery of superconductivity in mercury with zero electrical resistivity at 4.2K [10].

After the discovery of superconductivity in mercury, many metals, alloys and cuprates have been found to be superconducting at low temperatures. In the following years, studies on superconductors have been continued both in the search of materials with higher critical transition temperatures and in the establishment and development of theories to explain the physical origins of the phenomenon of superconductivity. In this context, the Bardeen-Cooper-Schrieffer (BCS) theory, the first theory of superconductivity, was derived in 1957. The BCS theory states that electron pairs called as Cooper pairs with opposite momentum and spin occur due to the electron-phonon interaction as shown in Figure 2. These quasi particles in superconducting material behave like bosonic particles due to their zero spin and hence occupy the same quantum state due to the quantum entanglement. Therefore, superconductors can be considered as giant quantum mechanical systems exhibiting Bose-Einstein Condensation (BEC) [11,12].

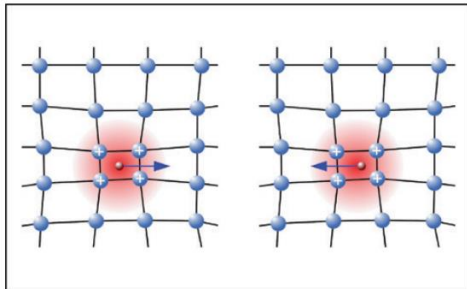


Figure 2. The formation of the Cooper (electron) pairs due to the attractive interaction between two electrons and phonons [13].

BEC in the quasi-2D copper oxide layered superconductors called as cuprates was suggested as the possible mechanism of superconductivity [5,14]. It was determined that with the plasma frequency, BEC in copper oxide layers extends to the whole layers in mercury based CuO_2 layered high temperature superconductors and hence three dimensional BEC were determined for superconducting material for the first time [15]. All electron pairs in the superconducting material have same wave function due to the BEC. Even if you break any electron pair in the superconducting system, the superconductivity in the system is destroyed.

The other main property of all superconductors is the Meissner effect. A superconducting material displays diamagnetic character [2,12,16]. Whereas in normal

state, the magnetic field applied to the sample penetrates to the material, it is completely expelled from the sample at superconducting state as seen in Figure 3. The magnetic levitation occurs due to expulsion of magnetic field from the superconducting sample. The magnetic field is completely expelled from the material in an ideal state while it penetrates a small shell of the surface of the superconducting material in reality [13].

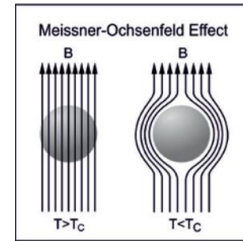


Figure 3. The schematic representation of Meissner effect at upper and below T_c [10].

Superconductors can be categorized as type I and II superconductors. Superconducting materials with type-I called low- T_c superconductivity are generally pure metals. Type-II called high- T_c superconductivity superconductors are alloys and oxides of ceramics. The Meissner effect manifests itself with perfect diamagnetism in the form of complete exclusion of magnetic flux up to a thermodynamically critical magnetic field value, H_c in type I superconductors as seen in Figure 4. In type II superconductors, the applied magnetic field is totally expelled from the type-II superconductor until the first critical field H_{c1} is reached. At magnetic field values above H_{c1} , the magnetic field penetrates the superconductor and vortices, which are the magnetic flux quantum, occur. In these regions where magnetic field penetrates to the sample, it is no longer superconductor. The rest of the material still has superconducting properties. If the magnetic field is increased to the second critical field, H_{c2} , the material is no longer superconducting. H_{c2} is generally upper than H_c of type I superconductors and this explains why type II superconductors are typically used for superconducting magnets [10,13].

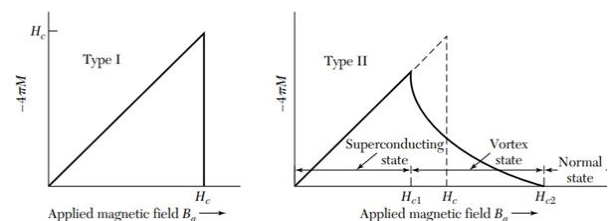


Figure 4. Magnetization versus applied magnetic field curve of type I and type II superconductors [3,10].

In 1962, the young theoretical physicist Brian Josephson observed two different physical phenomena at the Josephson junction (Figure 5), which consists of two superconducting layers separated by a thin insulating layer: d.c. and a.c. the Josephson effect [4].

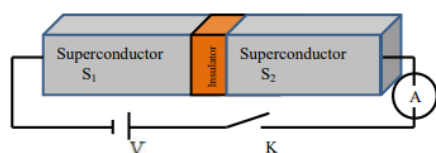


Figure 5. The schematic representation of ac Josephson junction [17].

In the dc Josephson Effect, even if no external voltage is applied to the Josephson junction, supercurrent flows through the junction as a result of electron pairs tunneling the junction, quantum mechanically. Cooper pairs (quasi-particles) in the superconducting regions in the right and left of the junction can be represented by an exponential wave function dependent on the phase difference. When no current flows in superconductors, since all Cooper pairs have the same phase, the system can be described by a single wave function. When superconductors are separated by a thin insulating layer, the wave functions of electron pairs on either side of the junction penetrate the insulator layer, locking them in same phase by quantum mechanical tunneling. In this case, without applying any voltage difference to the junction, a supercurrent proportional to this phase difference flows through the junction due to the phase difference $\Delta\phi$ between the wave functions of the electron pairs [18]. When a d.c. voltage difference is applied to the Josephson junction, an alternating supercurrent flows through the Josephson junction proportional to the voltage applied to the junction. The a.c supercurrent flowing through the Josephson junction can create electromagnetic fields within the junction. Relevant electromagnetic waves were first experimentally observed in 1965 [19].

The other property of the superconductors is quantum gravity phenomenon which has been observed at optimally doped mercury based superconductor for the first time. In mercury-based superconductor, at temperature lower than T_c , the effective mass of the quasi-particles is at maximum value and as an indicator of this event, the plasma frequency shifts from the microwave to the infrared region due to the quantum gravity [7,8].

3. THE SUPERCONDUCTIVITY IN LIVING ORGANISMS

Scientists have been studying that hydrogen-based compounds may be superconductor at ambient temperature and pressure. Some detailed analyses have shown that the highest critical temperatures for superconducting materials are achieved in the molecular and covalent hydrogen-hydrogen interaction materials [20]. Also, the small radius elements alloyed with hydrogen have new bonds instead of pure H-H bonds and these new bonds are more stable than H-H bonds [21]. In this context, materials containing hydrogen, such as living organisms are promising candidates to reach superconductivity at ambient temperature and pressure values.

In recent years, the number of studies on superconductivity and quantum processing of

information in living organism have been increasing [22]. Some studies have shown that living organisms being superconducting at room temperature exist in nature. The possibility of higher temperature superconductivity than the room temperature in organic polymers was proposed by W. A. Little in 1964 for the first time [23]. Mikheenko put forward a hypothesis that nature may have discovered the superconductivity in water being one of the most abundant substances in the planet very long time ago and he also stated that the enhanced coherence and quantum processing of information might be enabled by the properties of superconductivity. In this context, water might be the origin of the beginning of the existence of the intelligent life in the planet [22,24,25].

As is known, the ambient pressure like the chemical pressure affects the critical transition temperature of the superconducting system [26-28]. From this point of view, the high pressure is the other crucial parameter as well as water in other word hydrogen for appearing the intelligent life arisen from depth of oceans for the first time. Hydrogen being the lightest ion has very high phonon frequency leading to room temperature superconductivity and it has solid structure under high pressure environment [27]. The studies show that the superconductivity mechanism is related to the number of the hydrogen atoms. During water formation, extra oxygen from water could be release atmosphere and this explains initial high oxygen concentration on the early stages and also evaluation of life on the planet [22].

The studies show that brain water content in humans is approximately 75% for adults and 85% for infants [29]. There are some evidences that water could play essential role for formation of superconductivity and superconductivity could be responsible for coherent behavior of living organisms [24]. The brain and nervous system have the coherent features and could be analyzed by models developed for superconductivity [22]. Superconductivity in brain was suggested in 1972 to explain long-time memory and was explained that if there is room-temperature superconductivity, it should be in a system with high level of organization. Superconductivity in brain was also studied by Halpern and Wolf who explained that the superconductivity could be available in living organism and even consciousness of intelligent organisms [30].

The recent studies propound that if the dimensions of a material decreases, its critical temperature increases. William Little in 1964 developed a remarkable theory deriving very high critical temperature of about 2200 K in linear chains of organic molecules [23,25]. Microtubules being one dimensional structure with linear translational symmetry in living cells, which form the cytoskeleton, are organized as networks and in neurons [31]. It was suggested by scientists that superconductivity developing inside one dimensional microtubules inside neurons of brain could also be responsible for long-term memory [22,24]. Emily Toomey and her collogues suggested that the superconducting nanowires could be used for the

development of an artificial neuron. The artificial neuron has functions with multiple characteristics of biological neurons [32].

Neuromorphic computing systems are inspired by the biological concepts and functions of the human brain [33] and are of studying areas of artificial intelligence and machine learning applications [34]. Superconducting electronics including Josephson junctions and superconducting nanowires have been widely using in neuromorphic computing systems to provide bio-inspired functionality to the device. Neurons in brain exhibit the action potential and in order to make an analogy to action potential, Josephson junctions displaying naturally spiking behavior are used. Two Josephson junctions can imitate the ion channel dynamics observed in firing neurons, and the combination of nanowire resistor can simulate the relaxation oscillations determined in the brain due to the connections of several neurons [35]. Also it has been determined that Josephson junctions in conjunction with single photon detectors fulfill many neural operations occurring in brain and can be utilized to construct synapses for communication requiring a single photon [36].

It is supposed that the brain has a macroscopic quantum wave and quantum processes take in the cytoskeleton. The long-range coherent informational transfer in brain is explained by Bose-Einstein condensation. Nambu-Goldstone bosons, which are quanta of long-range correlation waves of aligned electric dipoles, are generated by the interaction between the water molecules and the local electromagnetic field in neurons [37,38].

Scientists Alain Aspect, John Clauser and Anton Zeilinger who took the Nobel physics award, have investigated entangled quantum states (Figure 6). In the quantum entanglement state, two quantum systems or quantum particles being entities lacking individuality [39] behave like a same system quantum mechanically and share the same quantum state. Due to this reason, the distance between two systems are not important, because they share same quantum state and have same collective attitude. The other crucial property of the entangled particles is that they should be opposite spin with same amplitude. In this point of view, a Cooper pair is considered as a quantum entangled system. Perfect quantum mechanical communication occurs between entangled systems [9]. Also, Anton Zeilinger and his research group have demonstrated that a phenomenon called quantum teleportation between particles is possible regardless of distance [40].



Figure 6. The schematic representation of quantum entanglement [41].

Brain, in which thoughts, intentions, dreams and ideas are created, is responsible for human awareness. The brain waves are produced by metabolic activities. If two individual entities can be considered as two independent human brains, their frequencies and corresponding energy levels in other words state of cognition are quantized. Hence, each state of mind is determined by quantum mechanical wave function. "Thought" has quantum mechanical wave character and one's thought cannot be read by any human made device because of collapsing of quantum wave function. The thought is in solitary wave character and the only possibility of reading of the thought is another brain. This situation is an example of quantum entanglement state between human beings [9]. In other way, when there is harmony between individuals, the flow of information between minds occurs without verbal communication. That is, for communication, individuals may not always need words or verbalizing.

4. DISCUSSION ON SUPERCONDUCTIVITY AND HUMAN BEINGS

Communication is the most important factor leading the formation of culture and civilization. In this context, the brain, in which thoughts, feelings, intentions and hopes are born, has important duties in the transmission of correct information. Hence, the brain and of course neurons have crucial missions and the connection between neurons and empathy is also known.

It has been reported that there is a big correlation between mirror neuron systems and empathy. Many studies have investigated that the mirror neuron system is involved in empathy and emotions. Functions of mirror neurons depend on the anatomy and physiological properties of the brain. As it is known, mirror neurons create a direct link between the sender of a message and the receiver of the message. Mirror neurons shaped the civilization provide a mechanism for action-understanding, imitation-learning, and the simulation of other people's behavior [42].

An individual who is an empath gives importance to the feelings and thoughts of other people and feels /knows their feelings/thoughts from their behaviors and actions and s/he experiences the same situation as if they were her/his own feelings. The question of "what makes these people with nonverbal communication skills different from other people" becomes important at this point. It is supposed that the mirror neurons of empaths who may exhibit quantum entanglement feature, work more actively and neurons have superconducting microtubule structures, too. In this context, it can be deduced that the neurons of empath people may contain more superconducting microtubules and in this case they may affect the brain waves of the person.

The collapse of the entangled states occurs due to the decoherence. Because of environment-induced decoherence, quantum systems settle into classical states and behave classically [43]. Hence, in which state entanglement occurs, is important. The highest states of

being of the eternal program must be the state of entanglement. The reality is obvious only in this state. Tegmark found that decoherence time scale in the brain is in 10^{-20} to 10^{-13} s. Characteristic processes in neuron activity in human brains, which are slower than the decoherence time scale, are in the order of 10^{-3} to 10^{-1} s [44]. The probability of the collapse of a system consisting of entangled particles can be calculated by using the hitting frequency, f which is as a function of total mass of entangled particles. If the frequency of the system is very low, the collapse of the system is nearly impossible. It has been still continuing some arguments which frequency values are very low or not. In this context, philosophical and phenomenological approaches rather than that of scientific are more guiding [45].

According to Ehret and Raymond, animals without systems of attention and long-term memory do not experience awareness of the content of something or consciousness about something to do [46]. Das says that the image of consciousness is stored as binary data in the microtubules structures of the neurons like computer memory [47]. Hence, the genetic structure of the living organisms affects the awareness and consciousness. It has been shown that the microtubule structures of some animals are different [48] and microtubules are also known to play a role in deoxyribonucleic acid (DNA) damage repair [49].

As is known, by using Josephson junction and superconducting nanowires, the artificial neurons are constructed and they display perfect communication between them. Another unusual property of superconductivity is its behavior in the presence of vortices being the non-superconducting regions in superconductor. Although superconducting system has vortices, it tries continuing superconducting properties. Because, by the spatial resonance, entities called vortices formed in a superconducting system are pinned and the superconducting system continues to exist. In this situation, vortices are non-functional entities. In short, in cases where the number of entangled states is greater, the vortices have no effect on the system.

4. DISCUSSION AND CONCLUSION

In this article, the analogy between superconductivity in the brain and superconducting systems has been investigated, especially in the context of the concepts of consciousness and empathy.

The mind's reactions to events shape the system and this can be considered as a part of the evolutionary processes of the systems. As it is known, intelligent systems want to protect their own security and the development of systems is managed and supported by minds. In this context, the superconductivity may conceptually guide us. In this study, superconductivity with its extraordinary properties such as the, quantum entanglement and bosonic state can be an important starting point for the positive change of individuals or systems in terms of long-term memory, empathy and consciousness.

Acknowledgement

I would like to thank Prof.Dr.Ülker Onbaşlı for her unforgettable conversations and guidance since the first day I met her.

REFERENCES

- [1] Onnes, H.K. The Superconductivity of Mercury. *Comm. Phys. Lab. Univ., Leiden*, (1911); 122-124.
- [2] Hirsch J.E. The origin of the Meissner effect in new and old superconductors. *Phys. Scr*, (2012); 85, 035704.
- [3] Kittel C. *Introduction to Solid State Physics*, John Wiley & Sons, Inc., New York (1996).
- [4] Josephson B.D. Possible New Effects in Superconducting Tunneling. *Phys. Lett.* (1962); 1/7, 251-253.
- [5] Adhikari S.K., Casas M., Puente A., Rigo A., Fortes M., Solís M.A, et al., Superconductivity as a Bose-Einstein condensation?, *Physica C.* (2000); 341-348, 233-236.
- [6] Casas M., de Llano M., Puente A., Rigo A., Solís M.A. Two-dimensional Bose Einstein condensation in cuprate superconductors. *Solid State Commun*, (2002); 123/3, 101-106.
- [7] Onbaşlı Ü., Güven Özdemir Z. Superconductors and Quantum Gravity. In: Luiz A. M. editor. *Superconductor*, Sciyu Company Press, India, 2010. pp. 291-310.
- [8] Aslan Çataltepe Ö. Mercury cuprates bring symmetry breaking of the universe to laboratory. In: Onbaşlı Ü. editor. *Lifetime of the Waves from Nano to Solitons in My Life*, Transworld Research Network, Kerala, India. 2012. pp 215-243.
- [9] Onbaşlı Ü.: Towards the logic of everything. In: Onbaşlı Ü. editor. *Lifetime of the Waves from Nano to Solitons in My Life*, Transworld Research Network, Kerala, India, 2012.
- [10] Ketterson, J.B., Song, S.N. *Superconductivity*, Cambridge University Press, 1999.
- [11] Cooper L.N. Bound electron pairs in a degenerate Fermi gas. *Phys. Rev.* 1956; 104, 4.
- [12] Bardeen J., Cooper L.N., Schrieffer J.R. Theory of Superconductivity, *Phys. Rev.* 1957; 108, 5.
- [13] Bussmann-Holder A., Keller H. High-temperature superconductors: underlying physics and applications. *Z Naturforsch. Pt. B.* 2019; 75,1-13.
- [14] de Llano M., Sevilla F. J. Tapia S.: Cooper Pairs As Boson. *Int. J. M. P. B.* 2006; 20/20, 2931-2939.
- [15] Özdemir Z. G., Aslan Ö., Onbaşlı Ü. Terahertz oscillations in mercury cuprate superconductors. *Pramana - J Phys.* 2009; 73/4, 755-763.
- [16] Bardeen J. Theory of the Meissner Effect in Superconductors. *Phys. Rev.* 1955; 97, 1724.
- [17] Maruf H.M.A.R., Islam M.R., Chowdhury F.U.Z. Analogy Between Ac Josephson Junction Effects and Optical Phenomena In Superconductors. *J. Bangladesh Soc. Physiol.* 2018; 23&24, 105-113
- [18] Tinkham, M. *Introduction to Superconductivity*. McGraww-Hill Inc.,Singapore, Japan, 1996.
- [19] Langenberg D.N., Scalapino D.J., Taylor B.N., Eck R.E. Investigation of Microwave Radiation

- Emitted By Josephson Junction. *Phys. Rev. Lett.* 1965; 15/7 294-297.
- [20] Belli F., Novoa T., Contreras-García J., Errea I. Strong correlation between electronic bonding network and critical temperature in hydrogen based superconductors. *Nat. Commun.* 2021; 12, 538.
- [21] Zhang Z., Cui T., Hutcheon M. J., Shipley A. M., Song H., Du M., et al. Design Principles for High-Temperature Superconductors with a Hydrogen-Based Alloy Backbone at Moderate Pressure. *Phys. Rev. Lett.* 2022; 128/ 047001.
- [22] Mikheenko, P. Possible superconductivity in the brain, *J. Supercond. Nov. Magn.* 2019; 32, 1121–1134.
- [23] Little W.A. Possibility of Synthesizing an Organic Superconductor. *Phys. Rev.* 1964; 134, A1416.
- [24] Messori C. Deep into the Water: Exploring the Hydro-Electromagnetic and Quantum-Electrodynamic Properties of Interfacial Water in Living Systems. *OALib Journal*, 2019; 6/e5435.
- [25] Mikheenko P. Nano Superconductivity and Quantum Processing of Information in Living Organisms Mikrotubulus, IEEE International Conference on Nanomaterials: Applications & Properties (NAP-2020), Sumy, Ukraine, 2020.
- [26] Drozdov A.P., Erements M.I., Troyan, I., Ksenofontov A.V., Shylin, S.I. Conventional superconductivity at 203 kelvin at high pressures in the sulfur hydride system. *Nature*, 2015; 525, 73.
- [27] Kresin, V.Z. Paths to Room-Temperature Superconductivity. *J. Supercond. Nov. Magn.* 2018; 31, 611-617.
- [28] Marezio M., Licci F., Gauzzi A. The Effect of Chemical Pressure on Tc of Layered Cuprate Superconductors: Advances. In: Koshizuka N., Tajima S. editors. *Advances in Superconductivity XI*, Springer, Tokyo, 1999. pp 31–36.
- [29] Demel A., Wolf M., Poets C.F., Franz A.R.: Effect of different assumptions for brain water content on absolute measures of cerebral oxygenation determined by frequency-domain near-infrared spectroscopy in preterm infants: an observational study. *BMC Pediatr.* 2014; 14:206.
- [30] Halpern, E.H., Wolf, A.A. Speculations of Superconductivity in Biological and Organic Systems. In: Timmerhaus, K.D., editors. *Advances in Cryogenic Engineering*, vol 17. Springer, Boston, MA. 1972. pp 109–115.
- [31] Sanchez-Castro N., Palomino-Ovando M.A., Singh P., Sahu S., Toledo-Solano M., Faubert J. et al. Microtubules as One-Dimensional Crystals: Is Crystal-Like Structure the Key to the Information Processing of Living Systems?. *Crystals.* 2021; 11(3), 318.
- [32] Toomey E., Segall K., Berggren K. K. Design of a Power Efficient Artificial Neuron Using Superconducting Nanowires. *Front. Neurosci.* 2019; 13/933.
- [33] Christensen D.V., Dittmann R., Linares-Barranco B., Sebastian A., Gallo M.L., Redaelli A., Slesazek S. et al.; Roadmap on neuromorphic computing and engineering. *Neuromorph. Comput. Eng.* 2, 022501. (2022)
- [34] Schuman C.D., Kulkarni S.R., Parsa M., Mitchell J.P., Date P., Kay B. Opportunities for neuromorphic computing algorithms and applications. *Nat. Comput. Sci.* 2022; 2, 10–19.
- [35] Schneider M., Toomey E., Rowlands G., Shainline J., Tschirhart P., Segall K.: SuperMind: a survey of the potential of superconducting electronics for neuromorphic computing. *Supercond. Sci. Technol.* 2022; 35/ 5.
- [36] Shainline J.M., Buckley S.M., McCaughan A.N., Chiles J.T., Salim A.J., Castellanos-Beltran M. et al. Superconducting optoelectronic loop neurons. *J. Appl. Phys.* 2019; 126, 044902.
- [37] Georgiev D.D. [Internet]. 2004 Bose-Einstein condensation of tunneling photons in the brain cortex as a mechanism of conscious action. [cited 202309 June]. Available from https://www.researchgate.net/profile/Jerzy-Achimowicz/publication/259782781_tunnellingINtheBRAIN/links/00b4952dde3816aa59000000/tunnellingINtheBRAIN.pdf.
- [38] Alexiou, A., Rekkas, J. Superconductivity in Human Body; Myth or Necessity. In: Vlamos, P., Alexiou, A. editors. *GeNeDis 2014. Advances in Experimental Medicine and Biology*, vol 822. Springer, Cham. 2015; 53–58.
- [39] Dieks D., Lubberdink A. Identical Quantum Particles as Distinguishable Objects, *J. Gen. Philos. Sci.* 2022; 53:259–274
- [40] Aspect A., Clauser J.F., Zeilinger A. [Internet] For experiments with entangled photons, establishing the violation of bell inequalities and pioneering quantum information science, 2022 [cited 2023 25 April]. Available from <https://www.nobelprize.org/uploads/2022/10/advanced-physicsprize2022-2.pdf>.
- [41] Jarnestad J. [Internet] 2022 [cited 2023 June 26] Available from: <https://www.nobelprize.org/uploads/2022/10/press-physics2022-figure1.pdf>.
- [42] Acharya S., Shuklav S. Mirror neurons: enigma of the metaphysical modular brain. *J Nat Sci Biol Med.* 2012; 3/2, 118–124.
- [43] Everth T., Gurney L. Emergent Realities: Diffracting Barad within a quantum-realist ontology of matter and politics. *Euro. Jnl. Phil. Sci.* 2022; 12, 51.
- [44] Tegmark, M. Importance of quantum decoherence in brain processes. *Phys. Rev. E.* 2000; 61(4), 4194–4206.
- [45] Koons R.C. Powers ontology and the quantum revolution. *Eur. J. Philos. Sci.* 2021; 11/ 14.
- [46] Ehret G., Romand R. Awareness and consciousness in humans and animals–neural and behavioral correlates in an evolutionary perspective. *Front. Syst. Neurosci.* 2022; 16, 941534.
- [47] Das T. Origin and storage of consciousness. *NeuroQuantology*, 2015; 13/1, 108-110.
- [48] Baas P.W., Rao A. N., Matamoros A. J., Leo L. Stability properties of neuronal microtubules. *Cytoskeleton (Hoboken)*, 2016; 73(9), 442–460.

- [49] Kim J. M.: Molecular Link between DNA Damage Response and Microtubule Dynamics. *Int J Mol Sci.* 2022; 23(13), 6986.

Aurora Kinases: Their Role in Cancer and Cellular Processes

Sibel SARI^{1*} , Elif Rumeysa ÖZSOY² 

¹Abdullah Gul University, Faculty of Life and Natural Sciences, Department of Molecular Biology and Genetics, Kayseri, Türkiye

²Abdullah Gul University, Graduate School of Engineering and Science, Department of Bioengineering, Kayseri, Türkiye

Sibel SARI ORCID No: 0000-0002-2505-5804

Elif Rumeysa ÖZSOY ORCID No: 0009-0008-6040-9875

*Corresponding author: sibel.sari@agu.edu.tr

(Received: 30.04.2023, Accepted: 14.05.2024, Online Publication: 28.06.2024)

Keywords

Aurora kinases,
Serine/Threonine
kinases,
Cancer,
Cell cycle
regulators,
Oncogenes

Abstract: Aurora kinases, belonging to a highly conserved family of serine/threonine kinases with critical roles in the regulation of the cell cycle, comprise three members: Aurora kinase A, B, and C, which serve as key mitotic regulators essential for maintaining chromosome stability. Aurora kinases play crucial roles in multiple events in mitotic such as the coordination of chromosomal and cytoskeletal events, regulation of the spindle assembly checkpoint pathway and cytokinesis to ensure the smooth progression of the cell cycle. Besides their mitotic functions, Aurora kinases are also involved in the regulation of meiosis. Gene amplification/mutation and overexpression of Aurora kinases have been detected in various solid and haematological cancers. In human tumours, Aurora kinases exhibit oncogenic roles associated with their mitotic roles, which drive the cancer cell proliferation and survival. Deregulation of Aurora kinase activity causes failure in centrosome function, spindle assembly, chromosomal alignment, and cytokinesis, eventually resulting in the mitotic abnormalities and genetic instability. These findings emphasize the crucial functions of Aurora kinases in cancer, prompting their recognition as valuable targets for cancer therapy. This review provides an overview of the structures and functions of Aurora kinases and sheds light on their oncogenic roles in cancer.

Aurora Kinazların Kanser ve Hücresel Süreçlerdeki Rolü

Anahtar Kelimeler

Aurora kinazlar,
Serin/Treonin
kinazlar,
Kanser,
Hücre döngüsü
düzenleyicileri,
Onkogenler

Öz: Aurora kinazlar, Aurora A, B ve C şeklinde tanımlanan üç üyeye sahip, hücre döngüsünün düzenlenmesinde kritik rolleri olan yüksek oranda korunmuş serin/treonin kinaz ailesine ait proteinlerdir. Aurora kinazlar, kromozom stabilitesinin korunmasında önemli rolleri olan mitotik düzenleyiciler olarak hizmet etmektedir. Mitozdaki çeşitli olaylarda kritik roller üstlenen Aurora kinazlar, kromozomal ve sitoskeletal olayların koordinasyonu, iğ ipliği oluşumu kontrolü ve sitokinez gibi olaylarda görev alarak hücre döngüsünün sorunsuz ilerlemesini sağlamaktadır. Mitotik fonksiyonlarının yanı sıra, Aurora kinazlar mayoz bölünmenin düzenlenmesi süreçlerinde de yer almaktadırlar. Aurora kinazların gen amplifikasyonu/mutasyonu ve aşırı ifadesi çeşitli solid ve hematolojik kanserlerde tespit edilmiştir. Aurora kinazlar mitotik rolleri ile ilişkilendirilen onkojenik fonksiyonları ile kanser hücrelerinin çoğalması ve hayatta kalmalarını sağlamaktadırlar. Aurora kinaz aktivitesinin bozulması, sentrozom fonksiyonunda, iğ ipliklerinin oluşumunda, kromozomal hizalanmada ve sitokineзде sorunlara neden olarak mitotik anormallikler ve genetik istikrarsızlığa yol açmaktadır. Bu bulgular, Aurora kinazların kanserdeki önemli fonksiyonlarını vurgulayarak kanser terapötikleri için değerli hedefler olarak tanınmalarını sağlamaktadır. Bu derleme, Aurora kinazların yapı ve fonksiyonlarına genel bir bakış sunarak, bu kinazların kanserdeki onkojenik rollerini aydınlatmaktadır.

1. INTRODUCTION

1.1 Aurora Kinases

Aurora kinases (AURKs) belong to the family of serine/threonine kinases that serve as mitotic regulators with crucial roles in various molecular events and structures involved in cell division such as centrosome duplication, chromosome condensation and separation, kinetochore-microtubule interactions, mitotic spindle formation, and completion of cytokinesis [1,2]. Aurora kinases are not only involved in the regulation of different steps during cell division but also contribute to the regulation of checkpoints that ensure proper cell cycle progression. Therefore, precisely coordinated temporal and spatial functions of Aurora kinases are crucial for maintaining chromosomal and genomic integrity during mitotic and meiotic processes (Figure 1) [3]. Because of their fundamental roles in cell cycle regulation, Aurora kinases were first identified in the late 1980s through genetic screening aimed at identifying the genes involved in controlling cell division. They were named after *Drosophila melanogaster* mutants displaying spindle defects resembling the phenomenon of the Northern Lights, also known as Aurora borealis [4]. Subsequently, additional homologs of Aurora kinases have been identified across in various species. In *Drosophila*, a second Aurora homolog was discovered, while *Caenorhabditis elegans* possesses two Aurora-related kinases, namely AIR-1/Aurora A and AIR-2/Aurora B [5,6]. In the budding yeast *Saccharomyces cerevisiae*, the single Aurora kinase gene, Ipl1 (Increased in Ploidy 1), has been detected, and phylogenetic trees show that Aurora members evolved from this single ancestor gene originating in *Urochordata* [7]. Similar to *Drosophila* and *C. elegans*, non-mammalian vertebrates such as the frog *Xenopus* possess two kinases, Aurora-A and -B [8]. Unlike other eukaryotes, only mammals have a third Aurora kinase called Aurora-C [9].



Figure 1. Functional diversity of Aurora kinases (AURKs) [2]

1.1.1. Structure and Functions of Aurora Kinases

Three Aurora kinases have been identified in humans: Aurora kinase A (AURKA), Aurora kinase B (AURKB) and Aurora kinase C (AURKC). Although AURKA and

AURKB are ubiquitously expressed, the cellular distribution of AURKC is limited to meiotic cells including sperms and oocytes [10]. The size of Aurora kinases ranges from 309 to 403 amino acids, and they are composed of three domains: a highly conserved catalytic domain (250–300aa) involving the activation T-loop, a short C-terminal domain (15–20aa) regulating protein levels via proteasomal degradation and an N-terminal domain (39–139aa) with different lengths between kinases providing their different localization inside cells (Figure 2). Moreover, Aurora kinases have different percentages of homology in their catalytic domains as follows: 60% between AURKA and AURKC, 71% between AURKA and AURKB and 75% between AURKB and AURKC [7]. Although Aurora kinases are similar to each other in terms of the structure of the highly conserved catalytic domain, their N-terminal can vary in size and sequence, which allows for selective protein-protein interactions [11]. All members of the Aurora kinases display differences in their localization, substrates, regulatory partners, and function. Aurora A primarily regulates centrosome maturation and the assembly of bipolar spindles, whereas Aurora B and C play essential roles in condensation, kinetochore attachment, chromosome alignment during (pro-) metaphase, and cytokinesis [7].

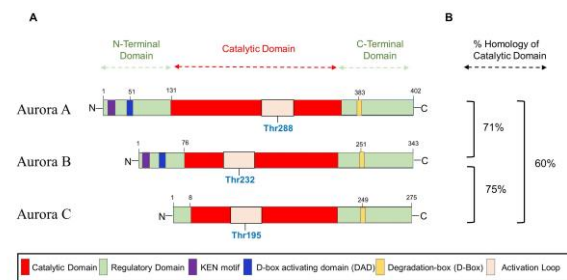


Figure 2. Structure and domains of Aurora kinases [7] Schematic representation of the Aurora A, B and C proteins with the indicated domains. The N-terminal and C-terminal domains contain regulatory motifs. The KEN regulatory motif is present in Aurora A and B and acts as an anaphase-promoting complex recognition signal. The D-box (Degradation Box) tag for ubiquitin identification and the D-box activating domain (DAD, or A-box), which is absent in Aurora B and C. Phosphorylation of conserved threonine residues at Thr288 (AURKA), Thr232 (AURKB) and Thr195 (AURKC), within the activation loop of the catalytic domain is required for kinase activity.

a. Percentages of homology of the catalytic domains are shown.

1.1.1.1. Aurora Kinase A (AURKA)

AURKA (also known as AIK, ARKI, STK6, STK7 and STK15) maps to the 20q13.2 human chromosomal region and its cellular distribution is ubiquitous [12]. AURKA activity of AURKA is regulated through multiple mechanisms including phosphorylation/dephosphorylation events and ubiquitin-mediated degradation [1]. The phosphorylation of AURKA by TPX2 (Targeting Protein for Xenopus kinesin-like protein 2) provides its activation and facilitates access to AURKA substrates. Moreover, the autophosphorylation of its activation segment at Thr288 (in humans) in the kinase domain is known to be critical for kinase activity [13]. Its inactivation can occur via the dephosphorylation of Thr288 by protein phosphatase 1 (PP1). During cell cycle

progression, AURKA proteins begin to localize around the replicated centrosomes during the S phase. Their activity and protein levels increased from the late G2 through to M phase. Finally, they undergo degradation by cadherin-1 (Cdh1)/anaphase-promoting complex/cyclosome complex (APC) during mitosis and mitotic exit [14]. AURKA is involved in the regulation of several mitotic events occurring from late S-phase through the M phase such as centrosome maturation and separation, formation of bipolar spindle by interacting pericentriolar material (PCM), stimulation of mitotic entry, chromosome alignment during metaphase, mitotic exit and cytokinesis [15,16]. AURKA also plays a crucial role in spindle orientation by regulating the localization of nuclear mitotic apparatus protein (NuMA), thereby organizing mitotic spindle poles and coordinating spindle orientation [17,18]. Studies of AURKA mutations in *Drosophila melanogaster* have demonstrated defective chromosome and centrosome segregations, leading to the formation of polyploid cells [19]. Furthermore, defective AURKA activity results in impaired PCM function which is crucial for microtubule anchoring, and impaired mitotic spindle assembly, causing a transient spindle checkpoint-dependent mitotic arrest and subsequent apoptotic cell death [3,20]. Similarly, reduced AURKA activity results in proper NuMA distribution during metaphase, consequently impairing the orientation of bipolar spindles [12]. Apart from mitosis, AURKA plays a role in meiosis by stimulating oocyte maturation, polar-body extrusion, spindle positioning, and metaphase I exit [1]. Consequently, the diverse involvement of AURKA throughout cell division underscores its critical functions and potential implications during this dynamic period of cellular activity.

1.1.1.2. Aurora Kinase B (AURKB)

AURKB (also known as *AIK2*, *AIM1*, *ARK2*, *AIRK2*, *IPL1*, *STK1*, *STK5*, and *STK12*) is located on the 17p13.1 human chromosomal region, and its expression, like AURKA, is ubiquitous [12]. The kinase activity and protein expression levels of Aurora kinase B change based on the stages of cell cycle progression, and its expression peaks at the transition from G2 to M phase and functions until the end of mitosis [11]. Mainly, AURKB plays crucial roles in chromosome condensation, alignment and biorientation, spindle-assembly checkpoint, kinetochore-microtubule interaction, direction of metaphase-to-anaphase transition process and completion of cytokinesis [21,22]. In early mitosis, AURKB localizes to in the inner centromere, where it phosphorylates histone H3 on Serine residues Ser10 and Ser28 and recruits other proteins of the large Chromosomal Passenger Complex (CPC) protein complex. AURKB acts as a kinase module of CPC with three non-enzymatic subunits: survivin, borealin and inner centromere protein (INCENP), to ensure accurate chromosome segregation [23]. During prophase, AURKB binds to and phosphorylates INCENP. This binding, in turn, triggers AURKB auto-phosphorylation of Thr232 within the activation loop of the catalytic domain, altering its conformation to induce kinase activity. Subsequently, the binding of survivin and borealin proteins completes the CPC. In prometaphase, AURKB, as part of the CPC,

localizes to the kinetochores, and it is subjected to spindle assembly checkpoints (SAC), which play a role in the correction of impaired spindle kinetochore attachments. During the transition from metaphase to anaphase, AURKB relocates to the microtubules, ensuring proper alignment and segregation of sister chromatids. During late mitosis, AURKB phosphorylates several proteins, including vimentin and Rac-GTPase activating protein-1 (MgcRacGAP-1), which are involved in the formation of the cleavage furrow to complete cytokinesis [7,22,24]. Apart from its mitotic roles, AURKB extends its functionality to the DNA damage response (DDR), a critical process that determines cell fate by directing cells to either repair damage or undergo self-destruction [25]. AURKB suppresses the activity of the p53 protein by phosphorylating it at various subcellular regions, including S183, T211, and S215. This phosphorylation leads to rapid degradation of p53 through the polyubiquitination-proteasome pathway. This results in the downregulation of p53 target genes involved in regulating the cell cycle and apoptosis [11]. Furthermore, during meiosis, AURKB localizes to chromosomes at metaphase, where it regulates kinetochore-microtubule attachments and chromosome alignment, and to the spindle midzone during anaphase to facilitate cytokinesis [26]. Inhibition of AURKB leads to defective chromosome alignment and dysfunctional mitotic spindle checkpoint, resulting in impaired cytokinesis and endoreduplication followed by apoptosis induction [20]. In summary, the pivotal role of AURKB in orchestrating various aspects of cell division highlights its ability to maintain genomic stability and ensure the accurate chromosomal segregation during cell division processes.

1.1.1.3. Aurora Kinase C (AURKC)

A third and the most elusive member of the Aurora kinase family, *AURKC* (also known as *AIK3*, *AIE2*, *ARK3*, and *STK13*), maps to the 19q13.43 human chromosomal region, and its expression is predominantly in meiotically dividing gametes [10,12]. AURKC is predominantly expressed at its highest level in the mammalian testis, whereas low expression is detected in several somatic cells such as the placenta, lung, bladder, and skeletal muscle [27]. Aurora C protein and mRNA levels are low during the S phase and peak in the G2/M phase [28]. Similar to AURKB in mitosis, AURKC is the catalytic module of CPC and plays a role in the regulation of kinetochore-microtubule attachments, chromosome segregation, SAC, and cytokinesis in meiosis [29]. Therefore, as a member of the CPC, the subcellular localization of Aurora C was found to be similar to that of Aurora B [27]. AURKC also concentrates on the microtubule-organizing center to keep the integrity of bipolar spindles and coordinates the localization and function of both AURKA and AURKB in meiotic cells [29]. Regarding the regulation of AURKC, similar to AURKA and AURKB, autophosphorylation of a threonine within the activation loop activates the kinase activity of AURKC. However, AURKC lacks protein degradation markers, such as KEN and D-box activating domain motifs found in AURKA and AURKB, suggesting that they are differentially regulated.

Additionally, this situation also demonstrates that AURKC provides a longer-lasting form of AURKB during meiosis [10,30]. Several studies have shown that defective AURKC in male mice results in blunted sperm heads, abnormalities in acrosome detachment and chromatin condensation, highlighting the critical role of AURKC in male fertility [31]. Moreover, mutations in AURKC cause meiotic arrest in meiosis-I [32], resulting in larger sperms with multiple flagella and misshapen heads, a condition called macrozoospermia [10,33]. Similar to male mice, AURKC deletion causes subfertility and arrests embryonic development in female mice owing to abnormalities in meiosis [34].

1.1.2. Aurora Kinases and Cancer

The connection between Aurora kinases and cancer development relies on their crucial functions in different stages of the cell cycle. As mentioned above, these mitotic kinases are essential for maintaining genomic integrity and proper cell division, playing critical roles in mitotic entry, centrosome and kinetochore function, spindle assembly, microtubule dynamics, spindle assembly checkpoint, chromosome segregation, and cytokinesis. Consequently, any dysregulation of Aurora kinase activity can cause mitotic abnormalities and genetic

instability. Given that genetic instability, and subsequently to uncontrolled cell proliferation, constitutes a hallmark of tumorigenesis, the aberrant expression of Aurora kinases may emerge as a potential catalyst for cancer development [35]. Overexpression and/or gene amplifications of AURKs has been demonstrated in various human cancers (Figure 3). Moreover, AURKA, B, and C exhibited intrinsic instability, with frequent defects, amplifications, and mutational regions identified at 20q13.2, 17p13.1, and 10q13, respectively. These observations highlight the abnormal expression of Aurora kinases in human cancers, offering a clear explanation for their dysregulation in such contexts [14]. Overexpression of AURKA and AURKB is frequently observed in aneuploid tumours, which constitute approximately 90% of human malignancies [7,36] and gene amplification of AURKs has been linked to chemotherapy resistance and higher grades of malignancy [37]. Despite the overexpression and/or gene amplifications, there is no reported evidence of a natural deficiency of AURKs in human tumours thus far [14]. Moreover, Aurora kinase gene polymorphisms have been found to be related to an increased risk or early onset of cancer [38]. These findings underscore the intricate role of Aurora kinases in cancer pathogenesis and highlight their potential implications for therapeutic strategies.

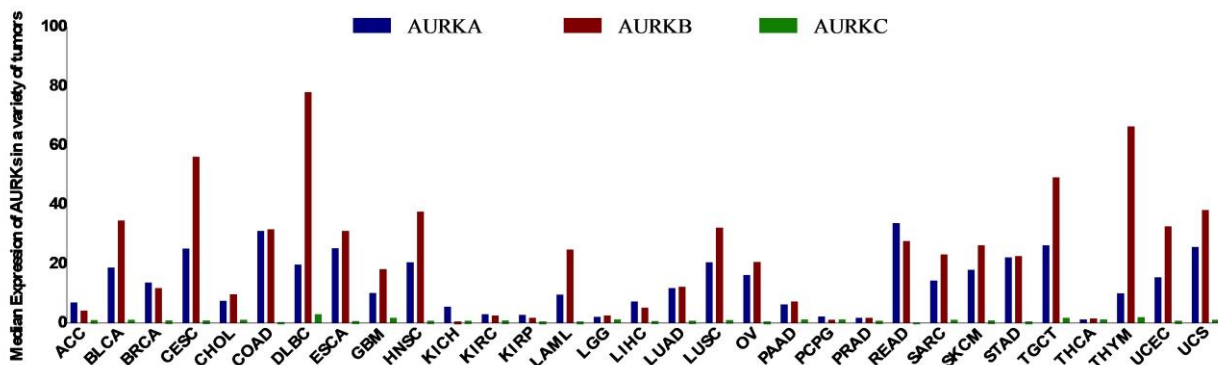


Figure 3. The median expression of AURKs in a variety of tumours. The data is obtained from Gene Expression Profiling Interactive Analysis (GEPIA) [39]. ACC—Adrenocortical carcinoma, BLCA—Bladder Urothelial Carcinoma, BRCA—Breast invasive carcinoma, CESC—Cervical squamous cell carcinoma and endocervical adenocarcinoma, CHOL—Cholangio carcinoma, COAD—Colon adenocarcinoma, DLBC—Lymphoid Neoplasm Diffuse Large B-cell Lymphoma, ESCA—Esophageal carcinoma, GBM—Glioblastoma multiforme, HNSC—Head and Neck squamous cell carcinoma, KICH—Kidney Chromophobe, KIRC—Kidney renal clear cell carcinoma, KIRP—Kidney renal papillary cell carcinoma, LGG—Brain Lower Grade Glioma, LIHC—Liver hepatocellular carcinoma, LUAD—Lung adenocarcinoma, LUSC—Lung squamous cell carcinoma, OV—Ovarian serous cystadenocarcinoma, PAAD—Pancreatic adenocarcinoma, PCPG—Pheochromocytoma and Paraganglioma, PRAD—Prostate adenocarcinoma, READ—Rectum adenocarcinoma, SARC—Sarcoma, SKCM—Skin Cutaneous Melanoma, STAD—Stomach adenocarcinoma, TGCT—Testicular Germ Cell Tumours, THCA—Thyroid carcinoma, THYM—Thymoma, UCEC—Uterine Corpus Endometrial Carcinoma, UCS—Uterine Carcinosarcoma

1.1.2.1. Aurora Kinase A in Cancer

Aurora kinase A is a bona-fide oncogene, and its expression in tumours is frequently related to gene amplification, genetic instability, malignant transformation, poor histological differentiation, and prognosis [38]. Amplification of AURKA has been observed in various solid and haematological cancers (Table 1). Furthermore, AURKA tissue expression has been demonstrated to be a predictive and prognostic factor in several cancers, including colorectal, breast and gastric tumours [7]. High AURKA expression stimulates carcinogenesis by promoting epithelial-mesenchymal

transition (EMT), metastasis, cancer cell proliferation, self-renewal of cancer stem cells, and resistance to apoptosis [40]. Mutation or upregulation of AURKA also leads to therapeutic resistance such as cisplatin resistance, by enhancing the DNA repair pathway [37]. In addition to the well-known phenomenon of overexpression of Aurora kinase A, it can interact with a variety of other proteins, including tumour suppressors and oncogenes, thus contributing to carcinogenesis. AURKA interacts with tumour suppressor genes that control centrosome duplication, cell cycle checkpoints and chromosomal stability, thereby contributing to centrosome amplification and cytokinesis failure. For instance,

AURKA interacts with the p53 tumour suppressor at multiple levels through phosphorylation of Ser315 residues, which enhances Mdm2-mediated p53 degradation [28], and on Ser215, which inactivates its transcriptional activity [41], subsequently inhibiting downstream targets such as PTEN and p21 [42]. Another tumour suppressor protein associated with AURKA, BRCA1, is involved in coordinating DNA replication with the centrosome duplication cycle. Phosphorylation of BRCA1 by AURKA at Ser308 disrupts the G2/M checkpoint, leading to centrosome amplification and chromosomal instability [43]. Regarding the relationship between oncogenes and AURKA, it has been found that AURKA facilitates the oncogenic effects of well-known oncogenes such as Myc and FOXM1 in cancers, and that the overexpression or activation of these oncogenes and AURKA are frequently found together in human cancers [14,44]. Furthermore, AURKA engages with a multitude of substrates crucial in various cancer-promoting signalling pathways, notably polo-like kinase 1 (PLK1), β -catenin, and Akt. PLK1 acts as a pivotal cell cycle regulator, with its phosphorylation at the Thr210 region by AURKA being linked to essential processes like chromosome segregation, spindle assembly, and centrosome maturation [45]. AURKA's role is required for the activation of PLK1 to stimulate mitotic entry [46]. Overexpression of AURKA promotes PLK1 activity, accelerating centrosome amplification, chromosomal instability, faulty chromosomal segregation, and ultimately tumorigenesis [43]. Moreover, AURKA contributes to the downregulation of β -catenin and E-cadherin expression that is pivotal in regulating cell-cell adhesion, thereby promoting EMT [14]. In human osteosarcoma cells, AURKA stimulates the phosphorylation of Akt and mTOR oncoproteins to increase the tumorigenicity [47]. Consequently, aberrant AURKA expression drives tumorigenesis by enhancing proliferation, evading apoptosis, inducing EMT, and promoting genomic instability. Given its critical role in cancer development, AURKA emerges as a potential target for cancer therapy. In this regard, several small molecules designed to inhibit AURKA have been developed. These inhibitors have undergone preclinical testing, and some have advanced to clinical trials, either as monotherapies or in combination with traditional treatments [40].

1.1.2.2. Aurora Kinase B in Cancer

Aurora B is frequently expressed at high levels in several human cancers, and its expression level has been related to aneuploidy and genetic instability [38]. AURKB overexpression has been detected in a wide range of human cancers (Table 1). Overexpression of AURKB promotes the impaired chromosome segregation, cytokinesis failure and chromosome lagging in metaphase in cancer cells [48]. In addition, AURKB plays a significant role in tumorigenesis by interacting with specific proteins, including the MYC oncogenic protein, Breakpoint Cluster Region-Abelson Leukemia (Bcr-Abl) oncoprotein, p53, and Cyclin-dependent kinase 1 (Cdk1) [11]. In human retinoblastoma, the direct regulation of AURKB by MYCN, a member of the MYC proto-

oncogene family, has been elucidated, highlighting the enrichment of a MYCN binding motif on the AURKB promoter [22]. Additionally, the upregulation of both AURKA and AURKB by c-MYC has been demonstrated in B-cell lymphoma [49]. Furthermore, Jiang et al. (2020) showed that AURKB stabilizes the MYC oncoprotein by phosphorylating it at the Ser67 position in T-cell acute lymphoblastic leukemia [50]. The Bcr-Abl oncoprotein, a product of the Philadelphia chromosome in human leukemias, is associated with constitutively activated tyrosine kinase, which plays a role in regulating various biological processes such as survival, invasion, growth, and angiogenesis in carcinogenesis [51,52]. Yang et al. (2014) showed that the Bcr-Abl oncoprotein stimulates the expression of both AURKA and AURKB via the AKT signalling pathway to promote clonogenic growth [53]. Furthermore, another study revealed that the progression of Chronic Myeloid Leukemia, a neoplastic disease arising from hematopoietic stem cells driven by the BCR-ABL oncogene, is associated with the aberrant expression of the AURKB gene [54]. Importantly, AURKB induces proteasome-mediated degradation of p53 by phosphorylating it at the Ser183, Thr211, and Ser215 regions to suppress its activity [11]. In addition, AURKB suppresses the expression of downstream target genes regulated by p53, thereby contributing to cell cycle inhibition. For instance, the overexpression of AURKB reduces the level of the p53 target p21Cip1 (cyclin-dependent kinase-interacting protein-1), known as a cell cycle inhibitor, and its inverse correlation has been demonstrated in human leukemias. This illustrates the contribution of AURKB to tumorigenesis by suppressing the activity of the cell cycle inhibitor p21Cip1 and promoting chromosomal instability [55]. Additionally, the decreased expression of the cell cycle inhibitor p21Cip1 by AURKB causes abnormal activation of Cdk1, allowing cell cycle progression and thus promoting cell survival. Moreover, Cdk1 induces the activation of the acetyltransferase TIP60, resulting in the acetylation and activation of AURKB, which in turn leads to aneuploidy and uncontrolled cell cycle progression [14]. In addition to its pivotal roles in tumorigenesis, the overexpression of AURKB also serves as a significant indicator of disease progression and overall survival in various cancers. Studies have demonstrated its association with reduced overall survival in metastatic colorectal cancer [56] and breast cancer [57]. Similarly, patients with adenocarcinoma subtype of non-small cell lung carcinoma exhibit notably shorter survival times when AURKB is overexpressed in their tumour cells [58]. Moreover, AURKB expression correlates with poor prognosis and is often observed in higher grades of malignancy across various neoplastic lesions, suggesting its potential utility as a prognostic marker and predictor for aggressive tumours [59]. Furthermore, AURKB expression has been investigated as a prognostic marker in gastric cancer [60], oral cancer [61] and glioblastoma [62]. Variants of AURKB in hepatocellular carcinoma have been linked to advanced stages, poor prognosis, and tumour recurrence [63]. Notably, in colorectal cancer, prostate cancer, ovarian, and thyroid carcinomas, the degree of AURKB overexpression is directly proportional to disease grade or dedifferentiation status, indicating its

role in disease progression [64–68]. High expression of AURKB was detected in papillary and anaplastic thyroid carcinomas, the, with further overexpression observed in advanced stages, suggesting a growth advantage for neoplastic cells [59,68,69]. This evidence points to the targeting of AURKB for cancer therapy and the development of small AURKB inhibitors. These inhibitors have been extensively studied in preclinical and clinical studies across various tumour types [70].

1.1.2.3. Aurora Kinase C in Cancer

AURKC is highly expressed in several cancers (Table 1). Even though AURKC overexpression has been observed across various cancer types, its precise oncogenic function remains unclear due to insufficient understanding of its role within the cellular context [71]. However, it is hypothesized that AURKC may contribute to centrosome amplification and multinucleation in cancer cells, potentially providing a survival advantage [72]. Moreover, Bejar et al. (2021) demonstrated that meiotic gene activation can drive tumour progression, further highlighting the potential significance of AURKC as a

target for novel anti-cancer therapy [29]. Additionally, AURKC may exert an oncogenic role by phosphorylating several proteins involved in carcinogenesis, such as transforming acidic coiled-coil 1 protein (TACC1) [73] and telomeric-repeat binding factor 2 protein (TRF2) [74]. Notably, the overexpression of TACC1 has been shown to stimulate cell transformation and serve as a prognostic marker in breast cancer [75,76]. Similarly, TRF2 plays a critical role in telomere length regulation, and its phosphorylation by AURKC has been implicated in promoting tumorigenesis by reducing telomere length [10,74,77]. In conclusion, investigating the normal function of AURKC in meiotic cells through ongoing studies is essential for a comprehensive understanding of its role in cancer progression. While AURKA and AURKB have been extensively studied in this context, the association of AURKC in carcinogenesis remains relatively unexplored, with only a few AURKC inhibitors developed thus far [78]. Therefore, further investigation into AURKC's role in cancer and the development of targeted inhibitors may reveal new therapeutic options for cancer treatment and prevention.

Table 1. Summary of Aurora kinases and their overexpression/amplification in a wide range of tumour types [14].

Kinases	Localization	Function	Tumour Types	References
AURKA	Centrosome Spindle microtubule Midbody	Mitotic entry, Centrosome maturation/separation, Bipolar spindle microtubule formation, Chromosome alignment, Cytokinesis, Mitosis exit	Breast cancer	[79,80]
			Cervical cancer	[81,82]
			Colorectal cancer	[83,84]
			Esophageal squamous cell carcinoma	[85,86]
			Gastric/Gastrointestinal cancer	[87,88]
			Glioma	[89,90]
			Leukemia	[91,92]
			Lung cancer	[93,94]
			Oral cancer	[95,96]
			Ovarian cancer	[97,98]
Prostate cancer	[99,100]			
AURKB	Chromosome Kinetochore Midbody	Chromosome condensation, Chromosome Alignment, Chromosome Biorientation, Regulating SAC Kinetochore-microtubule-interaction, Cytokinesis	Breast cancer	[80,101]
			Cervical cancer	[102]
			Colorectal cancer	[103,104]
			Gastric/Gastrointestinal cancer	[87]
			Glioma	[89,105]
			Leukemia	[106]
			Lung cancer	[107,108]
			Oral cancer	[61,109]
			Ovarian cancer	[98,110]
			Prostate cancer	[100,111]
Tyroid Cancer	[68]			
AURKC	Chromosome Midbody	Kinetochore-Microtubule Attachment, Regulating SAC, Meiotic chromosome segregation Cytokinesis	Breast cancer	[112]
			Cervical cancer	[113,114]
			Colorectal cancer	[114,115]
			Glioma	[105]
			Prostate cancer	[100,112]

2. CONCLUSION

The Aurora kinase family offers a novel perspective for understanding the processes of mitosis, carcinogenesis, and their potential relationship. Aurora kinases serve as mitotic regulators and play an indispensable role in cell cycle progression. They interact with various partners to sustain their kinase activity and influence numerous downstream targets, including critical tumour suppressor

proteins and oncoproteins. Therefore, exploring the link between interacting substrates and their effects on Aurora kinase regulation is significant, highlighting the importance of establishing regulatory networks for each Aurora kinase. Notably, the deregulation of a single mitotic regulator can significantly increase the risk of tumorigenesis. Amplification and overexpression of Aurora kinases have been found in numerous human tumours, and their aberrant expression triggers oncogenic

transformation, leading to the deregulation of multiple tumour suppressor and oncoprotein-regulated pathways. This ultimately results in genomic instability and tumorigenesis. The extensive network of Aurora kinases, encompassing different protein-protein interactions across a wide range of signalling pathways, supports the choice of Aurora kinases as potent targets for further exploration in drug discovery. The development of Aurora kinase inhibitors with fewer side effects and enhanced pharmacokinetic efficiency is required to counteract the overexpression of Aurora kinases and the deregulation of associated kinases involved in carcinogenesis. Therefore, Aurora kinases have emerged as promising targets to inhibit tumour cell growth and revealing the molecular functions of Aurora kinases will yield valuable insights for comprehending cell cycle control and provide novel strategies for drug design in cancer therapy.

Acknowledgement

We would like to express our gratitude to Mehmet Emin Orhan for his valuable assistance in editing this manuscript.

REFERENCES

- [1] Carmena M, Earnshaw WC. The cellular geography of aurora kinases. *Nat Rev Mol Cell Biol* 2003;4:842–54. <https://doi.org/10.1038/nrm1245>.
- [2] Moreira-Nunes CA, Mesquita FP, Portilho AJ de S, Mello Júnior FAR, Maués JH da S, Pantoja L da C, et al. Targeting aurora kinases as a potential prognostic and therapeutical biomarkers in pediatric acute lymphoblastic leukaemia. *Sci Rep* 2020;10:21272. <https://doi.org/10.1038/s41598-020-78024-8>.
- [3] Mou PK, Yang EJ, Shi C, Ren G, Tao S, Shim JS. Aurora kinase A, a synthetic lethal target for precision cancer medicine. *Exp Mol Med* 2021;53:835–47. <https://doi.org/10.1038/s12276-021-00635-6>.
- [4] Glover DM, Leibowitz MH, McLean DA, Parry H. Mutations in aurora prevent centrosome separation leading to the formation of monopolar spindles. *Cell* 1995;81:95–105. [https://doi.org/10.1016/0092-8674\(95\)90374-7](https://doi.org/10.1016/0092-8674(95)90374-7).
- [5] Schumacher JM, Golden A, Donovan PJ. AIR-2: An Aurora/Ipl1-related Protein Kinase Associated with Chromosomes and Midbody Microtubules Is Required for Polar Body Extrusion and Cytokinesis in *Caenorhabditis elegans* Embryos. *The Journal of Cell Biology* 1998;143:1635. <https://doi.org/10.1083/jcb.143.6.1635>.
- [6] Schumacher JM, Ashcroft N, Donovan PJ, Golden A. A highly conserved centrosomal kinase, AIR-1, is required for accurate cell cycle progression and segregation of developmental factors in *Caenorhabditis elegans* embryos. *Development* 1998;125:4391–402. <https://doi.org/10.1242/dev.125.22.4391>.
- [7] Willems E, Dedobbeleer M, Digregorio M, Lombard A, Lumapat PN, Rogister B. The functional diversity of Aurora kinases: a comprehensive review. *Cell Div* 2018;13:7. <https://doi.org/10.1186/s13008-018-0040-6>.
- [8] Brown JR, Koretke KK, Birkeland ML, Sanseau P, Patrick DR. Evolutionary relationships of Aurora kinases: Implications for model organism studies and the development of anti-cancer drugs. *BMC Evolutionary Biology* 2004;4:39. <https://doi.org/10.1186/1471-2148-4-39>.
- [9] Bernard M, Sanseau P, Henry C, Couturier A, Prigent C. Cloning of STK13, a third human protein kinase related to *Drosophila aurora* and budding yeast Ipl1 that maps on chromosome 19q13.3-ter. *Genomics* 1998;53:406–9. <https://doi.org/10.1006/geno.1998.5522>.
- [10] Quartuccio SM, Schindler K. Functions of Aurora kinase C in meiosis and cancer. *Front Cell Dev Biol* 2015;3:50. <https://doi.org/10.3389/fcell.2015.00050>.
- [11] Borah NA, Reddy MM. Aurora Kinase B Inhibition: A Potential Therapeutic Strategy for Cancer. *Molecules* 2021;26:1981. <https://doi.org/10.3390/molecules26071981>.
- [12] Pandya PN, Mankad AU, Raval RM. Role of Aurora Kinases in Cancer: A Comprehensive Review. *RJLBPCS* 2018;04.
- [13] Garrido G, Vernos I. Non-centrosomal TPX2-Dependent Regulation of the Aurora A Kinase: Functional Implications for Healthy and Pathological Cell Division. *Front Oncol* 2016;6:88. <https://doi.org/10.3389/fonc.2016.00088>.
- [14] Tang A, Gao K, Chu L, Zhang R, Yang J, Zheng J. Aurora kinases: novel therapy targets in cancers. *Oncotarget* 2017;8:23937–54. <https://doi.org/10.18632/oncotarget.14893>.
- [15] Nikonova AS, Astsaturov I, Serebriiskii IG, Dunbrack RL, Golemis EA. Aurora A kinase (AURKA) in normal and pathological cell division. *Cell Mol Life Sci* 2013;70:661–87. <https://doi.org/10.1007/s00018-012-1073-7>.
- [16] Janeček M, Rossmann M, Sharma P, Emery A, Huggins DJ, Stockwell SR, et al. Allosteric modulation of AURKA kinase activity by a small-molecule inhibitor of its protein-protein interaction with TPX2. *Sci Rep* 2016;6:28528. <https://doi.org/10.1038/srep28528>.
- [17] Sun G, Rong D, Li Z, Sun G, Wu F, Li X, et al. Role of Small Molecule Targeted Compounds in Cancer: Progress, Opportunities, and Challenges. *Front Cell Dev Biol* 2021;9:694363. <https://doi.org/10.3389/fcell.2021.694363>.
- [18] Polverino F, Naso FD, Asteriti IA, Palmerini V, Singh D, Valente D, et al. The Aurora-A/TPX2 Axis Directs Spindle Orientation in Adherent Human Cells by Regulating NuMA and Microtubule Stability. *Curr Biol* 2021;31:658-667.e5. <https://doi.org/10.1016/j.cub.2020.10.096>.
- [19] Berdnik D, Knoblich JA. *Drosophila* Aurora-A is required for centrosome maturation and actin-dependent asymmetric protein localization during mitosis - PubMed 2002. <https://pubmed.ncbi.nlm.nih.gov/11967150/> (accessed April 4, 2024).

- [20] Kaestner P, Stolz A, Bastians H. Determinants for the efficiency of anticancer drugs targeting either Aurora-A or Aurora-B kinases in human colon carcinoma cells. *Mol Cancer Ther* 2009;8:2046–56. <https://doi.org/10.1158/1535-7163.MCT-09-0323>.
- [21] Li M, Liu H, Zhao Q, Han S, Zhou L, Liu W, et al. Targeting Aurora B kinase with Tanshinone IIA suppresses tumor growth and overcomes radioresistance. *Cell Death Dis* 2021;12:152. <https://doi.org/10.1038/s41419-021-03434-z>.
- [22] Borah NA, Sradhanjali S, Barik MR, Jha A, Tripathy D, Kaliki S, et al. Aurora Kinase B Expression, Its Regulation and Therapeutic Targeting in Human Retinoblastoma. *Invest Ophthalmol Vis Sci* 2021;62:16. <https://doi.org/10.1167/iovs.62.3.16>.
- [23] Bavetsias V, Linardopoulos S. Aurora Kinase Inhibitors: Current Status and Outlook. *Front Oncol* 2015;5:278. <https://doi.org/10.3389/fonc.2015.00278>.
- [24] Titova E, Shagiya G, Dugina V, Kopnin P. The Role of Aurora B Kinase in Normal and Cancer Cells. *Biochemistry (Mosc)* 2023;88:2054–62. <https://doi.org/10.1134/S0006297923120088>.
- [25] Marima R, Hull R, Penny C, Dlamini Z. Mitotic syndicates Aurora Kinase B (AURKB) and mitotic arrest deficient 2 like 2 (MAD2L2) in cohorts of DNA damage response (DDR) and tumorigenesis. *Mutat Res Rev Mutat Res* 2021;787:108376. <https://doi.org/10.1016/j.mrrev.2021.108376>.
- [26] Nguyen AL, Schindler K. Specialize and Divide (Twice): Functions of Three Aurora Kinase Homologs in Mammalian Oocyte Meiotic Maturation. *Trends Genet* 2017;33:349–63. <https://doi.org/10.1016/j.tig.2017.03.005>.
- [27] Yan X, Wu Y, Li Q, Cao L, Liu X, Saiyin H, et al. Cloning and characterization of a novel human Aurora C splicing variant. *Biochem Biophys Res Commun* 2005;328:353–61. <https://doi.org/10.1016/j.bbrc.2004.12.168>.
- [28] Katayama H, Sasai K, Kawai H, Yuan Z-M, Bondaruk J, Suzuki F, et al. Phosphorylation by aurora kinase A induces Mdm2-mediated destabilization and inhibition of p53. *Nat Genet* 2004;36:55–62. <https://doi.org/10.1038/ng1279>.
- [29] Bejar JF, DiSanza Z, Quartuccio SM. The oncogenic role of meiosis-specific Aurora kinase C in mitotic cells. *Experimental Cell Research* 2021;407:112803. <https://doi.org/10.1016/j.yexcr.2021.112803>.
- [30] Abdul Azeez KR, Chatterjee S, Yu C, Golub TR, Sobott F, Elkins JM. Structural mechanism of synergistic activation of Aurora kinase B/C by phosphorylated INCENP. *Nat Commun* 2019;10:3166. <https://doi.org/10.1038/s41467-019-11085-0>.
- [31] Kimmins S, Crosio C, Kotaja N, Hirayama J, Monaco L, Höög C, et al. Differential functions of the Aurora-B and Aurora-C kinases in mammalian spermatogenesis. *Mol Endocrinol* 2007;21:726–39. <https://doi.org/10.1210/me.2006-0332>.
- [32] Dieterich K, Soto Rifo R, Faure AK, Hennebicq S, Ben Amar B, Zahi M, et al. Homozygous mutation of AURKC yields large-headed polyploid spermatozoa and causes male infertility. *Nat Genet* 2007;39:661–5. <https://doi.org/10.1038/ng2027>.
- [33] Ounis L, Zoghmar A, Coutton C, Rouabah L, Hachemi M, Martinez D, et al. Mutations of the aurora kinase C gene causing macrozoospermia are the most frequent genetic cause of male infertility in Algerian men. *Asian J Androl* 2015;17:68–73. <https://doi.org/10.4103/1008-682X.136441>.
- [34] Schindler K, Davydenko O, Fram B, Lampson MA, Schultz RM. Maternally recruited Aurora C kinase is more stable than Aurora B to support mouse oocyte maturation and early development. *Proceedings of the National Academy of Sciences* 2012;109:E2215–22. <https://doi.org/10.1073/pnas.1120517109>.
- [35] Gavriilidis P, Giakoustidis A, Giakoustidis D. Aurora Kinases and Potential Medical Applications of Aurora Kinase Inhibitors: A Review. *J Clin Med Res* 2015;7:742–51. <https://doi.org/10.14740/jocmr2295w>.
- [36] Sansregret L, Swanton C. The Role of Aneuploidy in Cancer Evolution. *Cold Spring Harb Perspect Med* 2017;7:a028373. <https://doi.org/10.1101/cshperspect.a028373>.
- [37] Gupta D, Kumar M, Saifi S, Rawat S, Ethayathulla AS, Kaur P. A comprehensive review on role of Aurora kinase inhibitors (AKIs) in cancer therapeutics. *Int J Biol Macromol* 2024;265:130913. <https://doi.org/10.1016/j.ijbiomac.2024.130913>.
- [38] Gautschi O, Heighway J, Mack PC, Purnell PR, Lara PN, Gandara DR. Aurora kinases as anticancer drug targets. *Clin Cancer Res* 2008;14:1639–48. <https://doi.org/10.1158/1078-0432.CCR-07-2179>.
- [39] Tang Z, Li C, Kang B, Gao G, Li C, Zhang Z. GEPIA: a web server for cancer and normal gene expression profiling and interactive analyses. *Nucleic Acids Res* 2017;45:W98–102. <https://doi.org/10.1093/nar/gkx247>.
- [40] Du R, Huang C, Liu K, Li X, Dong Z. Targeting AURKA in Cancer: molecular mechanisms and opportunities for Cancer therapy. *Mol Cancer* 2021;20:15. <https://doi.org/10.1186/s12943-020-01305-3>.
- [41] Liu Q, Kaneko S, Yang L, Feldman RI, Nicosia SV, Chen J, et al. Aurora-A abrogation of p53 DNA binding and transactivation activity by phosphorylation of serine 215. *J Biol Chem* 2004;279:52175–82. <https://doi.org/10.1074/jbc.M406802200>.
- [42] Fu J, Bian M, Jiang Q, Zhang C. Roles of Aurora kinases in mitosis and tumorigenesis. *Mol Cancer Res* 2007;5:1–10. <https://doi.org/10.1158/1541-7786.MCR-06-0208>.
- [43] D'Assoro AB, Haddad T, Galanis E. Aurora-A Kinase as a Promising Therapeutic Target in Cancer. *Front Oncol* 2016;5:295. <https://doi.org/10.3389/fonc.2015.00295>.
- [44] Naso FD, Boi D, Ascanelli C, Pamfil G, Lindon C, Paiardini A, et al. Nuclear localisation of Aurora-A: its regulation and significance for Aurora-A functions in cancer. *Oncogene* 2021;40:3917–28. <https://doi.org/10.1038/s41388-021-01766-w>.

- [45] Lin X, Xiang X, Hao L, Wang T, Lai Y, Abudoureyimu M, et al. The role of Aurora-A in human cancers and future therapeutics. *Am J Cancer Res* 2020;10:2705–29.
- [46] Tavernier N, Thomas Y, Vigneron S, Maisonneuve P, Orlicky S, Mader P, et al. Bora phosphorylation substitutes in trans for T-loop phosphorylation in Aurora A to promote mitotic entry. *Nat Commun* 2021;12:1899. <https://doi.org/10.1038/s41467-021-21922-w>.
- [47] Taga M, Hirooka E, Ouchi T. Essential Roles of mTOR/Akt Pathway in Aurora-A Cell Transformation. *Int J Biol Sci* 2009;5:444–50.
- [48] Dar AA, Goff LW, Majid S, Berlin J, El-Rifai W. Aurora Kinases' Inhibitors – Rising Stars in Cancer Therapeutics? *Mol Cancer Ther* 2010;9:268. <https://doi.org/10.1158/1535-7163.MCT-09-0765>.
- [49] den Hollander J, Rimpì S, Doherty JR, Rudelius M, Buck A, Hoellein A, et al. Aurora kinases A and B are up-regulated by Myc and are essential for maintenance of the malignant state. *Blood* 2010;116:1498–505. <https://doi.org/10.1182/blood-2009-11-251074>.
- [50] Jiang J, Wang J, Yue M, Cai X, Wang T, Wu C, et al. Direct Phosphorylation and Stabilization of MYC by Aurora B Kinase Promote T-cell Leukemogenesis. *Cancer Cell* 2020;37:200-215.e5. <https://doi.org/10.1016/j.ccell.2020.01.001>.
- [51] Druker BJ, Sawyers CL, Kantarjian H, Resta DJ, Reese SF, Ford JM, et al. Activity of a specific inhibitor of the BCR-ABL tyrosine kinase in the blast crisis of chronic myeloid leukemia and acute lymphoblastic leukemia with the Philadelphia chromosome. *N Engl J Med* 2001;344:1038–42. <https://doi.org/10.1056/NEJM200104053441402>.
- [52] Greuber EK, Smith-Pearson P, Wang J, Pendergast AM. Role of ABL family kinases in cancer: from leukaemia to solid tumours. *Nat Rev Cancer* 2013;13:559–71. <https://doi.org/10.1038/nrc3563>.
- [53] Yang J, Ikezoe T, Nishioka C, Udaka K, Yokoyama A. Bcr-Abl activates AURKA and AURKB in chronic myeloid leukemia cells via AKT signaling. *Int J Cancer* 2014;134:1183–94. <https://doi.org/10.1002/ijc.28434>.
- [54] Marsola APZC, Simões BP, Palma LC, Berzoti-Coelho MG, Burin SM, de Castro FA. Expression of Hippo signaling pathway and Aurora kinase genes in chronic myeloid leukemia. *Med Oncol* 2018;35:26. <https://doi.org/10.1007/s12032-018-1079-6>.
- [55] González-Loyola A, Fernández-Miranda G, Trakala M, Partida D, Samejima K, Ogawa H, et al. Aurora B Overexpression Causes Aneuploidy and p21Cip1 Repression during Tumor Development. *Mol Cell Biol* 2015;35:3566–78. <https://doi.org/10.1128/MCB.01286-14>.
- [56] Pohl A, Azuma M, Zhang W, Yang D, Ning Y, Winder T, et al. Pharmacogenetic profiling of Aurora kinase B is associated with overall survival in metastatic colorectal cancer. *Pharmacogenomics J* 2011;11:93–9. <https://doi.org/10.1038/tj.2010.18>.
- [57] Huang D, Huang Y, Huang Z, Weng J, Zhang S, Gu W. Relation of AURKB over-expression to low survival rate in BCRA and reversine-modulated aurora B kinase in breast cancer cell lines. *Cancer Cell Int* 2019;19:166. <https://doi.org/10.1186/s12935-019-0885-z>.
- [58] Vischioni B, Oudejans JJ, Vos W, Rodriguez JA, Giaccone G. Frequent overexpression of aurora B kinase, a novel drug target, in non-small cell lung carcinoma patients. *Mol Cancer Ther* 2006;5:2905–13. <https://doi.org/10.1158/1535-7163.MCT-06-0301>.
- [59] Chieffi P. Aurora B: A new promising therapeutic target in cancer. *Intractable Rare Dis Res* 2018;7:141–4. <https://doi.org/10.5582/irdr.2018.01018>.
- [60] Nie M, Wang Y, Yu Z, Li X, Deng Y, Wang Y, et al. AURKB promotes gastric cancer progression via activation of CCND1 expression. *Aging (Albany NY)* 2020;12:1304–21. <https://doi.org/10.18632/aging.102684>.
- [61] Qi G, Ogawa I, Kudo Y, Miyauchi M, Siriwardena BSMS, Shimamoto F, et al. Aurora-B expression and its correlation with cell proliferation and metastasis in oral cancer. *Virchows Arch* 2007;450:297–302. <https://doi.org/10.1007/s00428-006-0360-9>.
- [62] Zeng WF, Navaratne K, Prayson RA, Weil RJ. Aurora B expression correlates with aggressive behaviour in glioblastoma multiforme. *J Clin Pathol* 2007;60:218–21. <https://doi.org/10.1136/jcp.2006.036806>.
- [63] Yasen M, Mizushima H, Mogushi K, Obulhasim G, Miyaguchi K, Inoue K, et al. Expression of Aurora B and alternative variant forms in hepatocellular carcinoma and adjacent tissue. *Cancer Science* 2009;100:472–80. <https://doi.org/10.1111/j.1349-7006.2008.01068.x>.
- [64] Tatsuka M, Katayama H, Ota T, Tanaka T, Odashima S, Suzuki F, et al. Multinuclearity and increased ploidy caused by overexpression of the aurora- and Ipl1-like midbody-associated protein mitotic kinase in human cancer cells. *Cancer Res* 1998;58:4811–6.
- [65] Chieffi P, Cozzolino L, Kisslinger A, Libertini S, Staibano S, Mansueto G, et al. Aurora B expression directly correlates with prostate cancer malignancy and influence prostate cell proliferation. *The Prostate* 2006;66:326–33. <https://doi.org/10.1002/pros.20345>.
- [66] Sinisi AA, Chieffi P, Pasquali D, Kisslinger A, Staibano S, Bellastella A, et al. EPN: a novel epithelial cell line derived from human prostate tissue. *In Vitro Cell Dev Biol Anim* 2002;38:165–72. [https://doi.org/10.1290/1071-2690\(2002\)038<0165:EANACL>2.0.CO;2](https://doi.org/10.1290/1071-2690(2002)038<0165:EANACL>2.0.CO;2).
- [67] Staibano S, Franco R, Mezza E, Chieffi P, Sinisi A, Pasquali D, et al. Loss of oestrogen receptor beta, high PCNA and p53 expression and aneuploidy as markers of worse prognosis in ovarian granulosa cell tumours. *Histopathology* 2003;43:254–62. <https://doi.org/10.1046/j.1365-2559.2003.01706.x>.
- [68] Sorrentino R, Libertini S, Pallante PL, Troncone G, Palombini L, Bavetsias V, et al. Aurora B overexpression associates with the thyroid carcinoma undifferentiated phenotype and is

- required for thyroid carcinoma cell proliferation. *J Clin Endocrinol Metab* 2005;90:928–35. <https://doi.org/10.1210/jc.2004-1518>.
- [69] Libertini S, Abagnale A, Passaro C, Botta G, Barbato S, Chieffi P, et al. AZD1152 negatively affects the growth of anaplastic thyroid carcinoma cells and enhances the effects of oncolytic virus dl922-947. *Endocrine-Related Cancer* 2010;18:129–41. <https://doi.org/10.1677/ERC-10-0234>.
- [70] Nguyen TT, Silva FN, Golemis EA. Aurora Kinases as Therapeutic Targets in Head and Neck Cancer. *Cancer J* 2022;28:387–400. <https://doi.org/10.1097/PPO.0000000000000614>.
- [71] Stefani A, Piro G, Schietroma F, Strusi A, Vita E, Fiorani S, et al. Unweaving the mitotic spindle: A focus on Aurora kinase inhibitors in lung cancer. *Front Oncol* 2022;12:1026020. <https://doi.org/10.3389/fonc.2022.1026020>.
- [72] Khan J, Ezan F, Crémet J-Y, Fautrel A, Gilot D, Lambert M, et al. Overexpression of Active Aurora-C Kinase Results in Cell Transformation and Tumour Formation. *PLoS One* 2011;6:e26512. <https://doi.org/10.1371/journal.pone.0026512>.
- [73] Gabillard J-C, Ulisse S, Baldini E, Sorrenti S, Cremet J-Y, Cocco C, et al. Aurora-C interacts with and phosphorylates the transforming acidic coiled-coil 1 protein. *Biochem Biophys Res Commun* 2011;408:647–53. <https://doi.org/10.1016/j.bbrc.2011.04.078>.
- [74] Spengler D. The protein kinase Aurora C phosphorylates TRF2. *Cell Cycle* 2007;6:2579–80. <https://doi.org/10.4161/cc.6.20.4781>.
- [75] Cully M, Shiu J, Piekorz RP, Muller WJ, Done SJ, Mak TW. Transforming acidic coiled coil 1 promotes transformation and mammary tumorigenesis. *Cancer Res* 2005;65:10363–70. <https://doi.org/10.1158/0008-5472.CAN-05-1633>.
- [76] Ghayad SE, Vendrell JA, Bieche I, Spyrtos F, Dumontet C, Treilleux I, et al. Identification of TACC1, NOV, and PTTG1 as new candidate genes associated with endocrine therapy resistance in breast cancer. *J Mol Endocrinol* 2009;42:87–103. <https://doi.org/10.1677/JME-08-0076>.
- [77] Shamma MA. Telomeres, lifestyle, cancer, and aging. *Curr Opin Clin Nutr Metab Care* 2011;14:28–34. <https://doi.org/10.1097/MCO.0b013e32834121b1>.
- [78] Umene K, Banno K, Kisu I, Yanokura M, Nogami Y, Tsuji K, et al. Aurora kinase inhibitors: Potential molecular-targeted drugs for gynecologic malignant tumors. *Biomed Rep* 2013;1:335–40. <https://doi.org/10.3892/br.2013.91>.
- [79] Cirak Y, Furuncuoglu Y, Yapicier O, Aksu A, Cubukcu E. Aurora A overexpression in breast cancer patients induces taxane resistance and results in worse prognosis. *J BUON* 2015;20:1414–9.
- [80] Hole S, Pedersen AM, Lykkesfeldt AE, Yde CW. Aurora kinase A and B as new treatment targets in aromatase inhibitor-resistant breast cancer cells. *Breast Cancer Res Treat* 2015;149:715–26. <https://doi.org/10.1007/s10549-015-3284-8>.
- [81] Sun J-M, Yang L-N, Xu H, Chang B, Wang H-Y, Yang G. Inhibition of Aurora A promotes chemosensitivity via inducing cell cycle arrest and apoptosis in cervical cancer cells. *Am J Cancer Res* 2015;5:1133–45.
- [82] Gabrielli B, Bokhari F, Ranall MV, Oo ZY, Stevenson AJ, Wang W, et al. Aurora A Is Critical for Survival in HPV-Transformed Cervical Cancer. *Mol Cancer Ther* 2015;14:2753–61. <https://doi.org/10.1158/1535-7163.MCT-15-0506>.
- [83] Casorzo L, Dell'Aglio C, Sarotto I, Risio M. Aurora kinase A gene copy number is associated with the malignant transformation of colorectal adenomas but not with the serrated neoplasia progression. *Human Pathology* 2015;46:411–8. <https://doi.org/10.1016/j.humpath.2014.11.016>.
- [84] Saiprasad G, Chitra P, Manikandan R, Sudhandiran G. Hesperidin induces apoptosis and triggers autophagic markers through inhibition of Aurora-A mediated phosphoinositide-3-kinase/Akt/mammalian target of rapamycin and glycogen synthase kinase-3 beta signalling cascades in experimental colon carcinogenesis. *Eur J Cancer* 2014;50:2489–507. <https://doi.org/10.1016/j.ejca.2014.06.013>.
- [85] Jin S, Wang X, Tong T, Zhang D, Shi J, Chen J, et al. Aurora-A enhances malignant development of esophageal squamous cell carcinoma (ESCC) by phosphorylating β -catenin. *Mol Oncol* 2015;9:249–59. <https://doi.org/10.1016/j.molonc.2014.08.002>.
- [86] Wang X, Li X, Li C, He C, Ren B, Deng Q, et al. Aurora-A modulates MMP-2 expression via AKT/NF- κ B pathway in esophageal squamous cell carcinoma cells. *Acta Biochim Biophys Sin (Shanghai)* 2016;48:520–7. <https://doi.org/10.1093/abbs/gmw030>.
- [87] Honma K, Nakanishi R, Nakanoko T, Ando K, Saeki H, Oki E, et al. Contribution of Aurora-A and -B expression to DNA aneuploidy in gastric cancers. *Surg Today* 2014;44:454–61. <https://doi.org/10.1007/s00595-013-0581-x>.
- [88] Katsha A, Belkhiri A, Goff L, El-Rifai W. Aurora kinase A in gastrointestinal cancers: time to target. *Mol Cancer* 2015;14:106. <https://doi.org/10.1186/s12943-015-0375-4>.
- [89] Premkumar DR, Jane EP, Pollack IF. Cucurbitacin-I inhibits Aurora kinase A, Aurora kinase B and survivin, induces defects in cell cycle progression and promotes ABT-737-induced cell death in a caspase-independent manner in malignant human glioma cells. *Cancer Biol Ther* 2015;16:233–43. <https://doi.org/10.4161/15384047.2014.987548>.
- [90] Reichardt W, Jung V, Brunner C, Klein A, Wemmert S, Romeike BFM, et al. The putative serine/threonine kinase gene STK15 on chromosome 20q13.2 is amplified in human gliomas. *Oncology Reports* 2003;10:1275–9. <https://doi.org/10.3892/or.10.5.1275>.
- [91] Kim S-J, Jang JE, Cheong J-W, Eom J-I, Jeung H-K, Kim Y, et al. Aurora A kinase expression is increased in leukemia stem cells, and a selective Aurora A kinase inhibitor enhances Ara-C-induced apoptosis in acute myeloid leukemia stem cells. *Korean J Hematol* 2012;47:178–85. <https://doi.org/10.5045/kjh.2012.47.3.178>.

- [92] Wei T-YW, Wu P-Y, Wu T-J, Hou H-A, Chou W-C, Teng C-LJ, et al. Aurora A and NF- κ B Survival Pathway Drive Chemoresistance in Acute Myeloid Leukemia via the TRAF-Interacting Protein TIFA. *Cancer Res* 2017;77:494–508. <https://doi.org/10.1158/0008-5472.CAN-16-1004>.
- [93] Lo Iacono M, Monica V, Saviozzi S, Ceppi P, Bracco E, Papotti M, et al. Aurora Kinase A expression is associated with lung cancer histological-subtypes and with tumor de-differentiation. *J Transl Med* 2011;9:100. <https://doi.org/10.1186/1479-5876-9-100>.
- [94] Gu J, Gong Y, Huang M, Lu C, Spitz MR, Wu X. Polymorphisms of STK15 (Aurora-A) gene and lung cancer risk in Caucasians. *Carcinogenesis* 2007;28:350–5. <https://doi.org/10.1093/carcin/bgl149>.
- [95] Tatsuka M, Sato S, Kitajima S, Suto S, Kawai H, Miyauchi M, et al. Overexpression of Aurora-A potentiates HRAS-mediated oncogenic transformation and is implicated in oral carcinogenesis. *Oncogene* 2005;24:1122–7. <https://doi.org/10.1038/sj.onc.1208293>.
- [96] Tanaka H, Nakashiro K, Iwamoto K, Tokuzen N, Fujita Y, Shirakawa R, et al. Targeting Aurora kinase A suppresses the growth of human oral squamous cell carcinoma cells in vitro and in vivo. *Oral Oncol* 2013;49:551–9. <https://doi.org/10.1016/j.oraloncology.2013.02.002>.
- [97] Do T-V, Xiao F, Bickel LE, Klein-Szanto AJ, Pathak HB, Hua X, et al. Aurora kinase A mediates epithelial ovarian cancer cell migration and adhesion. *Oncogene* 2014;33:539–49. <https://doi.org/10.1038/onc.2012.632>.
- [98] Davidson B, Nymoen DA, Elgaaen BV, Staff AC, Tropé CG, Kærn J, et al. BUB1 mRNA is significantly co-expressed with AURKA and AURKB mRNA in advanced-stage ovarian serous carcinoma. *Virchows Arch* 2014;464:701–7. <https://doi.org/10.1007/s00428-014-1577-7>.
- [99] Toughiri R, Li X, Du Q, Bieberich CJ. Phosphorylation of NuMA by Aurora-A kinase in PC-3 prostate cancer cells affects proliferation, survival, and interphase NuMA localization. *J Cell Biochem* 2013;114:823–30. <https://doi.org/10.1002/jcb.24421>.
- [100] Lee ECY, Frolov A, Li R, Ayala G, Greenberg NM. Targeting Aurora kinases for the treatment of prostate cancer. *Cancer Res* 2006;66:4996–5002. <https://doi.org/10.1158/0008-5472.CAN-05-2796>.
- [101] Zhang Y, Jiang C, Li H, Lv F, Li X, Qian X, et al. Elevated Aurora B expression contributes to chemoresistance and poor prognosis in breast cancer. *Int J Clin Exp Pathol* 2015;8:751–7.
- [102] Twu N-F, Yuan C-C, Yen M-S, Lai C-R, Chao K-C, Wang P-H, et al. Expression of Aurora kinase A and B in normal and malignant cervical tissue: high Aurora A kinase expression in squamous cervical cancer. *Eur J Obstet Gynecol Reprod Biol* 2009;142:57–63. <https://doi.org/10.1016/j.ejogrb.2008.09.012>.
- [103] Tuncel H, Shimamoto F, Kaneko Guangying Qi H, Aoki E, Jikihara H, Nakai S, et al. Nuclear Aurora B and cytoplasmic Survivin expression is involved in lymph node metastasis of colorectal cancer. *Oncol Lett* 2012;3:1109–14. <https://doi.org/10.3892/ol.2012.633>.
- [104] Subramaniam B, Kumar V, Mathan G. Effect of sodium salt of Butrin, a novel compound isolated from *Butea monosperma* flowers on suppressing the expression of SIRT1 and Aurora B kinase-mediated apoptosis in colorectal cancer cells. *Biomed Pharmacother* 2017;90:402–13. <https://doi.org/10.1016/j.biopha.2017.03.086>.
- [105] Diaz RJ, Golbourn B, Shekarforoush M, Smith CA, Rutka JT. Aurora kinase B/C inhibition impairs malignant glioma growth in vivo. *J Neurooncol* 2012;108:349–60. <https://doi.org/10.1007/s11060-012-0835-2>.
- [106] Hartsink-Segers SA, Zwaan CM, Exalto C, Luijendijk MWJ, Calvert VS, Petricoin EF, et al. Aurora kinases in childhood acute leukemia: the promise of aurora B as therapeutic target. *Leukemia* 2013;27:560–8. <https://doi.org/10.1038/leu.2012.256>.
- [107] Takeshita M, Koga T, Takayama K, Ijichi K, Yano T, Maehara Y, et al. Aurora-B overexpression is correlated with aneuploidy and poor prognosis in non-small cell lung cancer. *Lung Cancer* 2013;80:85–90. <https://doi.org/10.1016/j.lungcan.2012.12.018>.
- [108] Smith SL, Bowers NL, Betticher DC, Gautschi O, Ratschiller D, Hoban PR, et al. Overexpression of aurora B kinase (AURKB) in primary non-small cell lung carcinoma is frequent, generally driven from one allele, and correlates with the level of genetic instability. *Br J Cancer* 2005;93:719–29. <https://doi.org/10.1038/sj.bjc.6602779>.
- [109] Pannone G, Hindi S a. H, Santoro A, Sanguedolce F, Rubini C, Cincione RI, et al. Aurora B expression as a prognostic indicator and possible therapeutic target in oral squamous cell carcinoma. *Int J Immunopathol Pharmacol* 2011;24:79–88. <https://doi.org/10.1177/039463201102400110>.
- [110] Chen Y-J, Chen C-M, Twu N-F, Yen M-S, Lai C-R, Wu H-H, et al. Overexpression of Aurora B is associated with poor prognosis in epithelial ovarian cancer patients. *Virchows Arch* 2009;455:431–40. <https://doi.org/10.1007/s00428-009-0838-3>.
- [111] Fadri-Moskwik M, Weiderhold KN, Deeraksa A, Chuang C, Pan J, Lin S-H, et al. Aurora B is regulated by acetylation/deacetylation during mitosis in prostate cancer cells. *FASEB J* 2012;26:4057–67. <https://doi.org/10.1096/fj.12-206656>.
- [112] Zekri A, Lesan V, Ghaffari SH, Tabrizi MH, Modarressi MH. Gene amplification and overexpression of Aurora-C in breast and prostate cancer cell lines. *Oncol Res* 2012;20:241–50. <https://doi.org/10.3727/096504013x13589503482978>.
- [113] Fujii S, Srivastava V, Hegde A, Kondo Y, Shen L, Hoshino K, et al. Regulation of AURKC expression by CpG island methylation in human cancer cells. *Tumor Biol* 2015;36:8147–58. <https://doi.org/10.1007/s13277-015-3553-5>.

- [114] Tsou J-H, Chang K-C, Chang-Liao P-Y, Yang S-T, Lee C-T, Chen Y-P, et al. Aberrantly expressed AURKC enhances the transformation and tumorigenicity of epithelial cells. *J Pathol* 2011;225:243–54. <https://doi.org/10.1002/path.2934>.
- [115] Hosseini S, Hashemzadeh S, Estiar MA, Ebrahimzadeh R, Fakhree MBA, Yousefi B, et al. Expression Analysis of Aurora-C and Survivin, Two Testis-Specific Genes, in Patients with Colorectal Cancer. *Clin Lab* 2015;61:475–80. <https://doi.org/10.7754/clin.lab.2014.141017>.